

An Analysis of Flows within Cell Culture Bioreactors with Vortex Breakdown

This thesis is submitted in fulfillment of the requirements for the degree of
Doctor of Philosophy

Department of Mechanical Engineering
Monash University
February 2006.

Jonathan Charles Dusting B.E. (Honours)

Declaration of Originality

I, Jonathan Charles Dusting, declare that this thesis is my own work and contains no information previously submitted for another degree or diploma at any university or other institute. To the best of my knowledge, information derived from the published and unpublished work of others has been acknowledged in the text of the thesis and a list of references is given in the bibliography.

Jonathan Dusting February 2, 2006

Summary

Selection of mixing vessels for the purposes of mammalian cell or tissue culture is usually conducted with little consideration of the fluid dynamics, despite the importance of physical properties such as stress on the culture outcomes. This thesis describes a demonstration of how advanced experimental fluid dynamics may be used to identify favourable flow conditions within bioreactors. Vortex breakdown flows within a cylindrical vessel with a rotating bottom and a free surface were considered in the context of their potential use in cell culture applications.

A bioreactor model matching this configuration was constructed for the purposes of experimentation. Flows corresponding to a height ratio of 1.5 were analysed using both flow visualisation and quantitative measurements. The majority of the results were derived from three-component velocity measurements captured using Stereoscopic Particle Image Velocimetry.

The first part of the study constituted a characterisation of flows occurring in a cell-suspension scenario, i.e. when there are no stationary submerged scaffolds. The observed flows were consistent with descriptions in the literature, however the measured velocity detail exceeded that which has been previously published. Distributions of principal stress magnitudes and directions across the meridional plane were estimated from the velocity data. Topological changes in the vortex breakdown region with Reynolds number were reflected in a redistribution of the peak stress regions.

The second part of the study investigated flows where stationary scaffold models were submerged in the vicinity of the vortex breakdown region. It was found that vortex breakdown was retained for all the cases studied. The degree to which the recirculation was affected depended on the size and location of the disks, as well as the Reynolds number. Radial displacement of the disks from the axis of symmetry also affected the flow structure; in particular, the breakdown region geometry became progressively asymmetric as the displacement was increased. Wall shear stress distributions along the upper and lower surfaces of the scaffold model were

derived and compared across the various cases. Generally, the wall shear stress was of larger magnitude near the disk radius, however the measured distribution varied subtly with the input parameters.

Acknowledgments

Thanks go firstly to my academic advisors, Professor John Sheridan and Professor Kerry Hourigan, who have each provided me with an excellent quality of supervision and who have had a critical influence on the work presented in this thesis.

More broadly, I would like to acknowledge the personal financial support provided to me by the Monash Research Graduate School in the form of an Australian Postgraduate Award. Funding for the research was provided through the Monash University Research Fund and an Australian Research Council Discovery Grant (DP0452664).

Two of my colleagues deserve special mention for their assistance. Mr. Andreas Fouras is thanked for his assistance in setting up the experiments, in particular his work on the PIV software and the SPIV calibration procedure. Thanks also go to Dr. Tan Boon Thong, who conducted numerical studies to compliment this work. Of my other colleagues and friends at Monash University, I would also like to particularly thank Josie Carberry, Karlis Atvars, Justin Leontini, Aran Fitzgerald, Anthony Buchanan, Katrina Swalwell, Michael Eaddy, Patrick Browne and Mark Thompson.

I would like to warmly thank my dear Christina for her ongoing dedication. Finally I thank my dear parents who, despite their own difficult times, have provided me with immense support throughout my candidature.

Nomenclature

Symbol	Parameter
β	camera displacement angle
β_τ	angle of resolved wall shear stress
γ	shear rate
Γ	circulation
$\bar{\gamma}$	spatially and temporally averaged shear rate
δ_E	Ekman layer thickness
δ_{ij}	Kronecker delta
Δl	light-sheet thickness
Δt	PIV time interval
$\Delta X, \Delta Y, \Delta Z$	displacements in SPIV coordinates
Δr_1	radial displacement bias associated with light-sheet thickness
ε	energy dissipation per unit mass
ε_{ave}	average energy dissipation per unit mass
ε_c	cumulative energy dissipated on suspended cells per unit volume
ε_r	reconstructed SPIV data uncertainty
ε_p	PIV measurement uncertainty
ε'	ratio of ε_r on ε_p
η	turbulent eddy size
μ	dynamic viscosity
ν	kinematic viscosity
ξ_b	distance of wall shear minimum from bioreactor axis
ξ_s	distance of wall shear minimum from scaffold axis
ρ	density
ρ_m	microcarrier density
σ_{ii}	normal stress component

σ_{ij}	shear stress component
$\sigma_1, \sigma_2, \sigma_3$	principal stresses
$\overline{\sigma_1}, \overline{\sigma_2}, \overline{\sigma_3}$	spatially averaged principal stresses
$\hat{\sigma}_1, \hat{\sigma}_2, \hat{\sigma}_3$	principal axis unit vectors
$\hat{\sigma}_1 \cdot \mathbf{i}$	radial component of principal axis unit vector
$\hat{\sigma}_1 \cdot \mathbf{j}$	axial component of principal axis unit vector
$\hat{\sigma}_1 \cdot \mathbf{k}$	azimuthal component of principal axis unit vector
τ	shear stress
$\bar{\tau}$	spatially averaged shear stress
$\tau_{max,1}, \tau_{max,2}, \tau_{max,3}$	maximum shear stresses
τ_w	wall shear stress
$\overline{\tau_w}$	spatially averaged wall shear stress
τ_e	eddy-scale particle shear stress
v_e	eddy velocity
ϕ	surface tension
ψ	streamfunction
ω	impeller rotation rate
ω_i	inner-cylinder rotation rate
Ω_θ	azimuthal vorticity
A, B, α_1, α_2	empirical constants
Ca	capillary number
d_m	microcarrier diameter
D_v	diffusion rate
\mathcal{D}	deformation tensor
E	turbulence energy
F_i	body force component
Fr	Froude number
g	gravitational constant
H	surface height above vessel bottom
ICS	impeller collision severity
ISF	integrated shear factor
k_L	mass transfer coefficient
k_{La}	oxygen transport rate

l	distance from tip along a flat plate
n	axis normal to surface
n_b	number of impeller blades
N_p	power number
N_{qd}	impeller discharge flow number
p	hydrostatic pressure
P	power
Q_d	impeller discharge flowrate
r, z, θ	cylindrical coordinates
$r_{\sigma p}$	radial position of peak stress
r_C	core vortex radius
r_F	field of view radius
r_i	mixing vessel impeller radius
r_s	scaffold radius
r_{vm}	radial position of axial velocity minimum
R	vessel radius
R_i	inner cylinder radius
R_o	outer cylinder radius
Ra	Rayleigh number
Re	Reynolds number
$s.d.$	standard deviation
S_i	surface element
Sc	Schmidt number
Sh	Sherwood number
SR	swirl ratio
SR_m	modified swirl ratio
t	time
t_i	impeller thickness
t_s	scaffold thickness
T_d	impeller rotation period
T_m	mixing time
T'_m	dimensionless mixing time
TCS	turbulent collision severity

\mathcal{T}	three-dimensional stress tensor
u_G	gas speed
u_{tip}	impeller tip speed
U	freestream velocity
V	volume
\mathbf{v}	three-dimensional velocity vector
v'_i	fluctuating velocity component
v_r, v_z, v_θ	velocity components in cylindrical coordinates
v_{r1}	radial velocity bias component associated with light-sheet thickness
$v_{\theta M}$	measured azimuthal velocity
$v_{\theta T}$	true azimuthal velocity
v_t	velocity component tangential to surface
VF_m	microcarrier volume fraction
VF_c	cell volume fraction
We	Weber number
x, y, z	Cartesian coordinates
x_s	scaffold radial displacement
X, Y, Z	SPIV measurement plane coordinates
X_a, Y_a, Z_a	coordinates of camera a
X_b, Y_b, Z_b	coordinates of camera b
X_{pa}, Y_{pa}	coordinates of displaced particle, as perceived by camera a
X_{pb}, Y_{pb}	coordinates of displaced particle, as perceived by camera b
X_t, Y_t, Z_t	true coordinates of displaced particle
\mathcal{X}	three-dimensional position vector
z_s	scaffold axial position

Contents

1	Introduction	1
2	Literature Review	3
2.1	Introduction	3
2.2	An Introduction to Cell and Tissue Culture and the Role of Fluid Mechanics . .	5
2.2.1	Examples of Cell and Tissue Culture Applications	6
2.2.1.1	Articular Cartilage	7
2.2.1.2	Bone	7
2.2.1.3	Cardiac Tissue	7
2.2.1.4	Neural Stem Cells	7
2.2.1.5	Haematopoietic Cells	8
2.2.1.6	Hybridoma Cells	8
2.2.1.7	Chinese Hamster Ovary (CHO) Cells	8
2.2.2	A Brief Summary of Observations of Flow-Mediated Cell Behaviour . .	8
2.2.2.1	Endothelial Cells	9
2.2.2.2	Osteoblasts	11
2.2.2.3	Chondrocytes	11
2.2.3	Signalling Mechanisms	12
2.3	Fluid Stresses	16
2.3.1	The Stress Tensor	16
2.3.2	Reynolds Stresses	18
2.3.3	Wall Shear Stresses	19
2.4	Stirred-Vessel Bioreactor Design for Cell and Tissue Culture	21
2.4.1	Spinner Flask Bioreactors	22
2.4.1.1	Effect of stirrer speed on cell and tissue culture	25
2.4.1.2	Effect of Impeller configuration on cell and tissue culture . .	27

2.4.1.3	Effect of culture time on cell and tissue culture	28
2.4.2	Rotating Wall Bioreactors	28
2.4.3	Alternative Bioreactor Designs	33
2.4.4	Use of Scaffolds in Cell and Tissue Culture Bioreactors	34
2.5	Mixing Vessel Fluid Dynamics	36
2.5.1	Nagata's Attempt to Characterise the Flow Within Mixing Vessels	36
2.5.2	A Summary of Empirical Design Parameters	37
2.5.3	Problems of Turbulence Affecting Spinner-flask Bioreactors	42
2.5.4	CFD Modelling of Mixing Vessel Flows	45
2.6	The Flow Within Cylindrical Vessels Driven by a Rotating Endwall	47
2.6.1	Vortex Breakdown Bubble Development	48
2.6.2	Free Surface Case	54
2.6.3	Onset of Unsteadiness	59
2.7	Summary of Previous Work and the Motivation for the Present Study	62
3	Experimental Methodology	67
3.1	Introduction	67
3.2	Experimental Model Configuration	68
3.2.1	Validation of the Reynolds Number Accuracy	71
3.2.2	Practical Issues Associated with the Model	72
3.2.3	Rig Maintenance	74
3.2.4	Incorporating Submerged Scaffold Models	74
3.3	Flow Visualisation Techniques	77
3.4	Quantitative Measurement Techniques	78
3.4.1	Particle Image Velocimetry	78
3.4.2	Equipment and Protocol	79
3.4.3	Techniques applied to enhance PIV accuracy	81
3.4.4	An Introduction to Stereoscopic PIV	82
3.4.5	SPIV Equipment and Protocol	84
3.4.6	Calibration	86
3.4.6.1	Background	86
3.4.6.2	New Technique	87
3.4.6.3	Calibration Field Derivation Procedure	88
3.4.7	Three-component velocity field reconstruction	92

3.4.8	Further techniques applied to enhance SPIV accuracy	94
3.4.9	SPIV Validation	99
3.5	Further Data Processing	101
4	Flows within a Cell-Suspension Bioreactor with Vortex Breakdown	103
4.1	Introduction	103
4.2	Flow Visualisation	105
4.3	Three-Component Velocity Field	114
4.4	Quantification of the effect of Re on Flow Topology	121
4.4.1	Axial Flow	121
4.4.2	Azimuthal Flow	129
4.4.3	Azimuthal Vorticity	138
4.5	Swirl Ratio	141
4.6	Temporal Variability	145
4.7	Principal Stress Fields	148
4.7.1	Stress Magnitudes: Full Field	148
4.7.1.1	Comparison with Numerically Derived Stress Fields	150
4.7.1.2	Stress Profile Comparison	151
4.7.2	Stress Magnitudes: Vortex Breakdown Region	154
4.7.3	Principal Axes	161
4.7.3.1	Re=1200, $\hat{\sigma}_1$	161
4.7.3.2	Re=1200, $\hat{\sigma}_3$	163
4.7.3.3	Re=2400	164
4.7.4	Shear Stress Components	166
4.8	Conclusions and Further Discussion	172
5	Flows within a Bioreactor with Vortex Breakdown and Stationary Submerged Scaffolds	179
5.1	Introduction	179
5.2	Review of Flow Topology at Re=1200 and Re=2400 Without Scaffolds Added .	181
5.3	Flow Topology With Scaffolds Added	182
5.3.1	Flow Visualisation	183
5.3.2	Case A: Small Disk, Re=1200	184
5.3.3	Case B: Large Disk, Re=1200	186

5.3.4	Case C: Large Disk, $Re=2400$	190
5.3.5	Effect of disk size on flow topology	194
5.4	Principal Stress Fields	202
5.5	Wall Shear Stresses	204
5.6	Radial Displacement of Scaffold Models	211
5.6.1	Axial Velocity Field	211
5.6.2	Wall Shear Stresses	214
5.7	Conclusions and Further Discussion	217
6	Conclusions and Recommendations for Further Research	223
6.1	Final Conclusions	223
6.2	Recommendations for Further Research	226

Chapter 1

Introduction

With the advent of new biotechnologies, the ability to harvest cell and tissue materials in large quantities has become an important goal (Martin *et al.* , 2004). The development of more advanced bioreactors is regarded as one means of improving culturing processes. Currently, the choice of bioreactor configuration and operating conditions is often made with scant consideration of the internal flow, even though the fluid dynamics plays an important role in achieving a successful yield. Very little parametric classification of stirred vessel bioreactors has been undertaken, let alone in terms of the fluid dynamics. The few empirical studies that have been conducted to determine the effect of particular input parameter on the culture outcomes, have mostly failed to adequately resolve the relevant mechanical quantities, such as stress. This, and the complicated nature of fluid - cell interactions, have made it difficult to achieve long-term progress in large scale bioreactor design.

A more fluid dynamics oriented approach to bioreactor selection involves considering better controlled flows. Rather than using turbulent flows, which are by nature difficult to define, some researchers have constructed stirred vessels that utilise laminar mixing (Freed & Vunjak-Novakovic, 2000). However, vortex breakdown flows generated within cylindrical vessels have not been applied to a cell or tissue culture application, despite the fact that they appear to have favourable low-shear mixing properties. The two most likely reasons for this are that (a), these flows are not well known to those undertaking cell culture and bioreactor design, and (b), the structure of these flows is highly sensitive to the vessel geometry and operating conditions, meaning that parameter-based classification is necessary to predict the conditions most suitable for cell culture.

In the current study, vortex breakdown flows within a cylindrical vessel with a rotating bottom and a free surface are analysed in such a manner. The purpose is to find conditions within these flows, if any, that are suited to cell or tissue culture applications. The study is

deliberately conducted from a broad perspective, focussing on the mechanics of the flow rather than the behaviour of a particular cell. For instance, the primary control parameter is the Reynolds number, which indicates the ratio of inertial to viscous forces acting on the fluid. To increase the scope of the investigation, both suspension culture and stationary scaffold culture are considered.

In order to characterise the flows, an experimental model of a scale similar to existing bioreactors was constructed for the purposes of visual analysis. To quantify the flow in appropriate detail, an advanced Stereoscopic Particle Image Velocimetry technique was implemented. This meant that three-dimensional velocity vectors could be measured, which could then be used to determine the distribution of the principal stresses throughout the bioreactor. This is particularly important because vortex breakdown flows within these vessels are yet to be quantified, prior to the current study, using an experimental three-component velocity measurement technique. Furthermore, the effect of placing disks within the vortex breakdown region has not previously been investigated. The results of the current study can therefore be used to add to the body of knowledge on vortex breakdown flows within cylindrical vessels.

Chapter 2 provides a description of the motivation behind bioreactor development. Previous bioreactor designs and studies are analysed in detail, along with the key biological and mechanical processes dependent on the bioreactor fluid dynamics. The flows within traditional mixing vessels and in cylindrical vessels with vortex breakdown are also described with reference to previous research described in the literature. The experimental methodology is detailed in Chapter 3, with extra information provided on the novel aspects of the experimental apparatus and the Stereoscopic Particle Image Velocimetry system. The results of the flow analysis are divided over two chapters. Chapter 4 focusses on free suspension culture in vortex breakdown flows, while Chapter 5 is concerned with scaffold/bioreactor systems involving vortex breakdown. Final conclusions and recommendations for further research are included in Chapter 6.

Chapter 2

Literature Review

2.1 Introduction

Research into animal cell culture bioreactors has traditionally been conducted from the perspective of one, as opposed to more than one, of the many relevant scientific disciplines. This field of study is of interest to a collection of sciences as diverse as Chemical Engineering, Tissue Engineering, Cell Biology, Biomedicine, Immunology, and Mechanical Engineering, and is therefore susceptible to complications arising from differing study goals, inconsistent parametric studies and knowledge gaps. For example, much of the existing literature describes work conducted entirely from a biological perspective, even though mechanics plays a key role in bioreactor processes.

This literature review describe previous work originating from a broad range of fields, in order to fulfil four functions:

1. To demonstrate the relevance of bioreactor technology to the broader field of tissue engineering and biomedical research.
2. To review some of the recent trends in bioreactor technology, and the knowledge acquired by previous research into bioreactor development.
3. To describe fluid mechanics research and concepts that are, or at least should be, considered important to bioreactor development.
4. To assist the reader in understanding the significance of the research described in this thesis.

Section 2.2 contains a brief and general introduction to cell and tissue culture, with a particular focus on the role of fluid flows in these processes. Some of the mechanotransductive

processes involved go beyond the level of biochemistry directly relevant to this thesis. However, a basic understanding of these processes is important for comprehending the role played by fluid shear stress toward mediating cell culture both *in vitro* and *in vivo*, and therefore their primary importance in bioreactor flows. As stress is a key concept in this research, the following Section, 2.3, includes a summary of classical mechanical stress theory. A review of stirred vessel bioreactor development is contained within Section 2.4, focussing mostly on two generic types of bioreactor: the simpler, more traditional spinner flask, and the more controlled, but complicated, Rotating Wall Bioreactor. The majority of the papers reviewed in Section 2.4 come from the field of biotechnology. As fluid dynamics studies on bioreactors are limited in number and scope, Section 2.5 describes recent advances in modelling more general mixing vessel flows. The limitations on categorising these complex and often turbulent flows are made apparent. The focus of Section 2.6 is on simpler vessel geometries that have common features with the mixing vessels described in Section 2.5, but have substantially more controllable flow conditions. This control primarily arises from the flows being driven by a flat rotating lid rather than an impeller of more complex geometry. Previous studies of the flow within this vessel configuration are reviewed, with the phenomenon of vortex breakdown receiving special attention due to its significance as a constituent of the flow and its potential to be utilised as part of a novel bioreactor flow. In the final section, 2.7, the problem of bioreactor optimisation is considered in light of the various topics covered in the literature review, thus foreshadowing the hypothesis formulation undertaken for the current research.

2.2 An Introduction to Cell and Tissue Culture and the Role of Fluid Mechanics

Scientists have been culturing mammalian tissue *in vitro* for around a century (Freshney, 2000). The primary motivation for tissue cultivation has traditionally been medical, biological and pharmacological research. This continues to be the case. Recently, however, accelerating interest in the field of tissue engineering has increased the plausibility that tissue will soon be commonly harvested for human implantation. There is great motivation to achieve such a goal, as such a breakthrough has the potential to alleviate many of the difficulties associated with current implantation practice, especially the availability of grafts; at present, many tissues are not stored in 'banks', and so supply problems exist. However, the potential benefits that could flow from progress in the field of tissue and stem cell engineering are not just confined to surgical supply. They are spread across many areas, and are too numerous to list here, but are described in recent review articles that summarise in detail the recent progress that has been made in tissue engineering sciences (Cascalho & Platt, 2005; Levenberg & Langer, 2004; Lavik & Langer, 2004).

Clinically feasible tissue grafts need to be derived from tissue or stem cells harvested from either the patient's body or human embryonic stem cells. The *in vitro* growth of functional tissue from the latter source appears unlikely to be realised in the short term, as research into the potential use of human embryonic stem cells is still at a relatively early stage. Instead, tissue has to be grown from tissue or stem cells isolated from patients prior to implantation. Consequently, the ability to quickly and reliably culture large scale tissue constructs is of vital importance. At present there are few tissues, excluding skin perhaps (Wood, 2003), that can be cultured and grafted in this manner.

The task of developing systems to assist the growth of tissue and cells *in vitro* is partly a problem of design, although much also remains to be learnt about the mechanisms of tissue growth. Engineers have recently become involved in finding solutions to some of the design problems and as a result the field of tissue engineering has become quite inter-disciplinary. The use of human cell bioreactor systems is among the more promising approaches to medically-applied tissue engineering, particularly as bioreactors have the potential to tackle the problems of scale-up and automation that are currently rendering many tissue engineering technologies unviable (Martin *et al.*, 2004). In part, bioreactor design has become an engineering problem, with a complex set of design requirements. Wu *et al.* (1999) summarised these requirements as marketability, manufacturability, the capability to produce tissue constructs of clinically

relevant size and shape, the capability to produce constructs with relevant structural properties, and the capability to produce constructs with functional properties.

It is arguable that there are few, if any, bioreactors currently available that meet all five criteria. It can also be said that there is much knowledge still to be acquired before such bioreactors become commonplace. The design of bioreactor systems is complicated by the fact that the requirements are often application specific; in particular, they greatly depend on the type of cell being cultured. The first subsection below, 2.2.1, includes a brief description of selected cell and tissue culture applications. These represent a small sub-set of all tissue engineering applications, and have each been chosen on the basis of a previous association with bioreactor technology.

To understand the full significance of bioreactor dynamics, and thereby proceed to design such systems, it is beneficial for an engineer to know as much as possible about the manner in which cells respond to their local environment. For example, cells of different phenotype will respond differently to certain shear levels as a result of having different sensitivities. An extreme case is mammalian stem cell culture, which involves the additional problem of trying to control differentiation. In the case of cell culture for tissue engineering purposes, a much greater cell yield or a more complex aggregate structure may be required than for a laboratory based application such as research or pharmacology. Several examples of how certain phenotypes respond to mechanical influence are described in Subsection 2.2.2. Particular attention is paid to the observations of how fluid forces can mediate cell behaviour.

In the final subsection, 2.2.3, a basic theoretical overview of intracellular mechanotransduction is provided. It is not the object of the current research to find further biochemical reasons for a particular cell behaviour. However, it is important to recognise that the intracellular and intercellular processes that stimulate cell adaptation and proliferation need to be understood to fully model culture outcomes as functions of bioreactor inputs. Therefore, the contents of Subsection 2.2.3, while being only a brief sample of the total knowledge of mechanotransductive signalling processes in cells, provides important background information.

2.2.1 Examples of Cell and Tissue Culture Applications

The surge of interest in biotechnology has coincided with research outlining new uses for *in vitro* cell culture and tissue engineering. There is no attempt to construct an exhaustive list of these applications in this subsection. Rather, there is a brief description of some of the more significant and common applications, particularly those for which it appears that bioreactor

technology may be of use. The extent of the progress already made is generally dependent on the complexity of the application.

2.2.1.1 Articular Cartilage

Articular cartilage is a tissue highly suited to *in vitro* culture; it requires no vascularisation, has a low cell density, can be cultured from the single cell level, and has a poor natural repair capability. Treatment of defects by implantation of cultured cartilage is already being practiced, although there is still a need to optimise culture techniques in order to reduce the necessary severity of the arthroscopic procedure and to improve the quality of implants (Brittberg *et al.* , 1994; Mandelbaum *et al.* , 1998).

2.2.1.2 Bone

Tissue engineering is facilitating the development of novel biological orthopaedic implants. Bone grafts developed from *in vitro* cultured osteoblasts would be preferable to the autologous and artificial grafts currently implanted in patients, as these are able to produce the biochemical components unique to the natural tissue (Laurencin *et al.* , 1999). There are culture techniques under development that aim to replicate the oscillatory flow dynamics and electrophoresis of interstitial fluid (Hillsley & Frangos, 1994). Bone cell culture has also been used by NASA to monitor bone mass loss under microgravity or slow flow conditions (Kizito *et al.* , 2004; Dillaman *et al.* , 1991).

2.2.1.3 Cardiac Tissue

In western countries there is a pressing need for cardiac tissue in heart disease treatment and cardiac repair applications. While replication of the functional properties of native cardiac tissue is by no means simple, attempts are being made to culture tissue in order to eventually reduce the need for full organ transplantation (Shachar & Cohen, 2003; Carrier *et al.* , 1999; Kannan *et al.* , 2005). In addition, the reliance of the endothelium on favourable haemodynamic conditions (see Subsection 2.2.2), indicates that bioreactors may be an important component of engineered arterial grafts.

2.2.1.4 Neural Stem Cells

Neural stem cells (NSCs) constitute an adult stem cell line that is currently generating great research interest as a consequence of its potential medical applications. The potency of these cells has been demonstrated by their ability to differentiate into all neural cell types, including

oligodendrocytes, neurons, and astrocytes. It is hoped that in the future NSCs may be used to generate transplants that will aid in the treatment of neurodegenerative disorders such as Parkinson's disease and Huntington's disease. Current research priorities involving NSCs are mostly aimed toward furthering the basic understanding of the phenotype characteristics (Gottlieb, 2002; Reubinoff *et al.* , 2001), however it will become imperative to enhance the NSC scale-up capabilities if they are eventually to be utilised for therapeutic purposes.

2.2.1.5 Haematopoietic Cells

Haematopoietic stem cells (HSCs) are stem cells contained within bone marrow, peripheral blood and umbilical cord blood, and are the precursor to all blood cells. The ability to culture large quantities of HSCs *ex vivo* should greatly improve bone marrow implantation procedures, as well as other medical techniques. Furthermore, there is now hope that large-scale blood supplies may eventually be maintained through *ex vivo* expansion (Nielsen, 1999).

2.2.1.6 Hybridoma Cells

Hybridoma cells are commonly cultured because of their ability to produce monoclonal antibodies which can be used for a variety of applications. The ability to cultivate large numbers of hybridomas is desirable and would perhaps facilitate an increase in their immunotherapy and immunopurification applications (Birch *et al.* , 1985).

2.2.1.7 Chinese Hamster Ovary (CHO) Cells

CHO cells are another relatively robust cell line commonly cultured for immunology research applications. As in the case of hybridomas, it would be desirable to have the capacity for large-scale cell growth.

2.2.2 A Brief Summary of Observations of Flow-Mediated Cell Behaviour

At this point in the review, the focus shifts toward the very reason why fluid dynamics has become an important component in various culture systems: that is, the flow-dependent nature of certain mammalian cells and tissues. A summary of how flow conditions have been observed to affect the behaviour of three very different mammalian cells is provided. The three cell types - endothelial cells, osteoblasts and chondrocytes - are by no means the only that are affected by *in vivo* fluid motion, but are particularly relevant because of the profound nature of their flow-coupled behaviour and the important consequences of this behaviour on the development of culture systems.

2.2.2.1 Endothelial Cells

Over the past 25 years, there have been many investigations into the cell-scale fluid mechanics occurring *in vivo* (Kamm, 2002). The circulatory system has received a substantial amount of attention as extracellular fluid flow is strongly linked to the cellular biology of arteries and consequently medical conditions such as atherosclerosis and thrombosis (Wootton & Ku, 1999). While progress has been made, the complex nature of the flows, the variability within human biological systems, and the gaps in knowledge associated with the intracellular biochemical processes and the cell-flow interactive relationship ensure that there is substantial research required before a clear and dependable understanding is formed.

An early demonstration of changed cell behaviour in response to controlled fluid shear stress levels is a much cited study of Dewey *et al.* (1981), during which endothelial cells changed shape and orientation when exposed to 0.5 to 1.0 N/m² shear stresses caused by a cone viscometer. This important result clarified earlier observations that increased blood flow rates caused changes along the vascular endothelium (Fry, 1968; Caro *et al.*, 1971; Stoker, 1973). The conclusion that Dewey *et al.* extrapolated from their findings was that haemodynamic forces can control endothelial tissue structure and function. A similar conclusion was subsequently drawn by Stathopoulos & Hellums (1984) regarding epithelial cells, after they exposed human embryonic kidney cells to shear stresses between 0.26 and 5.40 N/m², although in this case there was a more marked loss of viability, particularly at shear stresses greater than 2.6 N/m². Several studies have since presented similar findings on how cell behaviour depends on fluid dynamic conditions.

It was later claimed by Davies *et al.* (1986) that the response of endothelial cells is partly dependent on whether the flow is turbulent or laminar. When exposed to turbulent flow, the endothelial cells were found to have increased turnover, particularly at higher shear stresses. Curiously, the cells do not align in the same manner when exposed to laminar flow; this is perhaps a reflection of the variable directionality of the forces caused by turbulence.

From the mid-1980s onward, subsequent studies of endothelial cell response to fluid shear stress have provided an increasingly complicated picture of both the variations in flow characteristics that produce cell responses, and the biochemical nature of these responses. With mammalian endothelial cells being of such complicated construction, and the *in vivo* haemodynamic environment being so complex and variable, this is not altogether surprising. Davies *et al.* (1995) went so far as to suggest that heterogeneities in the response of endothelial cells to flow are caused by local three-dimensional microscopic shear stress gradients produced by the

unique features in the surface topography of individual cells, even in a confluent monolayer. This hypothesis is supported by Atomic Force Microscopy observations and CFD analyses, which have been used to estimate microscopic shear stresses along the cytoskeletal surface (Barbee *et al.* , 1994). Advances in microscale measurement, (Meinhart *et al.* , 1999) and computational techniques have facilitated an increase in these sub-cellular scale investigations (Barbee, 2002; Fukushima *et al.* , 2001; Woodroffe *et al.* , 2005).

Frangos *et al.* (1985) observed that endothelial cells exposed to a steady shear stress produce a great deal more prostacyclin (PGI₂), an important inhibitor of platelet aggregation, than those exposed to a stationary fluid. A pulsatory oscillating flow, simulating pulsatile shear stresses, results in an even higher PGI₂ production rate. This study was an important early example of the significance of fluid flow on cell function. The observation regarding the pulsatile flow effect was similar to that made by Levesque *et al.* (1989), who measured an increase in elongation for those cells exposed to pulsatile, rather than steady flow. This, coupled with the observations regarding the stimulatory effect of turbulence (Davies *et al.* , 1986), provided an early indication of the frequency-dependent nature of some cell signalling mechanisms (see Subsection 2.2.3). Furthermore, oscillatory shear stresses have been found to alter endothelial hydraulic conductivity (Hillsley & Tarbell, 2002) as well as the morphology of the cells (Helminger *et al.* , 1991). White *et al.* (2001) exposed cells to different flow profiles and concluded that temporal, more than spatial, gradients in shear stress result in increased cell proliferation. In the case of osteoblasts (precursor bone cells), it was found by Jacobs *et al.* (1998) that a sinusoidally oscillating flow provides even more stimulation than a uni-directional flow, probably because oscillatory flow dynamics more closely reflect the time-dependent profile of interstitial fluid flow typically found *in vivo*.

Here we have barely scratched the surface of previous work on how fluid dynamics affects endothelial cells. Yet despite the extensive research, a complete picture of how shear stresses affect cell behaviour still seems quite distant. The natural flow environment of endothelial cells is difficult to model, as it has a large and complex geometry, as well as temporal-dependency, and multiple scales. However there has been extensive work already undertaken to piece together the flows occurring in specific arteries, including the carotid arteries (Ku & Giddens, 1987; Anayiotos *et al.* , 1994), the aorta (Moore *et al.* , 1994), at arterial bifurcations (He & Ku, 1996), and in stenoses (Young, 1979). It may in fact be that until the circulatory system flow can be fully defined, it will not be possible to fully monitor the natural endothelial cell behaviour through *ex vivo* modelling. In addition, the physics and consequence of micro-fluid

flows through the endothelium also need to be understood (Hodgson & Tarbell, 2002), as they have been found to affect the functioning of sub-endothelium smooth muscle cells (Sharma *et al.*, 2002; Civelek *et al.*, 2002). A complicated link between fluid shear stress and the convective mass transport of water and other solutes through the interendothelial cleft has already been established (Jo *et al.*, 1991; Lever *et al.*, 1992). Tarbell (2003), as well as Wootton & Ku (1999), have published review articles containing more detailed summaries of the observed effects of fluid stress on the arterial wall.

2.2.2.2 Osteoblasts

It is by no means only endothelial cells that are highly affected by shear. Even cells from tissue not seemingly associated with fluid flow may respond dramatically to fluid shear stresses (Hooker *et al.*, 1989). Aside from the more intuitive observation that damage may occur when cells are exposed to high shear levels, many cell types produce and/or excrete specific chemicals and proteins in a controlled stress environment. In many cases, this implies a functional role of shear stress.

For example, the role of interstitial fluid flow on bone remodelling and formation has received attention in the last decade. Hillsley & Frangos (1994) postulated that interstitial fluid flow caused by natural mechanical loading and pressure gradients could, through the mechanisms of shear stress and streaming potential, stimulate osteoblast growth factors and osteogenesis. In support of this theory, osteoblasts have been observed to undergo increased calcium (Ca^{2+}) signalling when exposed to fluid flow (McDonald *et al.*, 1996). A detailed review of the important functions associated with fluid flow in bone can be found in Tate (2003).

2.2.2.3 Chondrocytes

Articular cartilage cells, or chondrocytes, undergo similar behavioural adaptations when exposed to flow shear. Smith *et al.* (1995) exposed a monolayer of cultured chondrocytes to a shear of 1.6 N/m^2 for 48 hours using a cone viscometer and compared the culture with one not exposed to shear, finding significant morphological differences between the two samples. The cells exposed to shear became more elongated, elliptical and aligned. Importantly, the quality and quantity of excreted extracellular matrix (ECM) components, in particular glycosaminoglycan and proteoglycan, were increased. Collagen, which determines the structural strength of the ECM, has also been found to increase when exposed to similar shear stresses (Saini & Wick, 2001).

Bachrach *et al.* (1995) found that proteoglycan synthesis in chondrocytes is induced by changes in the mechanical environment (including mechanical deformation, static pressure, fluid shear and osmotic stimulation). Thus the functionality and structural integrity of cartilage can be determined by the nature of the environment. By applying a dynamic, unconfined, compressive load to cartilage disks, Kim *et al.* (1995) identified that mechanical stiffness depends on loading frequency, and proteoglycan synthesis increases with fluid velocity and streaming potential gradient. This reaffirms the importance of compression-induced streaming potential and/or fluid flow in natural cartilage stiffening, and highlights the benefits fluid flow may provide in an *in vitro* cell culture environment.

Guilak *et al.* (2002) altered the osmotic stress conditions within a cell culture medium containing chondrocytes, and found that the viscoelastic and physical properties of the chondrocytes were strongly influenced by the physicochemical environment. In particular, the outer membrane expanded and tautened when exposed to the hypo-osmotic medium (153mOsm, compared with 303mOsm under isosmotic conditions), while becoming crumpled and retracted when exposed to hyper-osmotic fluid (466mOsm). Such changes in osmotic conditions would not be uncommon within cartilage environments exposed to natural mechanical loading.

Similar studies have also been conducted on periosteum, a probable location of mesenchymal stem cells and the source of undifferentiated chondrocyte precursors. The results are similar to those of differentiated chondrocytes in monolayers or within tissue. Saris & O'Driscoll (1999) applied a dynamic fluid pressure to periosteal cells in order to determine whether these cells proliferate when stimulated in this manner. Their positive result affirmed that mechanical factors, including shear stress, are highly stimulatory at the early stages of chondrogenesis.

2.2.3 Signalling Mechanisms

As mentioned previously, the mechanisms associated with flow-induced cellular response are complex, phenotype-dependent, and not thoroughly understood at present. Cells proliferate, differentiate, and excrete proteins in response to intracellular chemical signalling, about which there is still much to be learnt. Signalling may be controlled by interactions between cells, by interactions between cells and their tissue extracellular matrix (Martins-Green, 2000), by mechanical loading, or by other environmental factors, and may involve complex feedback mechanisms (Shraiman, 2005). Davies (1995) published one of the most comprehensive reviews on the mechanisms of endothelial cell response to flow-induced forces. In summary, the most important aspects of the proposed endothelial cellular mechanotransductive process, as described by

Davies, are as follows:

- The tangential shear stress due to the friction of the moving fluid and the normal static haemodynamic pressure act in conjunction to deform the cell cytoskeleton and cell membrane and force a response in the intracellular pressure. This provides the means of *Direct shear stress-induced mechanotransduction*, which involves three general processes: displacement of sensors located at the surface of the cells, transmission of forces from the exterior to the remainder of the cell, and transduction of the same forces at internal sites. The force transmission and transduction processes are illustrated schematically in Figure 2.1.
- At the luminal cell surface, transmembrane glycoproteins extending into the extracellular space are displaced by the fluid shear, and therefore act as the mechanical sensor. As shown in the upper schematic in Figure 2.1, the membrane molecules then transfer the stress to the cytoskeleton in one part of the cell; a process which is modulated by changes in the structural and adhesive properties of the cell.
- There are numerous forms of transmembrane surface protein which may act as mechanotransducers. These include shear-sensitive ion-channels, integrins at focal adhesion sites, and receptors for certain agonists with flow-stimulated secretion. For example, secretion of Ca^{2+} , an important second messenger in many cells, is thought to be partly in response to agonist (adenine nucleotide) stimulation by shear.
- *Indirect shear stress-induced mechanotransduction* is a process conceptually distinct from that described in the above points, although both processes are flow mediated and are not mutually exclusive. In this case the flow affects the cell signalling processes at the surface membrane in two ways. Greater mass transport ensures enhanced agonist delivery but at the same time contributes to the agonist degradation process by causing an adverse chemical concentration gradient near the boundary layer.
- There are regulatory mechanisms within arteries that naturally prevent endothelial cells from being overstimulated by the mechanical environment. These mechanisms (which are most likely interactive) are categorised as either adaptive or filtering.

Adaptation- Mechanical over-stimulation will induce feedback mechanisms on both the interior and exterior of the cell that inhibit chemical activity. Examples of this

include the desensitisation of the ion channels, changing adenine nucleotide concentrations at the cell surface, and activation of calcium 'pumps' which remove Ca^{2+} from the internal regions of the cell.

Filtering- Many of the structural components only respond to specific frequencies, so there are pulse-rate dependent controls placed on various mechanotransductive processes. This is also the case for some other cell types (Jacobs *et al.* , 1998; Kim *et al.* , 1995).

The biochemistry involved with mechanotransduction is abbreviated considerably in the above description. Furthermore, these processes are still not completely understood by experts in the field of endothelial cell biochemistry. Considerable work is being undertaken by researchers to illuminate the mechanisms by which stresses control cell function, not only in the endothelium (Helmke, 2004), but also in bone (Alam *et al.* , 2005; Bacabac *et al.* , 2005; Genetos *et al.* , 2005; Pavalko *et al.* , 2003), cartilage (Szafranski *et al.* , 2004; Millward-Sadler & Salter, 2004; Lee *et al.* , 2002), smooth muscle cells (Ainslie *et al.* , 2005; McKnight & Frangos, 2003), and the urothelium (Woodroffe *et al.* , 2005), amongst others. A number of review papers covering multiple cell types have also been written recently (Huang *et al.* , 2004; Chen *et al.* , 2004). While some signalling mechanisms are common amongst different mechanosensitive cells, most responses are phenotype-specific (Iqbal & Zaidi, 2005).

As a result of the extremely complex mechanisms and phenotype dependency of the flow-induced cell responses, attempts to mathematically model these responses have been rare, greatly simplified and generally limited to empirical correlations of shear-induced effects of relatively predictable cell lines (Born *et al.* , 1992). Humphrey (2001) pointed out that while such correlations can be useful, the ultimate goal of scientists should be to understand and quantify the entire network that makes up intracellular physics. Building a definitive analytical or numerical model of the mechanics of a particular cell response system currently seems a long way off, although modelling of the isolated intracellular signals appears to be commencing in earnest (see Latimer *et al.* (2003); Humphrey (2002) and Steck *et al.* (2003)). For example, techniques are being developed to numerically model ion channel behaviour (Wilson & Duncan, 2002; Wiggins & Phillips, 2005), whilst others have attempted to model the strain resulting from the interaction between cells (Shraiman, 2005) and between cells and the surrounding tissue matrix (Han *et al.* , 2004). Such modelling is important if accurate predictions of cultivated bioreactor product based on flow-field input conditions are to be coupled with bioreactor flow models to form an integrated bioreactor optimisation process.

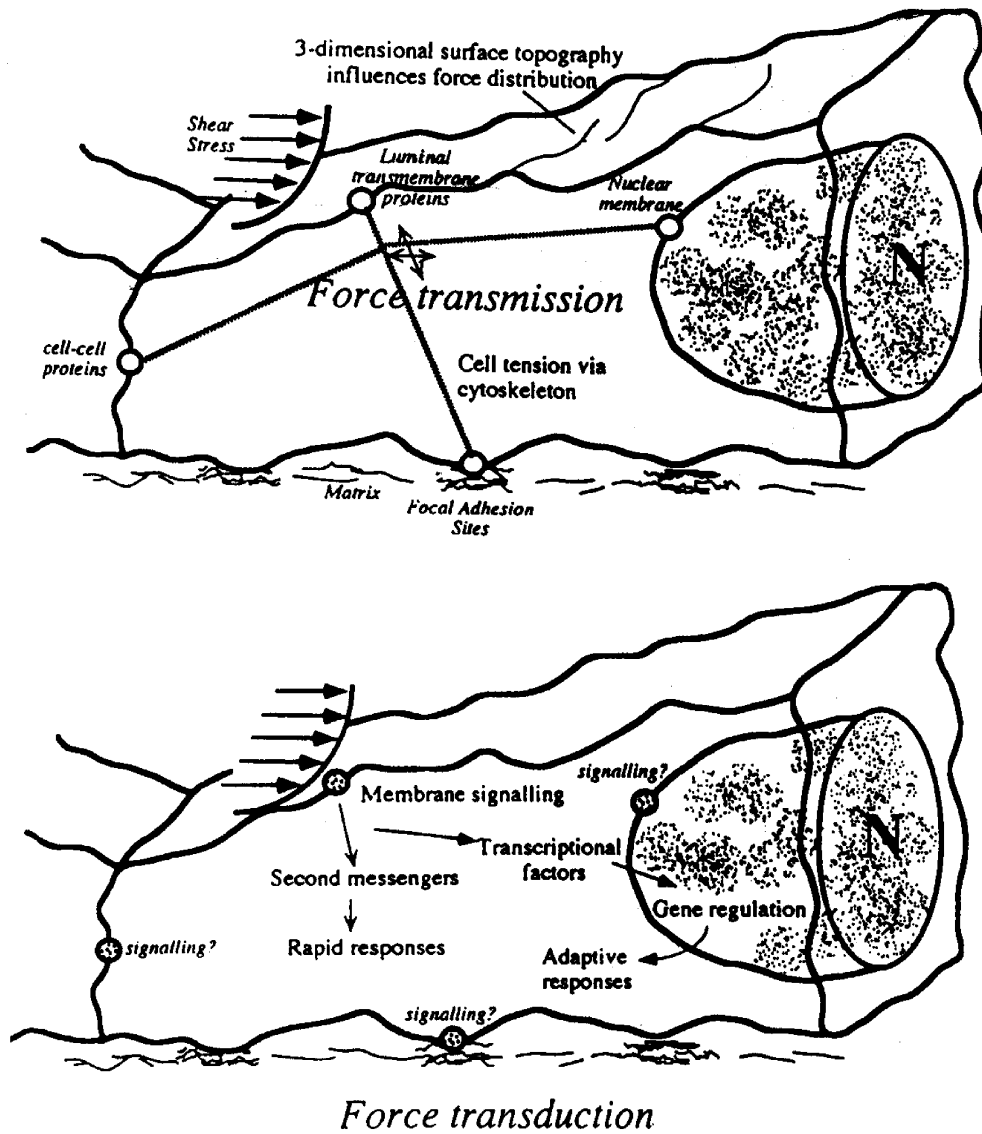


Figure 2.1: (from Davies (1995)) Intracellular force transmission and force transduction processes within an endothelial cell. Both processes are important components of *Direct shear stress-induced mechanotransduction*.

2.3 Fluid Stresses

As has already been described in some detail in this review, animal cells are sensitive to hydrodynamic forces, in particular shear stress. Consequently, fluid shear is an important parameter in biotechnological applications. As a precursor to the current research, it is necessary to understand the concept of fluid stress. In many biological flows, such as those within standard stirred vessel bioreactors operating in either laminar or turbulent regimes, the internal fluid stresses have a highly variable magnitude and are significantly three-dimensional. The primary focus of this chapter is on the classical stress theory derived from continuum mechanics. The empirically derived methods applied in previous research to characterise the overall stress levels within bioreactors, such as the rather broad ‘Integrated Shear Factor’ (or *ISF*), are not described in the current section but are discussed in Section 2.5. Expertise in the concept of stress is a key example of what the mechanical scientist can bring to understanding problems of mechanotransduction and stress-dependent cell culture; problems which are, perhaps, too often left exclusively to the biological scientist. Bringing the analysis of biological stresses back to more fundamental mechanical principles will help to deliver greater insight and accuracy.

2.3.1 The Stress Tensor

The fundamental theorem on the stress tensor was published by Cauchy in 1829 as part of his *Exercices de Mathématiques* (Truesdell, 1968). The fundamental theorem is not described here in its entirety. For more information, the reader is referred to one of the numerous texts on continuum mechanics that cover this topic (Aris, 1962; Truesdell, 1977; Eringen, 1967; Frederick & Tien, 1965). The stress tensor, \mathcal{T} , in three-dimensional form, contains nine components describing the stresses corresponding to the axes, which are, in general, defined arbitrarily. If the axes are defined as x , y and z , then the components of the stress tensor, in matrix form, are:

$$\mathcal{T} = \begin{bmatrix} \sigma_{xx} & \sigma_{xy} & \sigma_{xz} \\ \sigma_{yx} & \sigma_{yy} & \sigma_{yz} \\ \sigma_{zx} & \sigma_{zy} & \sigma_{zz} \end{bmatrix} \quad (2.1)$$

σ_{xi} , σ_{yi} and σ_{zi} represent orthogonal stress vectors acting on surface elements S_x , S_y and S_z respectively, where the normals to the surface elements are parallel to the three axes. For surface element S_x , σ_{xx} represents the normal stress. σ_{xy} and σ_{xz} represent shear stresses on surface element S_x . In general, σ_{ii} (or the main diagonal) components of \mathcal{T}_{ij} are normal stresses while σ_{ij} (or the non-diagonal) components are shear stresses. In the typical case for a continuous

medium where there are no body moments acting, \mathcal{T}_{ij} is symmetric about the main diagonal - in other words, there are at most only three independent shear stress magnitudes.

For fluids, the stress component σ_{ij} (in N/m²) is given by:

$$\sigma_{ij} = \tau_{ij} = \mu \left(\frac{\partial v_i}{\partial x_j} + \frac{\partial v_j}{\partial x_i} \right) \quad (2.2)$$

where \mathcal{X} and \mathbf{v} are, respectively, the three-dimensional position and velocity vectors at a point, and μ is the dynamic viscosity. On occasions the term $\left(\frac{\partial v_i}{\partial x_j} + \frac{\partial v_j}{\partial x_i} \right)$ is referred to as the two-dimensional shear rate or strain rate (γ). The equivalent expression for each shear component in two-dimensional Cartesian coordinates is:

$$\sigma_{xy} = \tau_{xy} = \mu \left(\frac{\partial v_y}{\partial x} + \frac{\partial v_x}{\partial y} \right) \quad (2.3)$$

The normal components σ_{xx} , σ_{yy} and σ_{zz} are made up of stresses due to deformation, as well as a local hydrostatic pressure component, which is invariant to the direction of the coordinates. Changing the directions of x , y and z will change the components of \mathcal{T} . This of great significance for the measurement of biological flows and bioreactor internal stresses, as often the measured shear stresses are based on an arbitrary set of axes, and so do not necessarily represent well the full stress tensor.

One means of characterising the stress at a point in a manner independent of axis orientation is the definition of the principal stress components σ_1 , σ_2 and σ_3 . The principal stresses are the values which occur along the main diagonal of \mathcal{T} when the stress tensor is oriented in such a way that its reference axes are aligned with the stress vectors acting on the element. In other words, when there are no shearing components acting on S_x , S_y and S_z , as in Equation 2.4:

$$\mathcal{T} = \begin{bmatrix} \sigma_1 & 0 & 0 \\ 0 & \sigma_2 & 0 \\ 0 & 0 & \sigma_3 \end{bmatrix} \quad (2.4)$$

The directions, $\hat{\sigma}_1$, $\hat{\sigma}_2$ and $\hat{\sigma}_3$, along which the principal stresses act, are known as the principal axes. If the principal stresses are different, then the principal axes are orthogonal to one another. The principal stresses can be derived by finding the eigenvalues of \mathcal{T} , and the principal axes are given by their respective eigenvectors.

The three maximum shearing stresses act on planes oriented in such a way that they contain one of the principal axes and make 45° angles with the other two. Their magnitudes are related to the principal stresses by the following equations:

$$\tau_{max,1} = \frac{1}{2} |\sigma_2 - \sigma_3| \quad (2.5a)$$

$$\tau_{max,2} = \frac{1}{2} |\sigma_3 - \sigma_1| \quad (2.5b)$$

$$\tau_{max,3} = \frac{1}{2} |\sigma_1 - \sigma_2| \quad (2.5c)$$

An obvious conclusion to draw from mechanical stress theory is that the principal stresses could be used to quantify biological stresses in a more meaningful manner than is currently applied. Such a course has also been suggested by Humphrey (2001). One drawback affecting many applications, which is worthwhile noting, is that quantification of all nine tensor components is often difficult to obtain. Unless the flows being measured are simple and/or one or two-dimensional, advanced computational or experimental techniques may be required to obtain \mathcal{T} , and therefore the principal stresses.

2.3.2 Reynolds Stresses

In Subsection 2.3.1 it was noted that for a continuous medium where there are no body forces acting, the stress tensor is made up of stresses due to deformation, determined by the product of spatial gradients in velocity and the viscosity, as well as a hydrodynamic pressure component which acts normal to the element surface in all directions. In other words, for an incompressible fluid:

$$\mathcal{T}_{ij} = -p\delta_{ij} + \mu\mathcal{D}_{ij} \quad (2.6)$$

where $-p$ is the hydrostatic pressure, δ_{ij} is the Kronecker delta, and \mathcal{D}_{ij} is the deformation tensor.

However, for turbulent flows, stresses due to the random velocity fluctuations should also be considered. These fluctuating velocity components, (v'_i , where $i = x, y, z$), occur along with the time-mean components (v_i) in turbulent conditions. Reynolds rewrote the instantaneous equations of motion (or Navier-Stokes equations) for an incompressible Newtonian fluid as the following:

$$\rho \left(\frac{\partial v_i}{\partial t} + v_j \frac{\partial v_i}{\partial x_j} \right) = -\frac{\partial p}{\partial x_i} + \frac{\partial}{\partial x_j} \left(\mu \frac{\partial v_i}{\partial x_j} - \rho \overline{v'_i v'_j} \right) + F_i \quad (2.7)$$

In addition to the viscous time-averaged deformation stress and hydrostatic pressure stress there is a third stress term that arises from these equations, which is $\rho \overline{v'_i v'_j}$, or Reynolds Stress. So for turbulent flow, Equation 2.6 becomes:

$$\mathcal{T}_{ij} = -p\delta_{ij} + \mu\mathcal{D}_{ij} - \rho\overline{v'_i v'_j} \quad (2.8)$$

Broken down into nine components based on Cartesian coordinates, the Reynolds stress tensor components are similar to the deformation stress tensor components, in that there are three normal-stress components ($\rho\overline{v'^2_x}$, $\rho\overline{v'^2_y}$ and $\rho\overline{v'^2_z}$) along the main diagonal, and three independent shear stress components ($\rho\overline{v'_x v'_y}$, $\rho\overline{v'_y v'_z}$ and $\rho\overline{v'_x v'_z}$) off the diagonal. For laminar flows the Reynolds stresses can be ignored, but for turbulent flows these stresses may become important. Turbulent flows are relevant to some biological applications. For example, it has previously been stated that biologists have observed different cell response to turbulent and laminar flows. In addition, turbulence occurs within certain physiological flows, such as in the wakes of stenoses, as well as in some bioreactors, such as spinner flasks. As Reynolds stresses are often significant in these flows, care has to be taken to not only include them in an analysis of the internal stresses, but to recognise that they may act three-dimensionally. The effect of the three-dimensional nature of Reynolds stresses, like that of $\mu\mathcal{D}_{ij}$, has often been overlooked in previous studies involving turbulent biological flows.

2.3.3 Wall Shear Stresses

Wall shear is a component of stress that is often crucial in the context of biological flows. In *in vivo* conditions or for *in vitro* flows involving adherent cells, the stresses occurring at the cell-layer/fluid interface are of special concern. This is not only because this region often represents the location of the shear-affected cells (e.g. the endothelium), but also because the wall shear is often large compared to the stresses within the bulk fluid. For this reason, the wall shear is often the main stress quantified in biological flow studies, such as those investigating scaffolds submerged within bioreactors (Sucosky *et al.*, 2004), or those investigating arterial flow (Tarbell, 2003; Caro *et al.*, 1971; Hodgson & Tarbell, 2002). Usually, wall stress is simply calculated as the gradient of the velocity component tangential to the wall (v_t) in the direction normal to the wall (n), as in Equation 2.9. It is often necessary to measure both the in-plane and out of plane flow in order to adequately resolve v_t .

$$\tau_w = \mu \frac{\partial v_t}{\partial n} \quad (2.9)$$

Schlichting (1968) compiled a classic review of the forces present at the fluid-solid wall interface under a variety of different conditions. For simplified two-dimensional laminar conditions, the wall shear stress along a flat plate at zero incidence to the flow at a distance l from

the tip is approximately given by:

$$\tau_w = \frac{0.332\rho^{1/2}\mu^{1/2}U^{1.5}}{\sqrt{l}} \quad (2.10)$$

On the other hand, biological flows and surface geometries are rarely this simple, and so a measurement or simulation of the wall stress distribution is often preferable to the analytical approach.

2.4 Stirred-Vessel Bioreactor Design for Cell and Tissue Culture

Techniques developed to mechanically stimulate cells *in vitro* are numerous and varied. Brown (2000) summarised these into different categories, including compressive loading systems, longitudinal stretching systems, substrate bending systems, substrate distension systems, specialised distension systems, and fluid shear systems. Electrical stimulation has also been used as an aid to tissue culture, with promising results (Bee *et al.* , 1994). Tissue structures, such as heart valve (Engelmayr *et al.* , 2003) and connective (Dussault *et al.* , 2002; De Witt, 1982) tissue, have been cultivated by direct mechanical stimulation not involving flow. In recent times, hybrid mechanical/fluid stimulation systems have also been developed (Demartean *et al.* , 2003).

In many cases fluid shear stimulated systems mimic more closely the *in vivo* environment than other mechanical stimulation systems and have thus become the focus of a new field of research. However, control of the stimulatory forces within flow systems is often more difficult, particularly when complex flows are involved, and when the background of the researchers is not in fluid mechanics. Bioreactors represent probably the most popular type of fluid shear system used for mammalian cell culture. The relative popularity of bioreactors has seemingly arisen from the fact that prior to their recent use for mammalian cell culture, their use was already common in microbial cell fermentation processes and recombinant protein production. In a general sense, bioreactors have been defined by Martin *et al.* (2004) as, “devices in which biological and/or biochemical processes develop under closely monitored and tightly controlled environmental and operating conditions.” With their favourable mixing ability and their potential to produce suitable hydrodynamic force distributions, bioreactors are often considered appropriate vessels for culturing cells within optimised cell culture media (which usually has fluid dynamic properties similar to those of water) (Tsao *et al.* , 2000; Sen & Behie, 1999). In addition, various studies investigating how different plant cells react to certain shear levels in bioreactors have shown promising results (Doran, 1999; Scragg *et al.* , 1988; J.-J. Zhong & Yoshida, 1994; Leckie *et al.* , 1991; Takeda *et al.* , 1997; Dunlop & Namdev, 1993), which has reinforced notions that bioreactors potentially have a useful role in animal cell culture.

This section focusses on stirred vessel bioreactor systems for cell culture and tissue engineering, which are divided into two categories: mixed flask bioreactors and rotating wall bioreactors. These configurations are reviewed at moderate length in separate subsections (2.4.1 and 2.4.2), while a third subsection, 2.4.3, briefly describes alternate bioreactor designs that are not a focus of the current research but demonstrate the importance of trying new approaches. The

use of scaffolds in conjunction with bioreactor technology is also discussed. For an additional review of recent tissue engineering bioreactor technology, see Martin *et al.* (2004) or Freed & Vunjak-Novakovic (2000). There are also separate reviews of bioreactor technology specifically for, among others, cartilage (Darling & Athanasiou, 2003) and cardiac (Shachar & Cohen, 2003) tissue applications.

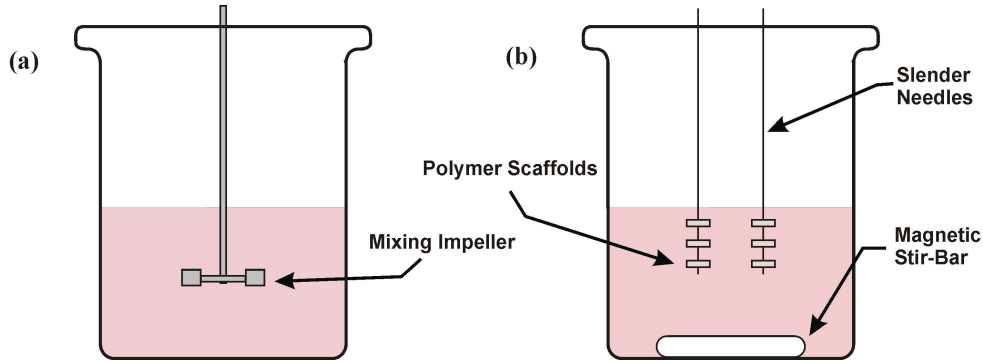


Figure 2.2: The fluid region of the spinner flask stirred by (a), shaft-mounted impeller and (b), magnetic stirrer (similar to that used by Vunjak-Novakovic *et al.* (1996)). In practice, many bioreactors also feature lids with gas feed points and aseptic seals.

2.4.1 Spinner Flask Bioreactors

For animal cell or tissue culture the preferred bioreactor configuration, particularly in early studies, has been a small scale stirred-flask similar in configuration to those successfully used for microbial cell culture and other bioindustrial applications. Spinner flasks, compared with other bioreactor technologies, are relatively simple to set up, operate and maintain. The mixing mechanism normally consists of an impeller mounted on a motor-driven shaft, or a magnetic stirrer resting at the base of the vessel (see Figure 2.2). Cells are typically suspended by individual or microcarrier fluidisation (Cherry & Papoutsakis, 1986, 1988), or otherwise attached to scaffolds held stationary on needles (Vunjak-Novakovic *et al.* , 1996). Magnetic stir bars are often preferred for culture involving stationarily mounted scaffolds, presumably because they can provide directionally-variable, low-magnitude shear conditions. Problematically, they can restrict the ability to use a sparger in cases where it is necessary to provide additional oxygenation (Doran, 2000). The typical diameter of a mixed flask bioreactor is 60 – 100mm, holding between 120 and 800mL of cell culture medium, a capacity which varies depending on the number and phenotype of cells. Interestingly, there seems to have been scant experimental work on scaling these vessels to larger dimensions. This is possibly because previous characterisations of bioreactor performance have generally neglected to use dimensionless parameters.

The optimum stirring speed for cell culture provides adequate mass transfer and mechanical stimulation to the cells without damaging them. Often, to the detriment of control, the flow within spinner flask bioreactors is intentionally made highly turbulent in the belief that turbulence is necessary to provide adequate mixing (Vunjak-Novakovic *et al.* , 1996). The optimal speed is in most cases selected as a result of trial and error, rather than by an analysis of the physical conditions. In general, baffles are not used on mixed flask vessels, as researchers have found that cell cultures within bioreactors with baffles tended to lose viability at a lower stirrer speed compared with those grown in bioreactors without baffles (Leckie *et al.* , 1991). In contrast to this, corrugating the bioreactor wall has been found to improve chondrocyte production for particular input conditions (Bueno *et al.* , 2004). It is worth noting once again that it appears that all these trends in bioreactor technology have arisen as a result of empirical observation, rather than an understanding of the flow physics.

The decision to use suspended microcarrier beads or stationary frames to hold adhesion-dependent cells depends on several factors. Cells seeded onto microcarrier beads are exposed to variable forces as the bead tumbles, and so are likely to have enhanced mechanotransductive stimulation. On the other hand, microcarriers will frequently experience collisions with the vessel walls, other microcarriers, and possibly even the impeller, all of which cause cell damage (Cherry & Papoutsakis, 1986). Furthermore, in the likely case that the smallest turbulent eddy size η is comparable to or smaller than the size of the microcarrier or scaffold, the turbulent energy will be dissipated on the surface of the carrier rather than through the kinematic acceleration of the carrier itself. Thus more energy will be imparted on the cells, resulting in an increased likelihood of damage (Cherry & Papoutsakis, 1988). As a consequence of the uncertain conditions, parameters such as the Turbulent Collision Severity (*TCS*), Impeller Collision Severity (*ICS*) and η , as described in Section 2.5, have been used to characterise the bioreactor fluid dynamics. However, the use of such parameters to describe a spatially and temporally heterogeneous flow is often problematic. Venkat *et al.* (1996) measured the flow in the impeller region of a shaft-driven spinner flask using three-dimensional particle tracking velocimetry, albeit with quite low resolution. They found that turbulent energy dissipation is highly variable with respect to temporal and spatial position. Therefore, the forces experienced by cells on microcarriers are not easy to control in the turbulent conditions typically found in spinner flasks.

Unlike cell scale-up, *in vitro* tissue culture for therapeutic application requires not only large-scale growth, but also appropriate levels of extracellular matrix component secretion, to

ensure that the mechanical properties and functionality of the cultured tissue is comparable to that of natural tissue. Studies undertaken comparing growth of cartilage (Vunjak-Novakovic *et al.* , 1996; Freed *et al.* , 1998, 1999) and cardiac muscle (Carrier *et al.* , 1999) under mixed and static conditions have illustrated that mixed conditions increase cell yield and the histological properties of the resulting tissue. Vunjak-Novakovic *et al.* (1996) and Vunjak-Novakovic *et al.* (1999) found that the composition of the cartilage grown in mixed flasks was superior to that grown in static flasks, containing higher levels of collagen type II and glycosaminoglycan.

Considering recent advances in stem-cell technology, the potential for bioreactors to maintain undifferentiated stem-cell lines is of significant interest, although issues associated with control and direction of differentiation in pluripotent or totipotent stem cells must be overcome (Edgington, 1992). Recent attempts to culture Neural Stem Cells (NSCs) (Sen *et al.* , 2002a; Sen & Behie, 1999; Kallos *et al.* , 1998; Sen *et al.* , 2001, 2002b) and human haematopoietic stem cells (Kwon *et al.* , 2003) within stirred bioreactors have been quite promising. Murine NSCs have been successfully cultured in suspension within flasks mixed by magnetic stirrer. These 10 – 15 μ m diameter cells are non-adherent and so float freely rather than attaching to microcarrier beads or scaffolds. By division and combination with other cells, the NSCs aggregate into spherical neurosphere-like clusters consisting of stem cells and progenitor cells. The suspended aggregates initially increase in size at a fairly rapid rate, and tend to develop a multiple layered structure consisting of a surface layer of immature cells enclosing the older more differentiated cells within. Oxygen and nutrients are dispersed throughout the aggregates by diffusion. The maximum diffusion distance of oxygen through tissue is between 125 and 150 μ m, meaning that the maximum size of healthy aggregates is limited by necrosis to a diameter of less than 300 μ m. Necrosis is the phenomenon in which adequate oxygen and nutrient supply is unable to reach the central region of the aggregates; an undesirable situation leading to cell death in the central region and release of waste products that inhibit cell growth throughout the vessel. However, necrosis can be prevented by limiting aggregate diameter and by frequent dissociation (Sen *et al.* , 2001), although the dissociation process itself can destroy large numbers of cells (Sen *et al.* , 2004). Importantly, the aggregates retain their pluripotency and tendency to proliferate after being serially passaged, indicating the continual presence of stem cells (Sen *et al.* , 2002b). Thus spinner flask bioreactors are possibly a viable means of maintaining relatively large scale NSC lines.

The results from most previous major studies have demonstrated the importance of several spinner flask parameters on the culture outcome. These include stirrer speed, impeller type,

and culture time, which are discussed individually below. It would seem preferable to define spinner flasks by dimensionless parameters to provide a universality to the results and simplify comparison between studies. However, this approach has not been applied to the majority of bioreactor tests described in the literature, so likewise in the following section basic dimensional parameters such as ‘stirrer speed’ are discussed rather than Reynolds number (Re), which is commonly used in the field of theoretical fluid mechanics to describe the relative dominance of inertial forces over viscous forces.

2.4.1.1 Effect of stirrer speed on cell and tissue culture

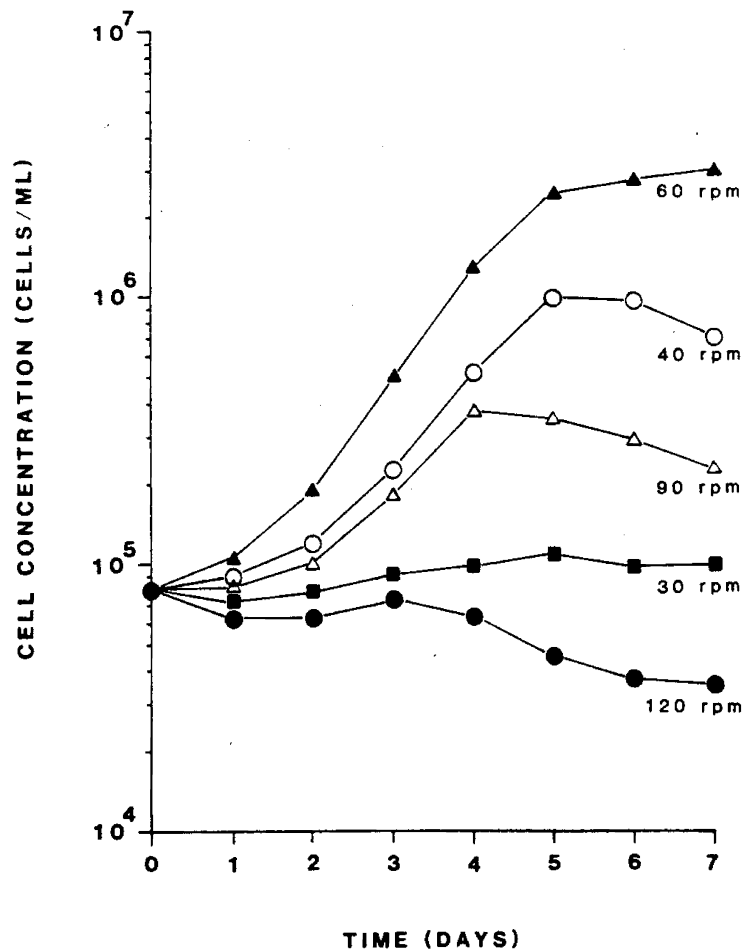


Figure 2.3: (from Croughan *et al.* (1987)) Effect of stirrer agitation speed on Vero cell growth.

Given that the range of intracellular processes arising as a result of shear stress-induced mechanotransduction is substantial, and that nutrient mass transfer is vital for cell health, it is not surprising that previous studies have found that cell and tissue culture yields depend on stirrer speed. Selected experiments are described here. Note that the critical rotational

velocity quantities mentioned are specific to the laboratory set-up and cell type used in the studies they originate from, but nevertheless indicate the importance of tuning the bioreactor flow conditions.

Firstly, Croughan *et al.* (1987) grew Vero cells on microcarriers in identical bioreactors for 7 days at stirrer speeds of 30, 40, 60, 90 and 120rpm. Comparisons of cell yield indicated that there is an optimum stirrer speed around 60rpm in this case. They hypothesised that the poor growth achieved at low velocity is due to limited mass transport and that the similarly poor growth at high velocity is due to cell damage resulting from excessive agitation (see Fig 2.3). In a separate study, Wu also observed increased cell death during Vero, CHO-K1 and BHK-21 cell culture at agitation rates greater than approximately 70rpm (Wu *et al.* , 1999).

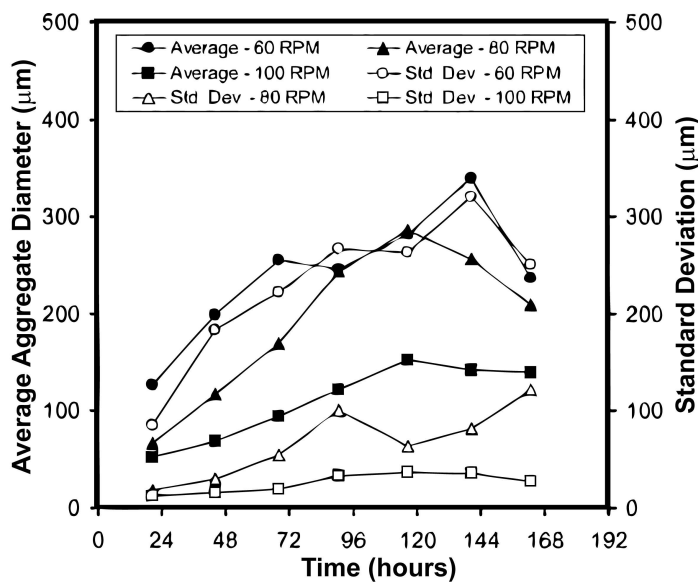


Figure 2.4: (from Sen *et al.* (2001)) Effect of stirrer speed on mean and standard deviation of cultured neurosphere size.

Outcomes of NSC suspension culture are also dependent on the agitation rate of the magnetic stirrer (Sen *et al.* , 2001). Cell aggregates exposed to an agitation rate of 60rpm were on average larger, but not as densely packed, as those exposed to agitation rates of 80rpm or 100rpm (see Figure 2.4). The high standard deviations shown in Figure 2.4 reflect the large variation in neurosphere size which occurs in bioreactor NSC culture. As previously discussed, necrosis often occurs in larger NSC aggregates, reducing the quality of the aggregates. Additionally, larger aggregates require a higher mass transfer of oxygen, which may mean that there is a deficiency at lower agitation speeds. Therefore in the case of NSC suspensions stirred using a magnetic stir bar, it may be preferable to use a higher stirrer speed to more tightly control the

size of the aggregates and raise the viable stem cell density.

It is important to recall that the optimal level of stirrer velocity (and, one would infer, Re) is fundamentally phenotype dependent. Haematopoietic cells, for instance, tend to be more sensitive to the shear induced in a mixed flask than other cell lines, and stirrer speeds as low as 30rpm are preferable to 60rpm when culturing these cells (Collins *et al.* , 1998). In contrast, an agitation rate of 60rpm was found to be favourable for chick embryo fibroblast culture (Sinskey *et al.* , 1981). The authors deemed it more appropriate to relate cell growth to the Integrated Shear Factor, which takes into account, to some extent, the geometry of the tank as well as the stirrer speed (see Equation 2.19). However, it is important when trying to correlate growth rates to stirrer speed to also consider mass transfer. Altering stirrer rates will not only alter the internal stresses, but will also affect the mass transfer coefficient k_L .

2.4.1.2 Effect of Impeller configuration on cell and tissue culture

It is well documented that a localised region of high magnitude shear stress occurs in the vicinity of impellers (Boysan *et al.* , 1988; Nagata, 1975; Sharp & Adrian, 2001; Perrard *et al.* , 2000). The impact of this region on cells primarily depends on the robustness of the cells. For example, Rushton turbines are commonly used in industry for the culture of microbial populations, however their impact on more sensitive cell lines may be excessive under typical operating conditions. Aunins *et al.* (1989) undertook an extended investigation of the turbulence around impellers, and found that both the size and type of impeller affect turbulence levels. In general, larger flat-bladed impellers were observed to induce higher turbulence than smaller stir-bar impellers. Doran (1999) studied a wider range of impeller configurations, including marine, pitched blade and Rushton impellers of various size and number of blades. Her results indicated that axially-pumping turbines improved mixing and mass transfer properties at lower shear levels. However, no detailed study of the location and size of the high shear region was undertaken. Most likely this region would correspond with the impeller discharge flow, where higher vorticity is present. A summary of the effects of impeller configuration on plant cell culture performance has been completed (Doran, 2000). The optimum configuration is not well defined, partly due to the fact that performance indicators vary across different cell types and experimental methodologies. Unfortunately there do not appear to be many similar studies for mammalian cell culture bioreactors, however the general trend in bioreactor mixing appears to be toward the use of smoother and less invasive stirring apparatus.

2.4.1.3 Effect of culture time on cell and tissue culture

As growth rates and sub-culture requirements vary significantly between different types of cells, the appropriate culture periods are primarily chosen on a phenotype basis. Growth rate studies involving mixed flask bioreactors show that in successful batches the total number of viable cells plateaus after a certain period of time. This is generally due to nutrient-transfer limitations occurring with larger cultures.

Sen *et al.* (2002b) developed passaging protocols with or without disaggregation for their NSC culture, which enabled high cell densities (1.0×10^6 cells/mL) to be achieved for long periods of time. This appears to be a necessary procedure for large scale culture of any cell or tissue. The culture of vascularised tissue is of particular concern; for example, it is intuitive that construct thicknesses should not exceed the maximum distance between capillaries found *in vivo*.

2.4.2 Rotating Wall Bioreactors

One recent development in the field of bioreactor animal cell culture has been the design of a new category of bioreactor originally formulated to simulate microgravity conditions. The generic configuration, which involves two independently-rotating concentric cylinders, is referred to here as the rotating wall bioreactor (RWB), although a variety of slightly different models of similar configuration have been designed, experimented with, and referred to in the literature by a variety of different names, including the Rotating wall perfused vessel, the High aspect ratio vessel and the Slow turning lateral vessel (STLV) (Freed & Vunjak-Novakovic, 2000, 1995; Freed *et al.*, 1997). These devices, more complicated than the spinner flask but with more flow control, have become increasingly popular, and have been used to culture a range of cells and tissues. The STLV tested by Freed and Vunjak-Novakovic consists of concentric cylinders, the inner of which is hollow and covered with a thin silicone membrane. The annular space between the outer (57.5mm diameter) and inner (20mm diameter) cylinder is completely filled with a standard cell culture medium, creating a total fluid volume of approximately 110cm³. Gas is pumped into the fluid via the inner cylinder, although the transfer of oxygen from the inner cylinder is not sufficient to grossly influence the motion of the cell culture medium. When rotated at operating speed ($20\text{rpm} \lesssim \omega \lesssim 40\text{rpm}$, according to Freed & Vunjak-Novakovic (1995)), the cylinders, with their longitudinal axis in a horizontal position, produce a low shear laminar flow resulting in the suspension of cell or tissue constructs within the medium. The concentric cylinder design is one of the key characterising features of RWBs,

along with the closed fluid region that necessitates oxygenation via perfusion. A schematic of a typical RWB system, first presented by Goodwin *et al.* (2003), is reproduced in Figure 2.5. The mechanical complexity of the RWB, particular when compared with spinner flasks, is apparent from this drawing. The complexity is further increased as more degrees of freedom are added, e.g. with a rotating inner cylinder.

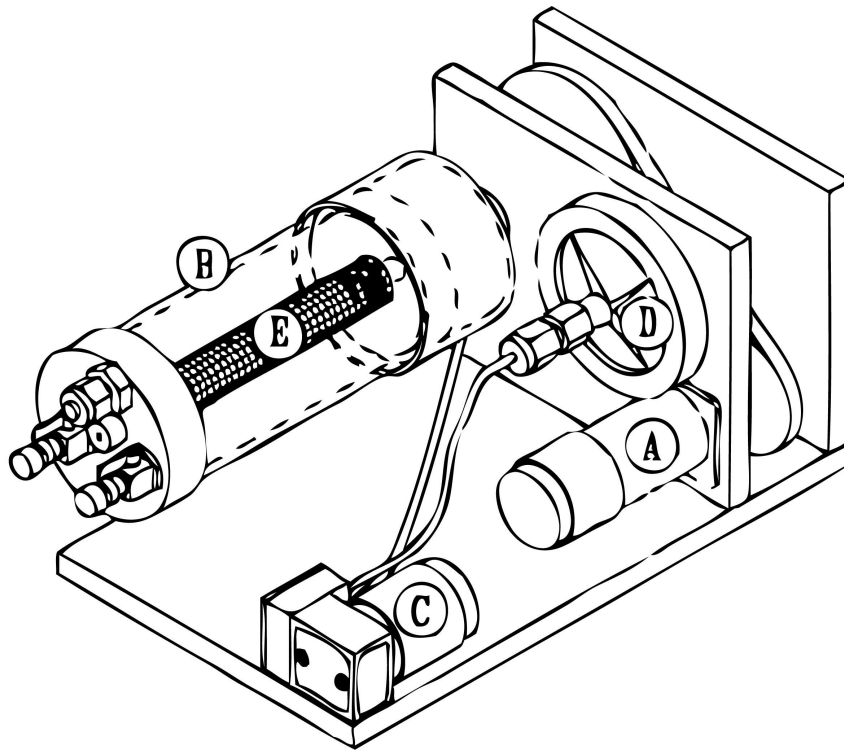


Figure 2.5: (from Goodwin *et al.* (2003)) Schematic of a RWB system. In this case, a DC motor (A) drives the outer cylinder of the vessel (B). Oxygen is delivered to the vessel by an air pump (C) that draws air into the vessel via a filter (D) and the inner cylinder of the vessel (E).

NASA have recently designed and tested an RWB labelled the Rotating wall perfused vessel (RWPV) (Begley & Kleis, 2000, 2002; Kleis *et al.* , 1990; Hammond & Hammond, 2001). The configuration resembles that of the STLV, except that a circular disk is mounted to one end of the bioreactor in order to enhance mixing by creating an effective secondary circulatory motion (see Fig 2.6). Gas is pumped into the bioreactor through the end containing the stirrer, and out through the porous filter-covered inner cylinder. The primary appeal of the RWPV results from the claim that it has the ability to suspend particles, to provide a well dispersed gas exchange, and to provide good mixing conditions all at low mechanical stress levels. Begley & Kleis (2000, 2002) have undertaken Computational Fluid Dynamics (CFD) and Laser

Doppler Velocimetry (LDV) studies that produced results supporting this claim. This theoretically means that suspended particles are subjected to variable, multi-directional hydrodynamic forces, have access to adequate gas and nutrient supply, and are not exposed to excessive shear stress levels (Kleis *et al.* , 1990). Culture of carcinoma lines in the RWPV has resulted in high cell yields, although there seems to be little literature regarding more complicated cell lines (Jessup *et al.* , 1994).

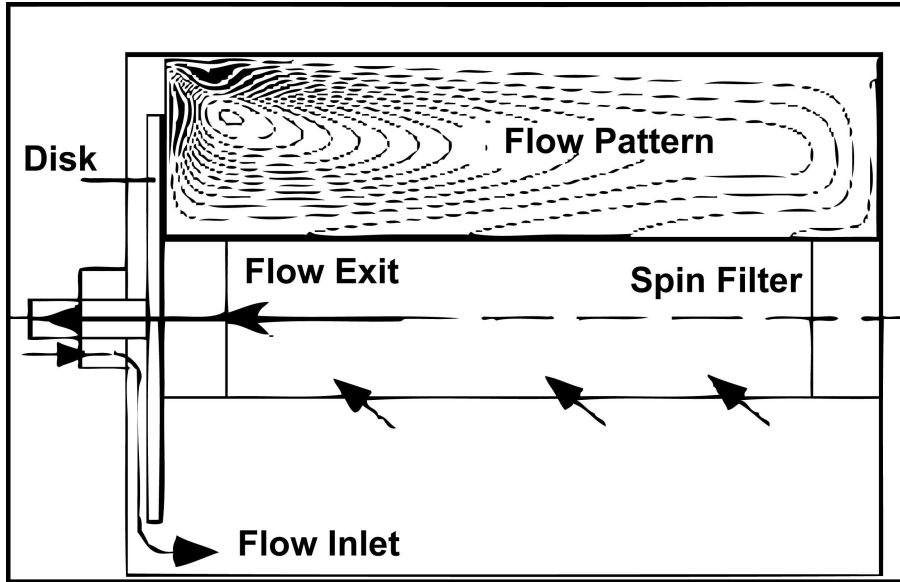


Figure 2.6: (from Begley & Kleis (2002)) Streamlines derived through CFD analysis, illustrating the secondary flow topology in the NASA-designed RWPV.

It has already been stated that cells cultured in RWB benefit from having controlled flow conditions. The analytically derived formula for the radially-dependent azimuthal-plane shear stress in the annular region for stable Couette flow is given by Bird *et al.* (1960) as:

$$\tau_{r\theta}(r) = -2\mu\omega_i R_o^2 \left(\frac{1}{r^2}\right) \left(\frac{(R_i/R_o)^2}{1 - (R_i/R_o)^2}\right) \quad (2.11)$$

where μ is the dynamic viscosity, ω_i is the rotation rate of the inner cylinder, and R_i and R_o are the radii of, respectively, the inner and outer walls of the annular region. Equation 2.11 was used by Williams *et al.* (2002) to successfully validate their CFD model of an RWB flow. In their review of RWB technology, Hammond & Hammond (2001) listed additional mathematical models, including an expression for $\tau_{r\theta}$ for the differentially rotating cylinder case, as well as mathematically-predicted particle paths and diffusion constants. Mathematical modelling has been subsequently used by Ramirez & Lim (2003) to investigate the fluid and particle dynamics within RWBs. The fact that the flow, and in particular the shear stress, can

be described in this manner (albeit as an idealised flow) illustrates the important advantage, (i.e. enhanced flow control), that laminar-flow stirred vessels such as the RWBs have over the simpler spinner flask.

Attempts have been made to compare culture performance in RWBs with that of spinner flask bioreactors. That said, it is difficult to judge definitively if one configuration is preferable to the other, particularly considering the great many variables involved. Notably, comparison between the two vessels has failed to fully quantify the differences in fluid dynamics. In two comparative studies, cardiac and cartilage tissue were grown in a static flask, spinner flask, and an RWB for a period of 2 and 6 weeks respectively. Compared to those grown in magnetically stirred spinner-flasks, the RWB cartilage constructs were larger, exhibited a more homogeneous cross-section (Freed & Vunjak-Novakovic, 1998), and contained, by percentage of wet weight, more glycosaminoglycan and collagen (Vunjak-Novakovic *et al.*, 1999) (see Fig 2.7). The RWB also yielded cardiac tissue constructs with higher cellularity and greater aerobic metabolism (Carrier *et al.*, 1999). Furthermore, Sanford *et al.* (2002) compared endothelial cells culture within a RWB to that within a spinner flask and found that while both produced large aggregates, the RWB yield surpassed that of the spinner flask. Finally, rotating vessels have been used to grow neurospheres of relatively large size (Hoi *et al.*, 2001), although the author is not currently aware of any direct comparisons with neurospheres cultured in spinner flask bioreactors.

Despite the development of these concentric cylinder rotating bioreactors, the potential for Taylor-Couette flows to form the basis of an animal cell culture reactor has not been fully explored. This is perhaps surprising considering their previous use in blood detoxification (Ameer *et al.*, 1999), algal cell culture, and as immunoadsorption devices (Ameer *et al.*, 2001). The Taylor-Couette flow (or “vortex flow”) refers to the flow instability established in the annular region of two similarly-sized concentric cylinders when the ratio of centrifugal to viscous forces (or Taylor number, Ta) exceeds a critical value required to create striking ring vortices which are evenly spaced in the axial direction. The Taylor number is defined as:

$$Ta = \frac{\omega R_i (R_o - R_i)}{\nu} \left(\frac{R_o - R_i}{R_i} \right)^{0.5} \quad (2.12)$$

Further increases in Ta induce azimuthal travelling waves which are superposed onto the Taylor vortices, and eventually induce chaotic behaviour and turbulent breakdown. Like Re , Ta is usually controlled in a particular vessel by changing ω . Since Taylor (1923) famously predicted the critical conditions using linear stability theory, the flow has been used in various

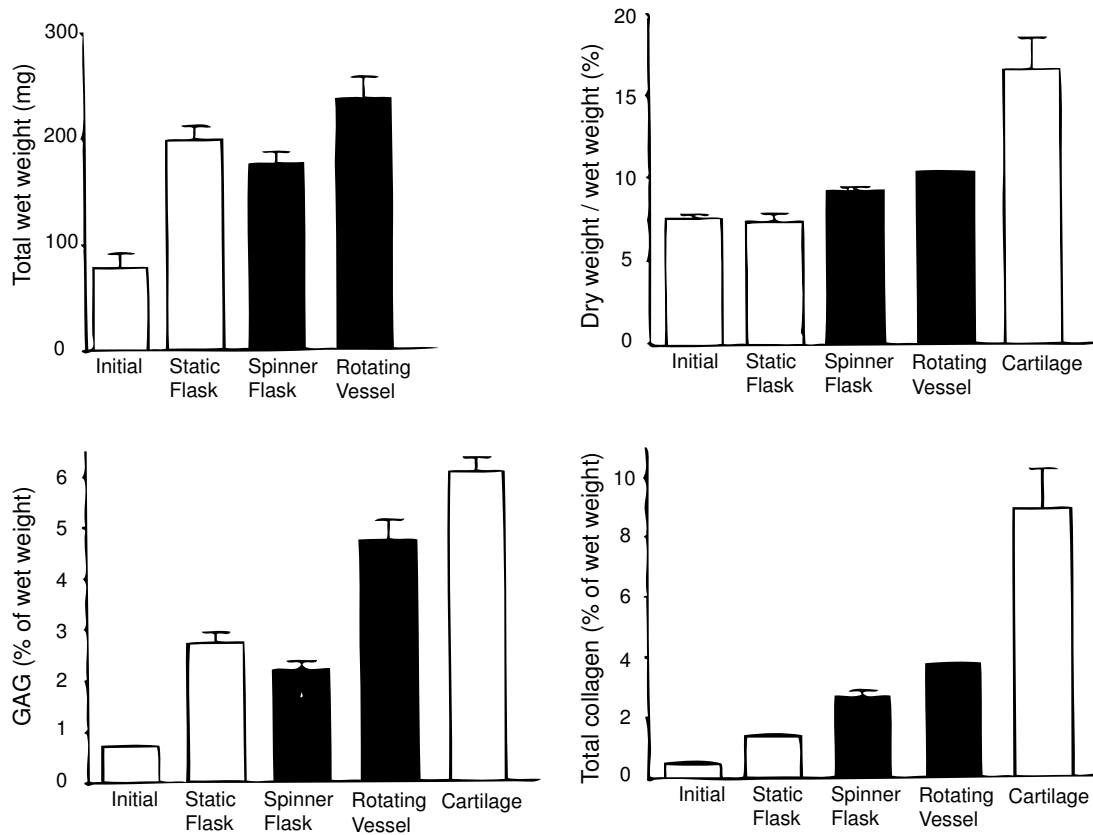


Figure 2.7: (from Vunjak-Novakovic *et al.* (1999)) Cartilage tissue composition after 6 weeks of culture in static flasks, spinner flasks, and RWBs, compared with initial and naturally-occurring levels. The properties compared include the total wet weight, the dry weight / wet weight ratio, the glycosaminoglycan levels, and the collagen levels, as indicated by the vertical axis labels.

applications due its definability and shear rate predictability (Donnelly, 1991). Theoretical models describing mass transport and particle movement in Taylor-Couette flow have been derived (Iosilevskii *et al.* , 1993). These may be beneficial for predicting cell or microcarrier behaviour in an animal cell culture bioreactor based on Taylor-Couette flow.

Curran & Black (2004) completed one of the few studies of Taylor-Couette flows for the application of cell culture. Cell viability, suspension and fluid stress levels were characterised independently against Taylor number in the range $28.8 \leq Ta \leq 288.1$. Two-dimensional flow measurements, acquired using Laser Doppler Anemometry, showed stresses increasing with Ta , and a corresponding change in the cell viability curve. They also found that the stresses were highly variable across the meridional plane, particularly in the higher Ta regimes. Aside from illustrating the potential of Taylor-Couette flows in bioreactor design, this research, along with that of Williams *et al.* (2002), Sucusky *et al.* (2004) and Venkat *et al.* (1996), demonstrates that fresh insight can be gained by approaching the problem of bioreactor design from a fluid

dynamics perspective.

2.4.3 Alternative Bioreactor Designs

While rotating wall bioreactors and spinner flasks have demonstrated promising cell culture capabilities, many other novel bioreactors have been developed and tested contemporaneously. These bioreactors are usually application-specific rather than generalist, but are often designed around the same common principle of attempting to maximise flow-induced cell response. A few examples are summarised below.

A variety of low speed perfusion reactors have been developed to culture animal cells that require a high medium supply at very low shear rates. These bioreactors typically consist of a channel with a small cross-sectional area through which cell culture media is pumped and have been used to culture both adherent and non-adherent cells. Nielsen (1999) summarised the perfusion reactors used for hematopoietic cell culture and suggested that the flatbed multipass reactor provides the greatest growth rates. The potential for large scale culture in perfusion reactors is limited by the fact that partial harvesting is very difficult and that in typical designs the culture volume is quite restricted. On the other hand, the relatively simple flow conditions make it possible to predict the internal flow and mass transport conditions (Pathi *et al.* , 2005). A perfusion bioreactor has been used for the successful growth of smooth muscle cells on tubular polymer scaffolds pumped with a pulsatile medium flow (Niklason *et al.* , 1999). The smooth muscle cells formed a blood vessel-like morphology on the scaffolds, including reasonable levels of collagen, cell density and a smooth luminal surface suitable for seeding an endothelial layer. Several varieties of perfused bioreactor have been designed, including a multi-chamber, closed-loop perfusion system designed to facilitate mass transport and mechanical stimulation appropriate for the culture of vascular tissue (Sodian *et al.* , 2002). Finally, there has been quite extensive use of perfused hollow-fibre bioreactors as a means of culturing and researching hepatocytes seeded both in suspension and on surfaces (Planchamp *et al.* , 2003).

Shaking bioreactors of 5-10L working volume have been used by Liu & Hong (2001) to culture several robust cell lines (including Chinese Hamster Ovary (CHO) cells, hybridomas, HeLa and insect cells). The use of shakers to culture micro-organisms is an old technique, yet had rarely been practiced on animal cells prior to this study. Shakers generally improved the cell yield and protein expression compared to static cultures, however additional research into flow conditions during shaking would be necessary to predict its performance when culturing more shear-sensitive cells.

2.4.4 Use of Scaffolds in Cell and Tissue Culture Bioreactors

Polymer scaffolds provide a means of culturing adherent cell and tissue constructs (Schreiber *et al.*, 1999) by functioning as a temporary synthetic extracellular matrix, and the incorporation of scaffolds into a fluid system can improve the culture outcomes. The functional arteries grown by Niklason *et al.* (1999) illustrate the great potential associated with incorporating special cell and tissue culture scaffolds into bioreactor systems.

A common example of a tissue engineering scaffold is a 5 – 10mm diameter by 2 – 5mm thick disk consisting of a 97% porous mesh constructed from 14 μ m diameter polyglycolic acid (PGA) fibres. PGA is a suitable material for the culture of chondrocytes, bone marrow stromal cells and heart cells, as these cells readily attach to the fibres (Freed & Vunjak-Novakovic, 1998). Other polymers commonly used include poly(L-lactic acid) (PLLA) and poly(lactic acid-co-glycolic acid) (PLGA). The high porosity and surface to volume ratio of scaffolds allows for increased attachment area, ingrowth of material, nutrient transport, product transport and possibly even pre-vascularisation of cultured implants (Fournier, 1999). The material also needs to be bioresorbable, particularly if the scaffolds may potentially be used for grafting; PGA for example will degrade to approximately 50% of its initial mass within four weeks of cell culture (Freed *et al.*, 1994). Furthermore, tissue cultivation may be enhanced by coating the scaffolds with growth factors found in the natural extracellular-matrix (Fournier, 1999; Ma *et al.*, 2000).

Scaffolds have been incorporated into both spinner flasks and RWBs with favourable results (Freed & Vunjak-Novakovic, 2000, 1998), although there is some evidence that the performance of some types of polymer scaffolds is altered slightly when they are used within bioreactors (Pei *et al.*, 2002). Effective seeding of the scaffolds can be achieved within spinner flasks. Applying mixing to media containing isolated chondrocytes promotes the aggregation and attachment of cells onto submerged scaffolds. After 24 hours of stirring, Vunjak-Novakovic *et al.* (1998) observed that essentially all cells seeded in a bioreactor were attached to scaffolds, in a uniform distribution. A detailed fluid mechanics study of the flows within the vicinity of stationary tissue engineering scaffolds submerged in spinner flask bioreactors was recently undertaken by Sucusky *et al.* (2004). Both flow simulations and time-resolved two-dimensional PIV were used to analyse the stresses on the surface of the tissue constructs. Not surprisingly, given the periodic and turbulent nature of the flow, they found that the stress distributions are time-variant and differ between surfaces. The effect of parameters such as the number of scaffolds, and the scaffold location and size, on the stresses experienced by adherent cells, was not

investigated.

Suspended tissue scaffolds have also been used to culture cells in RWBs, as well as spinner flasks. The problems associated with the lack of control over the forces experienced by suspended scaffolds in turbulent flow spinner flasks (see Subsection 2.4.1) can be more readily overcome in RWBs, where the flow is more predictable. At appropriate rotational velocities, the centrifugal, drag, and gravitational forces acting on the tissue constructs can be balanced so that the constructs remain stationary relative to the vessel, or stationary in absolute space (Freed & Vunjak-Novakovic, 1995). Tsao *et al.* (1994) observed different microcarrier trajectories resulting from the variation of input vessel rotation rates; these are reasonably predictable via computer simulation. The flow around scaffolds suspended in RWBs has been modelled by Williams *et al.* (2002), using a commercial computational fluid dynamics (CFD) package, and by Botchwey *et al.* (2004), using flow visualisation and a numerical code. The former study measured shear stress and oxygen distribution on the surface of scaffolds, while the latter concentrated on scaffold dynamics and interior flows.

2.5 Mixing Vessel Fluid Dynamics

In Section 2.5 we turn our attention to some of the fluid dynamics problems that are associated with bioreactor design. Within the literature, much has already been written about the nature of the flows within RWBs and the manner in which they affect bioreactor performance. While some of the principles associated with the development of RWBs are relevant to the work presented in this thesis, such as the desire for greater flow control, the focus of the bioreactor fluid dynamics study is not on this particular vessel configuration. This is because the configuration of the vessel studied in this thesis is marginally closer to that of the simpler and more common impeller-driven flask. Fluid dynamics based investigations of spinner flask bioreactors can be linked to earlier studies on mixing tanks designed for purposes that were usually very different to mammalian cell or tissue culture, such as industrial mixing or fermentation. Despite their different application, the majority of mixing vessel configurations have some similarity to spinner flask bioreactors, in that they are mostly impeller-driven turbulent flows which recirculate in the meridional plane and have an unconstrained (free) upper surface. This section provides a somewhat condensed review of previous investigations into the fluid mechanics of impeller-driven mixing vessels from a variety of perspectives, including the early attempts to characterise the generic flow pattern (Subsection 2.5.1), the empirical parameters that have very often been used to describe the flow (2.5.2), the impact and measurement of turbulence on these vessels (2.5.3), and the use of Computational Fluid Dynamics techniques to model the flow (2.5.4).

2.5.1 Nagata's Attempt to Characterise the Flow Within Mixing Vessels

Nagata (1975) attempted to summarise the generalised flow pattern within impeller-driven mixing vessels. He defined four Re flow regimes applicable to non-baffled vessels. These regimes, also illustrated in Figures 2.8 and 2.9, consisted of:

- The Completely Laminar Regime, for which there is slow laminar flow in the vicinity of the impeller, and stationary fluid toward the periphery of the tank.
- The Partly Laminar Regime, for which there is significant impeller discharge flow toward the outer regions of the tank, and hence the stagnant fluid is confined to small regions near the upper and lower parts of the impeller.
- The Transition Regime, for which the impeller discharge flow reaches a maximum, and there is flow throughout the entire vessel. In the transition regime, flow is neither fully

laminar or turbulent but a combination of the two. The turbulent region exists near the azimuthal plane of the impeller.

- The Completely Turbulent Regime, for which there are two flow regions:
 - A cylindrically-shaped, strongly-rotational core vortex zone centred around and within a small radial distance (r_C) from the central axis. In the central vortex the radial velocity is small, and the tangential velocity approaches that of the impeller:

$$r_C \geq r \gg 0 : v_\theta = r\omega \quad (2.13)$$

- A weaker, meridional plane, secondary flow, that produces a three-dimensional torus-shaped ring vortex outside the core vortex zone and above the impeller plane, if there is sufficient impeller clearance from the free surface. This recirculation pattern is illustrated in Figure 2.9. If there is sufficient impeller clearance from the base, a second torus may be formed beneath the impeller plane. This phenomenon is caused by the radial discharge flow from the impeller being forced against the tank wall, and being deflected vertically, generating angular momentum. While flow in the azimuthal direction remains the dominant fluid motion, the tangential velocity decreases as the radial coordinate increases outside the central vortex:

$$R \geq r \geq r_C : v_\theta r^{0.8} = A \quad (2.14)$$

Nagata's summary was important as it provided a general introduction to the field of mixing vessel and bioreactor fluid mechanics. As this topic is highly relevant to various process industries, it has subsequently received more detailed attention. For instance, numerical simulations of the flow fields in similar unbaffled tanks were completed by Ciofalo *et al.* (1996), producing velocity fields, turbulence fields and free surface profiles not dissimilar to those described by Nagata.

2.5.2 A Summary of Empirical Design Parameters

The description of the mixing vessel flows provided in Subsection 2.5.1 is only an approximate idealisation; in reality, the flow in stirred bioreactors and other mixing vessels can be complex in form and structure. Three-dimensional flow modelling is considered prohibitively challenging for most practical design purposes, particularly since, (a), flows are usually turbulent and (b), many simulations are needed to cover the broad range of input parameters (e.g. vessel aspect ratio, Reynolds number, impeller position, impeller size, etc.). Instead, for most

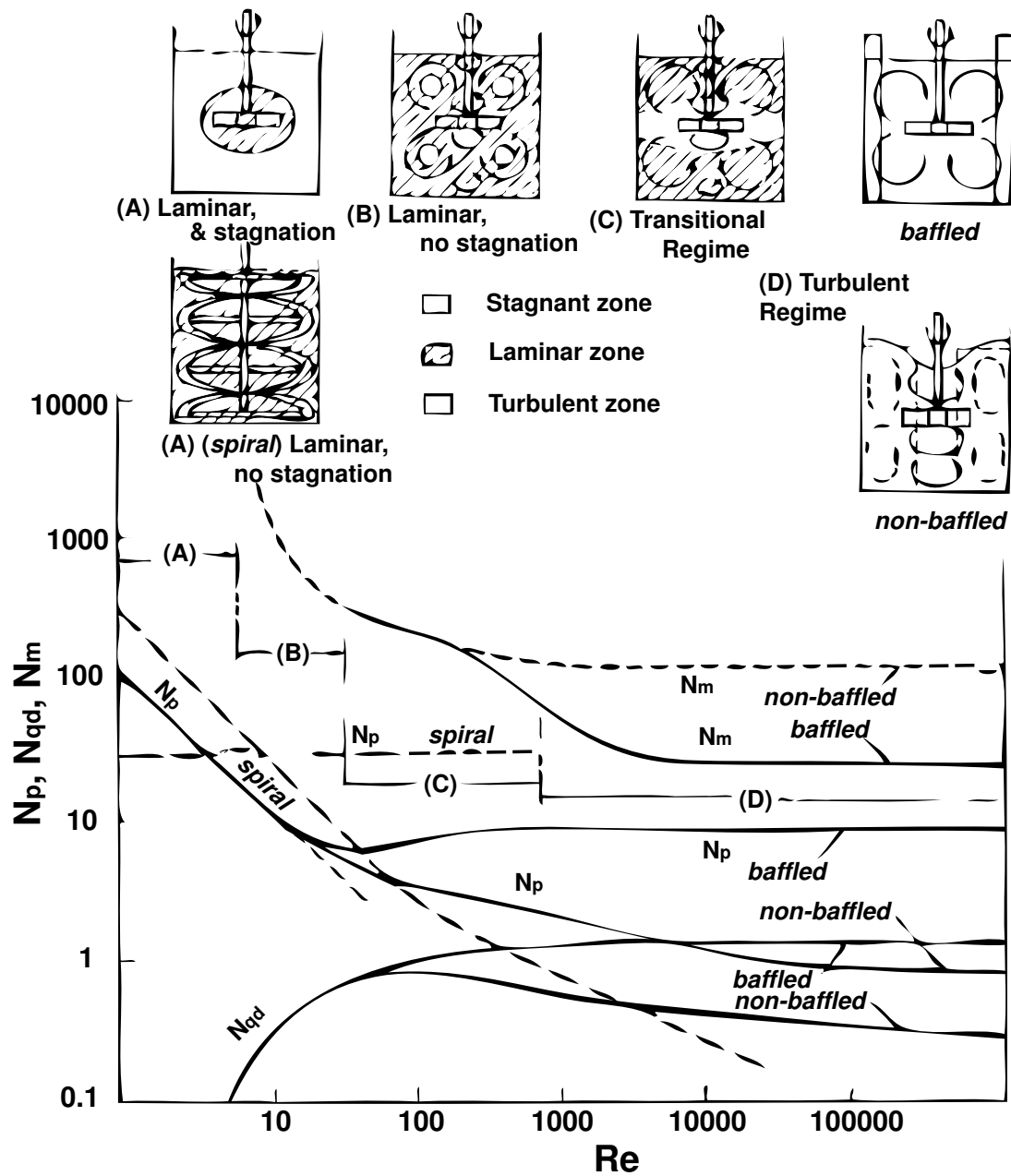


Figure 2.8: (from Nagata (1975)) Characteristic N_p , N_{qd} and N_m curves across four Re -dependent flow regimes (illustrated diagrammatically) for a mixing vessel with 8-blade paddle impeller. Baffled, non-baffled, and spiral-impeller cases are shown for the sake of comparison.

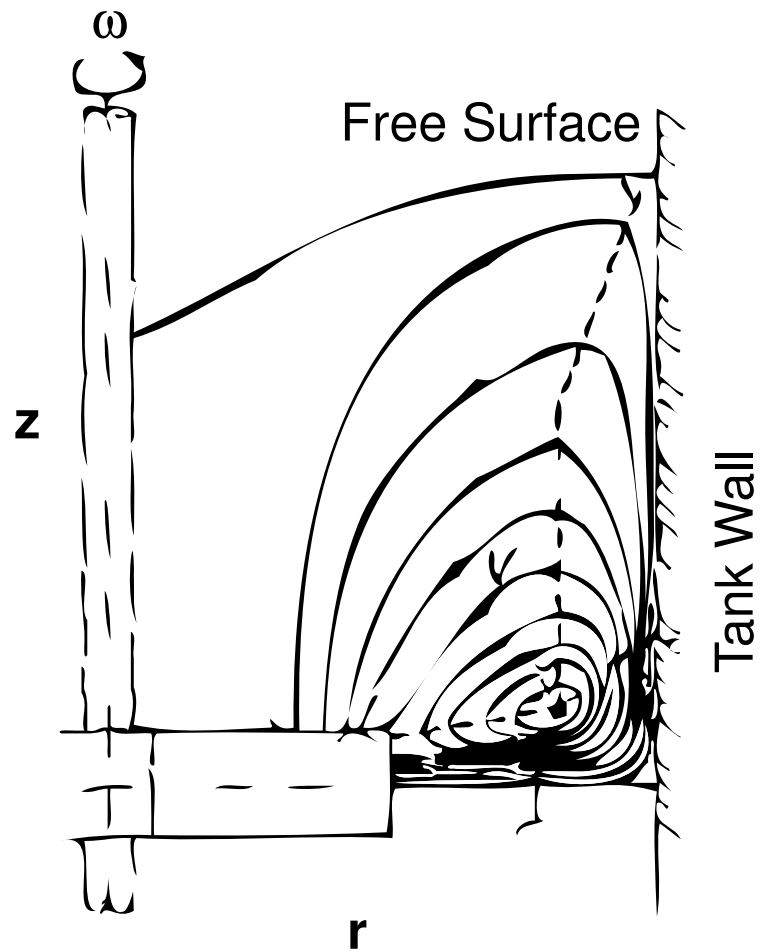


Figure 2.9: (from Nagata (1975)) Secondary flow pattern in a non-baffled vessel in the Completely Turbulent Regime, as described by Nagata. The right half of the meridional plane is shown and the streamlines represent the time-averaged flow.

applications involving these vessels, including cell culture, design has traditionally involved the optimisation of key dimensionless variables. The most fundamental of these are the power number, N_p , the impeller discharge flow number, N_{qd} , and the dimensionless mixing time, T_m' , which were defined respectively by Nagata (1975) as:

$$N_p = \frac{Pg}{\rho\omega^3(2r_i^5)} \quad (2.15)$$

$$N_{qd} = \frac{Q_d}{\omega(2r_i)^3} \quad (2.16)$$

$$T_m' = T_m\omega \quad (2.17)$$

In Equation 2.17, T_m is the mixing time, defined as the time required for the intensity of segregation to be reduced to an allowable limit. Q_d , in equation 2.16, is the flow discharged radially from the impeller.

$$Q_d = 4\pi r_i \int_0^{t_i} v_r dz \quad (2.18)$$

It should also be noted that there is by no means a single standard definition for these parameters, a recurring trait of the empirical approach that constitutes one of its major limitations. Nagata's definitions are presented here because of their common usage. A large number of empirical curves of N_p , N_{qd} , and N_m against Re , covering a multitude of bioreactor configurations, mixing materials and impeller configurations, were also provided by Nagata. Some of these, covering paddle and spiral impellers and baffled and unbaffled vessels, are reproduced in Figure 2.8. Additions and improvements to these correlations have been made since Nagata's study; for example, variations on N_p relating to the extent of gassing were summarised by Doran (1999) for various impeller configurations. Aunins *et al.* (1989) suggested the need to differentiate between the power dissipation mechanisms in small, unbaffled spinner flasks and larger, baffled vessels, and thereafter developed a range of power number correlations specifically for spinner flasks.

While these standardised parameters have fulfilled a highly practical design purpose in the process industries (Harnby *et al.* , 1992), along with, to a lesser degree, axial dispersion coefficient, oxygen dispersion coefficient, mass transfer coefficient and heat transfer coefficient (Kawase & Moo-Young, 1990), they provide a far from comprehensive picture of flow conditions inside mixing vessels. For an application requiring information regarding dynamic

properties in specific local regions, such as cell culture, non-dimensional constants based on general bioreactor configuration are generally not appropriate. While power number has often been used to estimate the energy dissipation per unit mass ϵ_{ave} (Sen *et al.*, 2002a; Cherry & Papoutsakis, 1986), the spatially-averaged nature of the parameter still limits its accuracy.

Recognising that shear stress may play a part in the production of cell derived products within bioreactors, Sinskey *et al.* (1981) defined a term to approximate shear levels. Known as the Integrated Shear Factor (*ISF*), it is related to the impeller radius (r_i), and speed (ω), by:

$$ISF = \frac{2\pi\omega r_i}{(R - r_i)} \quad (2.19)$$

Vunjak-Novakovic *et al.* (1996), amongst others, utilised the *ISF* to approximately quantify shear in their stirred cell culture bioreactor. The use of such simplified equations rapidly becomes problematic. This is because the *ISF*, as presented in Equation 2.19, neglects fluid and vessel parameters that are likely to be significant in a cell culture application. Moreover, the equation takes no account of those subtle variations in vessel configuration or fluid properties that may in fact result in non-subtle changes to the flow field; for example, the axial position of the impeller, or the fluid viscosity. Finally, the *ISF* provides no indication of the existence of regional shear heterogeneities, a matter of significance if it is necessary to identify regions of abnormal or extreme shear.

Another early approximation of two-dimensional, spatially and temporally averaged shear rate ($\bar{\gamma} = \bar{\tau}/\mu$), in an impeller-driven cylindrical mixing vessel was developed by Croughan *et al.* (1987) using Nagata's equations describing the rotational velocity on planes above or below that of the impeller.

$$\bar{\gamma} = \frac{112.8\omega r_i^{1.8}(R^{0.2} - r_i^{0.2})(r_C/r_i)^{1.8}}{(R^2 - r_i^2)} \quad (2.20)$$

The inclusion of suspended particles, such as cell clusters or microcarrier beads, constitutes an additional complication to the system. Since the mass transfer and collisions between particles are of interest in cell culture applications, equations for collision frequency (Hinze, 1971), collision severity (Cherry & Papoutsakis, 1986), mass transfer correlations (Nienow, 1975) and oxygen transport rate (Sinskey *et al.*, 1981; Tramper *et al.*, 1987) have been formulated. Cherry & Papoutsakis (1988) subsequently extended the methods of quantifying microcarrier and cell cluster damage by deriving equations for turbulent collision severity (TCS), which predicts carrier-carrier collisions and impeller collision severity (ICS), which predicts impeller-carrier collisions.

$$TCS = \left(\frac{N_p \omega^3 (2r_i)^5 v_e}{V} \right)^{3/4} \left(\frac{\pi^2 \rho_m V F_m d_m^2}{72} \right) \quad (2.21)$$

$$ICS = \frac{9\pi^4 \rho_m n_b \omega^3 (2r_i)^4 d_m^4}{512V} \quad (2.22)$$

In Equations 2.21 and 2.22, v_e is the velocity of the smallest eddies, $V F_m$, d_m and ρ_m are, respectively, microcarrier volume fraction, microcarrier diameter and microcarrier density.

Particle mass transfer coefficient k_L and its associated oxygen transfer rate $k_L a$, like the *ISF*, are reported to influence cell culture performance and are relatively straightforward parameters to estimate and compare across similar vessels. Doran (2000) compared a large range of stirred plant cell culture bioreactors using $k_L a$ to describe gas-liquid oxygen transfer. The correlation used by Doran is of the ‘‘agitation-type independent’’ form presented in Equation 2.23 (from van’t Riet (1979)), where A , α_1 and α_2 are constants and u_G is the gas velocity .

$$k_L a = A \left(\frac{P}{V} \right)^{\alpha_1} u_G^{\alpha_2} \quad (2.23)$$

A notable deficiency in this correlation form is the fact that turbulence, which in some bioreactor configurations can be a significant factor affecting gas-liquid mass transfer (Kawase & Moo-Young, 1990), is neglected. Another method used to correlate mass transfer is the characteristic Sherwood number, $Sh = (k_L r_i) / D_v$, which accounts for differences caused by impeller geometry (Aunins *et al.* , 1989). Typically, the correlation is of the form (Levins & Glastonbury, 1972):

$$Sh = A + B \times Re Sc^{\alpha_1} \quad (2.24)$$

where Sc is the Schmidt number ($Sc = \nu / D_v$) and A , B , and α_1 are constants.

2.5.3 Problems of Turbulence Affecting Spinner-flask Bioreactors

According to Nagata (1975), the flow is completely turbulent in mixing vessels driven by a turbine impeller at Re greater than approximately 10^3 . In addition, turbulence is known to affect mass transport. Therefore, turbulence is a matter of significance for many impeller driven bioreactor flows. For this reason, some of the empirical design parameters, described in Subsection 2.5.2, which correlate to cell growth, depend on the turbulence (Nagata, 1975; Saarenrinne & Piiro, 2002; Townsend, 1976). Kawase & Moo-Young (1990) also correlated a number of

design parameters with energy dissipation per unit mass (ϵ) as defined by Kolmogorov. According to the isotropic turbulence theory, turbulent flow consists of low energy, large scale eddies; high energy, intermediate scale eddies; and low energy, small scale terminal eddies. The majority of the kinetic energy due to velocity fluctuations is transferred from non-isotropic intermediate eddies to the small eddies, and is then dissipated by viscous losses in the smallest terminal eddies. These terminal eddies are independent of the bulk flow and of their size η and velocity v_e . Assuming that all the turbulent energy is dissipated in this fashion, then the local energy dissipation rate per unit mass can be assumed to equal:

$$\epsilon = \frac{v^3}{\eta^4} = \frac{v_e^4}{v} \quad (2.25)$$

While the energy dissipation per unit mass is a parameter which is often used to predict cell *damage* in mixing vessels, v_e and η have also been used in relation to cell *culture*, as they are an indication of the scale upon which eddy energy is being dissipated (Cherry & Papoutsakis, 1988). Using ϵ , shear stress acting on particles of eddy-sized scale can be estimated as:

$$\tau_e = \mu \left(\frac{\epsilon}{v} \right)^{1/2} = \rho(\epsilon v)^{1/2} \quad (2.26)$$

Calculation of power dissipation per unit mass using Kolmogorov's energy cascade model is most suited to investigating local values, rather than vessel-averaged values. In cases where little is known about the flow, the volume-averaged energy dissipation rate is usually calculated using the power number, as written in Equation 2.27. However this is problematic as the energy dissipation rate is non-uniformly distributed throughout the vessel (Levins & Glastonbury, 1972; Venkat *et al.*, 1996).

$$\epsilon_{ave} = \frac{N_p \omega^3 (2r_i)^5}{V} = \frac{Pg}{\rho V} \quad (2.27)$$

Additionally, it should be noted that the cumulative energy dissipated per unit volume on cells in a reactor was estimated by Wongsamuth & Doran (1997) as a simple time-integral of power input multiplied by the volume fraction of cells in the culture VF_c .

$$\epsilon_c = \frac{1}{V} \int PVF_c dt \quad (2.28)$$

More spatially-resolved methods of estimating energy dissipation can be obtained using field measurements. Modern flow measurement techniques mean the fluctuating velocities can

be calculated, from which periodicity due to blade motion can be removed, meaning local ε values can be estimated (Sharp & Adrian, 2001; Venkat *et al.* , 1996).

The production of Reynolds stresses as a result of the fluctuating component of velocity in turbulent flows has been described in Subsection 2.3.2. Nagata stated that in turbulent mixing vessels the peak Reynolds stresses are located around the impeller, in particular the region where the discharge flow combines with the axial flow (Nagata, 1975). Details of the Reynolds shear stress distributions in mixing vessels is limited by the difficulties associated with experimental measurement or numerical simulation of turbulence in unbaffled vessels (Aunins *et al.* , 1989; Ciofalo *et al.* , 1996). The Reynolds stresses measured in a baffled tank by Pettersson & Rasmuson (1998) using three-dimensional phase-Doppler anemometry were found to be greatest near the impeller tip, and proportional to the square of the impeller tip speed, u_{tip} . They found that measurement of the Reynolds stress is complicated by the periodicity of the Rushton impeller action. Similarly, Perrard *et al.* (2000) found that the discharge flow from a common Rushton impeller is not particularly stable, and has a cyclical radial velocity which fluctuates between $0.4u_{tip}$ and $0.8u_{tip}$ at a frequency corresponding to that of the blades. This situation is likely to be exacerbated when using a magnetic stir bar. The true turbulent stresses may be estimated by removing the periodic shear stresses, which are calculated using auto-correlation functions.

Recent advances in flow measurement techniques such as PIV mean that time dependent velocity fields can be captured with improved spatial resolution. Sharp & Adrian (2001) undertook a detailed PIV study of the impeller discharge flow from a Rushton impeller at a high tank Reynolds number ($Re = 4580$). The time progression of Reynolds stress contours in the interval between two impeller blades passing a fixed position is shown in Figure 2.10. The PIV resolution was sufficient to allow observation of tip vortices behind the leading blade, which appeared to be a major contributor to the turbulence energy within the vessel. This finding has assisted in clarifying the previous observations that the impeller region is the peak Reynolds stress region. On the other hand, none of these studies, including that of Sharp and Adrian, quantified the three-dimensionality of the Reynolds stresses.

The description of empirical vessel design parameters provided in this subsection illustrates their inadequacy as a basis for cell culture bioreactor design. The most serious limitation arises from the fact that few of the parameters take into account the spatially and temporally heterogeneous nature of the hydrodynamic forces, or the dependence of these forces on crucial properties such as Reynolds number or impeller design. That such important factors are omitted

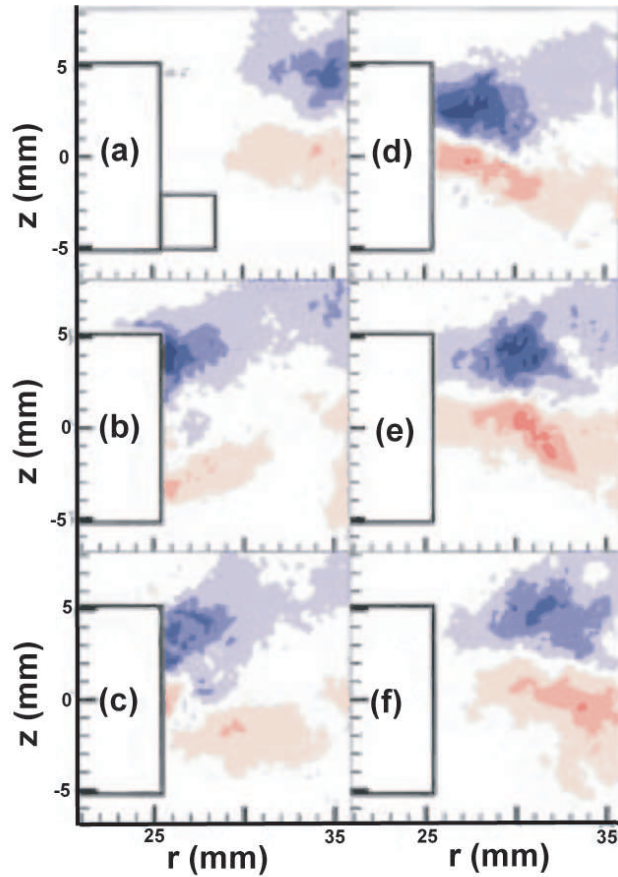


Figure 2.10: (from Sharp & Adrian (2001)) Contours of phase-averaged Reynolds stress, normalised by u_{tip}^2 , at (a) 0° , (b) 10° , (c) 20° , (d) 30° , (e) 40° , and (f) 50° behind the blade passage.

in traditional mixing vessel design equations indicates that they are inadequate for bioreactor applications.

The inclusion of turbulence significantly complicates mixing vessel fluid dynamics. While turbulence may sometimes benefit the nutrient transfer within bioreactors, the associated loss of flow control poses an impediment to the task of controlling the hydrodynamic conditions. Indeed, it can be assumed that the use of laminar mixing within upright, impeller-driven bioreactors would more readily facilitate the identification of shear stress conditions suitable for cell culture and tissue engineering applications.

2.5.4 CFD Modelling of Mixing Vessel Flows

To conclude this section, the use of CFD to model mixing vessel and bioreactor flows is briefly discussed. CFD is becoming a powerful tool for modelling these flows because it can be used

not only to derive the flow field, but also to model, in a temporally and spatially resolved manner, properties that are important to the vessel function, for example the local turbulent energy dissipation, shear stresses, and the internal transport of fluids, nutrients, particles or gasses.

The equations usually solved numerically to describe cylindrical mixing vessel flows include the continuity and Navier-Stokes equations described in terms of r , z and θ coordinates. Typically, $k - \varepsilon$ eddy viscosity models are used to model the Reynolds stresses. A paper by Jenne & Reuss (1999) reviews and compares a number of CFD studies on mixing vessel flows undertaken with this approach. Schmalzriedt *et al.* (2003) summarised the results of numerical studies in which CFD results were coupled to models of mass transport and mechanically-induced microbial cell response. Many of the studies described in these papers demonstrate the usefulness of deriving flow information for the sake of bioreactor optimisation.

2.6 The Flow Within Cylindrical Vessels Driven by a Rotating End-wall

The impeller-driven vessel flows discussed in Section 2.5 form a broad family due to the large number of potential configurations and operating conditions. This has serious consequences for generalising the hydrodynamic conditions within mixing vessels; for example, a forward-bladed impeller located at 50% of the fluid depth will produce a very different flow to a magnetic stirrer rotating about the axis. It can generally be said that if the vessel configuration is not pre-specified, then it is worthwhile designing or selecting one that provides the control and hydrodynamic features that are better suited to the potential application. For the purposes of cell or tissue culture a controlled mixing flow with low shear levels and the potential for easy scale up is preferred.

Cylindrical tanks containing fluid driven by a rotating bottom at constant velocity are an example of a vessel capable of low shear mixing. Flows within these vessels are examined in this thesis. Section 2.6 provides an overview of previous research undertaken on these flows. The majority of previous work on these has focussed on the phenomenon of Vortex Breakdown (VB), which occurs under certain parametric conditions. These vessel configurations have also been used to study coupled free surface/rotating fluid behaviour (Goller & Ranov, 1968; Muite, 2004; Miraghaie *et al.*, 2003).

The flow states within cylindrical vessels driven by rotating endwalls are usually classified in terms of two dimensionless parameters. The first of these, the Reynolds number (Re), is the ratio of inertial to viscous forces, and is defined here as:

$$Re = \frac{\omega R^2}{\nu} \quad (2.29)$$

where ν is the kinematic viscosity of the fluid, ω is the rotational velocity of the circular impeller and R is the radius of the vessel. The second parameter is the ratio H/R , where H is the depth of fluid between the upper and lower surfaces. A cylindrical coordinate system (r, z, θ) is used here to define the fluid region, with the origin taken as the centre of the bottom disk, so that the spatial domain consists of $0 \leq r \leq R$, $0 \leq z \leq H$ and $0 \leq \theta < 2\pi$.

Section 2.6 contains a summary of the flows within this vessel configuration, and is divided into subsections on vortex breakdown development (Subsection 2.6.1), the free surface case (2.6.2) and unsteady flows (2.6.3).

2.6.1 Vortex Breakdown Bubble Development

Vortex breakdown has attracted interest from fluid dynamicists for several decades. There have been several reviews published on vortex breakdown observation and theory, e.g. Hall (1972), Leibovich (1978), Escudier (1988) and Lucca-Negro & O'Doherty (2001). As well as being an intriguing natural phenomenon, VB has generated this research interest due to its applicability to a range of engineering fields, including aeronautics (Gai *et al.* , 2004), combustion (Ishizuka, 2002) and swirling pipe flows (Harvey, 1962). However as far as the author is aware, it has not received any attention in the context of bioreactor design, despite the fact that many of these vessels incorporate a swirling flow.

There is some conjecture over the precise definition of VB, and indeed there are conflicting theories over its physical mechanisms. It is most often described as being an abrupt change in the flow structure of a vortex core caused by a variation in the ratio of axial velocity to azimuthal velocity, or swirl ratio, although the cause of the structural change has also been attributed to changes in the azimuthal component of vorticity near the axis (Brown & Lopez, 1990). Several analyses of swirling pipe flows seem to support the theory that the VB recirculations in the steady regime are initiated by a super-critical swirl condition (Lopez, 1994; Wang & Rusak, 1996, 1997; Rusak *et al.* , 1998).

VB is normally associated with a stagnation zone upstream of the breakdown region, with the breakdown region itself having either a helical or recirculating 'bubble' structure. While Vogel (1968) appears to have recorded the first observation of VB within a closed cylindrical vessel driven by a rotating lid, it was Escudier (1984) who first provided a detailed characterisation of the VB bubble development in this vessel configuration. Photographic images of laser-illuminated dye patterns were used to categorise the various flow states in terms of Re and H/R . The diagrammatic representation of Escudier's characterisation study is reproduced in Figure 2.11.

Many of the general features of the flow within cylindrical mixing vessels have already been described in Subsection 2.5.1. In particular, the dominant flow is in the azimuthal direction, however at higher Re there is a secondary flow pattern in the meridional plane that develops as a result of a radial jet emanating from the impeller region. In the special case of a flat rotating bottom, the radial pumping still occurs, but from the boundary layer. As the disk rotates, fluid is transported down the central axis towards this boundary (or Ekman) layer. The centrifugal forces of the disk then act to transport the fluid in the Ekman layer toward the cylinder wall. The theoretical thickness of the Ekman layer is:

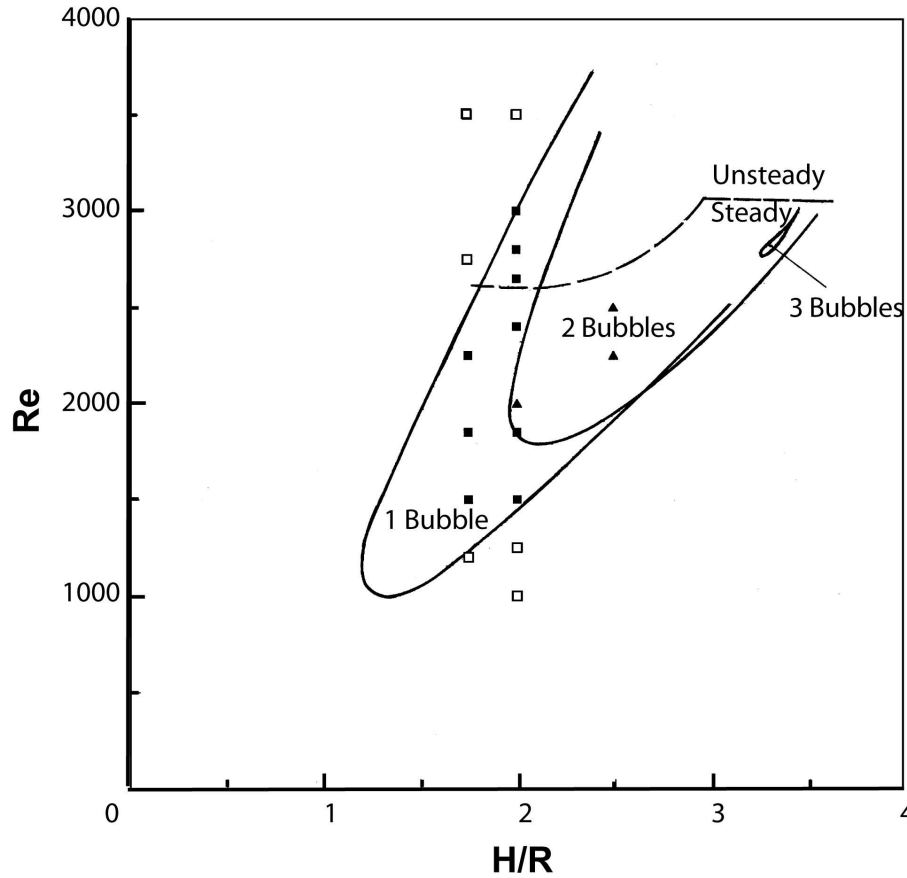


Figure 2.11: (from Spohn *et al.* (1998)) Flow states observed experimentally for various cases by Spohn *et al.* and Escudier (1984) for the rigid cover configuration. The \square symbols represent cases within the *no bubble* regime, the \blacksquare symbols represent cases within the *single bubble* regime and the \blacktriangle symbols represent cases within the *two bubble* regime.

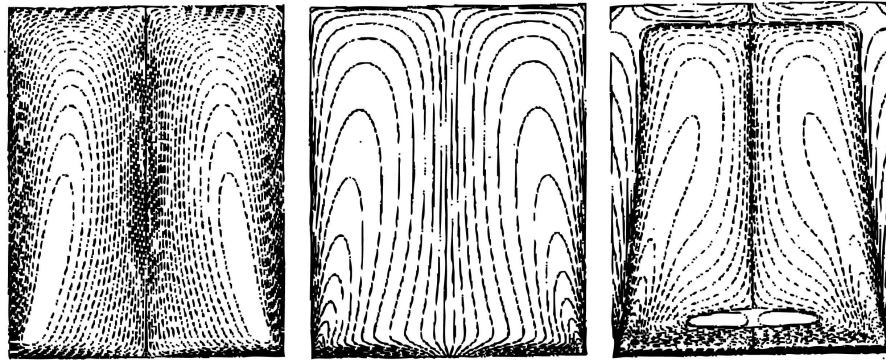
$$\delta_E \approx \left(\frac{\nu}{\omega}\right)^{1/2} \quad (2.30)$$

The discontinuity at the interface of the cylinder wall and the rotating disk causes an abrupt change in the direction of fluid momentum in this region. The fluid transported from the Ekman layer is forced by the presence of the wall boundary layer to travel in the positive axial direction. The flow adjacent to the sidewall constitutes the Stewartson layer. For the enclosed cylinder case, the upper surface, like the sidewall, has a no-slip boundary condition. Therefore, the fluid travelling from the bottom of the vessel must again change direction, this time toward $r = 0$ (i.e. the axis of symmetry). The directional change near the rigid-surface/sidewall interface is not nearly as abrupt as at the rotating-surface/sidewall interface. Both the sidewall and the top surface develop shear layers of a certain thickness controlled by the Ekman suction, although the sidewall layer has a jet-like profile in the azimuthal direction due to the high angular

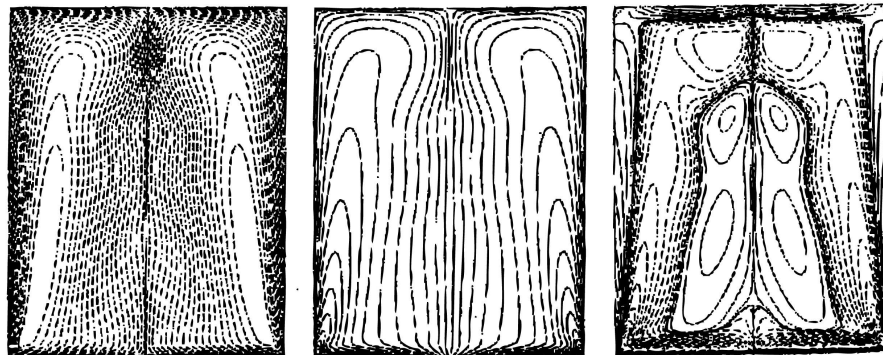
momentum (Lopez *et al.* , 2004), whereas the stationary lid has a boundary layer with a profile similar to that described by Bödewardt (1940) for a rotating flow on an infinite disk (Spohn *et al.* , 1993). $r = 0$ represents the centre of the vortex core, and it is immediately around this that the fluid is returned, in a tight spiralling motion, toward the bottom disk. As the fluid is drawn back into the Ekman layer, the secondary flow completes its recirculation in a manner similar to the pattern described by Nagata (see Subsection 2.5.1).

As can be seen in Figure 2.11, VB occurs above certain threshold values of Re and H/R . Its appearance dramatically alters the fluid motion in the vortex core region. Figure 2.12, reproduced from Lopez (1990), illustrates the numerically derived axisymmetric steady flow solution at three Re cases for $H/R = 2.5$. At Re values just below the VB threshold for a particular H/R , the streamlines of the downwards moving flow near the axis of symmetry diverge and converge slightly. The same pattern is observed in the contours of circulation ($\Gamma = v_\theta r$) near the core region. A region of azimuthal vorticity, (Ω_θ), of a direction opposite to the vorticity in the main recirculation region, correspondingly appears along the central axis. The streamlines, Γ contours, and Ω_θ contours are plotted adjacent to one another in Figure 2.12. Experimental studies of flows immediately prior to the Re threshold of breakdown bubble formation have on different occasions included the observation of what appear to be spiral flow structures on the central axis (Escudier, 1984; Spohn *et al.* , 1993). Hourigan *et al.* (1995) studied these spiral formations and found that, rather than being evidence of an asymmetric flow structure, they are streaklines resulting from slightly off-axis dye seeding. The spiral pattern enlarges in diameter at the axial position corresponding to the change in Ω_θ .

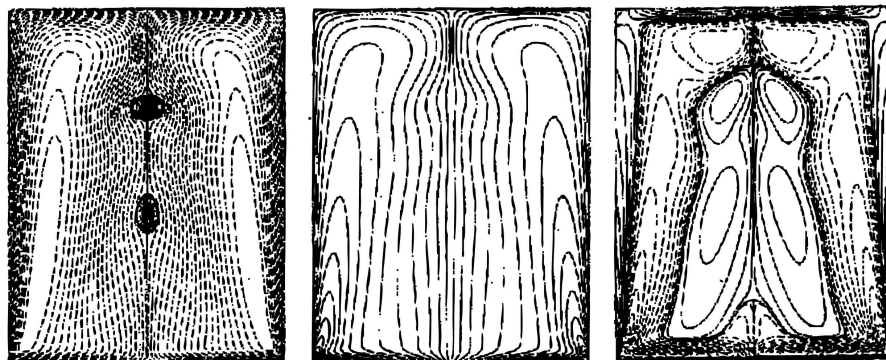
Above the threshold for the onset of VB, one or more bubbles appear on the central axis once the flow has reached steady state. The number of bubbles that form is dependent on Re and H/R ; Escudier's diagram categorises this (see Figure 2.11). In most cases, each bubble has its own upstream stagnation point, although in some states the flow consists of two recirculation bubbles joined together so that the bubble nearest the disk has a circular saddle line, rather than an on-axis stagnation point, immediately upstream of it. Axisymmetric simulation of the flow indicates that there is also a stagnation point immediately downstream of each bubble or conjoined-bubble pair, meaning that the VB region is fully enclosed (Lopez, 1990). However, despite careful rig construction this feature of the flow does not appear to be reproducible experimentally (Spohn *et al.* , 1998). Furthermore, Sotiropoulos & Ventikos (2001) and Sotiropoulos *et al.* (2001, 2002) simulated the Lagrangian motion of particles through a three-dimensional computationally derived flow field, and observed that particles released upstream of the bubble



(a)



(b)



(c)

Figure 2.12: (from Lopez (1990)) Numerically derived contours of streamfunction $\psi(r, z)$ (left), circulation $\Gamma = v_\theta r$ (centre), and Ω_θ (right) for the rigid lid, $H/R = 2.0$ case at (a) $Re = 1000$, (b) $Re = 1800$ and (c) $Re = 1994$. The contour levels are non-uniformly spaced, with 20 positive (solid) and 20 negative (dashed) levels. The spatial region shown is the meridional plane, or the region bounded by $-R \leq r \leq R$ and $0 \leq z \leq H$.

at a radial position just off the central axis are sucked into the bubble, thus implying that there is sufficient asymmetry in the flow to prevent the formation of a downstream stagnation point. Despite this, there is still controversy as to whether the true nature of the flow is axisymmetric or asymmetric, and whether the steady bubble is open or closed. Thompson & Hourigan (2003) completed a three-dimensional simulation of the $H/R = 2.0$, $Re = 1850$ case. White noise perturbation was added to the velocity field to monitor the asymmetric perturbations, but was found to decay rapidly, returning the flow to a purely axisymmetric state. Interestingly, a tilting of the disk as minute as 0.01° was found to cause asymmetries and open the downstream end of the bubble, thus offering a possible explanation for the asymmetric, open structures that have been observed experimentally.

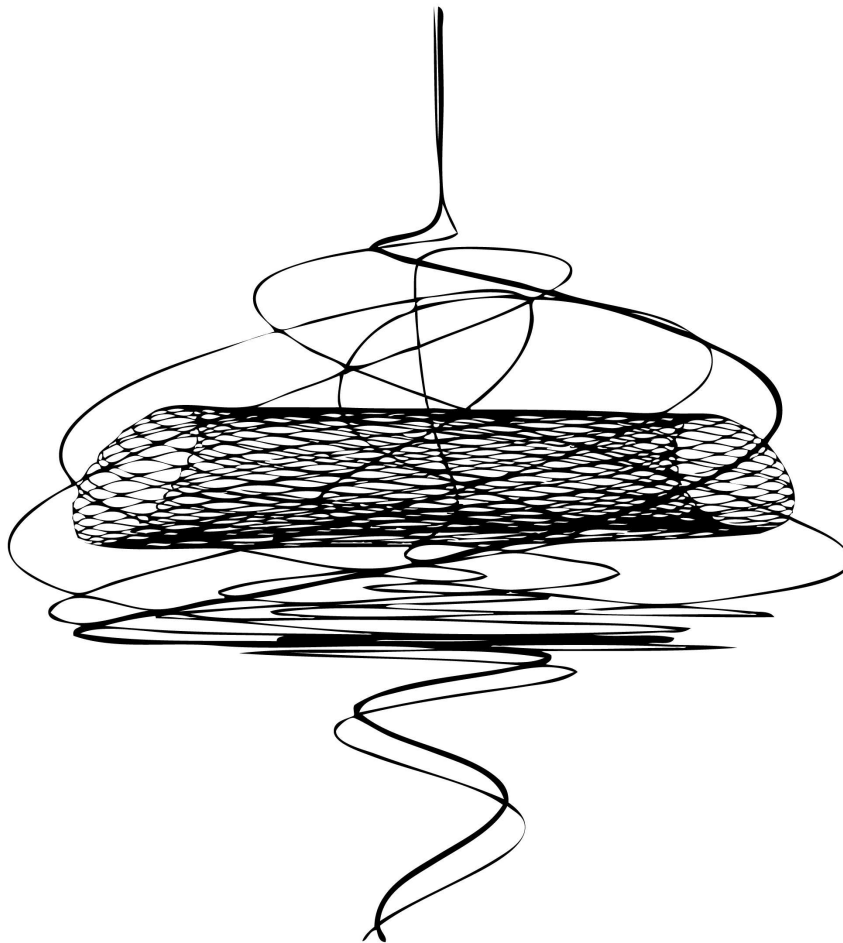


Figure 2.13: (from Sotiropoulos *et al.* (2001)) Simulated three-dimensional particle trajectories around the breakdown bubble region at $(Re, H/R) = (1850, 1.75)$ for the rigid lid case. Three typical trajectories are shown.

The Eulerian fluid motion in the internal region of steady VB bubbles has been solved with the aid of axisymmetric modelling, (e.g. by Lugt & Abboud (1997), Lopez (1990) and Shtern

et al. (1997)). The meridional plane projection of the spiralling flow results in the streamlines presented in case (c) of Figure 2.12. The recirculation described by these streamlines is in the opposite direction to the standard recirculation pattern resulting from the Ekman layer pumping. The velocity magnitudes within the VB bubble are smaller than those external to the bubble. The Lagrangian particle motions derived by Sotiropoulos *et al.* (2001) present the internal flow as being chaotic in nature. In these simulations, such as the one reproduced in Figure 2.13, particles drawn around and into the bubble were exposed to arbitrary perturbations which result in a wide variety of orbital trajectories about the axis of symmetry. After a residence time of arbitrary length, the particles eventually spiralled downwards around the central axis and out the bottom end of the bubble.

Regardless of the true nature of the flow within the breakdown bubble, the axisymmetric models generally resemble the experimentally observed flows quite closely. Below a certain Re , fully developed bubbles appear stationary in space for both flow visualisation and simulations. At higher Re , the bubbles either compact and disappear (for low H/R), or begin to oscillate and distort at the onset of flow instabilities (for higher H/R). The instability mechanisms leading to the collapse of vortex breakdown are described in Subsection 2.6.3, following a description of vortex breakdown development in the free surface case (Subsection 2.6.2).

2.6.2 Free Surface Case

With their well-defined boundary conditions, the rotating flows within cylinders enclosed by a rigid lid are useful for studying the phenomenon of vortex breakdown. On the other hand, they are not necessarily appropriate for bioreactor applications. For instance, cell culture bioreactors require a certain level of aeration that enclosed flasks do not provide without the inclusion of a sparger or a similar internal aeration device. Such devices would be likely to disrupt the flow through the release of bubbles and through bluff body effects, thus making the hydrodynamic conditions substantially more difficult to control. An alternative solution to the problem of aeration may be to provide a free surface to the medium, thus giving cells access to oxygen through natural gas transfer.

Studies of flow in free surface cylindrical containers with rotating bottoms are relatively rare compared to the closed lid cylinder case. Spohn *et al.* (1993) were the first to characterise the VB states for the free surface case. This was done in much the same way as Escudier had characterised the fixed lid case. Figure 2.14, reproduced from a later paper by the same authors (Spohn *et al.*, 1998), categorises the various flow states in terms of Re and H/R . Note that while on-axis bubbles once again occur, there are some significant differences to the closed cylinder case plotted in Figure 2.11.

With the removal of the rigid surface, the three-dimensional no-slip condition along the top of the cylinder no longer applies. The free surface gives rise to very different boundary flows, which are discussed in more detail later in this subsection. The conservation, in theory, of the azimuthal momentum at the upper surface has a profound effect on the VB flow structure. Significantly, the absence of the $v_\theta = 0$ condition at $z = H$ allows the vortex breakdown bubble to attach to the surface. In other words, the upstream stagnation point is replaced with a circular stagnation line as the bubble remains toroidal at its upper end. Indeed, there exist only a narrow band of cases, corresponding to lower Re values, for which VB bubbles do not attach to the free surface. Other key differences to the rigid surface case include the formation of VB at lower Re and H/R values and the failure to observe upper limits for VB. The surface attachment of the breakdown bubble leads to a different range of flow topologies to the rigid surface case.

For an aspect ratio of $H/R = 1.5$, on-axis bubbles were observed by Spohn *et al.* (1993) at Re as low as 770, several hundred less than the onset of bubble breakdown in an enclosed cylinder. Initially, the toroidal-shaped bubble appears below the free surface, a state referred to here as the *axis bubble* regime. As Re increases, the bubble enlarges and elongates similar to the rigid-cover case, and the stagnation point moves toward $z = H$. Spohn *et al.* observed that the

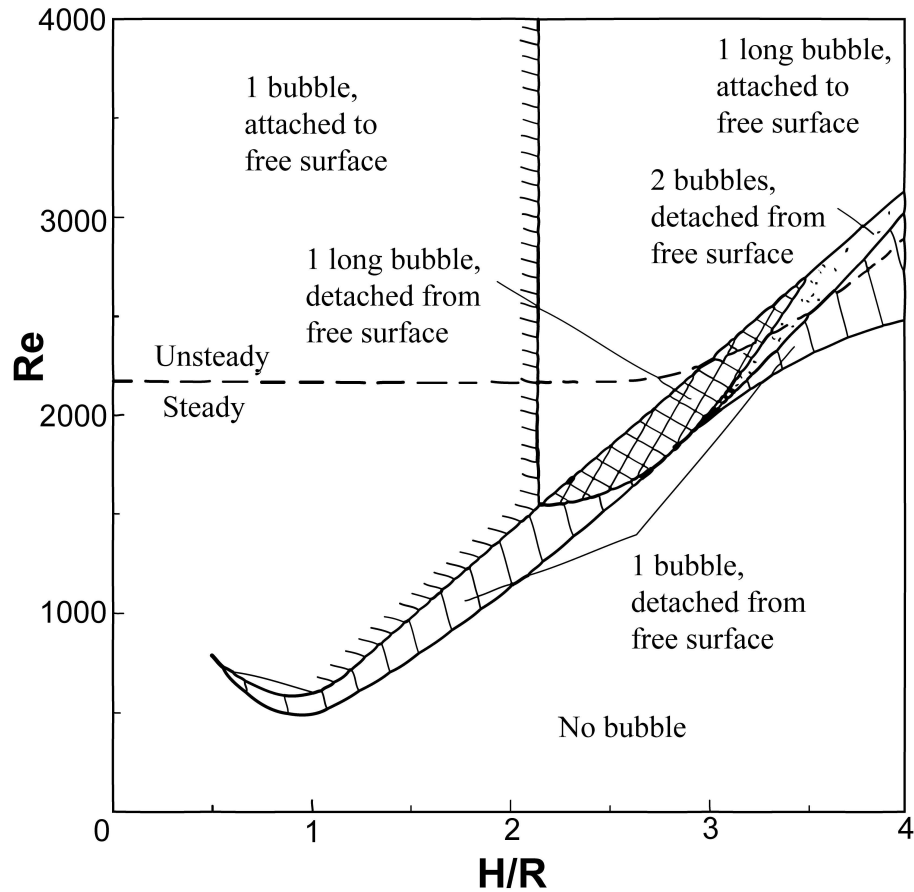


Figure 2.14: (from Spohn *et al.* (1998)) Flow states observed experimentally by Spohn *et al.* for the free surface configuration.

bubble becomes attached to the free surface at $Re = 975$, although the threshold values reported by subsequent numerical studies are lower still (Brøns *et al.*, 2001; Valentine & Jahnke, 1994; Iwatsu, 2005). Once the bubble is attached to the surface, the stagnation ring increases in diameter with higher Re . Likewise, the outer diameter of the VB recirculation increases in diameter. At a sufficiently high Re (not specified by Spohn *et al.*), this *corner bubble* state is replaced by a *surface bubble* state, in which the toroidal recirculation region becomes detached from the axis. The stagnation ring, as well as the inner and outer radii of the recirculation torus, continue to move away from the central axis with a further increase in Re , although this movement has not been quantified. As with the rigid lid case, the steadiness of the breakdown bubbles eventually gives way to radial oscillations at sufficiently high Re . Spohn *et al.* nominated a stability limit of $Re \approx 2100$, although they conceded that this value was determined on the basis of whether the oscillations were visible to the human eye. The formation of two vertically aligned bubbles, relatively common in the rigid surface case at $H/R \geq 2.0$, also occurs in the free surface case, but for a much smaller range of $(Re, H/R)$.

Since Spohn *et al.*'s visualisation experiments, the free surface case flows have been studied numerically on several occasions; albeit often indirectly through the co-rotating top and bottom case which produces a very similar flow (Gelfgat *et al.* , 1996b; Valentine & Jahnke, 1994; Okulov *et al.* , 2005; Lopez *et al.* , 2004). Brøns *et al.* (2001) derived two-dimensional stream functions $\psi(r, z)$ across a similar range of $(Re, H/R)$ to that studied by Spohn *et al.* Their numerical simulations revealed a greater level of complexity in the flow structure than was observed experimentally. In addition, by systematically identifying bifurcations in the flow topology, they were able to identify several VB regimes not listed by Spohn *et al.* Furthermore, a higher stability limit was derived than that seen in experiments, possibly as a result of the ideal conditions that were enforced. The various topologies derived by Brøns *et al.* are reproduced in Figure 2.15, with alphabetic notations assigned to each regime. At H/R values of around 1.5, the two new topologies identified were (i) and (j), which correspond to, respectively, a corner bubble with internal corner bubble regime, and a surface bubble with adjacent corner bubble regime. Both of these topologies only occur over a relatively small parameter domain. Brøns *et al.* themselves remarked that these new states, while being important for completeness of the overall flow regime diagram, may be very difficult to isolate under experimental conditions.

Numerical simulation of the axisymmetric flow has also been undertaken by Iwatsu (Iwatsu, 2005, 2004). These solutions qualitatively replicated most of the regimes derived by Brøns *et al.*, although there was some disagreement over the estimated critical points. For example, Brøns *et al.* evaluated the critical point for the initiation of regime (i) in Figure 2.15 as being $(H/R, Re) = (1.42, 1686)$ whereas Iwatsu estimated $(H/R, Re) = (1.43, 1732)$. Iwatsu also identified a corner bubble with internal axis bubble regime, a state which exists in a very narrow parameter range preceding the development of regimes (i) and (j).

The measurement of velocity fields within experimental rigs has been relatively rare. Young *et al.* (1995) used laser doppler velocimetry (LDV) to measure the time-periodic behaviour of the flow at $H/R = 2.0$, although their results were not spatially resolved. Spohn *et al.* (1998) estimated velocity fields in the meridional ($r - z$) plane as well as several horizontal ($r - \theta$) planes for $(H/R, Re) = (1.75, 1850)$. As these fields were determined from particle streak lengths recorded using long-exposure photography, rather than a well recognised, statistically based method such as PIV, there were significant gaps in the data and possibly large uncertainties. Hirska *et al.* (2002) acquired PIV measurements with care, however the results they presented were limited to a small Re range ($1500 \leq Re \leq 2500$) and to a few horizontal planes. Meridional plane measurements are made especially difficult by the large dynamic range and

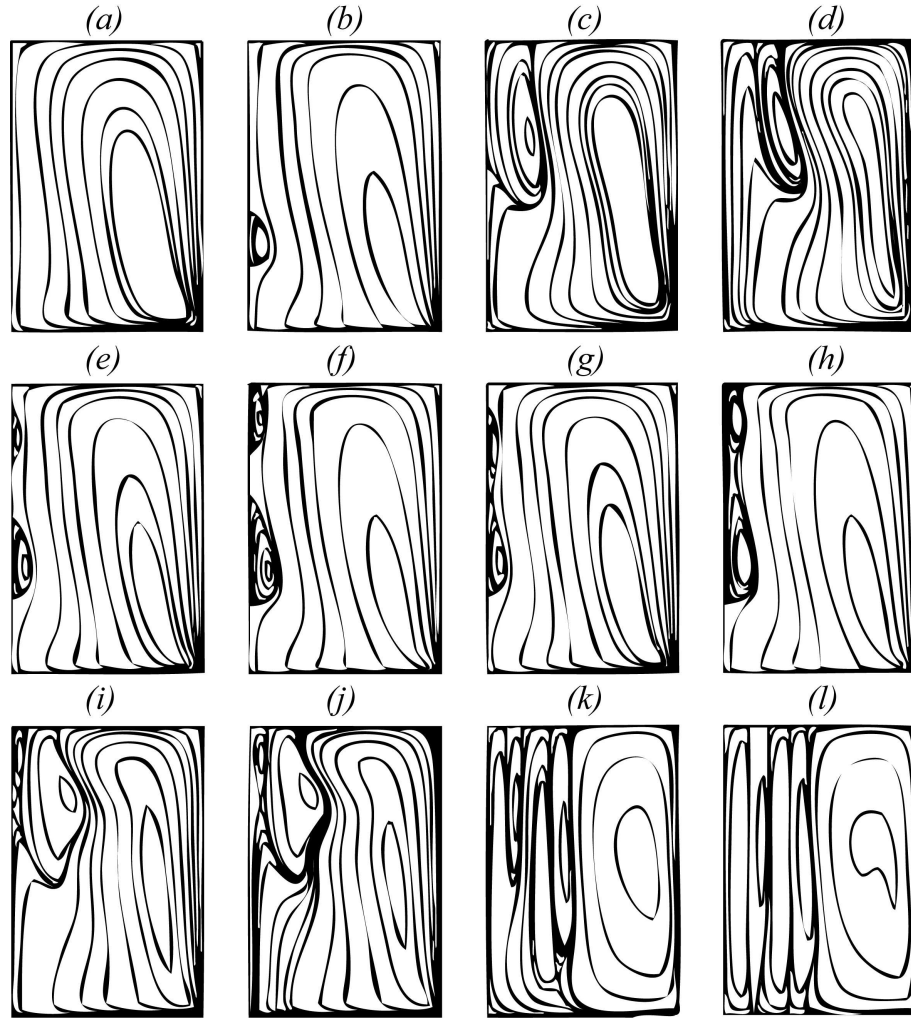


Figure 2.15: (from Brøns *et al.* (2001)) Contours of the stream function in the right half of the meridional ($r-z$) plane. The regimes derived by Brøns *et al.* are: (a) $(Re, H/R) = (1000, 2.0)$, no bubble. (a) $(Re, H/R) = (1000, 2.0)$, no bubble. (b) $(Re, H/R) = (2800, 4.0)$, axis bubble. (c) $(Re, H/R) = (1000, 1.0)$, corner bubble. (d) $(Re, H/R) = (1700, 1.0)$, surface bubble. (e) $(Re, H/R) = (1950, 3.0)$, two axis bubbles. (f) $(Re, H/R) = (3000, 4.0)$, axis and corner bubble. (g) $(Re, H/R) = (1700, 2.7)$, conjoined axis bubbles. (h) $(Re, H/R) = (3100, 4.0)$, conjoined bubbles with surface attachment. (i) $(Re, H/R) = (2500, 1.9)$, corner bubble with internal corner bubble. (j) $(Re, H/R) = (2800, 2.0)$, surface bubble with adjacent saddle loop. (k) $(Re, H/R) = (1500, 0.3)$, shallow cylinder multi-cell topology. (l) $(Re, H/R) = (2100, 0.3)$, shallow cylinder multi-cell topology.

the high velocity component normal to the light-sheet. Spohn *et al.* attempted to alleviate this problem by opting for a thick light-sheet. However, increasing the light-sheet thickness can lead to additional uncertainties due to lower light intensity (Raffel *et al.* , 1998), and increased depth-averaging. This is undesirable, as an accurate analysis of the meridional plane dynamics can produce useful information about the flow structure.

An important matter regarding the free surface case which has not yet been discussed in

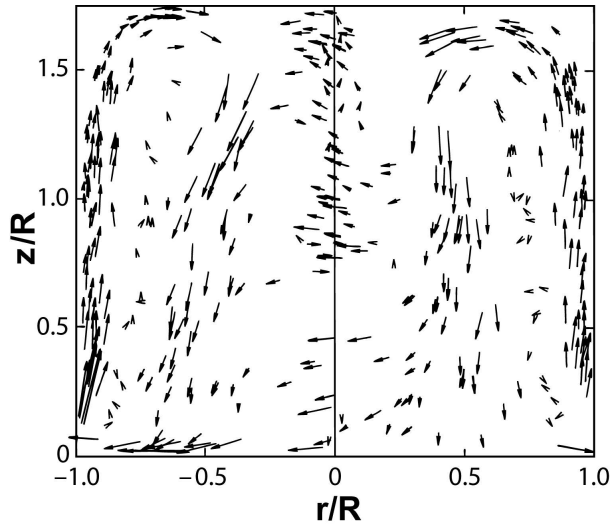


Figure 2.16: (from Spohn *et al.* (1998)) Velocity field measurements of the meridional plane for the free surface case where $H/R = 1.75$ and $Re = 1850$.

this subsection is the common assumption that there is a shear free condition at the air-water interface, and thus no viscous boundary layer at this surface. While a perfectly stress-free surface condition has been integrated into numerical simulations, it is impossible to realise experimentally, as even tiny contaminating substances form surface monolayers and surfactant concentration gradients that impact on the near-surface flow. Hirs *et al.* (2001), Lopez & Hirs (1998), and Lopez & Hirs (2000) tested the effect of small levels of contamination on the surface of a controlled open-channel rotating flow. The proportion of the surface covered by a surfactant layer, which positively correlates with the degree of contamination, was varied to determine its effect on the surface and bulk flows. Compared with the flow topology in the perfectly clean, zero concentration case, the near-surface topology is noticeably affected by a partial coverage of the surface with surfactant. The surfactant is swept toward $r = 0$ by the recirculation in the bulk fluid, and so the flow in the inner radial region is most affected. While there is a noticeable change in the azimuthal flow component with varying surfactant concentration, it is more pronounced in the meridional flow. The meridional near-surface flow in the case where the surface is fully covered by a surfactant monolayer appears similar to the case of a radially stagnant top, whereas the azimuthal near-surface flow resembles the stress free case far more closely. The authors suggested that rotating free surface flows are likely to have a $v_r = 0$ condition at $z = H$, while it is probably reasonable to assume a free slip condition for v_θ . These findings also imply that experimental measurement of a free surface flow is likely to more closely predict the conditions in a practical application than a numerical simulation

with an idealised surface condition.

Numerical studies will also typically assume a perfectly flat surface. In reality, a finite deformation is inherent to rotational, free surface flows, although surface curvature can be minimised by extremely careful setup (Hirsa *et al.*, 2002; Lopez *et al.*, 2004). Surface deformation is controlled by gravitational and capillary effects, and so the governing parameters are the Froude number (Fr), the Capillary number (Ca) and the Weber number (We). The Froude number is the ratio of inertial to gravitational forces, given by:

$$Fr = \frac{\omega R}{\sqrt{gH}} \quad (2.31)$$

The ratio of surface deformation displacement to the cylinder radius can be estimated as the square of Fr . Ca and We are, respectively, the ratio of viscous forces to surface tension and the ratio of centrifugal forces to surface tension, defined by:

$$Ca = \frac{\mu\omega R}{\phi} \quad (2.32)$$

$$We = \frac{\rho\omega^2 R^3}{\phi} \quad (2.33)$$

where ϕ represents surface tension. If We and Ca are low, then the surface tension can act to dampen the effect of other surface forces. For example, the degree of wetting at the three phase (liquid/gas/sidewall) interface caused by the viscous forces on the fluid can be reduced by increasing the surface tension. While the gravitational and capillary forces cause only very small surface deformation under standard experimental conditions in water (Spohn *et al.*, 1993, 1998), these forces are important in the context of the surface and upper boundary flows. For example, Miraghaie *et al.* (2003) measured the longitudinal wave-like motion on the free surface of the spinning lid flow caused by the instabilities occurring at higher Re . By noting the non-linear coupling between the surface and bulk flow dynamics, they postulated that the mechanisms linked to the onset of instability in this flow could be fundamentally altered by a change in the relationship of surface forces.

2.6.3 Onset of Unsteadiness

The early characterisation studies of vortex breakdown flows within cylinders with or without a fixed lid mention the development of time-periodic bubble behaviour and increasing flow unsteadiness at sufficiently high Re (Escudier, 1984; Spohn *et al.*, 1993), but little regarding the processes associated with the transition to turbulence. The axisymmetric solutions derived

computationally by Lopez (1990) for the rigid lid, $H/R = 2.5$ case took an increasingly long time to reach a steady state as the Re increased beyond approximately 2000. At $Re = 2765$ the flow was found to be oscillatory and unsteady.

The LDV study conducted by Young *et al.* (1995) on the free surface, $H/R = 2$ cylinder flow at $1500 \leq Re \leq 4000$ revealed periodic behaviour at $Re \approx 1900$, well below the $Re \approx 2100$ limit reported by Spohn *et al.* (1993). The strength of the single frequency oscillation increases between $1900 \leq Re \leq 2200$, before the occurrence of a subharmonic bifurcation at $Re = 2200$ resulting in the addition of a second frequency of half the value of the original. At $Re = 2400$ a new mode develops, this time with four frequencies; at a value close to the original observed frequency, at half the original frequency, at $3/4$ of the original frequency, and at $1/4$ of the original frequency. At $Re \gtrsim 2600$ the flow was observed to become increasingly aperiodic.

More recently a large number of numerical studies have been conducted in order to provide a more detailed understanding of the transition processes (Sørensen & Christensen, 1995; Stevens *et al.*, 1999; Gelfgat *et al.*, 1996b,a, 2001; Sotiropoulos & Ventikos, 1998; Serre & Bontoux, 2002; Lopez *et al.*, 2004; Lopez & Marques, 2004). The transition process is not simple, as stability analyses have identified a range of competing axisymmetric and asymmetric instability modes. While there is a strong axisymmetric instability that develops (Gelfgat *et al.*, 1996b; Lopez & Perry, 1992; Sørensen & Christensen, 1995), the development of asymmetric instabilities is also an important part of turbulent transition (Sotiropoulos & Ventikos, 1998; Blackburn & Lopez, 2000; Marques & Lopez, 2001). Three-dimensional flow simulation at Re values associated with time-variant flow structures has revealed that symmetry breaking in rigid lid vessels can lead to the formation of rotating waves. These waves, which precess about the axis of symmetry, have been observed in a number of studies, although there still does not seem to be consensus on their occurrence. A variety of rotating wave modes have been observed numerically to exist and co-exist, depending mainly on the $(H/R, Re)$ condition. The physical origin of the symmetry breaking has been attributed to asymmetric flow separation in the Stewartson layer (Spohn *et al.*, 1998; Sotiropoulos & Ventikos, 1998), but also to an instability originating from the axially and azimuthally swirling flow in the region near the disk/sidewall interface (Blackburn & Lopez, 2000; Marques & Lopez, 2001).

The rotating wave asymmetries have also been observed both experimentally and numerically for the free surface case (Hirsa *et al.*, 2002; Miraghaie *et al.*, 2003; Lopez *et al.*, 2004; Lopez & Marques, 2004). Lopez *et al.* (2004) compared numerical and experimental results for $H/R = 2.0$. Symmetry breaking to a $k = 4$ mode rotating wave was recorded at $Re = 1925$

in the simulation, well below the threshold of the axisymmetric instability mode detected previously by Brøns *et al.* (2001). At $Re \approx 1990$, the steady $k = 4$ wave became unstable to a low-energy $k = 2$ wave, similar to the period doubling observed by Young *et al.* (1995) for the same H/R value. The $k = 2$ mode became increasingly energetic at higher Re . According to the simulations, at $Re \approx 2090$ the flow became significantly complicated by the introduction of a $k = 3$ component with time-periodic energy levels. The dominant $k = 4$ mode was apparent in the experimental data for $H/R = 2.0$, despite the inherent imperfections affecting surface flatness and stresses. Experimentally, the $k = 2$ component was barely detected, and the $k = 3$ component was not resolved, although this was attributed to the relatively low energy levels of these modes.

2.7 Summary of Previous Work and the Motivation for the Present Study

There have been many studies investigating the feasibility of using stirred vessel bioreactors for cell and tissue culture applications, with the majority producing positive results. Indeed, in many cases it has been noted that these systems produce superior yields to the traditional static flask cell culture. Yet despite this, in current practice static flasks remain the commonly preferred apparatus. The reasons for this are varied, but include the relative simplicity of the system and the lack of need, until recently, to develop large scale quantities of animal cell and tissue.

The factors that have in the past impeded the standardisation of bioreactor technology include the following:

Lack of a generalist bioreactor. Most bioreactor designs have been application based, as has been the focus of the literature reporting them. One result of this is that novel bioreactors lack exposure and marketability. In contrast, static flasks have a reputation for being a reliable, albeit limited, culture vessel for most cell types.

The large range of applications. The considerable variability in cell behaviour between different phenotypes makes it difficult to find an appropriate starting point. This problem is compounded by the wide range of desired outcomes that exist. For example, the conditions required to keep a stock of haematopoietic stem cells alive may be vastly different to the conditions suitable for a massive scale-up of osteoblasts.

The high cost of bioreactors compared with static flasks. At present, the cost of the simpler and more commonly available vessels suitable for static culture (e.g. petri dishes, bottles) is significantly lower than most commercially available bioreactor technologies. However, further bioreactor development may reduce this.

The lack of existing knowledge regarding the causes of variability in culture outcomes. This is due to both the complexity of most biological systems and the need for more research by practitioners of the various fields associated with cell culture bioreactor development. The differences in cell culture yields caused by modifications to bioreactor design have not sufficiently been explored from either a biological or a fluid dynamics perspective. Crucially, not knowing precisely how cells respond to particular stress conditions makes it difficult to formulate the most appropriate bioreactor solution.

Progress in various fields related to cell culture, such as stem cell and tissue engineering research, has increased the likelihood that functional, massive-cellularity batches will be needed in the future. Consequently, intensified demand should increase the interest in producing bioreactors and other cell culture systems capable of consistently reproducing the required aggregates or constructs. A lack of thoroughness and uniformity when it comes to cell culture bioreactor design processes means that current technology is mostly unable to meet these requirements. These deficiencies reflect knowledge gaps in both the bioreactor physics and the biological response of cells to these physical conditions. For this reason, it is a pertinent time to concentrate on these areas of research.

For instance, it is known that agitator speed affects growth in a mixed flask (see Section 2.4.1), yet the reasons behind this are somewhat vague; for example, could it be that increased speed causes excessive shear stresses in an unforeseen region of the vessel? Moreover, some of the important parameters related to cell growth in bioreactors probably remain unidentified. One of the more important mixing vessel characteristics concerning mammalian cell culture that *has* been identified in the literature is the internal stress distribution. However, there have so far been few comprehensive studies completed on the distribution of bioreactor fluid stresses in the vicinity of the actual cells and tissue constructs, and even fewer attempts made to accurately control this mechanism. In addition, the possible exploitation of various other physical flow phenomena for the purposes of cell culture is yet to be fully explored. For example, the formation of vortex breakdown bubbles within laminar cylinder flows could potentially produce stress and mixing conditions conducive to reliable cell or tissue culture. However, vortex breakdown is a fairly complex phenomenon, so a strong understanding of the relevant fluid dynamics is necessary for initial progress in this area.

The approach traditionally exercised in previous attempts to model bioreactor flows has been to commence with a measurement or adaptation of an established bioreactor technology. The study described in this thesis proceeds from a different angle, with an investigation of more fundamental flows derived as idealised examples of mixed flask bioreactor flows. The intention here has been to use experimental fluid dynamics to locate conditions within a simple mixing vessel that can potentially be applied to specific applications, which may include suspension cultures, cultures adhering to freely suspended microcarriers, or cultures adhering to stationary polymer scaffolds. Practical design issues such as oxygenation and nutrient replenishment have been addressed as part of the selection of a suitable flow, but not as the primary concern.

In other words, unlike previous bioreactor research, special emphasis is placed on identi-

fyng and controlling the fluid dynamics, meaning that all the results presented in this thesis describe flow conditions. The extent to which cells are affected is not considered directly. The decision to take this atypical approach has been motivated by a dearth of past opportunity to optimise bioreactor conditions in this general manner. Previous bioreactor optimisation work has typically been undertaken with the immediate aim of producing a large yield of a particular cell or tissue type; an approach which limits the universality of the results because the behaviour of the phenotype under consideration may not necessarily represent how other cells will behave. Furthermore, in many studies, bioreactor performance is measured solely by the properties of yields resulting from a very limited number of experiments over a small parameter space. While this methodology can be useful for providing a proof-of-concept for a particular bioreactor design as a worthwhile means of culturing cells, it does little to enhance the knowledge base required for users to predict *a priori* how a culture will behave when exposed to a particular set of bioreactor input conditions, let alone allow a prediction of the conditions at which the outcomes may be optimised. There are two main reasons for this.

The first of these is straightforward. By focussing too heavily on a particular outcome, the range of input conditions tested is likely to be more limited. A more methodical parameter study results in a more thorough modelling of system behaviour. Furthermore, the use of non-dimensionalised parameters and results also provides a universal relevance to the experiments.

Secondly, by drawing a direct relationship between the biological outcomes and the mechanical input conditions, there is no recognition of the mechanisms that link the two. To improve bioreactor characterisation, two systems in particular must be differentiated from one another and modelled independently. Firstly, a characterisation study is needed to model the mechanisms through which the bioreactor physical conditions, (e.g. flow properties, chemical properties, thermodynamic properties, etc.), are affected by the input conditions, (e.g. vessel geometry, stirrer speed, gas supply, etc.). Secondly, a description of how cells behave when exposed to these conditions is required. Both of these systems are exceedingly complicated, and require a great deal more investigation by researchers from a range of different specialisations. As mentioned previously, the current work focusses on a particular area of the former system, namely a characterisation of the flow conditions for a range of input conditions.

As the number of input conditions that could potentially be tested is quite vast, the scope of the investigation needs to be chosen carefully. For this reason, a single vessel geometry is used for this study, that of a cylinder with a rotating bottom and a free surface. In the chosen configuration, the diameter of the rotating bottom matches that of the cylinder, and the

remainder of the cylindrical working section is devoid of protruding objects that might disturb the flow. The free surface is included to enable gas transfer to the cell culture media. This is a similar configuration to other mixed flask bioreactors, however not identical. In this case the geometry is deliberately kept simple, with the utilisation, for example, of a flat rotating disk rather than a complicated impeller design. The Re range chosen is in the laminar and transition region, as these flow regimes allow for greater control than turbulent flows, as was discussed in Subsection 2.5.3. Having control over the flow ensures repeatability of the hydrodynamic conditions that cells are exposed to.

At the Re and H/R values chosen for this study, the phenomenon of vortex breakdown is an integral part of the flow, and is thus assessed in the context of cell culture applications. Moreover, vortex breakdown has been introduced to this bioreactor research because it has the potential to aid in the control of cell culture, just as it has been utilised to great effect in industrial flame control processes (see review by Ishizuka (2002)). For the VB region to be utilised effectively for cell culture there is a need to address properties such as bubble shape, internal stresses and particle residence time, as well as the effect of Re on these. This research closely examines the evolution of bubble shape and internal stress fields with Re . This investigation should also be regarded as being relevant to the general field of vortex breakdown. In particular, the three-dimensional velocity field of vortex breakdown in a cylindrical container is measured for the first time, and the results achieved further illuminate this complicated phenomenon.

Distancing this study from a bench test scenario in which yields are directly analysed does not mean that cell culture is not the primary motivator for this work. All the measurements presented, be they principal stress values, vector fields, or regions of high vorticity, are directly relevant as they are parameters that affect the performance of particular cell culturing processes. By placing emphasis on using non-dimensionalised values, the intention is to characterise the performance of this particular geometry in terms of properties relevant to cell culture. By coupling information of this type with information regarding the predicted response of cells to particular stress levels, it should eventually be possible to devise more sophisticated and standardised bioreactor engineering processes. A similar approach in other areas of bio-fluid dynamic interest has been quite successful. As one example, cardiovascular flow modelling has been undertaken in virtual conditions completely removed from the biological tissue, in order to investigate the hydrodynamic conditions that affect endothelial cells in a variety of situations (see Taylor & Draney (2004)). For bioreactors, only basic attempts have previously been made to couple the behaviour of very simple microbial cell populations with the internal

fluid dynamics to achieve complete system models (Lapin *et al.* , 2004; Bauer & Eigenberger, 1999, 2001; Bezzo *et al.* , 2003; Schmalzriedt *et al.* , 2003).

In summary, this thesis does not include an attempt to categorise all potential bioreactor flows, nor all possible flows within a cylinder with a rotating bottom. Rather, it demonstrates an alternative way of approaching the bioreactor design problem as the cell culture requirements evolve with the development of new biotechnologies.

Chapter 3

Experimental Methodology

3.1 Introduction

As the flows were investigated mostly in the context of potential cell culture applications, a controlled experimental approach was undertaken. The use of experimental techniques meant that the flow could be analysed without the idealisations typical in numerical simulations. The constructed bioreactor model was capable of producing the required vortex breakdown flows whilst facilitating optical-based visualisation and measurement techniques. The initial experiments consisted of qualitative flow visualisation, the purpose of which was to examine the various flow topologies occurring in the vessel at different Re . The primary measurement tool was Particle Image Velocimetry (PIV), as this could be used to acquire spatially and temporally resolved velocity fields. Rather than the common single camera PIV, a dual camera Stereoscopic PIV (SPIV) technique was used. SPIV was preferred as it provided greater measurement accuracy and facilitated the measurement of three-component velocity and stress fields. As hydrodynamic stresses strongly affect cell growth, SPIV is a powerful tool for predicting appropriate bioreactor flows. Despite this, SPIV has not previously been used to characterise bioreactor stress fields in this manner.

This chapter provides an overview of the experimental model configuration (Section 3.2), and the flow visualisation (3.3), PIV (3.4), and post-processing (3.5) procedures. Within Section 3.4 there is a specific focus on SPIV, with the novel aspects of the method emphasised in extra detail. Throughout the chapter, various sources of error are discussed, along with the actions taken to reduce the size and effect of the uncertainties.

3.2 Experimental Model Configuration

The experimental model consisted of a polished, transparent container with a 65mm diameter cylindrical centre hole, mounted on a stainless steel base, as illustrated in Figure 3.1. The exterior faces of the outer glass tank were kept flat in order to reduce optical distortion errors caused by refraction. The scale of the vessel was kept to that of stirred mammalian cell bioreactors found in the literature, which typically have a fluid volume of around 100 – 300mL. Careful assembly was necessary to diminish the misalignments and artificial perturbations that have been shown to change the VB structure (Thompson & Hourigan, 2003).

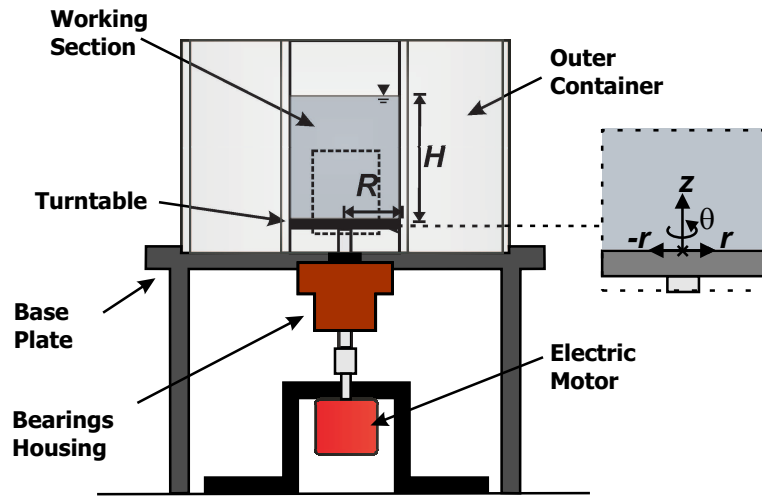
The swirling motion within the working section was controlled by a flat aluminium turntable maintained at constant speed using a high-resolution stepper motor. A motor drive and motion controller with micro-stepping (National Instruments), were used to control the 0.7 Ampere motor (Sanyo-Denki). The total number of micro-steps per revolution was 5.12×10^4 , corresponding to a micro-step angle of less than 0.01° . This resolution provided a sufficiently smooth rotation at angular velocities in the operating range $5\text{rpm} \leq \omega \leq 40\text{rpm}$. Motor settings such as the rotational rate, spin-up rate and spin-down rate were set on the basis of Re using software created with the programming language *LabVIEW* (National Instruments).

The coordinate system of the experimental model is illustrated in the inset of Figure 3.1(a). The axes were defined cylindrically, i.e. by radial (r), axial (z), and angular (θ) position. The origin corresponded to the top centre of the rotating disk, or the bottom centre of the working section. Positional data were normalised by the cylinder radius, R , in the radial direction and the surface height, H , in the axial direction.

Precise mounting of the turntable and accuracy of the input rotation rate helped to minimise any erroneous flow disturbances. Two sets of miniature ball bearings, contained within a housing as shown in Figure 3.1, were used to hold the 8mm diameter shaft in position. These were particularly effective in reducing radial movement of the disk as well as rotational movement of the disk in the $r - z$ plane. The various components of the rig were designed and constructed to reduce any misalignment between the rotational centre of the turntable and the cylinder axis. For instance, the base plate was milled with circular grooves for the Perspex cylinder and the bearing housing, which ensured that the axes of the impeller shaft and the cylindrical working section were co-linear.

The impeller itself consisted of a disk attached to the end of the drive shaft using three M3 screws. When coupled to the motor, the impeller sat just above the base plate. As the impeller diameter was initially chosen to match that of the cylinder, the top surface of the im-

pellor effectively acted as the vessel bottom for the purpose of the experiments conducted. The gap between the cylinder inner diameter and the impeller was carefully machined to prevent both impeller contact with the wall and, at the other extreme, any significant flow between the working section and the small region beneath the impeller. The maximum gap allowed was 0.05mm, corresponding to $< 0.2\%$ of the disk radius R . Any water that was found, over a long period of time, to leak into the region below the impeller was sealed into the vessel by a rubber shaft seal set into the base. This meant that leakage over a large time period was prevented, and thus H/R remained constant throughout the duration of an experiment. The working fluid was set to a particular H/R only when the region between the base plate and the impeller was completely filled with fluid. In addition to these precautions, the surface of the aluminium impeller was anodised black to minimise reflections and to provide a smooth finish. The ability to reduce reflectivity of the rig components was important for experiments involving intense light sources. Finally, the rotation of the impeller in the $r - z$ plane was measured using a sequence of 2000×2000 pixels images, and was found to have an amplitude of less than 0.2° , corresponding to a maximum displacement in the z direction of 0.1mm (or 0.2% of the total fluid depth when $H/R = 1.5$). Given that the impeller shaft was tightly constrained in this direction, it follows that the measured angle represents the ‘lid tilt angle’ described by Thompson & Hourigan (2003). They found that tilt angles as small as 0.01° forced lid-driven cylinder vortex breakdown flows to become asymmetric and opened at the downstream end.



(a)



(b)

Figure 3.1: (a) Annotated schematic illustrating the model bioreactor rig configuration, including the working section dimensions R and H and the coordinate system. (b) Three-dimensional drawing of the vessel assembly, including outer glass-walled tank.

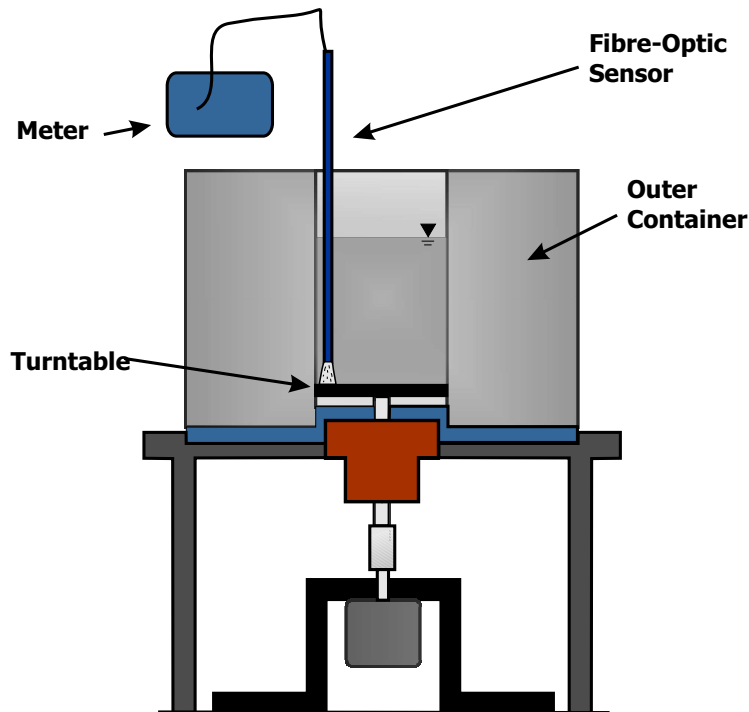


Figure 3.2: Configuration used to test rotational accuracy of the impeller.

3.2.1 Validation of the Reynolds Number Accuracy

Reynolds number accuracy was limited primarily by slight fluctuations in fluid temperature, however it could be controlled to within $\pm 1.4\%$. The temperature of the working fluid could be controlled to within $\pm 0.5^\circ\text{C}$, and any inaccuracies were mitigated by the use of water, the viscosity of which is not temperature-sensitive compared with other liquids commonly used in fluid dynamics experiments, such as glycerine. The use of a small fluid volume ($V = 161.8$ mL), a covering lid above the tank, and a settling period before the experiments, helped prevent the formation of significant thermal gradients across the working section. It is important to limit thermal gradients as vortex breakdown flows within cylindrical vessels have been shown to be sensitive to Rayleigh number (Ra), which represents the relative effect of heat transfer on the flow (Lugt & Abboud, 1997). The impeller radius was only 68% as large as that used by Spohn *et al.* (1998), who took similar measures to prevent excessive temperature gradients. This is significant, as Ra scales with R^3 , and so a reduced vessel size substantially limits thermal effects.

The accuracy of the turntable rotational velocity was validated using a photonic sensor capable of accurately measuring the frequency of rotation. A thin white strip was placed towards the edge of the rotating disk. The optical sensor, which detects slight changes in reflected

light, was carefully positioned directly above the radial position of the white strip, as shown in Figure 3.2. Thus, a signal was recorded for every rotation of the disk. After taking a 20 minute sample at a sample rate of 20kHz, the rotational frequency was found to match the frequency set on the *LabVIEW* program to within 0.1%, over the ω range used in the current study ($5\text{rpm} \leq \omega \leq 40\text{rpm}$).

3.2.2 Practical Issues Associated with the Model

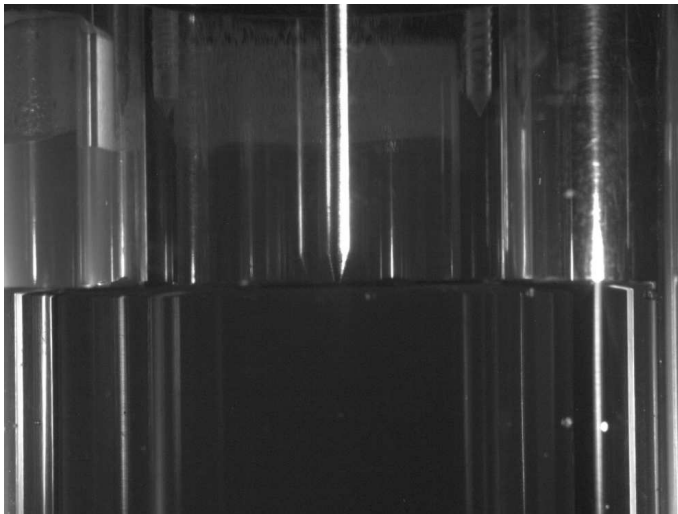
As discussed in Section 2.6, boundary conditions play an important role in determining the type of VB structure that will exist within the cylindrical vessel. From here arises a complication associated with using a free, rather than rigid, surface. Any minor perturbation on the upper surface is likely to cause a major disturbance of the VB bubbles. Therefore, mechanical shocks were avoided during experiments. A low power motor without a gearbox was used, as this induced very little mechanical vibration. Furthermore, the cylindrical container was screwed directly onto a precision-flat steel optical table (Melles-Griot), in order to minimise the effect of any shocks or vibrations.

For each case studied, a settling period was necessary before the flow became fully developed. This period, during which the flow could not be disturbed in any way, lasted longer than 10 minutes on some occasions. This posed a minor problem for PIV and visualisation experiments, as these time intervals were significant enough to cause minor settling, flocculation and centrifugal dispersion of heavier particles. As it was not possible to take thermometer readings without disturbing the flow, temperature measurements were taken subsequent to data acquisition rather than during the settling period.

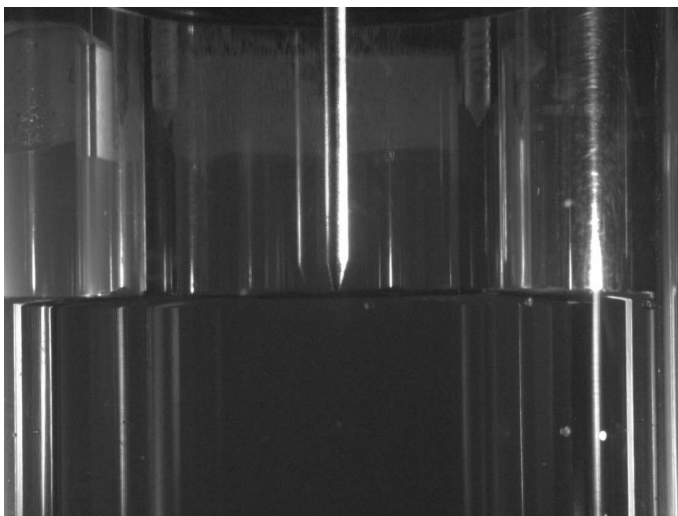
As previously mentioned, minor imperfections in the experimental rig construction cause the flow to become slightly asymmetric and the VB bubble to open. However as the primary aim of this investigation is to study vortex breakdown in the context of a practical application, rather than an idealised flow phenomenon, these minute artificial disturbances do not pose a significant problem. For instance, given the extreme sensitivity of VB flows to experimental imperfections, such as lid-misalignment and tilting, it is unlikely that there would be axisymmetric flow and closed bubble formation in a real bioreactor application.

It is documented that the boundary conditions at an air/water interface are hard to control, especially since any contamination of the surface leads to the presence of Marangoni stresses, meaning that a truly stress-free surface is in practice only obtained with great difficulty (Hirsa *et al.*, 2001). There is no recorded information about the natural surface properties occurring

in practical bioreactor applications, however it is unlikely that they would be too dissimilar to those of the current laboratory study. This is because a confluent surfactant monolayer is likely to form, and so similar surface stresses should occur in practice. In any case, the formation of such a monolayer is unlikely to have a major effect on the bulk flow, as previous comparisons between topologies derived experimentally (Spohn *et al.* , 1993) and computationally (Brøns *et al.* , 2001; Iwatsu, 2005) have not revealed any major discrepancies caused by differences in the surface stress conditions.



(a)



(b)

Figure 3.3: Photos illustrating surface deformation under (a), static, and (b), non-static ($Re = 2400$), conditions.

The surface condition during impeller rotation was verified using still and video photography. Colour photographs of the surface taken (a), under static conditions, and (b), at $Re = 2400$, are included in Figure 3.3. These images were captured using a digital still-image camera (Minolta). In both cases, the centre of the camera lens was positioned at a height corresponding to the nominal free surface position when $H/R = 1.5$. Aside from wetting very close to the water-solid interface, no surface deformation was observed. Spohn *et al.* (1993) also reported negligible deformation, despite having a much larger Froude number ($\sim 10^0$, compared with $\sim 10^{-2}$ in this case). For the experimental results described in this thesis, H/R was kept constant at 1.5, measured to an accuracy of $\pm 0.02\%$ using a height gauge (Mitutoyo).

3.2.3 Rig Maintenance

To ensure the success of the experiments, it was important to maintain a clean and functional rig. For example, the accumulation of dust and sedimentary particle residue adversely affects the image acquisition process for PIV, and so regular cleaning of the rig was necessary. As the rig was designed with a gap of less than $50\mu\text{m}$ between the cylinder and the impeller, prevention of particle build-up in this space was important. Therefore, the rig was deliberately designed for simple disassembly so as to facilitate easy cleaning. Repolishing of the Perspex cylinder was undertaken at regular intervals in order to remove slight scratches engraved on the sidewalls by the particles. A buffing tool mounted on a lathe was used to accomplish this.

3.2.4 Incorporating Submerged Scaffold Models

The experimental scaffold models consisted of a disk and a supporting column (see Figure 3.4). The disks were cylindrical in shape with a circular cross-section of radius r_s , and thickness t_s . The disk aspect ratio, r_s/t_s , was 2.50. The disks were constructed from Perspex, and had a non-compliant surface. Unlike tissue engineering scaffolds, which are usually porous in order to maximise the potential for extra-cellular matrix materials to penetrate between cells, the Perspex disks were 100% solid. However, due to the minuscule size of the scaffold pores, the effect of the models on the bulk flow should be the same as a scaffold. Sucosky *et al.* (2004) similarly used high aspect ratio, cylindrical Perspex disks in order to model the flow around tissue engineering scaffolds.

The use of a supporting column complicated the configuration of the system but was unavoidable if the scaffolds were to remain in position. It is also a necessary part of any practical system in which stationary scaffolds are submerged. In this case, a stainless steel needle of

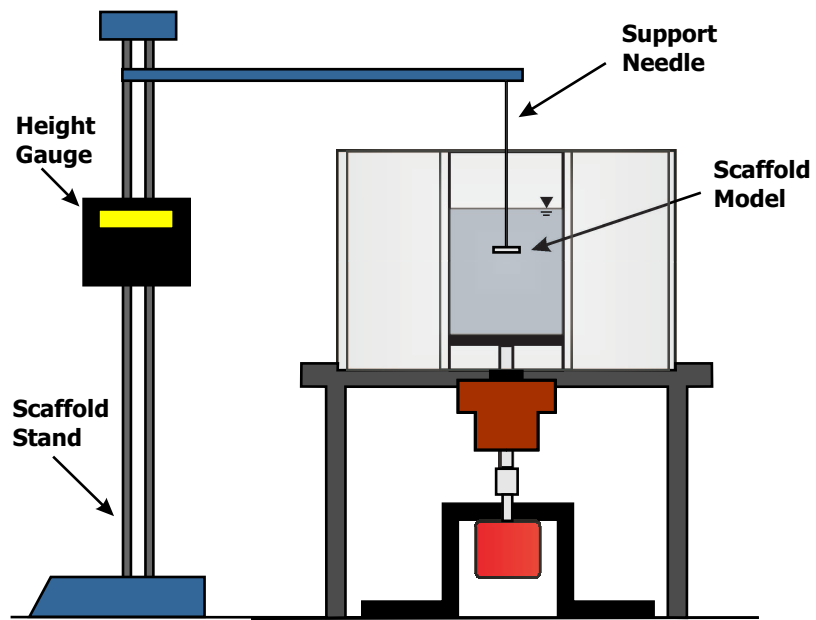
1.0mm diameter was used as the support. The diameter was large enough to prevent non-negligible bending deformation of the needle under the hydrodynamic forces, but was otherwise kept small to minimise obstruction of the flow. The supporting column joined the disk by tightly locating in a hole drilled through its centre. Attachment of the two components was strengthened with adhesive.

The opposite end of the supporting column attached to the precision height gauge, so that the disk was suspended from above, as shown in Figure 3.4(a). The height gauge was then calibrated so that the scaffold zero height position, $z_s = 0$, corresponded with the bottom of the bioreactor, thus facilitating accurate measurement of the scaffold vertical position. The gauge provided control of the vertical position of the scaffold to an accuracy of $\pm 0.01\text{mm}$.

The remaining degrees of freedom, including horizontal transverse position, (i.e. in the r direction), and angular position in the $r - z$ plane, were controlled separately. The angular position was set equal to 0 by vertically aligning the support column parallel to a vertical plane positioned at right angles to the optical table. The optical table was independently levelled.

The horizontal positioning of the scaffold models was accomplished with the aid of digital callipers. Two points on the internal wall of the cylinder, located at 90° from one another, were used as reference positions so that the horizontal position was known to an accuracy of $\pm 0.1\text{mm}$. For the majority of experiments, the scaffold model was located along the centreline of the bioreactor. For SPIV experiments, the $r = 0$ horizontal position could be verified photographically, as the position of the centreline on each camera image was known from the camera setup procedure.

In order to investigate the effect of varying the disk to cylinder diameter ratio r_s/R , three disks were used (see Figure 3.4(b)). The common features of each included the support mechanism, the needle diameter, and the disk aspect ratio. However, to investigate the effect of changing the scaffold to bioreactor diameter ratio r_s/R , the size of the three disks was varied. The dimensions of the smallest disk were $1\text{mm} \times 5\text{mm}$, and the dimensions of the other disks were multiples of this ($2\text{mm} \times 10\text{mm}$ and $3\text{mm} \times 15\text{mm}$). Therefore, the diameter ratios investigated were $r_s/R = 1/13$, $2/13$, and $3/13$. As the aspect ratio was constant, the thickness increased linearly with r_s , while the volume varied with r_s^3 .



(a)



(b)

Figure 3.4: (a) Annotated vertical cross-section of the bioreactor model with the scaffold suspension system. (b) Photograph of scaffold models.

3.3 Flow Visualisation Techniques

Flow visualisation was conducted by illuminating high-reflectance particles seeded in the fluid, using either a 532nm Nd:YAG laser (Spectra-Physics) or a 700W stage lamp. The particles follow the motion of the fluid, meaning that a long exposure image produces streaklines that describe the flow. A particular emphasis was placed on visualising particles entrained within the VB region, so that the geometry of the breakdown structure could easily be distinguished. This is a common method of visualising vortex breakdown flows within free surface cylinders, although more often the tracer material used previously has been fluorescent dye (Escudier, 1984; Spohn *et al.* , 1993, 1998).

Initially, silver-coated hollow glass spheres (Potters Industries) were used as tracer particles for the flow visualisation experiments. These particles, $12\mu\text{m}$ in diameter, were the same as those used for the SPIV experiments. However, these have a specific gravity of approximately 1.5, and so tended to settle relatively quickly. This also meant that isolation of particles in the central flow region was more difficult to accomplish over extended periods of time than if more buoyant tracers were used. $14\mu\text{m}$ diameter polymer spheres from Vestosint were subsequently chosen. While these particles have less reflectance than the silver-coated hollow glass spheres, they have a specific gravity of approximately 1.05. As this is much closer to 1.00 than the specific gravity of the hollow glass spheres, the Vestosint particles took a much longer period of time to be sucked out of the breakdown region and dispersed through the entire fluid volume. Particles could be isolated within the breakdown region by seeding them through the free surface at a location on or near the central axis.

Despite the lower reflectance of the Vestosint particles, it was possible to provide adequate illumination with either light source. During visualisation studies involving a laser light source, 45° incidence mirrors (Melles-Griot) were used to steer the beam toward the rig. The beam was narrowed using a collimating pair of plano-cylindrical lenses, and then expanded into a vertical sheet to illuminate the meridional plane of the rig. Since the particle and rig reflectances behave differently under white light and green laser illumination, a second set of flow visualisation images were produced using a vertical light-sheet constructed from the stage lamp. Special care had to be taken to record the flow visualisation images when scaffold models were submerged in the rig, as the disks partially blocked the light on one side of the vessel. To balance the light intensity on either side of the submerged disk, a mirror was placed on the opposite side of the rig to the lamp.

3.4 Quantitative Measurement Techniques

Quantitative flow measurement was undertaken using Stereoscopic Particle Image Velocimetry (SPIV). While the SPIV system implemented here was similar to the established method, some of the techniques developed were applied for the first time. This section contains a description of standard two-component PIV, focussing on both the generalities of the technique (Subsection 3.4.1), and its specific implementation in the current study (Subsections 3.4.2 and 3.4.3). The justification for the use of SPIV rather than single-camera PIV, is provided in Subsection 3.4.4, followed by a thorough description of the manner in which this technique was applied. The more novel aspects of the current SPIV calibration system are described in detail and various systematic errors are also considered.

3.4.1 Particle Image Velocimetry

Particle Image Velocimetry (PIV) is a technique used to acquire instantaneous velocity fields. While only introduced to fluid dynamics experimental research relatively recently (see Adrian (1986)), the usefulness of PIV has made it a popular technique. Among its advantages over non-spatially resolved measurement techniques such as Laser Doppler Velocimetry and Hot-wire Anemometry is the opportunity to obtain, from a single recording, contours of velocity, shear stress and vorticity; properties which help to build an understanding of the physics of flow systems.

In PIV, a flow field seeded with tracer particles is imaged at two instances in time separated by a known interval (Δt). The flow is typically illuminated by using a single short-duration laser pulse to produce an unblurred particle field, as opposed to the streaklines that result from a long duration illumination. The full image is divided into a number of small sub-regions (or 'windows'), in which the local displacement occurring between images is measured by statistically correlating the change in light intensity distribution and then applying an algorithm to locate the centroid of the correlation peak. This results in a sub-pixel accurate displacement vector describing the flow in each window. Whilst early PIV usually involved a double-exposed single image and auto-correlation to resolve the local displacements (Adrian, 1991), the use of two separate singly-exposed images and cross-correlation is preferred. The reasons for this are twofold: firstly, there is no directional ambiguity in the cross-correlation displacement results, and secondly, the $(0,0)$ correlation peak inherent to auto-correlation is removed. PIV is not without its limitations; these, along with methods used to overcome them, are discussed in Subsection 3.4.3.

3.4.2 Equipment and Protocol

Short-pulse 532nm Nd:YAG lasers (Spectra-Physics, New Wave) were used to illuminate the particle field during the PIV experiments. PIV required two lasers of similar power capable of independent lamp and Q-Switch (shutter) triggering. In addition, the lasers had to be powerful enough to produce sufficient light intensity in the working section. The combination of high power and high time accuracy improved the quality of the PIV by ensuring that a larger number of particles were illuminated and that the PIV timing could be tuned to an optimum setting. As with the laser flow visualisation experiments (see Section 3.3), the laser beams were directed toward the bioreactor model using 45° incidence flat mirrors designed specifically for use with high-energy 532nm beams, and transformed into a thin laser sheet using glass plano-cylindrical lenses (Melles-Griot). The lasers were fired for at least thirty minutes prior to experiments in order to reach their optimal operating temperature.

The 12 μ m diameter silver-coated hollow glass spheres were used as tracer particles, as the Vestosint particles used for flow visualisation were deemed to be of insufficient reflectance. The particles were pre-mixed in Triton-X surfactant before being added to the experimental working section to reduce flocculation. Once the flow had become fully developed, the seeding density differed inside and outside the Vortex Breakdown region. Despite this, it was possible to conduct PIV during a period where the differences in seeding levels across the measurement plane were low enough to permit particle image correlation in both regions.

Most contemporary PIV systems utilise digital CCD cameras rather than film, which is time-intensive to process and prone to distortion. Moreover, as cross-correlation PIV involves the capture of two separate images, a camera capable of double-buffering is required for the small Δt values suitable for PIV. This, as well as the quality of the CCD array and the timing capabilities required for digitally-recorded PIV, precludes the use of standard commercially-available digital cameras. The cameras used for the current PIV experiments were Pixelflys (PCO) with a resolution of 1360 \times 1024 pixels. Nikon Nikkor lenses were used, with focal lengths dependent on the desired measurement field of view and resolution, (typically 28mm). A computer with over 1 gigabyte of random access memory (RAM) was dedicated to the camera frame-grabber card and software.

Synchronisation between the camera and lasers was achieved with the aid of a custom-built electronic timing box. In a single cycle, the timing box was capable of sending individual TTL signals to trigger the camera, the laser lamps, and the laser shutters. The trigger sequence is described in Table 3.1. The exposure time of the first image was set at 1.0ms using the camera

control software package (Camware, PCO). The exposure time of the second image was of a fixed duration (104.0ms). The difference in exposure time did not result in a noticeable difference in image quality as the laboratory was darkened to minimise background light exposure to the CCD array. The time interval between the laser lamps and Q-Switches, i.e. between triggers 1 and 2 or 3 and 4 in Table 3.1, could be altered to the nearest $1\mu\text{s}$. As the output laser power is a function of this interval, the two laser sheet intensities could be matched by varying the delay on triggers 2 and 4, which improved particle image correlation. Once triggered, each shutter remained open for approximately 7ns. Therefore, the gap between the opening of the laser shutters, (i.e. between triggers 2 and 4 in this case), corresponded to the Δt interval used to convert particle displacements to velocities. As the gap between 3 and 4 was fixed according to the desired laser power, the gap between 2 and 3 was used to set Δt . With an increase in the magnitude of the particle displacement, there is an increase in the overall measurement signal to noise ratio, an increase in the number of particles entering and leaving the interrogation windows, and an increase in uncertainty caused by the assumption of zero particle acceleration and rotation over Δt . Finally, a large Δt can increase the error caused by rotation of the particle motion within the light-sheet, as is described more comprehensively in Subsection 3.4.8. Hence, there is an optimum value of Δt which is dependent on Re and the physical size of the interrogation windows. Appropriate Δt values corresponding to a particular Re were identified by trialling the performance of the PIV system over a range of Δt . Once the optimal Δt was found for 3 different Re cases, a curve was derived to predict the optimal Δt for the remaining cases. The curve approximated to the following:

$$\Delta t = \frac{\Delta l}{4\omega r_F} \quad (3.1)$$

where Δl denotes the thickness of the light-sheet, and r_F is the radial position at the edge of the FOV, assuming that the measurement plane is centred at $r = 0$. In the current experiments, Δt was varied between $6000\mu\text{s}$ and $65000\mu\text{s}$.

At the conclusion of each triggering cycle, time was needed to download each image pair from the camera to the computer RAM. As a result of this additional delay, the maximum reliable operating frequency of the Pixelfly cameras in full resolution, double-buffered mode was found to be 4.64Hz . Fortunately, the laser shutters could be triggered at this frequency. Sufficient memory was available to record a sequence of 150 image pairs, although the first 50 image pairs were routinely discarded due to the slightly lower image quality resulting from the laser warming up over the first few laser pulses.

Trigger	Delay (μs)	Signal Destination
0	—	Camera
1	500	Laser Lamp 1
2	~ 180	Laser Q-Switch 1
3	$(\Delta t - 180)$	Laser Lamp 2
4	~ 180	Laser Q-Switch 2

Table 3.1: PIV trigger sequence

Processing of the PIV images to produce displacement vector fields was conducted using software written in-house. Various techniques were applied during image capture and image processing to improve the quality of the PIV data. These are discussed in Subsection 3.4.3.

3.4.3 Techniques applied to enhance PIV accuracy

PIV heavily relies on statistical processes, and so system bias contributes significantly to the measurement uncertainty (Raffel *et al.*, 1998; Willert, 1996; Hart, 2000). During the current PIV experiments, care was taken to reduce these errors and to maximise the measurement resolution by addressing common problems associated with particles entering and leaving the interrogation window, inappropriate particle seeding densities, and inadequate particle illumination. In addition, error detection and correction were implemented during PIV processing.

An increase in the PIV field resolution, (i.e. the number of vectors per millimeter), can be achieved by using higher-resolution image acquisition, by using smaller interrogation windows, or by increasing the overlap between windows to up to 50%. The first approach is limited by the availability of high resolution CCD cameras. An alternative is to use film-based recording, however this technique can be time-intensive, susceptible to bias caused by film distortion, and is in any case still limited by scanner resolution.

Using smaller interrogation window sizes not only increases the PIV resolution, but also reduces the magnitude of errors caused by spatial gradients of particle displacement across the window. Problematically, smaller interrogation windows result in poorer correlation due to there being fewer particles and a higher percentage of particles entering and leaving the window between images. A method, described by Hart (2000), of recursively correlating multiple window sizes was implemented into the PIV software to improve the ability to correlate smaller windows with reduced error. The image data were typically analysed initially using large win-

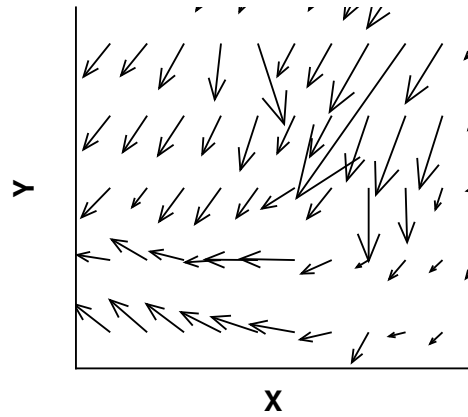
dow sizes (e.g. 128×128 pixels), which usually correlated with smaller random errors (Willert, 1996), and without any missing vectors. The data were then reanalysed with smaller windows (e.g. 64×64 pixels), but this time with each window on the second image shifted in the horizontal, (X), and vertical, (Y), directions by the displacement value estimated from the initial solution at that vector location. The data were then analysed for a third time; this time with the desired window size (e.g. 32×32 pixels), and using the second solution as the approximation. An example of the effectiveness of this technique is presented in Figure 3.5, which shows the same image data analysed with and without recursive image shifting used as part of the PIV analysis. The vector field derived without image shifting contains more erroneous vectors. In some cases, such as near the bottom of the measurement plane, the erroneous vectors give a false impression of the flow by appearing to describe a feature which is not there in reality.

The correlation can also be improved prior to the image processing stage, i.e. at the image acquisition stage. The importance of particle seeding density, particle displacement and particle size has been illustrated through previous studies (see Willert (1996) and Keane & Adrian (1992) for examples). The Δt selection technique used in this study for particle displacement optimisation has already been described in Subsection 3.4.2. The presence of vortex breakdown was found to make the process of particle displacement optimisation more complicated, as there is a large dynamic range caused by the stark difference in velocity between the regions of fluid near the axis of symmetry and the cylinder sidewall. VB was also found to complicate the particle seeding process, as the silver-coated glass particles were found to gradually move to the outer recirculation region as time progressed, and thus created a non-uniform particle seeding density. To ensure that there were adequate particle quantities inside the bubble, it was necessary to capture the PIV images soon after the flow had become fully developed.

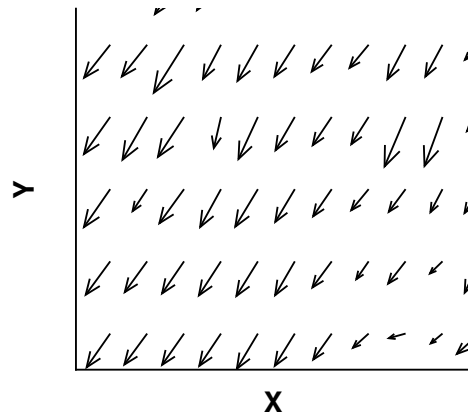
The use of small particles with a highly reflectant surface assisted in obtaining an appropriate distribution of particle image sizes and a sharp image quality. Moreover, the high-energy nature of the light sheets (typically 16 – 400 mJ/pulse), meant that a relatively small lens aperture, i.e. an f-stop of 8 or 11, could be used. This, in turn, reduced the measurement uncertainties that result from larger depths of focus and poorer image focus.

3.4.4 An Introduction to Stereoscopic PIV

The stereoscopic technique is an extension of traditional cross-correlation PIV that utilises two, rather than one, cameras in order to measure three, rather than two, components of each velocity vector on a two-dimensional grid across a planar field. The necessity in this study to measure all



(a)



(b)

Figure 3.5: PIV vector field analysed, (a), without recursive image shifting applied; and (b), with recursive image shifting.

three velocity components arose mainly for two reasons. Firstly, the high ratio of out of plane (v_θ) to in-plane (v_r, v_z) velocity components caused a relatively high perspective error during single camera PIV studies. Secondly, the capability to measure the third component of velocity added significant detail to the results. This was especially relevant in the present study, as one aim was to gain as much information as possible about the stresses acting within the fluid and along external scaffold surfaces. The capability to measure three velocity components across the plain meant that six velocity gradients could be obtained at every measurement point. This additional detail could then be used to enhance the stress measurements.

SPIV became recognised as an optical flow measurement technique not long after standard

two-component PIV (Prasad & Adrian, 1993). Several variations in SPIV technique have been developed since the early 1990s, most of which were summarised by Prasad (2000). The most common differences between techniques are associated with the camera displacement configuration and the reconstruction procedure. The camera displacement system used during the current experiments is schematised in Figure 3.6. This involved an angular displacement of the two cameras of 45° either side of the paraxial position. The reconstruction procedure involved calibration of the distorted images and then derivation of the out of plane component using basic geometry. Calibration consisted of a novel distortion mapping technique which is described in greater detail in Subsection 3.4.6.

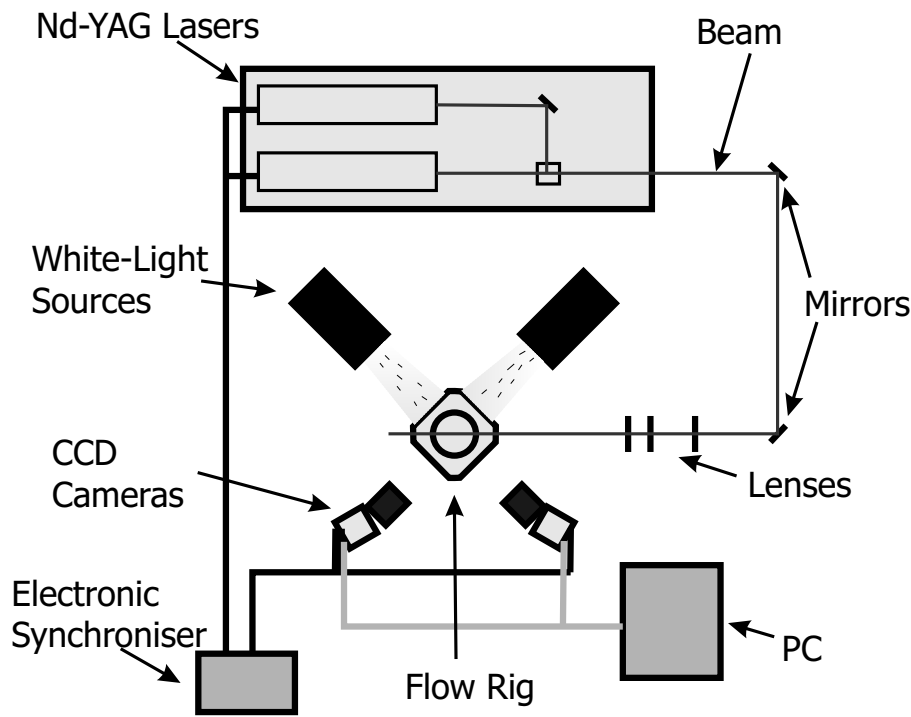


Figure 3.6: Annotated schematic of the SPIV configuration.

3.4.5 SPIV Equipment and Protocol

To facilitate adequate viewing of the meridional plane by the two displaced cameras, the outer glass walls of the rig were cut to the diameter of the cylinder and positioned in octagonal formation, as illustrated in Figures 3.1(b) and 3.7. The cameras were positioned on mounts at an equal radius from the centre of the measurement plane. Focus across the image plane was achieved by utilising the Scheimpflug condition, which involves rotating the camera's CCD array away from the camera lens.

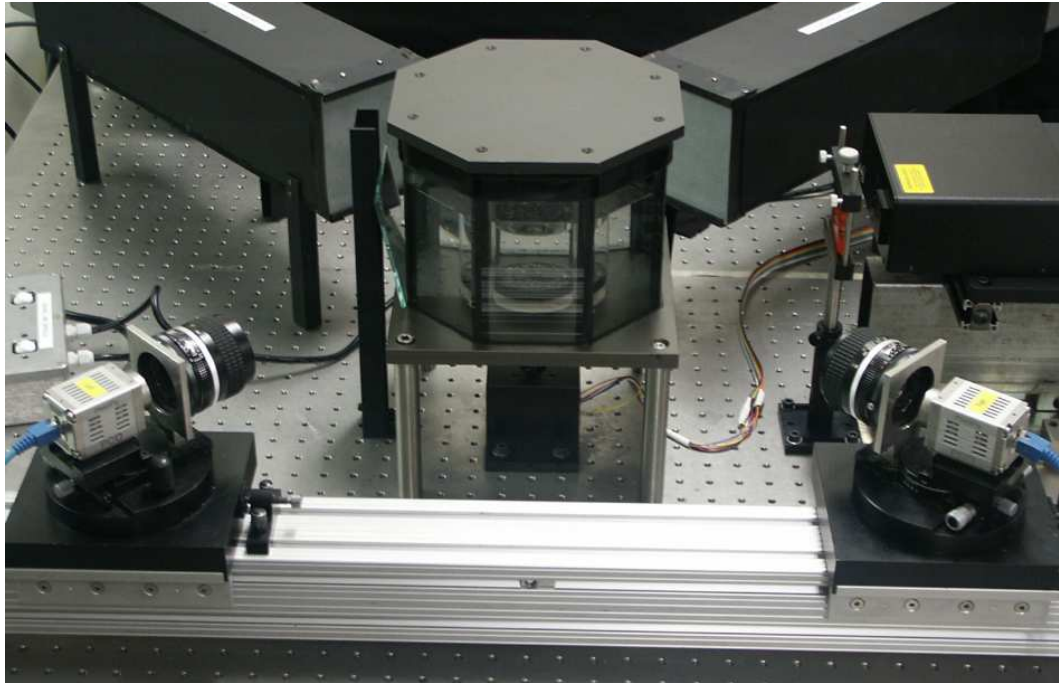


Figure 3.7: Photograph of SPIV system.

Due to restrictions on the camera timing, each camera had a dedicated PC. To ensure synchronisation of the two PIV sets, both image capture cards were triggered simultaneously, (i.e. in event 0 in Table 3.1). For standard two-component PIV, the undistorted nature of the measurement plane captured by the paraxial camera means square shaped interrogation windows produce a grid spacing of vectors that is equal in the X and Y directions. In contrast, a calibrated SPIV vector field derived using square interrogation windows has unequal X and Y grid spacing, since the Y axis is compressed relative to the X axis during the calibration process by a factor of $1/\sin(45^\circ)$. To compensate for this, the interrogation windows were stretched in the Y direction so that their height in pixels was as close as possible to their width divided by $\sin(45^\circ)$.

Aside from this, PIV data acquisition was as described in Subsection 3.4.2. The dimensions of the minimum window size were 28×40 pixels. With 50% window overlap, a regular grid of 96×50 vectors was obtained, although for the submerged disk cases, the number of acquirable vectors was reduced by light blockage and reflection caused by the supporting column. This provided adequate flow resolution across a maximum field of view encompassing $-0.96 \leq r/R \leq 0.96$. Due to the reduced field of view in the Y direction, (or the z axis of the bioreactor model), the entire vertical length of the meridional plane could not be measured at once. Therefore, different sets of data were acquired for the lower and upper portions of the bioreactor. The grid position uncertainty was $\pm 1.2\%$ in the r axis and $\pm 2.3\%$ in the z axis.

Following PIV processing of both image sets, the vector fields corresponding to the right and left vector fields were calibrated using a pre-defined distortion map. The corrected vector fields were then used to determine the three-component vector field. A detailed and general description of the calibration and three-component reconstruction procedures forms the basis of Subsections 3.4.6 and 3.4.7.

3.4.6 Calibration

3.4.6.1 Background

Calibration based SPIV reconstruction may be classified into two-dimensional or three-dimensional methods (Prasad, 2000). Both techniques involve the correction of distortion by a calibration process in the imaging plane. The difference lies in the way distortion is calibrated and the three velocity components are reconstructed using the two techniques. Two-dimensional methods usually require a two step process of distortion calibration and then three-component reconstruction using information relating to imaging parameters. Three-dimensional methods,

such as those described by Soloff *et al.* (1997), involve calibration in multiple planes parallel and close to the image plane. This additional information means that no information about the geometric parameters of the stereoscopic image acquisition is required.

Almost all calibration techniques utilise a calibration target, which usually consists of a discrete number of markers displaced on a regular Cartesian grid. Typically these targets contain on the order of 100 such markers, (i.e. a 10×10 grid). This coarse approach has inhibited the development of calibration techniques. The images of the target are related to the known position of the markers on the calibration target. The exact method depends on the PIV software, and is largely based on the PIV algorithms themselves and often requires the identification of markers in an image that have to be linked to a corresponding marker on the target. This calibration data are then fitted, by a method such as least squares, to obtain general data applicable to the entire measurement region. The whole process is usually time-intensive and not ideal.

3.4.6.2 New Technique

In partnership with Mr. A. Fouras at Monash University, a new technique was developed for use in the current study. This technique has similarities with other two-dimensional calibration methods. The primary difference is that a contiguous calibration target is used rather than a regular, discrete grid. Instead of comparing the target images with *a priori* knowledge, (which must be very precise), the target image is compared to a second image acquired through paraxial imaging. Importantly, this novel combination of a contiguous target and a reference paraxial calibration target image allows calibration data to be measured with any PIV interrogation software.

The distortion fields are derived by correlating the paraxial reference image with the left and right camera images of the calibration target. By performing this interrogation process with exactly the same input parameters as used to process PIV data derived from the left and right cameras, and by ensuring that only sampling windows in the angled camera images are shifted, the resulting vector fields are in fact 1:1 vector maps of the distortion caused by the angular offset.

After derivation of the two two-dimensional vector fields, the base positions of each vector are offset by the corresponding distortion vector. This means that each three-dimensional vector reconstruction is performed on the same measurement grid in object (or real) space. It is significant that no interpolation is performed during any stage of the calibration and reconstruction processes. The distortion field is differentiated to yield local magnification data, allowing ve-

locity vectors to be corrected to this second-order perspective error, thus providing an additional benefit. The differentiation can be performed to high accuracy using the technique described by Fouras & Soria (1998). This just leaves the step of reconstructing the three-dimensional vectors from matching pairs of two-dimensional vectors measured at the same location (see Subsection 3.4.7).

3.4.6.3 Calibration Field Derivation Procedure

Rather than using a regular grid, the reference plate was constructed from sandblasted glass. The distortion of the random ‘speckle’ pattern produced by sandblasting is better correlated by typical PIV analysis software than the distortion of a regular pattern. Indeed, sandblasted speckle patterns have been used successfully in other distortion measurement imaging techniques involving cross correlation (Fouras *et al.* , 2006). In addition, the sandblasted surface pattern is contiguous, and thus provides the versatility necessary for the calibration measurements to be performed on the same grid as the SPIV measurements. The reference plate was positioned in the camera field of view so that the speckle pattern aligned in such a way as to represent an artificial laser-illuminated particle field, i.e. at an angle of 45° to the camera lenses. In order to optimise the contrast in the reference plate images, the plate was back-illuminated using diffuse white light sources positioned in line with the CCD cameras, as shown in Figure 3.6.

The first stage of the calibration procedure involved capturing images of the reference pattern from the paraxial and the two angled perspectives. Careful attention was paid to aligning the field of view of the two images and to matching the light intensity levels. In order to match the field of view in the vertical (Y) direction as closely as possible, the paraxial image was stretched by a factor of $1/\sin(\beta)$ using a bicubic interpolation algorithm, where β , the camera displacement angle, was equal to 45° . When superimposed onto one another, the left and stretched paraxial reference images appeared similar to the example shown in Figure 3.8. In the combined image, the magnification heterogeneity across the field of view is clearly visible, as is the point where the magnifications of the two images are matched.

The image pair shown in Figure 3.8 was used to derive the left - paraxial calibration field shown in two-component vector form in Figure 3.9. The vectors quantify the degree to which each regularly-spaced interrogation window on the paraxial image is distorted in the left image. The coloured contour bands represent the distortion in the Y component. The left edge of Figure 3.9 has the greatest distortion in Y , which is representative of the fact that the left, (or near),

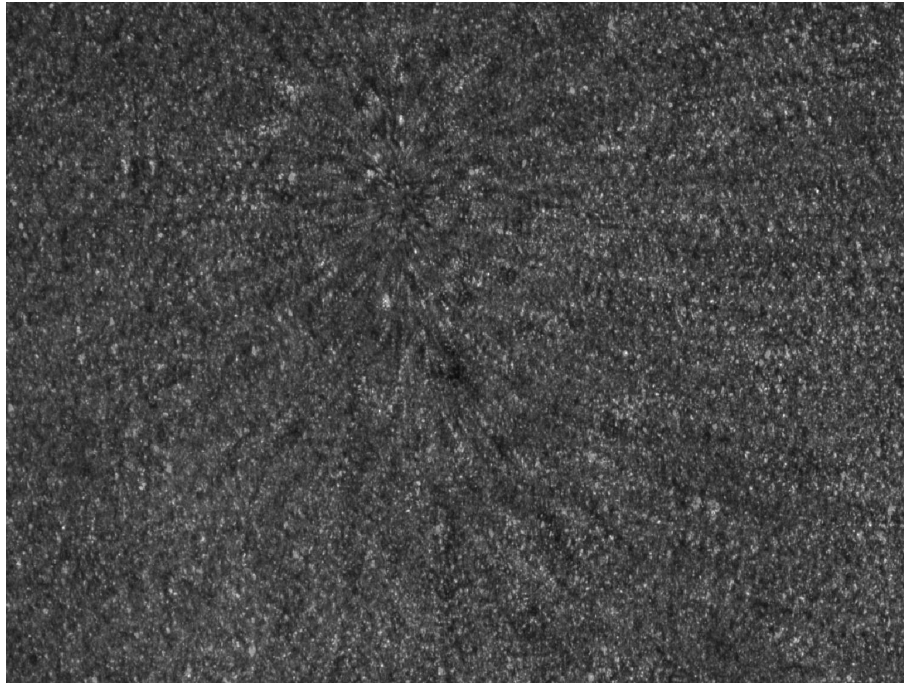


Figure 3.8: Superimposed paraxial and left target pattern images used to determine the left - paraxial distortion field via cross-correlation analysis.

edge of the left camera image receives the greatest magnification while the right, (or far), edge is less magnified. Stretching of the horizontal (X) component occurs across the entire field of view as the process takes into account any mismatch between the paraxial and displaced camera fields of view.

The corresponding right - paraxial calibration vector field is presented in Figure 3.10. In this case, the near edge of the field of view is on the right hand side of the right camera image, and the far edge is on the left hand side. Correspondingly, the Y stretching is much more pronounced toward the right edge of the vector field. Theoretically, the expectation is that this calibration field should resemble a Y -axis reflection of the left - paraxial calibration field. While this is approximately the case, in reality there are subtle differences between the two fields caused by slight discrepancies in camera positioning and magnification. Herein lies a demonstration of one of the advantages of the improved calibration technique; i.e. by directly measuring the distortion, the positional and magnification imprecision associated with the angularly displaced cameras is compensated for automatically.

As a final step in the calibration process, the distortion vector fields were applied as an offset to the measured left and right camera PIV fields. This simple procedure was conducted through the SPIV reconstruction software.

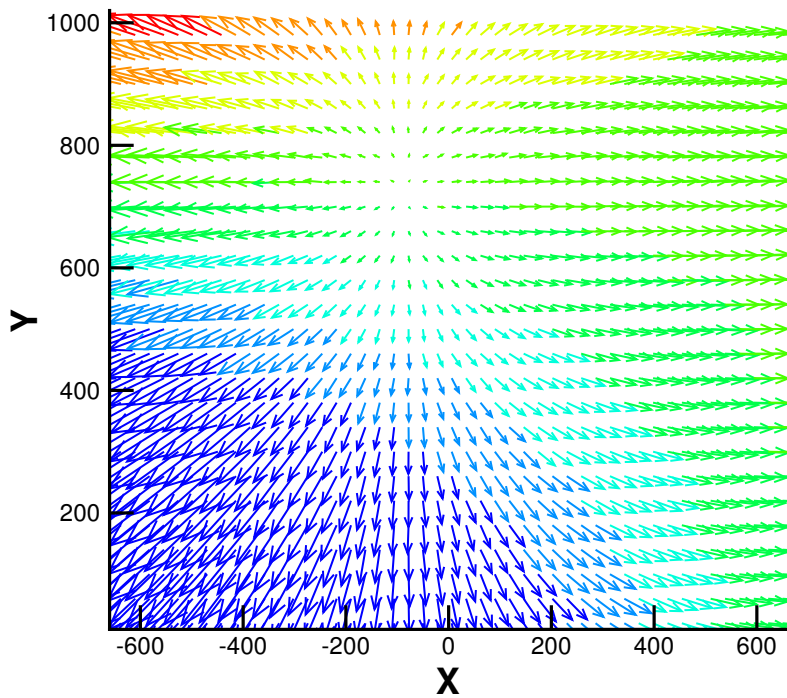


Figure 3.9: Left - paraxial calibration field in two-component vector form. The coloured contour levels represent vertical (Y) distortion. The X and Y axis scaling is arbitrary.

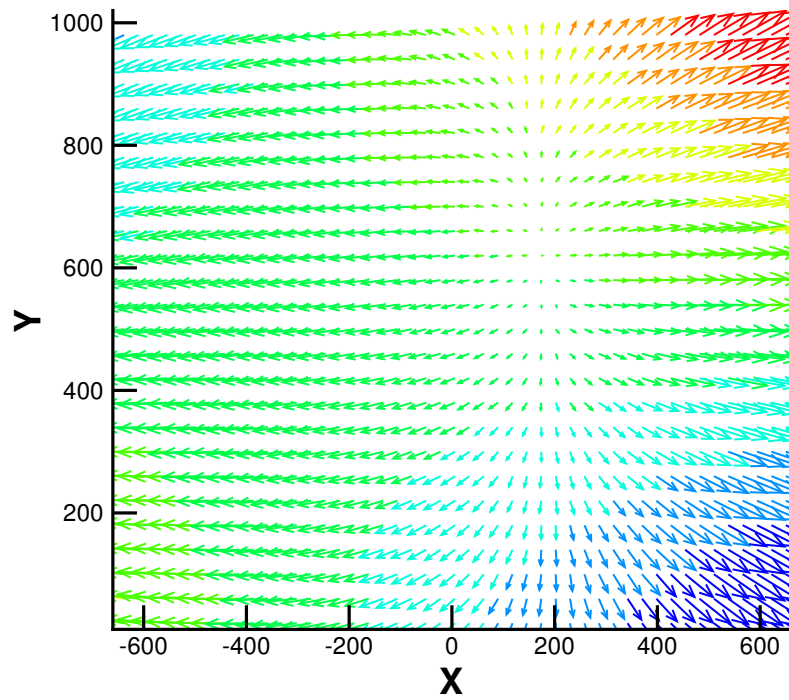


Figure 3.10: Right - paraxial calibration field in two-component vector form. The coloured contour levels represent vertical (Y) distortion. The X and Y axis scaling is arbitrary.

3.4.7 Three-component velocity field reconstruction

Following calibration, the reconstruction of the measured displacement vectors into three components was undertaken by geometrically deriving the true displacement components (ΔX , ΔY , and ΔZ) from the two two-dimensional PIV displacement fields. The displacement components were subsequently used to determine the velocity components v_r , v_z and v_θ respectively. The equations used to reconstruct the true coordinates of the displaced particle X_t , Y_t and Z_t were derived by first sketching the lines between the known object projection points and the lens centres corresponding to each of the two cameras, in three-dimensional Cartesian space (represented by X , Y and Z axes). Figure 3.11 shows the two-dimensional projection of this setup along the horizontal, ($X - Z$), plane. The origin of the Cartesian plane lies in the physical centre of the object plane. The left camera lens is located at (X_a, Z_a) and is displaced at an angle β_a from the centerline. The right camera lens is located at (X_b, Z_b) and is displaced at an angle β_b from the centerline. The left camera views the particle displacement point as (X_{pa}, Y_{pa}) in calibrated Cartesian space, while the right camera views the particle displacement point as (X_{pb}, Y_{pb}) .

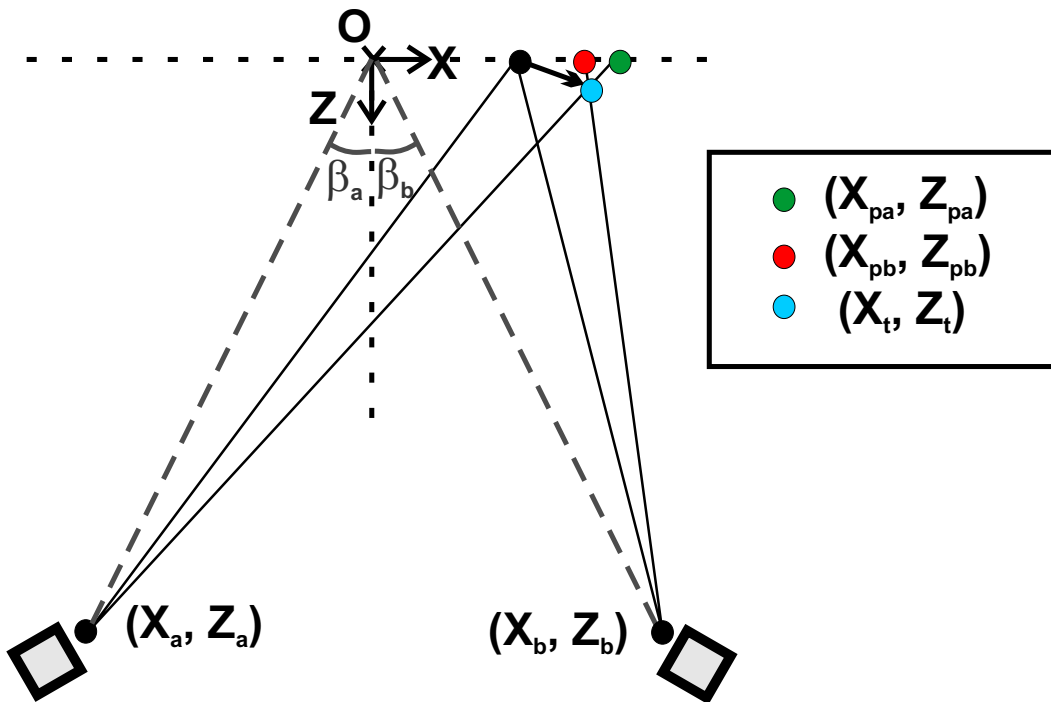


Figure 3.11: Horizontal-plane SPIV three-component reconstruction geometry.

The intersection of the two projection lines represents the point (X_t, Y_t, Z_t) . The coordinates of this intersection point can be most simply obtained by recognising the geometric similarity within the projection lines. Algebraically:

$$\frac{Z_t - Z_a}{X_t - X_a} = \frac{Z_{pa} - Z_t}{X_{pa} - X_t} \quad (3.2)$$

$$\frac{Z_t - Z_b}{X_t - X_b} = \frac{Z_{pb} - Z_t}{X_{pb} - X_t} \quad (3.3)$$

Thus the equations for the X and Z components of the true displaced vector in terms of known position variables are as follows:

$$Z_t = \frac{Z_b Z_a (X_{pa} - X_{pb})}{Z_b (X_{pa} - X_a) - Z_a (X_{pb} - X_b)} \quad (3.4)$$

$$X_t = \frac{Z_b X_{pb} (X_{pa} - X_a) - Z_a X_{pa} (X_{pb} - X_b)}{Z_b (X_{pa} - X_a) - Z_a (X_{pb} - X_b)} \quad (3.5)$$

Under typical conditions, $\beta_a = -\beta_b$, and so $X_a = -X_b$ and $Z_a = Z_b$, meaning that Equations 3.4 and 3.5 can be solved from a knowledge of β_a , the distance of each camera from the measurement plane, and the PIV displacement data from cameras a and b. The equation for Y_t is derived in a similar manner as the equation for X_t , although this time in the vertical ($Y - Z$) plane. As the cameras are mounted along the same horizontal plane, it follows that $Y_a = Y_b = 0$, and so the equation for Y_t is somewhat simpler.

$$Y_t = -\frac{Y_{pa}}{Z_a} (Z_t - Z_a) = -\frac{Y_{pb}}{Z_b} (Z_t - Z_b) \quad (3.6)$$

Because of the imperfect nature of PIV setup and processes, the values of Y_t derived from camera a and camera b data are slightly different. Therefore, the average of the Y -projections for the two cameras (Y_{pa} and Y_{pb}), was used to calculate the final value of Y_t . Displacements ΔX , ΔY and ΔZ are calculated by simply subtracting the origin coordinates from the displaced vector coordinates.

The error in the calculation of the displacement vector from the three-dimensional reconstruction equations is a function of the position of the two cameras. The ratio of error in the X direction, ϵ_{rX} , over the error in the two-dimensional PIV error, ϵ_{pX} , is denoted by ϵ'_X . ϵ'_Y and ϵ'_Z correspond to the same ratio in the Y and Z directions respectively. Assuming that $Z_a \gg Z_{pa}$ and $Z_b \gg Z_{pb}$, ϵ'_X is approximately given by:

$$\epsilon'_X = \frac{\left| \frac{\tan(\beta_a)}{\cos(\beta_b)} \right| + \left| \frac{\tan(\beta_b)}{\cos(\beta_a)} \right|}{\left| \tan(\beta_b) - \tan(\beta_a) \right|} \quad (3.7)$$

while ϵ'_Z is given by:

$$\varepsilon'_Z = \frac{1}{2} \left(\frac{1}{|\cos(\beta_2) \tan(\beta_2)|} + \frac{1}{|\cos(\beta_1) \tan(\beta_1)|} \right) \quad (3.8)$$

ε'_Y is similar to ε'_X when β_a and β_b are both equal to 0° in Equation 3.7. In other words, ε'_Y is theoretically equal to 1 and the reconstruction process does not add error to the measurement of ΔY .

Figure 3.12 illustrates the effect of camera angles β_a and β_b on (a), ε'_X and (b), ε'_Z . When β_a or β_b is very close to 90° , the assumptions $Z_a \gg Z_{pa}$ and $Z_b \gg Z_{pb}$ no longer both hold, and ε'_Z becomes very large. For this reason, only camera angles up to 85° are included in Figure 3.12. When both β_a and β_b are positive, i.e. when the two cameras are located on the same side of the measurement plane, ε'_X is generally much larger than when β_a and β_b are of opposite sign. For this reason, it is best to just consider the case where the cameras are located on opposite sides of the rig. Under these conditions, ε'_X tends to increase as both β_a and β_b increase, while ε'_Z increases as β_a and β_b decrease. An optimum camera position for reconstruction error can be determined from an average of the data in Figures 3.12(a) and (b). Figure 3.12(c) represents this average, $(\varepsilon'_X + \varepsilon'_Z)/2$, as a function of β_a and β_b . The optimum reconstruction error ratio corresponds to when $\beta_a = -45^\circ$ and $\beta_b = 45^\circ$, (or when $\beta_a = 45^\circ$ and $\beta_b = -45^\circ$), which were the camera displacement angles used in the current experiments.

The inclusion of $X_a, X_b, Y_a, Y_b, Z_a,$ and Z_b in the reconstruction equations renders accurate camera positioning extremely important. To achieve a high level of accuracy, lens mounts were constructed to hold the distance between the lens plane and the CCD array, and to lock the lenses into an angular orientation of 45° to the optical table screw-hole array, into which the rig was screwed directly. As shown in Figure 3.7, the camera mounts were attached to a single rail screwed to the optical table, which aided in keeping the distances from each camera to the origin as equal as possible (i.e. $Z_a \approx Z_b$ and $X_a \approx -X_b$). The calibration plate was manufactured with holes of 2 – 5 pixel diameter drilled precisely on its centreline. These holes were used to accurately position the two cameras and to ensure a matching field of view in the radial direction.

3.4.8 Further techniques applied to enhance SPIV accuracy

As SPIV is an extension of PIV, and incorporates all processes associated with PIV, the techniques for improving PIV accuracy described in Subsection 3.4.3 were all applicable to the SPIV system. Further improvements were made to the accuracy of the measurements that relate more specifically to SPIV and the current experimental configuration.

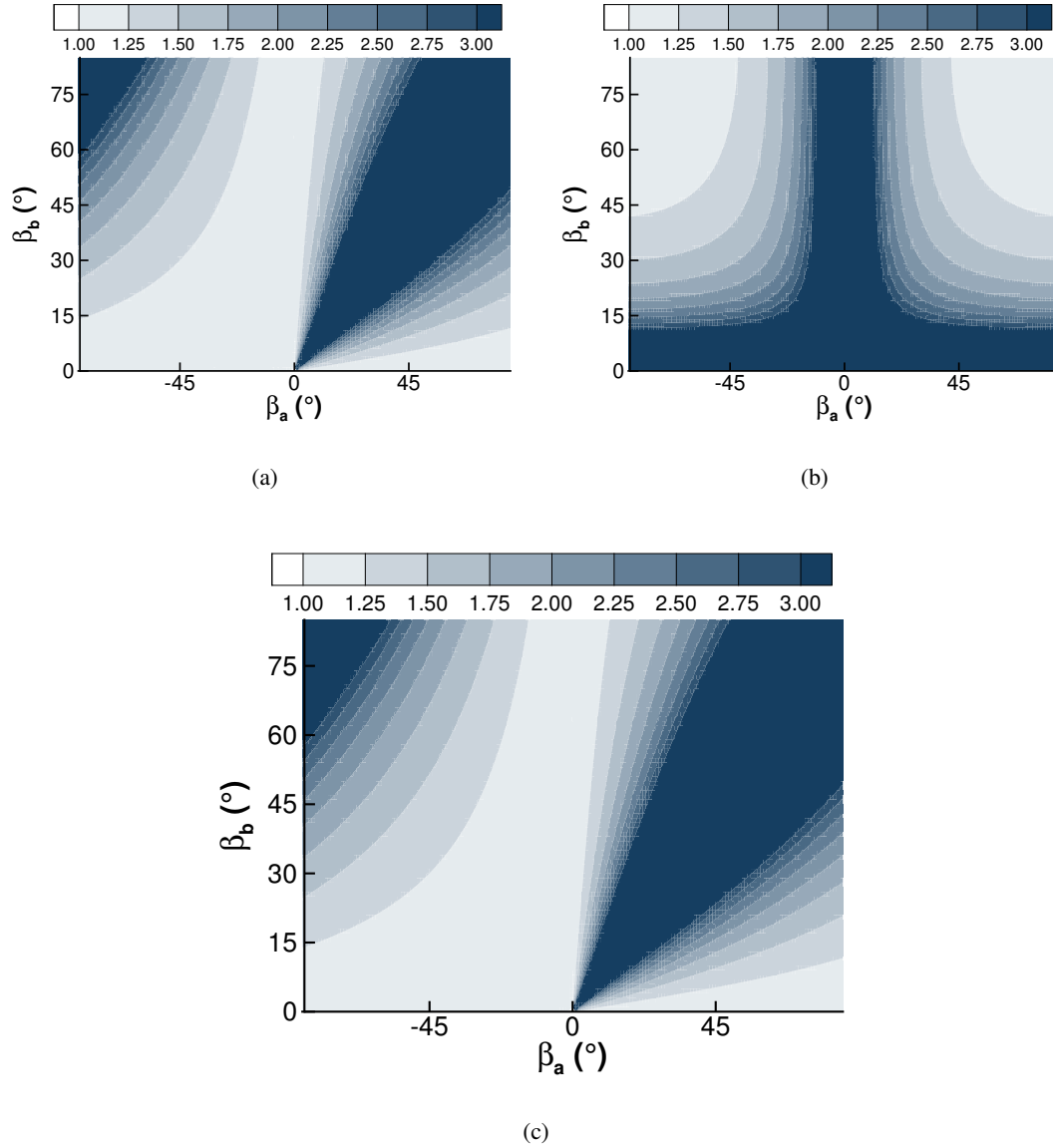


Figure 3.12: Error ratios as a function of β_a and β_b . (a) ϵ'_X ; (b) ϵ'_Z ; (c) Average of ϵ'_X and ϵ'_Z .

The first of these was a response to the problem of light-sheet thickness affecting the meridional plane flow measurements. As previously mentioned, SPIV can be used to separate the azimuthal velocity component from the in-plane components. However, in practice this capability is limited by the thickness of the light-sheet, (Δl), and the length of Δt . The secondary flow pattern, for which the meridional plane flow is viewed completely independently from the azimuthal flow, can theoretically only be observed within an infinitesimally thin sheet. Since a practically realistic light-sheet has finite thickness, it is impossible to completely avoid contamination of the in-plane measurement by the azimuthal flow. The azimuthal momentum causes the particles to turn across the meridional plane while passing through the light-sheet, thus re-

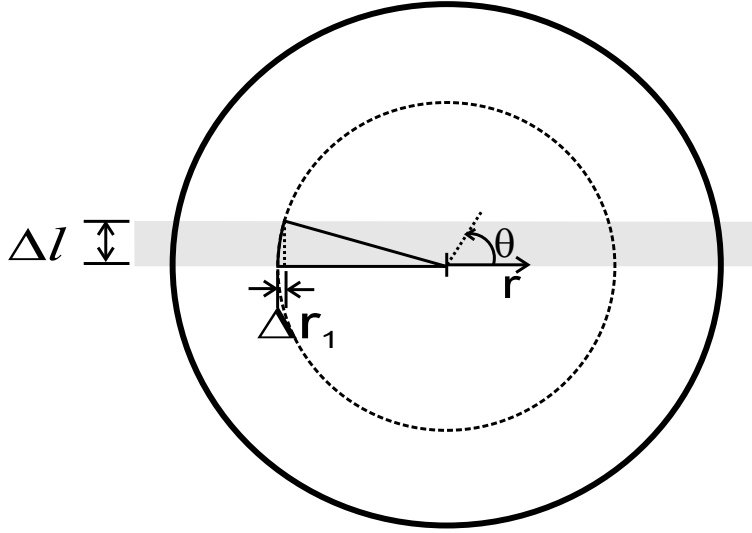


Figure 3.13: Schematic representation of the Δr_1 radial displacement component for a fluid particle in purely azimuthal flow. The view of the experimental set-up is from above. The shaded region represents a light-sheet of thickness Δl .

sulting in a bias component in the measured radial displacement, (Δr_1), as illustrated in Figure 3.13. This infers that the fluid is moving radially inward when in fact it may not be. Δr_1 causes a radial velocity bias error of $v_{r1} = \Delta r_1 / \Delta t$. Despite the fact that the rotation angle between both sides of the light-sheet is usually slight, this bias could potentially be significant. This is because v_r is generally of low magnitude in relation to v_θ for high swirl flows such as those under investigation.

Figure 3.14, derived using simple trigonometry, represents the maximum bias radial displacement component Δr_1 , non-dimensionalised by dividing by R , caused by azimuthal particle rotation across the light-sheet for a solid body rotation case. Curves representing several Δl values are shown, in each case normalised by R . The $\Delta l / R = 0.03$ case is the closest to that used during the current experiments. The Δr_1 potential error is largest at the inner radii, as the light sheet thickness represents a larger percentage of the circumferential path distance. At radii smaller than the light-sheet thickness, Δr_1 is entirely Δt -limited. At larger radii, where velocities are larger, Δr_1 is more likely to be Δl limited. For the case where Δr_1 is Δl limited, it is given by:

$$\Delta r_1 \leq -r \left(\cos\left(\frac{\Delta l}{r}\right) - 1 \right) \quad (3.9)$$

The inequality in 3.9 results from the fact that Δr_1 can be reduced by aligning the centre of the light-sheet with the meridional plane, rather than having it slightly off-set from this plane. When Δr_1 is Δt limited, it is given by:

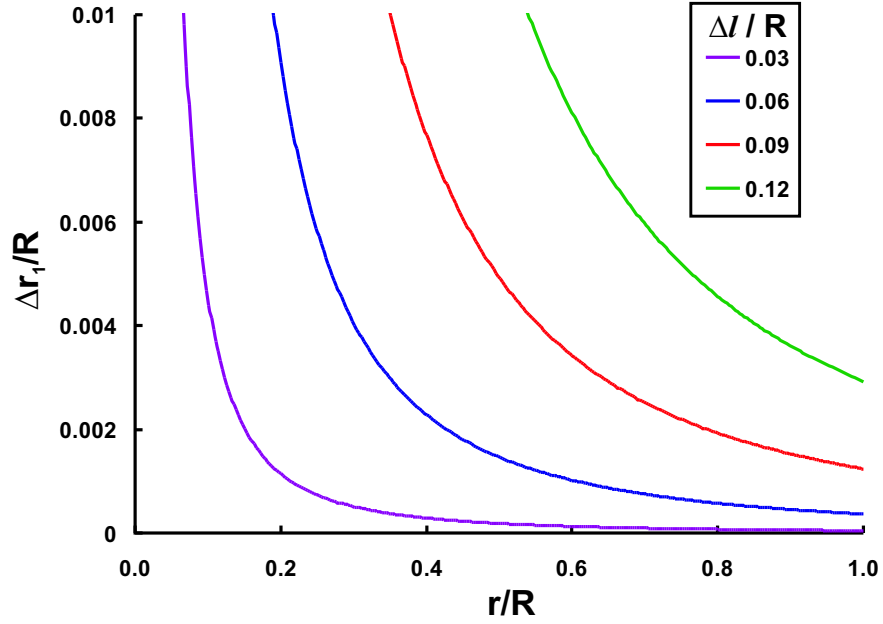


Figure 3.14: Maximum Δr_1 as a function of normalised radial position, r/R , when Δr_1 is Δl limited and a solid body rotation is assumed. The different curves represent different values of $\Delta l/R$.

$$\Delta r_1 \leq r(1 - \cos(\omega\Delta t)) \quad (3.10)$$

Figure 3.15 illustrates the variation of Δr_1 with r/R when it is Δt limited. Each curve represents a different value of the dimensionless product $\omega\Delta t$. The curves themselves are quite linear, but doubling the value of Δt results in Δr_1 more than doubling. Solid body rotation represents a worst case scenario. Typically, the angular rotation of the fluid in a bioreactor scenario is well below the angular rotation of the impeller. Despite this, the $\omega\Delta t$ cases in Figure 3.15 have been chosen on the basis that ω is the impeller rotation rate. Even still, the value of $\omega\Delta t$ closest to that used during the current experiments, 0.03, results in the profile with the lowest Δr_1 magnitudes of all the cases shown.

Measurement of v_θ is based on the assumption that it is equal to the out of plane velocity component derived using SPIV reconstruction. In reality, however, there is a minor discrepancy between $v_{\theta M}$, the measured value of v_θ , and $v_{\theta T}$, the true value of v_θ . This error can be related to the radial displacement error Δr_1 using Equation 3.11 below. Once again, a worst case solid body rotation scenario is assumed.

$$\frac{v_{\theta T}}{v_{\theta M}} = \frac{r \cos^{-1}\left(\frac{r - \Delta r_1}{r}\right)}{\sqrt{\Delta r_1(2r - \Delta r_1)}} \quad (3.11)$$

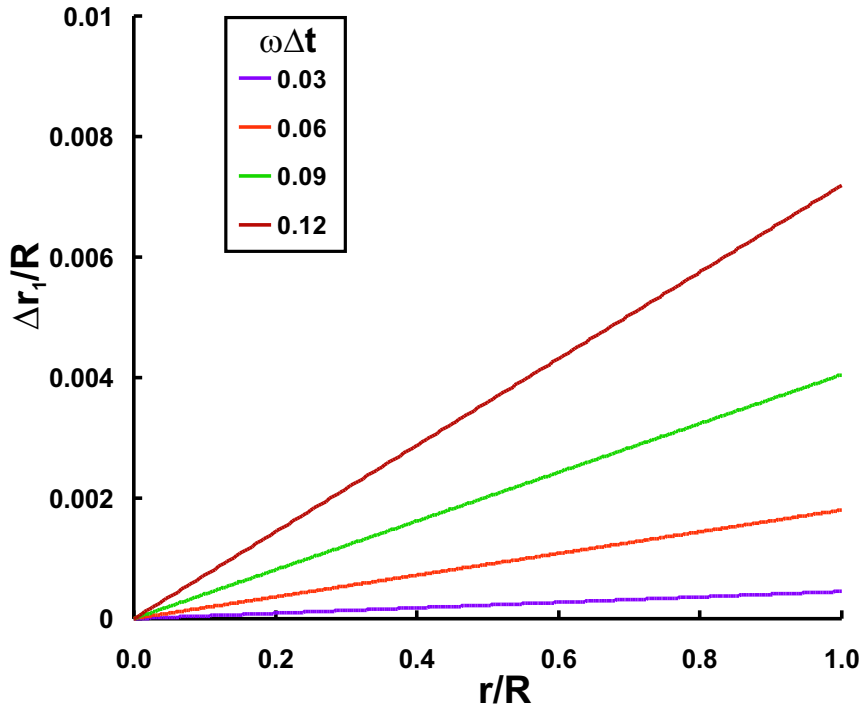


Figure 3.15: Maximum Δr_1 as a function of normalised radial position, r/R , when Δr_1 is Δt limited and a solid body rotation is assumed. The different curves represent different values of $\omega\Delta t$.

As shown in Figure 3.16, $v_{\theta T}/v_{\theta M}$ remains very close to 1.0 over the domain $0 \leq \Delta r_1/R \leq 0.01$, which represents the range of values included in Figures 3.14 and 3.15. It should be noted that a likely value of Δr_1 lies well below $0.01R$, which itself corresponds to an error of 0.3% in the measurement of v_{θ} .

Several steps were taken to reduce the magnitude of Δr_1 . Firstly, Δt was minimised until correlation errors almost became problematic. Similarly, Δl was minimised to just above the level at which inadequate illumination and out of plane particle loss became prohibitively excessive. Finally, a translational traverse system, as illustrated in 3.17, was constructed in order to accurately position the laser light-sheet. The traverse was integrated into the optical table, which aided in directing the light-sheet toward the centre of the rig. A 1mm lead screw and a digital position micrometer facilitated accurate positioning of the light-sheet on the centreline of the rig. The Δr_1 component could therefore be tested by comparing SPIV data captured with various light-sheet locations. Despite these measures, Δr_1 was not entirely eliminated from the radial velocity measurements. This was not of major concern as much of the flow can be described by axial and azimuthal velocity profiles.

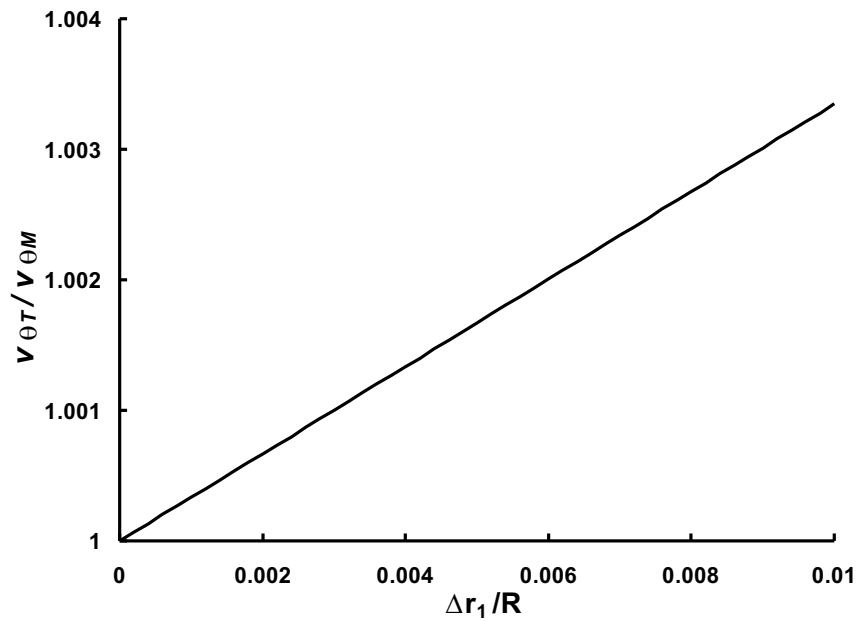


Figure 3.16: Ratio $v_{\theta T}/v_{\theta M}$ as a function of $\Delta r_1/R$, when a solid body rotation is assumed.

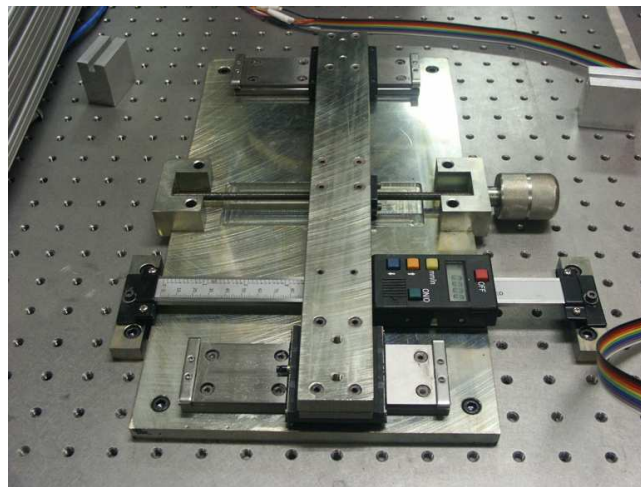


Figure 3.17: Translation stage developed to accurately position laser light-sheet in relation to the rig centre.

3.4.9 SPIV Validation

Various tests were undertaken to measure the accuracy of the SPIV setup. The data acquisition, calibration, correlation, and reconstruction processes were all included in these validation studies. Perhaps the most significant trial was a solid body rotation test case conducted within the bioreactor model working section with the cameras installed in their experimental configuration. A sandblasted glass plate was placed along the light-sheet plane and the rig was filled with water to reproduce the rig distortion inherent in the experimental conditions. The test

plate was illuminated with white light to allow imaging. The plate was rotated a known angle between images, which provided an opportunity to test the SPIV system under conditions involving large displacements, large displacement variations, and a large out of plane to in-plane displacement ratio. The three-dimensional vector field shown in Figure 3.18 corresponds to a rotation angle of $1.0^\circ \pm 0.06^\circ$, as determined using a dial gauge. The resultant field accurately describes solid body rotation. The rotation angle, determined by applying a linear regression to the ΔZ data, was found to be 1.0° to an accuracy well within that of the dial gauge measurement. The R^2 value of the ΔZ regression line exceeded 0.999. The measured ΔX values had a mean of 0.01 pixels and a standard deviation of 0.23 pixels. The ΔY data had a mean of -0.13 pixels and a standard deviation of 0.09 pixels. The higher standard deviation in the ΔX measurements was most likely caused by the additional uncertainty associated with the ΔX reconstruction, as described in Subsection 3.4.7.

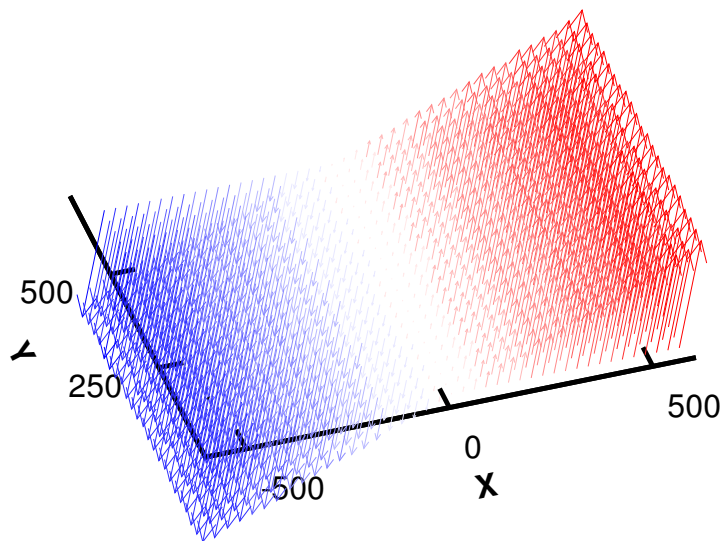


Figure 3.18: Reconstructed instantaneous vector field from the solid body rotation test case. Coloured contours indicate levels of ΔZ . The X and Y axis scaling is arbitrary.

3.5 Further Data Processing

Erroneous vectors were detected and replaced using an algorithm incorporated into the PIV processing software. Correlation peaks which did not fall within two pixels of that predicted by a deconvolution of the simplified Navier-Stokes equation fit through the surrounding vectors, were removed and replaced by the predicted value. If more than 5% of the vectors on either the left or right camera image were replaced in this manner, the data set was rejected.

Spatial displacement gradients were derived by χ^2 fitting a second-order interpolator curve through the vectors surrounding the interrogation point, rather than by a discrete finite difference approach. Fouras & Soria (1998) measured the gains in accuracy resulting from this approach when calculating quantities requiring velocity gradients, for example shear stress and vorticity.

Subsequent processing was undertaken using scripts written with the *MATLAB* (Mathworks) data manipulation and programming tool. Displacement vectors and spatial displacement gradients measured in pixels were calibrated to real-space velocity fields. Additional scripts were used to conduct a spectral analysis, and calculate the stress fields and other important flow properties.

Chapter 4

Flows within a Cell-Suspension Bioreactor with Vortex Breakdown

4.1 Introduction

This chapter focusses on flows suitable for suspension cell culture occurring within a free surface cylinder of aspect ratio $H/R = 1.5$. The measured flows have a Reynolds number in the range $600 \leq Re \leq 3000$, which includes a number of different regimes. Vortex Breakdown is observed at $Re > 760$ and so is a key feature of most of the cases presented here. The different breakdown topologies observed in the Re interrogation range are reviewed in Section 4.2 using photographic flow visualisation images. Following this, quantitative measurements of the fluid dynamics are presented. As the number of data sets recorded exceeds a reasonable limit for inclusion in this chapter, most of the quantitative results presented correspond to one of two Re cases. These are $Re = 1200$, which lies within the *corner bubble* regime, and $Re = 2400$, which lies within the *surface bubble* regime. However, unless otherwise stated, most of the main observations are also applicable at other Re within the same flow regime.

The focus of this chapter is on the velocity and stress fields calculated on the basis of the three-component SPIV measurements. The velocity fields assist the bioreactor design process by detailing the different laminar mixing patterns and by quantifying the variation in flow conditions in regions of the bioreactor through which cells may travel. The stress fields quantify the heterogenous distribution of fluid stress associated with local deformation of fluid elements. This is vital for a cell culture application, as many cell types have been found to increase their proliferation or produce important proteins when exposed to this type of stress (see Section 2.2). In Section 4.7 distributions of the principal stress vectors throughout the vessel are presented. The stress vector magnitudes are considered in detail, as this helps researchers and bioreactor engineers to determine regions of the flow that have inappropriate stress levels (e.g. excessively

high or low), and therefore take steps to avoid these regions. The orientation of the orthogonal axes along which the principal stresses act (or ‘principal axes’) are also considered for the first time in a bioreactor fluid dynamics study. This is significant, because the direction of the stresses relative to a cell or cell cluster is likely to affect the cell mechanotransduction processes.

The chapter addresses features of the Vortex Breakdown flow within open surface cylinders that have not previously been measured using three-component velocimetry. In particular, the central vortex region, the VB recirculation region, and the near-impeller region are examined using a combination of velocity and circulation profiles, as well as contour plots of swirl, azimuthal vorticity, and stress. In this manner, the internal mechanics of free surface cylinder flows and their dependence on Re are exposed in new detail.

4.2 Flow Visualisation

As mentioned in Subsection 2.6.2, a wide-ranging visualisation study on flows in free surface cylinders with Vortex Breakdown has previously been undertaken by Spohn *et al.* (1993). The flow visualisation undertaken as part of the current study does not contradict the work of Spohn *et al.*, but focusses more closely on the breakdown region geometry at a cylinder aspect ratio of $H/R = 1.5$. The images presented in Section 4.2 have a varying depth of field, particle distribution and illumination source. The contrasting visualisation techniques provide more information about the three-dimensional nature of the flow at $H/R = 1.5$ than those published previously.

The meridional flow field observed at Reynolds numbers above the critical value for VB formation is schematised in Figure 4.1. A larger, high-velocity region (shaded dark grey) contains the main recirculation pattern resulting from the rotating bottom lid, and is located near the cylinder wall. A smaller, low-velocity region (shaded light grey) is located closer to the axis of symmetry. A distinct feature of this central region is the VB recirculation bubble, which contains fluid rotating in the opposite direction to the larger recirculation, but at a much reduced velocity. Immediately upstream and downstream of the VB recirculation, the near-axis region reduces in diameter and the meridional-plane flow, represented by the v_r and v_z velocity components, diminishes in magnitude. The flow in the core vortex region is almost entirely azimuthal, although closer to the impeller the fluid is accelerated in the $-z$ direction.

The exact size and position of the VB recirculation zone is Re dependent, as documented previously. The lowest Re value at which a VB recirculation bubble was recorded is 760. At $Re = 700$, as shown in Figure 4.2(a), the outer recirculation region constitutes the sole meridional recirculation pattern. A narrow columnar flow, devoid of any particles, lies on the central axis. In the lower half of the vessel, the particles travelling toward the impeller diverge slightly from the axis. Similarly, at $Re = 720$ particles seeded in a clean fluid close to the axis of symmetry and travelling axially toward the impeller were observed to temporarily convect toward the positive radial direction so that they formed a wider spiral. Spohn *et al.* observed a similar effect at 740. These observations appear to be evidence of the region of opposite vorticity which, as shown by Lopez (1990), occurs about the axis of symmetry at Re slightly below the formation of the breakdown region.

When the breakdown bubble initially appears, it does so in the *axis bubble* regime, i.e. with the stagnation point and the recirculation region located entirely on the axis of symmetry. Figure 4.2(b) is the lamp visualisation image recorded at $Re = 760$. The on-axis region and the

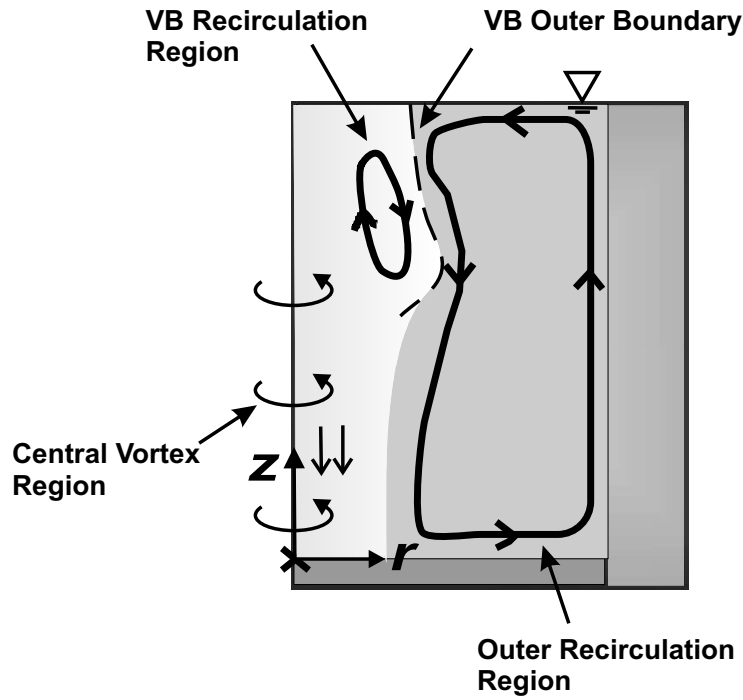
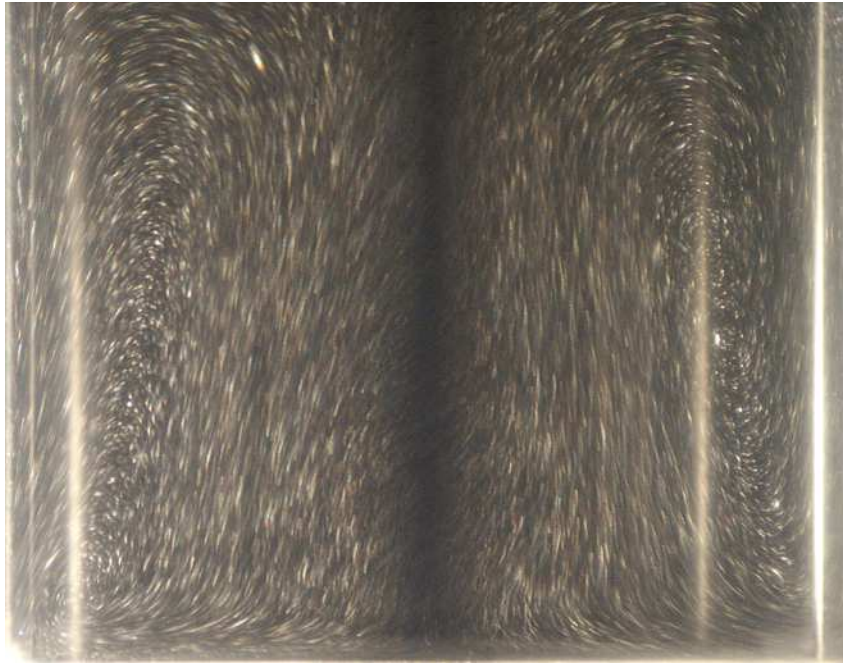


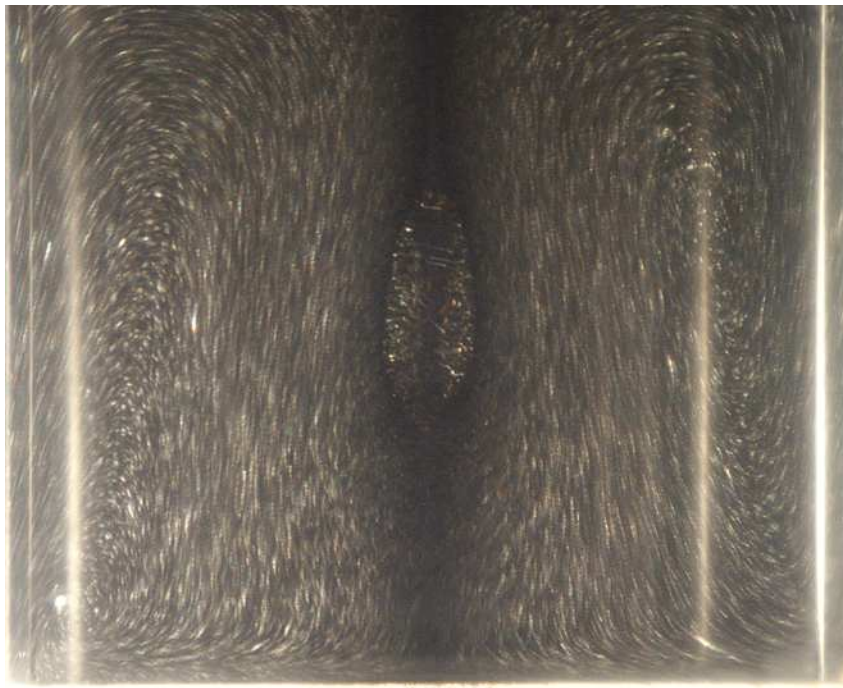
Figure 4.1: Annotated schematic of the vortex breakdown flow pattern

stagnation point are clearly identifiable, as the shear layer on the VB boundary does not contain particles. A similar flow is shown in Figure 4.3, for which $Re = 780$. In these images, there are fewer particles seeded in the flow than in Figure 4.2, and the particles are entrained near the boundaries of the recirculation regions, although once again the shear layer between the two regions is devoid of particles. In the close-up of the breakdown region shown in Fig. 4.3(b) it is possible to make out the spiralling pathline of particles approaching the bubble from upstream. As they approach the stagnation point, the particles diverge radially from the axis of symmetry and then enter the breakdown bubble from beneath. This motion is similar to that reported by Sotiropoulos *et al.* (2001), however it should be remembered that the asymmetries observed in the current study may be caused by slight off-axis particle seeding or cylinder misalignments and are therefore not necessarily attributable to an inherent asymmetry of VB flows. However, the observed particle motions represent positive evidence that certain cells or nutrients may be seeded into an on-axis breakdown bubble through the free surface at a position near the axis of symmetry.

The range of Re values for which the bubble is located entirely on the axis of symmetry is relatively small. The breakdown region expands in both the r and z directions as Re increases beyond $Re = 760$. As shown in Figure 4.4(a), by $Re = 950$ the breakdown region is attached to the free surface. The particles within the VB region form an elliptical pattern, which rep-



(a)



(b)

Figure 4.2: Lamp-particle visualisation images illustrating the meridional plane flow around the onset of Vortex Breakdown, at (a) $Re = 700$; and (b) $Re = 760$.

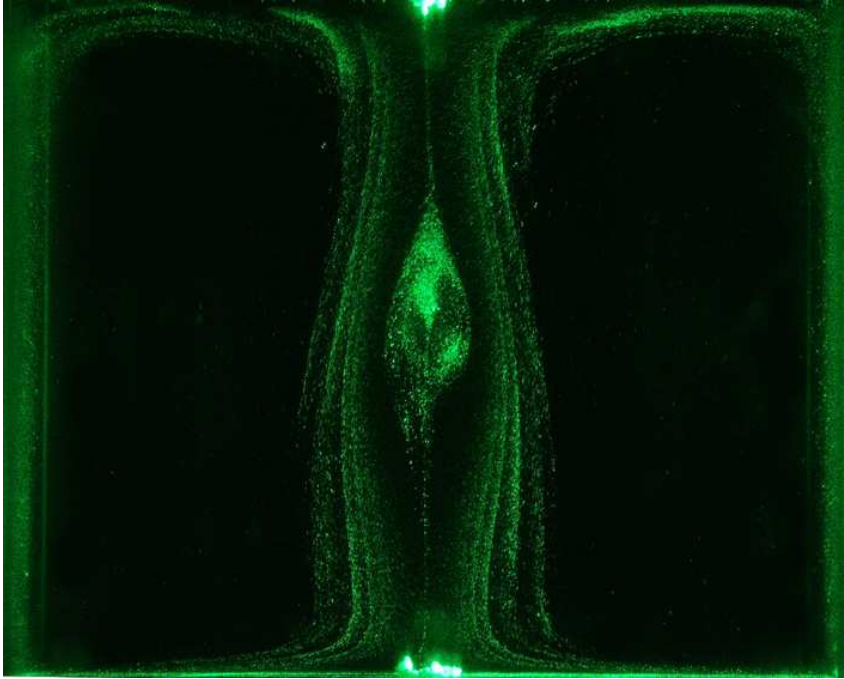
resents a meridional plane recirculation. Immediately below the recirculation, the dark shear layer closes in on the axis of symmetry, and the diameter of the breakdown region is reduced. A column then forms on the axis of symmetry in a similar fashion to the *no bubble* regime flow shown in Figure 4.2(a). Around the central column, the particles do not appear to move rapidly across the $r - z$ plane. In the lower portion of the vessel, the concentration of particles changes smoothly from a low concentration at the axis of symmetry to a higher concentration in the outer recirculation region. This implies that the transition from the central region to the outer recirculation region occurs gradually, rather than abruptly. In contrast, this transition occurs abruptly near the VB recirculation region, where there is a large difference in particle concentration either side of the boundary. The flow presented in Figure 4.4(b) at $Re = 975$ is similar to that of Figure 4.4(a). Fewer particles and a thicker light-sheet were used to present a three-dimensional perspective of the flow and to isolate the ‘shell’ of the inner flow region. Downstream of the VB recirculation region there is significantly less radial movement of the particles as they rotate about the axis of symmetry, except near the Ekman layer. The particles appear to have a high swirl component, however as they get closer to the impeller, the streaklines are lengthened in the axial direction. Interestingly, a few particles from outside the breakdown region are drawn into a similar low-velocity spiral path about the axis of symmetry, rather than being drawn radially outward. This observation demonstrates a mechanism by which particles and fluid may transfer into the inner region. Meanwhile, the radial distortion of the thin layer close to the impeller seems to indicate how the strong centrifugal forces imparted on the fluid in the Ekman layer gradually transport particles within the central region to the outer recirculation region.

Once attached to the free surface, the outer boundary of the VB region moves radially outward as Re increases. In addition, the downstream end of the VB recirculation region detaches from the axis of symmetry and then gradually increases both its axial and radial position. As an illustration of this, Figure 4.5 includes a photograph of the laser-illuminated flow field at $Re = 1350$. As the upstream part of the recirculation region still adjoins the axis of symmetry, this case is considered part of the *corner bubble* regime. The point $(Re, H/R) = (1350, 1.5)$ also falls within the *corner bubble* regime in the bifurcation diagram of Brøns *et al.* (2001). Note that the boundary of the breakdown region at the downstream end is once again less well defined than at the upstream end.

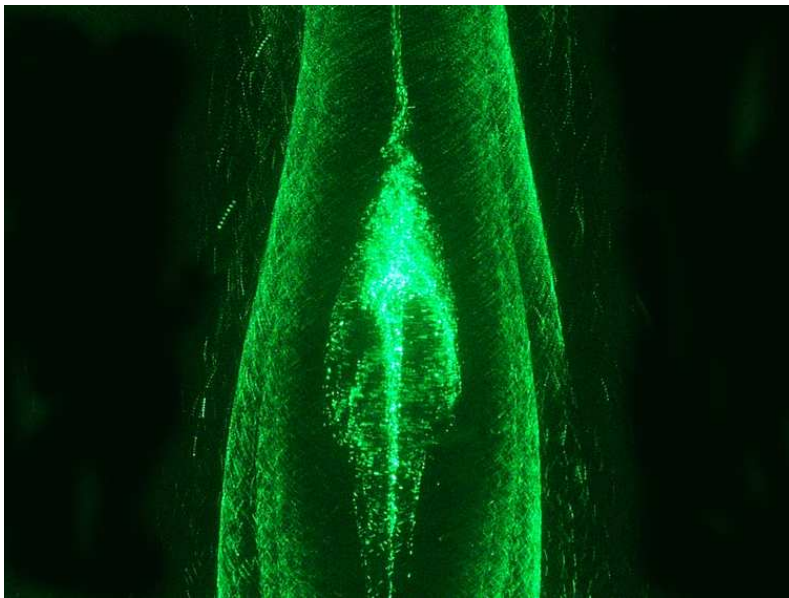
With a further increase in Re , the left edge of the VB recirculation bubble eventually becomes completely detached from the axis of symmetry, and the central vortex column extends

to the free surface. This is illustrated in Figure 4.6, which contains two photographs of *surface bubble* regime flows. The geometry of the breakdown region, shown here at $Re = 1920$ and $Re = 2000$, demonstrates a likeness to the image presented by Spohn *et al.* at $Re = 2095$. Once again, the laser-illuminated flow field, (a), was captured with particles seeded mostly in the central region, while the lamp-illuminated flow field, (b), was captured with particles distributed throughout the entire vessel but with different seeding levels corresponding to different regions of the flow. The resulting contrast illustrates how the different regions of the vessel can be used to provide different flow environments. Given the similar size and density of visualisation particles and cells, it is possible to draw tentative conclusions regarding cell suspension. That is, the successful isolation of particles in different fluid regions provides a preliminary validation of the ability to suspend cells in either the slow-mixing central region or the outer recirculation region.

At Re beyond 2000, the VB recirculation position moves very slightly in the radial direction, however the geometry of the bubble is qualitatively retained. As also observed by Spohn *et al.* (1993) and Young *et al.* (1995), the flow structure fails to become completely steady with respect to time at higher Re . However, the initial oscillations appear to be of low amplitude and low frequency. Generally, the current observations confirm the development described photographically by Spohn *et al.* (1993) and numerically by Brøns *et al.* (2001) for this aspect ratio. The close agreement between the flow structures observed at particular Re in this experiment and in previous studies instills confidence in the experimental setup and supports the validity of the assumptions made during construction of the bioreactor model. The use of lamp visualisation to complement the laser visualisation provides additional qualitative information regarding the distribution and relative speed of particles within the different flow regions, as well as particle motion at the downstream end of the breakdown region.

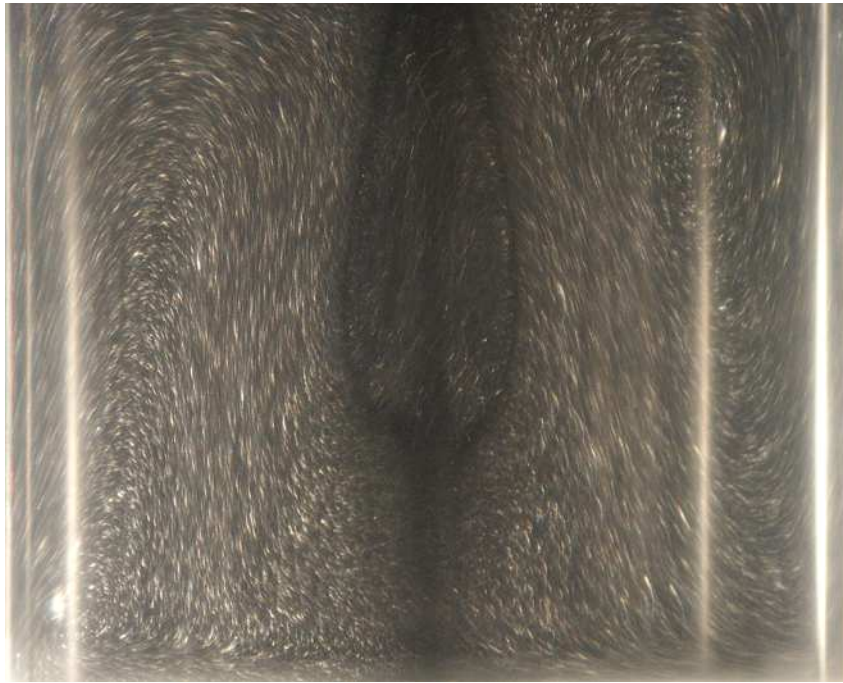


(a)



(b)

Figure 4.3: Laser-particle visualisation images illustrating the flow at $Re = 780$, where the field of view represents (a), the full meridional plane; and (b), a close-up of the breakdown region.



(a)



(b)

Figure 4.4: Lamp-particle visualisation images illustrating the meridional plane flow in the *corner bubble* regime when (a), $Re = 950$; and (b), $Re = 975$.

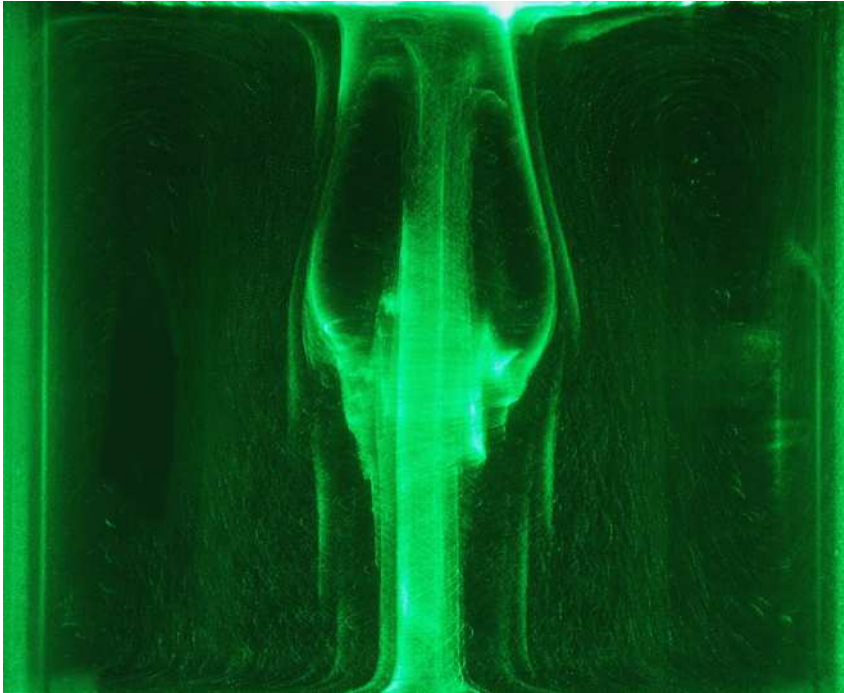


Figure 4.5: Laser-particle visualisation images illustrating the meridional plane flow in the *corner bubble* regime when $Re = 1350$.



(a)



(b)

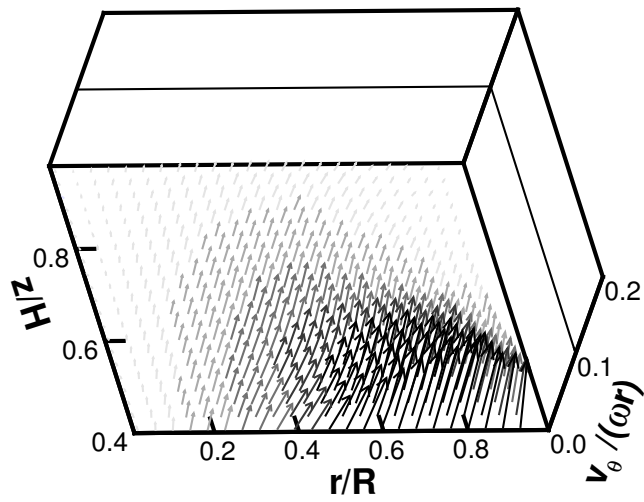
Figure 4.6: Photographs illustrating the meridional plane flow in the *surface bubble* regime. (a) $Re = 1920$, laser light source; (b) $Re = 2000$, lamp light source.

4.3 Three-Component Velocity Field

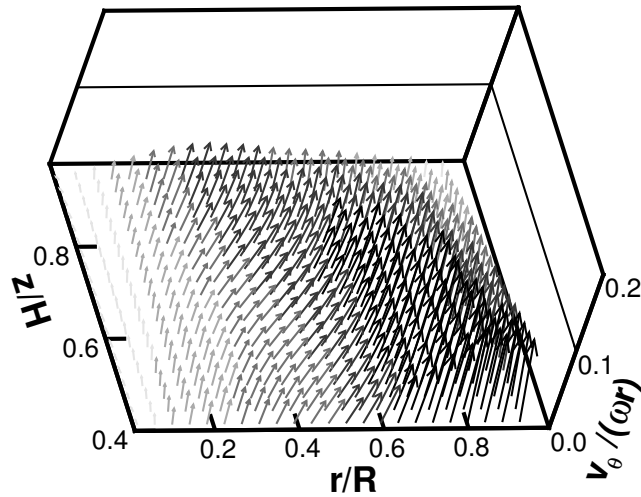
Naturally, quantitative measurements obtained using SPIV contain substantially more information than has hitherto been gained from flow visualisation. Velocity fields in three-dimensional vector form are shown in Figure 4.7 for Re values corresponding to (a), the *no bubble* regime ($Re = 600$), and (b), the *corner bubble* vortex breakdown regime ($Re = 1200$). The r/R and z/H axes denote the vector location in the meridional plane, while the third axis, $v_\theta/(\omega R)$, represents the magnitude of the azimuthal velocity component. For clarity, the vectors are shaded according to their v_θ magnitude. The field of view in the z domain is limited by the distorted nature of the SPIV measurement plane, however a comparison of the region $0.4 \leq z/H \leq 1.0$ is sufficient to highlight the difference between the two cases. Because of the approximate flow axisymmetry, only one half of the cylinder, $r/R \geq 0$, is presented. Despite the restricted field of view, both velocity fields exhibit a large dynamic range across the measurement region. At $Re = 600$ (Fig. 4.7(a)), there is insufficient momentum imparted on the fluid by the rotating disk to cause strong motion above $z/H \approx 0.7$. The in-plane motion is difficult to visualise when plotted in combination with the azimuthal recirculation. However, the vectors in the high-velocity region point in the $+z$ direction near the cylinder wall and in the $-z$ direction closer to the axis of symmetry, thus reflecting the single recirculation occurring in the meridional plane at Re below that at which Vortex Breakdown occurs.

At $Re = 1200$ (Fig. 4.7(b)), the three-component vector field appears markedly different. Here, the disk supplies sufficient inertia to cause both an azimuthal circulation and a secondary recirculation pattern that extends to the free surface. The distribution of the local velocity vectors is less regular than at $Re = 600$. For instance, the direction and magnitude of the spiralling motion changes several times across the field of view, whereas the recirculating motion at $Re = 600$ is relatively straightforward. The vortex breakdown region is contained within the low-velocity region near the axis, although its internal motion is not entirely clear in Figure 4.7(b) due to the perspective. An orthogonal or near-orthogonal projection of the $r - z$ plane is necessary to adequately present the breakdown region boundary and the flow contained within.

Closer to the impeller, the contrast between the higher and lower velocity regions is more stark. This is to be expected as the rotating disk represents the sole mechanical power source driving the flow. The impeller acts as a centrifuge on the adjacent fluid, strongly accelerating the low-velocity fluid near the central column in the azimuthal and radial directions. Three-dimensional vector plots within the region enclosed by $0 < z/H < 0.2$ and $0 < r/R < 0.92$ are presented in Figure 4.8. On this occasion, three cases are included ($Re = 1200$, $Re = 2000$, and



(a)



(b)

Figure 4.7: Three-component velocity vector fields corresponding to the (a), $Re = 600$, *no bubble*; and (b), $Re = 1200$, *corner bubble* cases. Vector shading represents v_θ levels.

$Re = 2800$) to broadly illustrate the general consistency but subtle differences between vector fields corresponding to different Re .

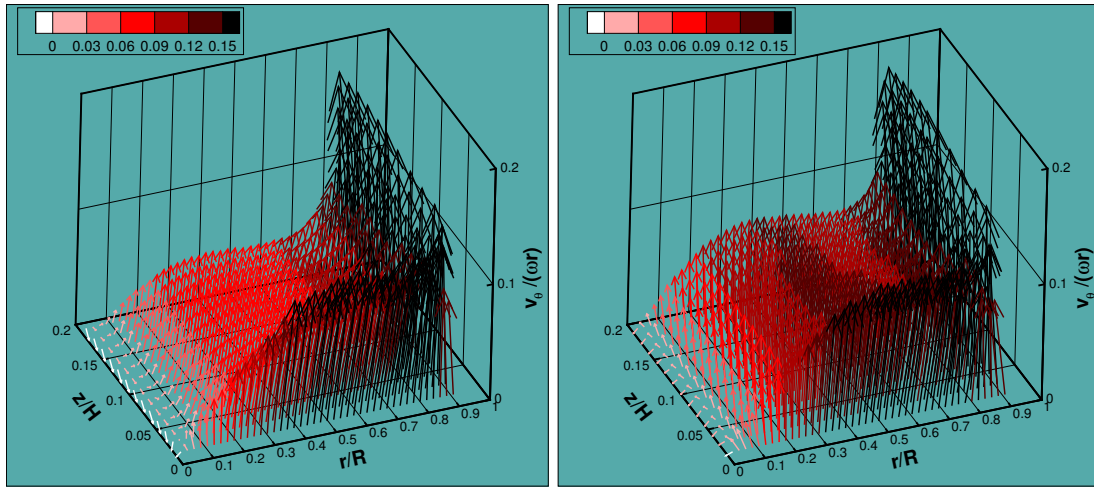
In the field of view presented, it is possible to summarise the flow in terms of four distinct regions. The first is a strong flow which occurs very near the $z = 0$ end of the bioreactor. The velocity vectors rise steeply from the others within the plane in Figure 4.8. This represents the Ekman layer, the bottom boundary region already mentioned several times in this thesis. The second region, located in the vicinity of the sidewall, is another containing large velocity vec-

tors. The fluid turned upward by the sidewall initially retains much of its momentum, and thus the sidewall profile resembles, at least from the perspective shown in Figure 4.8, a continuation of the Ekman profile along a different orientation. The Ekman region and the lower sidewall region do not alter significantly between the cases shown. This apparent Re -independence reflects the dominance of the inertial forces imparted by the disk on the flow in the immediate vicinity of the impeller.

The third region within Figure 4.8 is the near-columnar, vortical flow located at the cylinder core but above the Ekman layer. Here, the velocity vectors appear to lengthen linearly as r/R increases, before they plateau, forming a fourth region. When viewing the vector field through the perspective shown in Figure 4.8, the vectors in the central vortex region and the plateau region seem to be independent of z . The more detailed data analyses which follow in the current chapter show this not to be the case, however the uniform nature of these flow regions, particularly when contrasted with the Ekman and sidewall regions, is well illustrated by the three-dimensional velocity plots. The third and fourth regions also demonstrate a much stronger dependence on Re than the other two regions. At higher Re , the impeller is able to generate significantly more momentum through these regions than at lower Re .

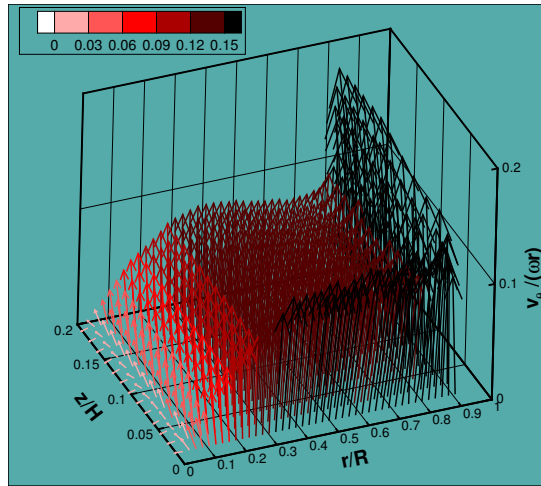
While the three-dimensional vector fields illustrate the flow in general terms, a more thorough understanding is gained by extracting data plots that are easier to conceptualise. A straightforward approach is to break the velocity vectors down to their three components, v_r , v_z , and v_θ . Figure 4.9 presents the $Re = 1200$ flow with a separate contour plot corresponding to each component. A larger field of view can be presented by combining the measurements of the upper portion of the cylinder, a selection of which are presented in Figure 4.7, with measurements of the impeller region, i.e. some of those shown in Figure 4.8. The joining of the two data sets results in a slight discontinuity at $z/H \approx 0.4$. In each plot, red contours represent motion in the positive direction and blue contours represent motion in the negative direction. In Figure 4.9(c), which illustrates the v_θ distribution, the motion is entirely in the positive direction. This is because only the right hand side of the meridional plane is included in the plot and there is no reversed azimuthal flow. The positive θ direction is defined here as being into the page.

Of the three contour maps, the v_r distribution is probably the least intuitive and the least instructive about the nature of the flow topology. A key feature of the v_r distribution is the $v_r = 0$ contour immediately below the free surface, which can be used to identify the approximate position of the stagnation line in the *corner bubble* and *surface bubble* regimes. In the case



(a)

(b)



(c)

Figure 4.8: Three-component velocity vectors in the vicinity of the impeller, when (a), $Re = 1200$; (b), $Re = 2000$; and (c), $Re = 2800$. Vector colouring represents contours of $v_\theta / (R\omega)$, as indicated by the colour bar.

shown, $Re = 1200$, the stagnation line occurs at a radial position slightly less than $0.2R$. The strongest radial motion occurs near the upper and lower surfaces; the free surface and the impeller, respectively. As expected, the radial momentum imparted by the impeller on the nearby fluid creates a region with a v_r magnitude far in excess of the rest of the vessel. The fluid does not return radially inward with strength until it reaches the upper part of the vessel, i.e. in the region $0.8 < z/H < 1$. Here, v_r is less intensely concentrated than in the Ekman region, where the local radial force is significantly larger. Throughout most of the meridional

plane, the radial velocity component is within the range $-0.02 < v_r/(R\omega) \leq 0.02$. The general dominance of axial flow over radial flow throughout the vessel, along with the cross-flow error v_{r1} (see Subsection 3.4.8), render the radial velocity component particularly difficult to use as a means of analysing the flow structure.

The v_z contour map (Fig. 4.9(b)) provides a clearer illustration of the dual recirculation pattern. There are two areas where the fluid moves in the positive direction. The largest and strongest of these is located near the sidewall of the cylinder, and is caused by radial and azimuthal momentum from the Ekman region being converted into positive axial momentum. The strong axial velocity is retained up to $z/H \approx 0.8$, at which stage the radial momentum increases once again. The fluid then accelerates in the negative radial direction and approaches the impeller to complete the recirculation labelled ‘outer recirculation region’ in Figure 4.1. The slant of the $-v_z$ contours in the upper half of the vessel reflects the divergence of the flow as it passes the breakdown region, located separately near the axis of symmetry. Fluid in the innermost recirculation bubble, labelled ‘VB recirculation region’ in Figure 4.1, rotates in the direction opposite to the outer recirculation. For this reason, the positive v_z contours are this time to the left, rather than to the right, of the negative v_z contours. The breakdown region boundary surface is not clear in Fig. 4.9(b), however a comparison between the two $+v_z$ regions indicates the key differences between the two recirculation zones. Firstly, the VB recirculation is smaller than the outer recirculation region. Furthermore, the fluid within it rotates with a much lower in-plane velocity, as evidenced by the wider contour spacing and the lesser $+v_z$ peak. The position of the VB recirculation is considered in more detail in Section 5.2. Below the VB recirculation, the axial flow remains slow, and the fluid travels toward the disk. Close inspection of Fig. 4.9 reveals that the flow is not independent of z in the inner region between the breakdown bubble and the disk, as could mistakenly be inferred from Figure 4.8. Between $z/H \approx 0.43$ and $z/H \approx 0.03$ the suction of the Ekman layer causes the fluid to gradually accelerate in both the axial and azimuthal directions.

The v_θ contours indicate the breakdown region less clearly than the v_z contours, primarily because the reversed flow associated with VB occurs in the $r-z$ plane, rather than the azimuthal plane. However, within $0.2 \lesssim r/R \lesssim 0.6$ the contour lines bulge radially outward around the vertical centre of the vessel. The slant of the $v_\theta/(R\omega) = 0.3$ contour in $0.6 \lesssim r/R \lesssim 0.9$ is similar to the slant of the v_z contours in the same part of the vessel. Since the v_z contours depict the approximate curvature of the breakdown bubble, this indicates that the v_θ distribution also reflects the upper breakdown bubble geometry to some extent. In turn, this provides strong

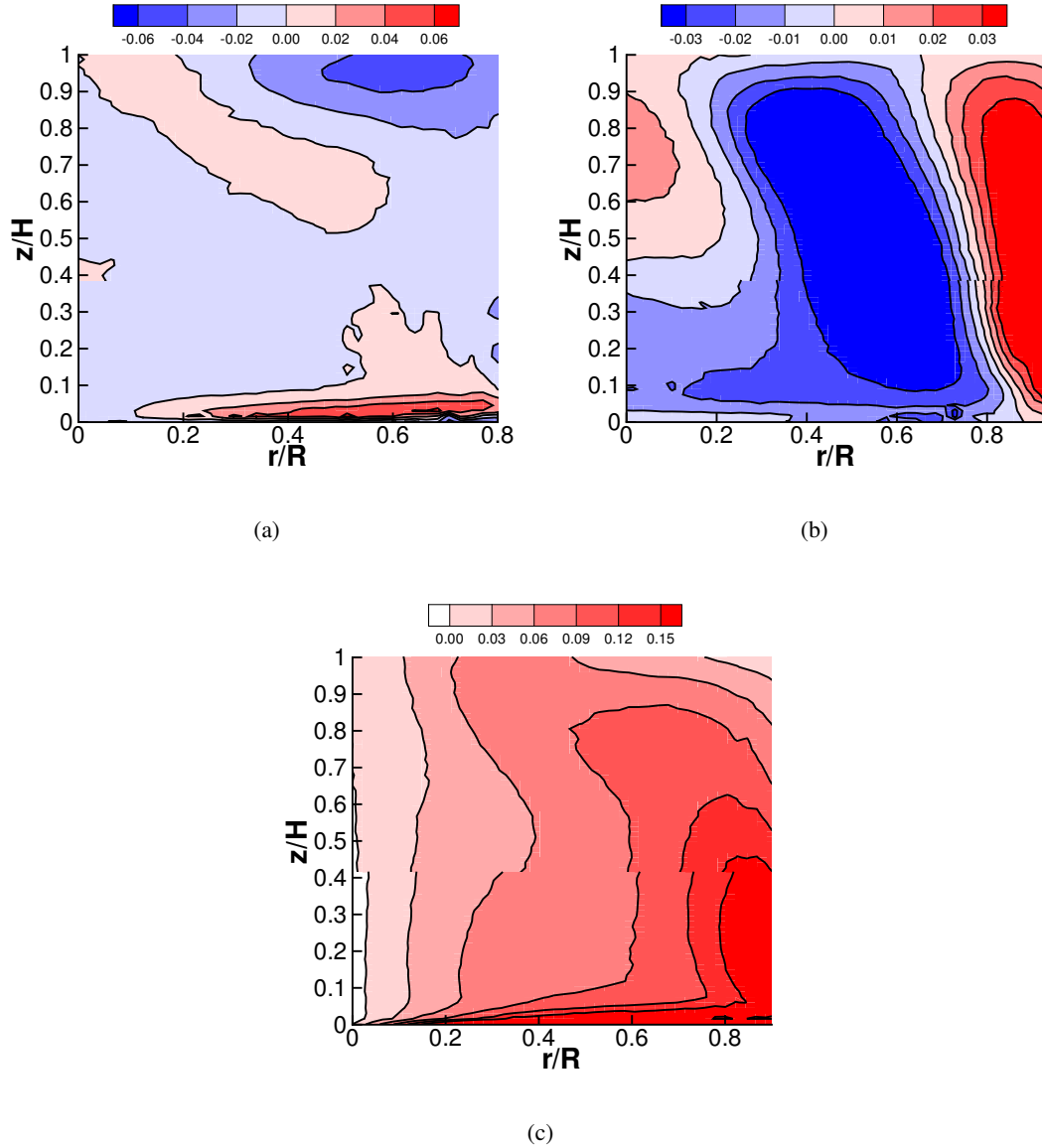


Figure 4.9: Distribution of individual velocity components across the right hand side of the meridional plane when $Re = 1200$. (a), $v_r/(R\omega)$; (b), $v_z/(R\omega)$; and (c), $v_\theta/(R\omega)$.

experimental evidence of reduced azimuthal velocity within the boundary of the VB region. Further quantification of the reduced azimuthal flow in the breakdown region is provided by the circulation profiles discussed in Section 4.4.2. In the bottom half of the vessel, the v_θ contours return toward the axis of symmetry, which corresponds to a narrowing of the breakdown region and an increase in swirl as the fluid travels toward the disk. At the sidewall, v_θ remains strong in the region $0 \leq z/H \leq 0.3$, and then steadily decreases as z increases. This trend appears to confirm a transition from azimuthal momentum to axial momentum in the sidewall region, as it coincides with an increase and maintenance of v_z until the fluid reaches the free surface.

Sotiropoulos & Ventikos (2001) reported a similar axial extension of the spiral flow pattern in the upper portion of their fixed lid cylinder. Given the documented critical nature of swirl ratio to vortex breakdown formation, this relationship between v_z and v_θ is worthy of more detailed discussion, which is provided in Section 4.5.

At this point, it should be noted that the measurements in the region $v_\theta \lesssim 0.002$ may be misleading, because it was not possible to accurately measure the disk rotation using the SPIV technique. Surface reflections increased the random error component in the aforementioned region, and SPIV windows containing part of the disk tended to have large peaks occurring around $(0,0)$ in correlation space, which resulted in three-dimensional velocity vectors of approximately zero magnitude. The v_θ measurements are particularly inaccurate, as under no-slip conditions v_θ should theoretically approach $r\omega$ as $z/H \rightarrow 0$. This error is not applicable for $v_\theta \geq 0.002$, where the disk was absent from all interrogation windows. To counteract this error, a bottom surface boundary condition of $v_\theta/(R\omega) = r/R$ was applied to the data shown in Figure 4.9(c) and subsequent plots.

4.4 Quantification of the effect of Re on Flow Topology

The conclusions regarding flow topology drawn thus far with the aid of vector fields and contour maps are generally applicable to the entire set of cases for which there is vortex breakdown. However, it has already been shown in the flow visualisation study (Section 4.2) that flow topology depends on Re from the onset of vortex breakdown ($Re \approx 760$) to within the unsteady regime. So that the effect of changing Re is quantified in a more meaningful way than can be accomplished using velocity vector or contour maps, the data are analysed in Section 4.4 using single-dimensional flow profiles extracted from the SPIV measurement set. The axial velocity profiles are analysed separately to the circulation profiles, although the same cases are presented in both subsections (4.4.1 and 4.4.2, respectively). Furthermore, in Subsection 4.4.3 contours of azimuthal vorticity, Ω_θ , are presented to illustrate the changes to the rotational fluid motion in the meridional plane caused by an increase or decrease in Re .

4.4.1 Axial Flow

The radial profiles of axial velocity are highly dependent on the axial location from which they are extracted, as the geometry of the recirculation bubbles is not straightforward, and transfers from azimuthal to axial momentum, and vice-versa, occur throughout the vessel. Figure 4.10 illustrates the normalised v_z profiles for the $Re = 1200$ case at six different axial locations: $z/H = 0.09$, $z/H = 0.24$, $z/H = 0.38$, $z/H = 0.5$, $z/H = 0.77$, and $z/H = 0.92$. $z/H = 0.09$ is situated near the impeller, just above the Ekman region. The profile is quite constant at a level of $v_z \approx -0.025R\omega$ for $0 \leq r/R \lesssim 0.7$, as the Ekman layer pulls fluid towards the impeller. Closer to the sidewall, the axial velocity increases rapidly to form the jet discharged from the Ekman layer. Between the limit of the measurement region and the sidewall, i.e. $0.96 < r/R < 1.0$, v_z necessarily approaches 0 due to the no-slip boundary condition. Closer to the vertical centre of the bioreactor, the profiles have a distinct maximum and minimum. These peaks correspond to the strongest points of the outer recirculation in the upward and downward directions respectively. From $z = 0.09H$ to $z = 0.38H$ the minimum v_z point moves radially inward and the uniformity of the flow between this point and the axis of symmetry decreases. Furthermore, the value of v_z at $r = 0$ approaches zero, illustrating that the fluid accelerates in the region between a stagnation point immediately below the VB recirculation and the bottom disk. By $z = 0.5H$, the fluid at the axis of symmetry moves in the direction away from the disk. This indicates that the profile passes through the VB recirculation region. The magnitude of v_z in the central region of the bioreactor is further increased at $z/H = 0.77$. In the outer recircu-

lation region, both the minimum and maximum points move progressively closer to the axis of symmetry. This reflects a gradual widening of the sidewall jet as z increases. Furthermore, the widening of the jet is associated with a decrease in the maximum v_z . In contrast, the downward jet narrows as the VB region widens, leading to an increase in the $-v_z$ peak. The magnitude of the v_z curve diminishes near the top of the bioreactor (e.g. at $z/H = 0.92$), as the recirculating flow progressively turns to the radial direction.

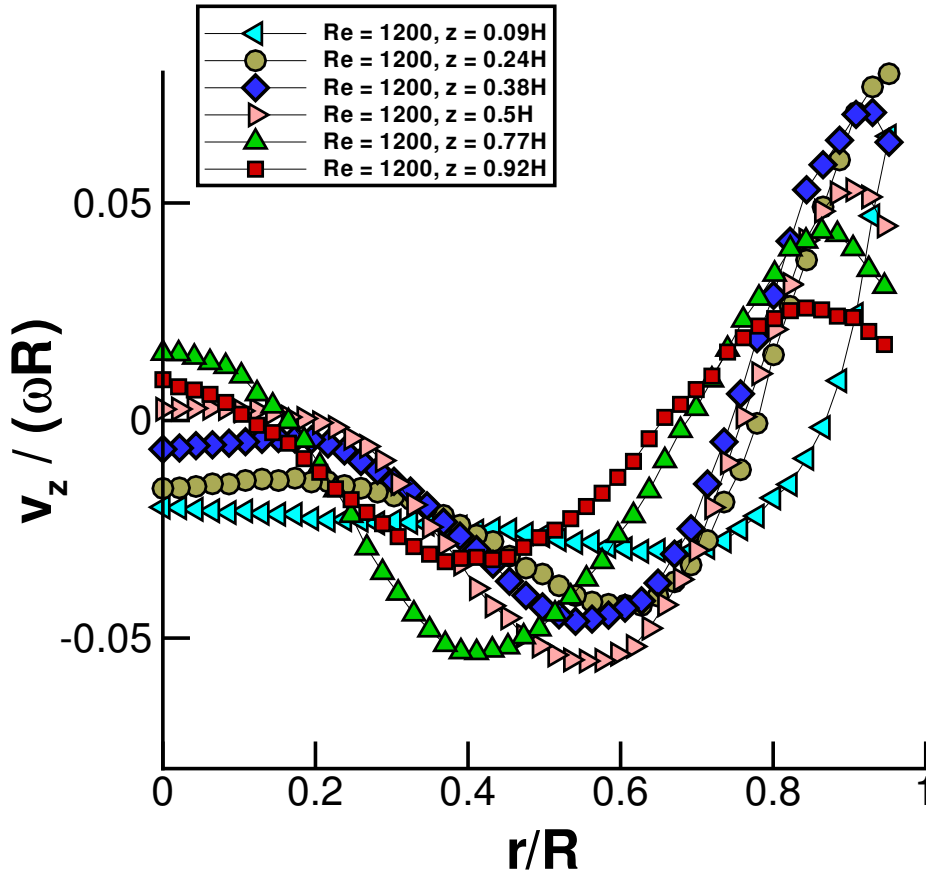


Figure 4.10: Radial profiles of $v_z/(\omega R)$ at $Re = 1200$. The different curves correspond to different axial cross-sections.

Figures 4.11, 4.12, 4.13, 4.15 and 4.16 each contain different v_z profiles extracted at a constant axial location. Several Re cases are included in each plot. In this manner, the effect of Re on the meridional flow is detailed. The symbol shape and colour is assigned according to Re , and for consistency the symbol designation is replicated in each of the plots.

Changing Re has very little effect on the axial flow in the impeller region, as illustrated by Figure 4.11 ($z/H = 0.09$). All profiles exhibit a similar slight gradient in the $-v_z$ region, alongside a strong peak of roughly constant magnitude near the sidewall. The radial locations

at which these peaks occur also appear similar, however close inspection reveals a very slight shifting of the peak toward the wall as Re increases. At $z/H = 0.24$, (Fig. 4.12), there is decreased similarity between the profiles, although once again the differences are not substantial. The axial flow in the direction toward the bottom of the vessel is relatively stronger at $Re = 1200$ than the other three cases shown. This difference is amplified at the v_z minimum, the value of which appears to be inversely proportional to Re . In general, however, the v_z profiles suggest that the meridional plane flow below the axial position of the VB recirculation is relatively insensitive to changes in Re .

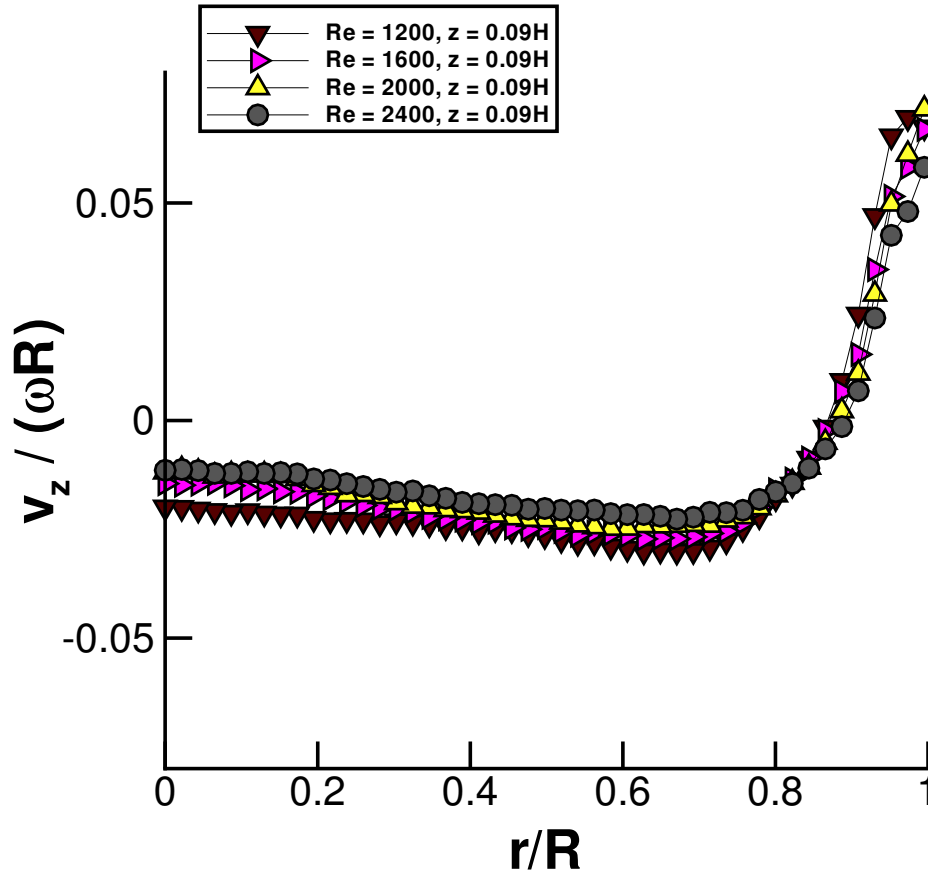


Figure 4.11: Radial profiles of $v_z/(\omega R)$ at $z/H = 0.09$. The different curves correspond to different Re values.

Figure 4.13 contains the flow profiles at $z/H = 0.50$, the vertical centre of the rig. A larger number of curves are shown, as there is a wider variety of profile geometries across the Re domain. The $z/H = 0.5$ cross-section passes through the lower part of the VB region, and so the v_z profiles quantify the flow both inside and outside the VB boundary. Hence, the varying curve geometries reflect the nature of the vortex breakdown region as it changes with Re . For

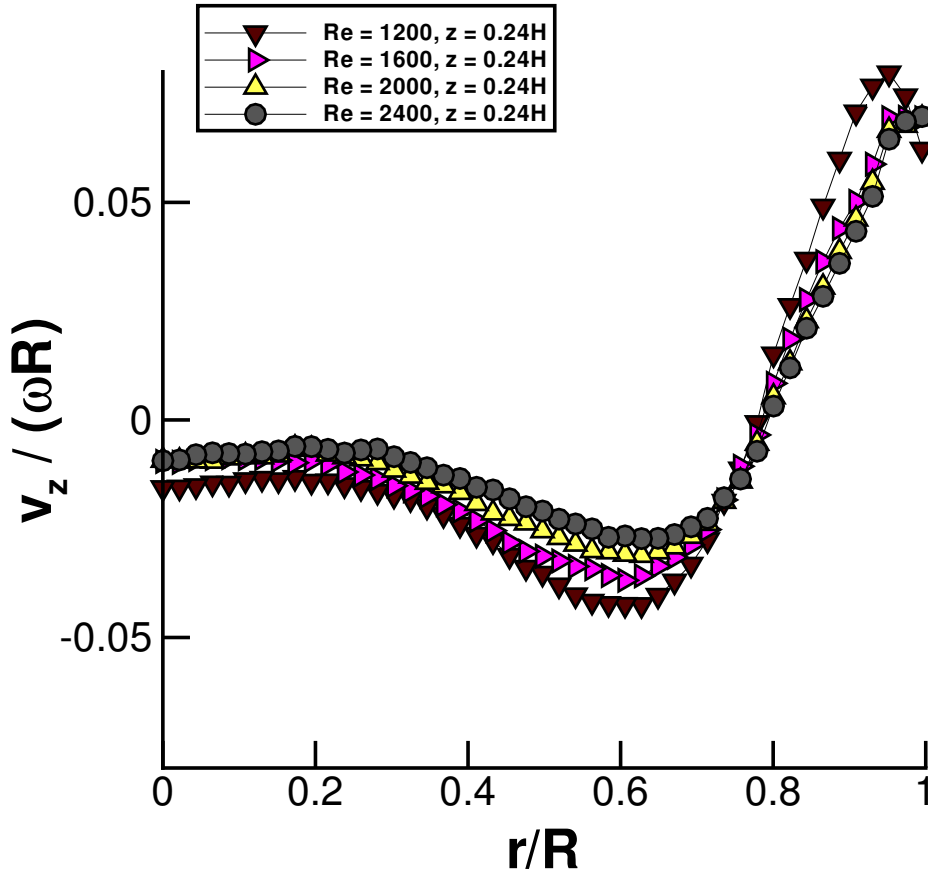


Figure 4.12: Radial profiles of $v_z/(\omega R)$ at $z/H = 0.24$. The different curves correspond to different Re values.

example, the locations of both the maximum and minimum velocity move radially outward as Re increases. This is indicative of the outer recirculation region distorting as the vortex breakdown region shifts and widens. Secondly, the axial velocity at $r = 0$ gradually moves from positive to negative. This can be explained by the transition from the *corner bubble* regime to the *surface bubble* regime. As the VB recirculation torus detaches from the axis of symmetry, it leaves a region of fluid with negative axial velocity that adjoins the central vortex region. Therefore, the transition from positive to negative corresponds to the detachment of the VB recirculation from the central axis at this particular axial location. For the cases where $v_z < 0$ at $r = 0$, (i.e. $Re \geq 1400$), the VB recirculation, indicated by the leftmost positive axial flow, occurs at a similar position away from the axis. For $Re = 600$, v_z is approximately 0 for $r \lesssim 0.15$, and the outer recirculation is significantly weaker than for the VB cases.

The radial position of the point of minimum velocity, r_{vm} , is controlled by the radius of the VB region. This is because the downward flow is strongest just outside the VB recirculation,

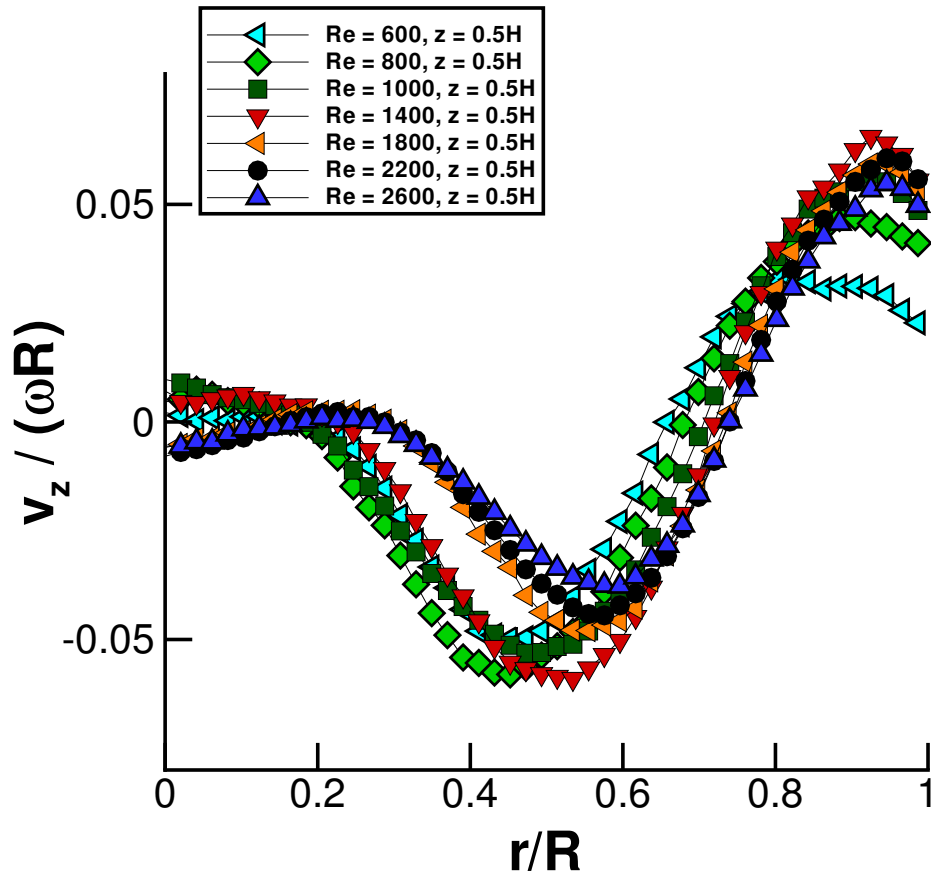


Figure 4.13: Radial profiles of $v_z/(\omega R)$ at $z/H = 0.50$. The different curves correspond to different Re values.

and the v_z profile between the boundary and r_{vm} is consistent over $800 \leq Re \leq 3000$. The relationship between r_{vm} and Re over the experimental domain is plotted in Figure 4.14. In order to tackle the uncertainty associated with determining r_{vm} , three techniques were used to identify the v_z minimum point at each Re : by locating the smallest measured v_z value directly from the averaged data set, by fitting a high-order polynomial function to the full data set, and by fitting a high-order polynomial function to the data local to the minimum point. The r_{vm} values identified via these three techniques are denoted in Fig. 4.14 with red, green and blue squares respectively. The smallest value of r_{vm} is at $Re = 800$, the lowest case recorded using SPIV at which VB occurs. As Re increases the outer diameter of the bubble grows rapidly at first, before becoming more constant. At $Re \gtrsim 2400$, r_{vm} appears independent of Re to within the experimental uncertainty limits, indicating that the girth of the breakdown region at $z/H = 0.50$ is asymptotic. Similar trends were observed when r_{vm} was derived from radial profiles at other axial locations in the upper half of the vessel. As discussed later in this chapter,

this is significant in the context of utilising VB as part of a cell suspension bioreactor.

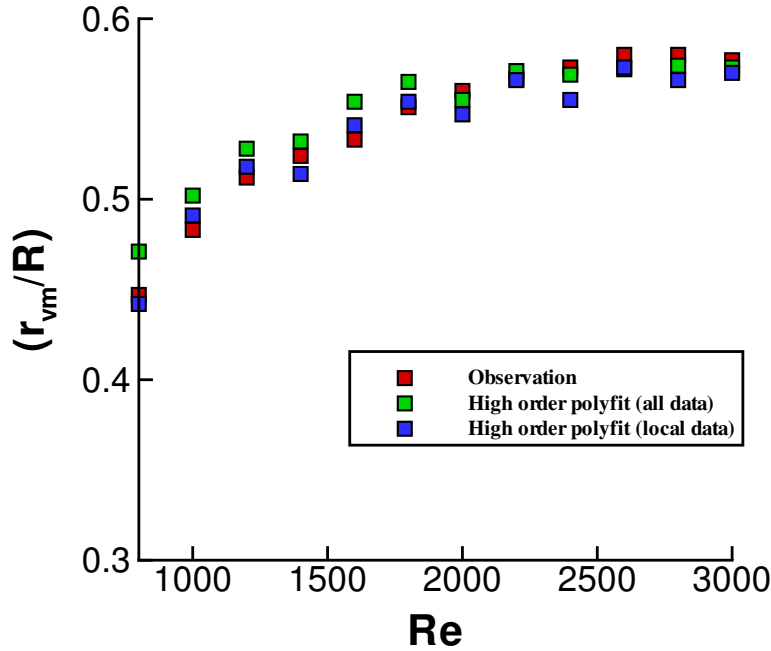


Figure 4.14: Location of $v_z/(\omega R)$ minimum value on radial profiles at $z/H = 0.50$. The different curves correspond to different identification techniques.

The $z/H = 0.77$ axial section is closer to the centroid of the vortex breakdown recirculation than $z/H = 0.50$. As illustrated by Figure 4.15, the profiles differ markedly, particularly within the radius of the v_z minimum. The major differences occur across changes in the VB regime. In the *corner bubble* regime, v_z has a local maximum at $r = 0$, the value of which is Re dependent. The v_z at $r = 0$ is greatest at $Re = 1400$, the Re where the VB recirculation is strongest at $z/H = 0.77$. When $Re = 1800$, the downstream end of the VB recirculation is just detached from the axis at $z/H = 0.77$. The corresponding profile is close to those of the *surface bubble* cases shown ($Re = 2200$ and $Re = 2600$). For these cases, v_z has a local minimum value at $r = 0$. v_z increases with r so that it eventually crosses $v_z = 0$, an event that designates the radial location of the inner surface of the VB recirculation torus. Eventually it reaches a local maximum and then becomes negative at the other side of the VB recirculation. The radial distance between the local maximum and the location at which v_z crosses 0 reflects the width of the VB recirculation, the slant of the recirculation, and the axial location of the recirculation relative to the interrogation cross-section. This distance increases between $Re = 800$ and $Re = 1400$ as the bubble moves axially upward and widens. It then narrows slightly up to $Re = 2200$, and remains constant for the final case shown, $Re = 2600$. The constancy between $Re = 2200$

and $Re = 2600$ is reminiscent of the curve plateau at higher Re values in Figure 4.14. For all cases, the $-\partial v_z / \partial r$ gradient increases outside the VB recirculation, as the axial velocity peaks in the outer recirculation are roughly five times larger than those in the VB recirculation. Aside from the $Re = 600$ case, the different profiles are far more aligned in the outer recirculation region than in the inner region. The magnitude and radial location of the maximum v_z peak is close to constant, with the exception that there are slight velocity deficits at $Re = 800$ and $Re = 1000$. When $Re = 600$, the fluid does not recirculate in the upper portion of the bioreactor, which explains the flat $v_z \approx 0$ curves recorded at $z/H = 0.77$ (Fig. 4.15), and $z/H = 0.92$ (Fig. 4.16).

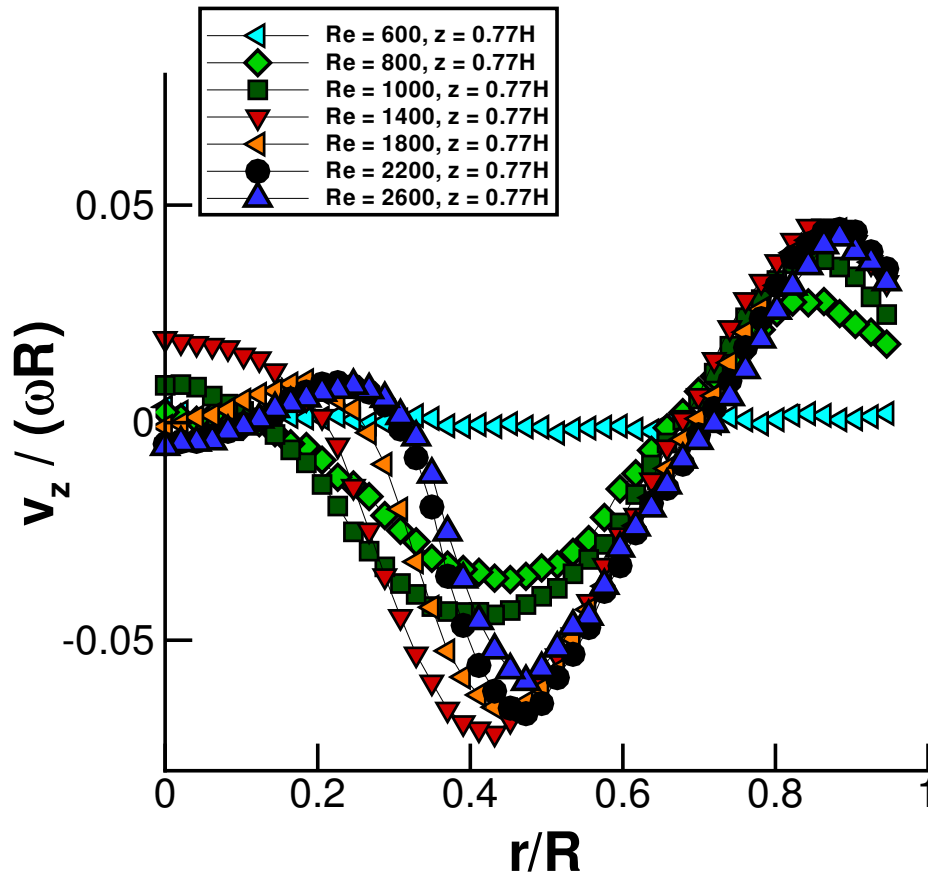


Figure 4.15: Radial profiles of $v_z / (\omega R)$ at $z/H = 0.77$. The different curves correspond to different Re values.

The final set of radial profiles presented in the current subsection are those measured at $z/H = 0.92$, which corresponds, regardless of Re , to a vertical position above the VB recirculation centroid. This location is significantly closer to the upper surface than $z/H = 0.77$, so the v_z component is consistently lower across the radius of the cylinder. As the outer recirculation

causes a large $-v_r$ component around $z/H = 0.92$, v_z is particularly reduced near the maximum and minimum points. The axial flow progressively weakens as Re decreases, due to the lack of sustained momentum in this region of the vessel at low Re . The v_z curve corresponding to the $Re = 1800$ case is positive at $r = 0$. This contrasts with the $Re = 1800$ curve at $z/H = 0.77$ or at axial positions closer to the impeller, which have a negative value of v_z on the axis of symmetry. Thus, the flow on the upper part of the axis is in the positive axial direction, and hence forms the inner edge of the VB recirculation, and the remainder of the flow at $r = 0$ is in the direction of the disk. The partial attachment of the VB recirculation to the axis of symmetry suggests that $Re = 1800$ lies within the *corner bubble* regime. Interestingly, the curve is closer in shape to the higher Re cases, meaning that the flow structure is more reminiscent of the *surface bubble* geometry, as shown in Figure 4.6, than the geometry of other *corner bubble* cases, such as the $Re = 1350$ case shown in Figure 4.5. The local maxima within the VB recirculation region corresponding to $Re = 2200$ and $Re = 2600$ are approximately 20% closer to the axis of symmetry at $z/H = 0.92$ than at $z/H = 0.77$. The translation of this point conveys the slanted nature of the VB recirculation, as well as the consistency of the slant angle for these two cases. At $Re = 1800$ the VB recirculation is slanted slightly more toward the axis of symmetry.

An analysis of the $v_z = 0$ contour lines corresponding to selected cases illustrates the axial translation of the downstream stagnation point as Re changes. For the *corner bubble* cases, the exact location of the stagnation point is identified by the vertical-axis intercept of the $v_z = 0$ contour downstream of the VB region. The cases for which the $v_z = 0$ contour does not cross the z -axis fall into the *surface bubble* category. Five cases are compared in Figure 4.17. The $v_z = 0$ contour corresponding to $Re = 1000$ is denoted by the black dashed and double-dotted line. For this case, the stagnation point is located downstream of the field of view. When $Re = 1200$ (blue dashed line) the stagnation point is higher up the z axis, and the upper portion of the contour line is located further from the axis of symmetry. This trend continues with a further increase in Re , as illustrated by the $v_z = 0$ contours corresponding to $Re = 1600$ (red dashed and dotted line) and $Re = 1800$ (green dotted line). The contour shapes also indicate that a larger percentage of the downstream end of the recirculation zone becomes detached from the axis of symmetry as Re increases. By $Re = 2400$ (orange solid line) the $v_z = 0$ contour no longer intersects with the z axis as the VB recirculation is completely detached. Figure 4.17 quantifies the observations recorded in previous studies by Spohn *et al.* (1993), Brøns *et al.* (2001), and in the flow visualisation experiments (see Section 4.2), regarding the gradual detachment of the recirculation region from the axis of symmetry. This is important

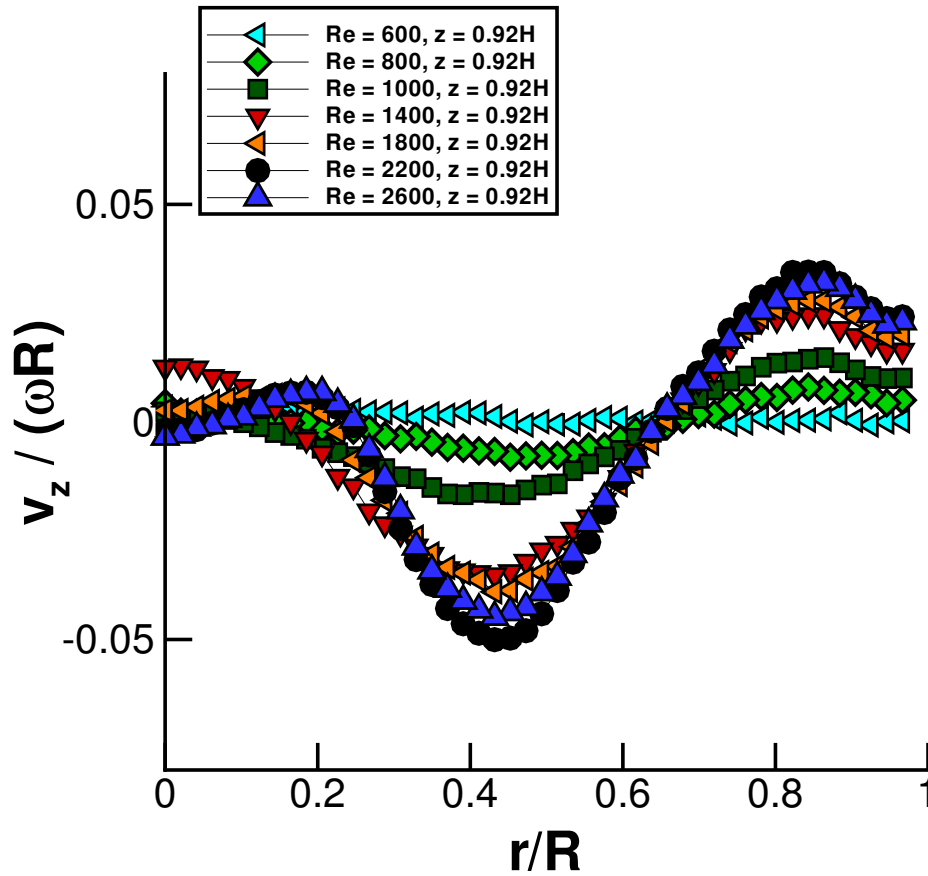


Figure 4.16: Radial profiles of $v_z/(\omega R)$ at $z/H = 0.92$. The different curves correspond to different Re values.

in a suspension culture application, as the enclosed VB recirculation may be more difficult to access for seeding purposes if it is located away from the axis of symmetry.

4.4.2 Azimuthal Flow

Previous authors have presented the flow in the azimuthal direction using the spatially variable circulation component defined by $\Gamma = v_\theta r$ (Spohn *et al.*, 1998; Lopez, 1990). Like v_z , Γ is a useful variable to plot using radial profiles because it helps distinguish the separate flow regions. Typically, the inner radial region has a relatively flat, low magnitude Γ profile and the outer radial region has a higher magnitude, jet-like profile. In this subsection, radial profiles of Γ , normalised by ωR^2 , are presented to describe in detail the variations in the azimuthal flow caused by a change in Re . The alteration of the azimuthal flow with Re differs to that described in Subsection 4.4.1 for the meridional flow, and has not been extensively quantified. For this reason, the current subsection includes Γ profiles at the same locations and for the same cases as the v_z profiles presented in the previous subsection. For ease of comparison, the symbol

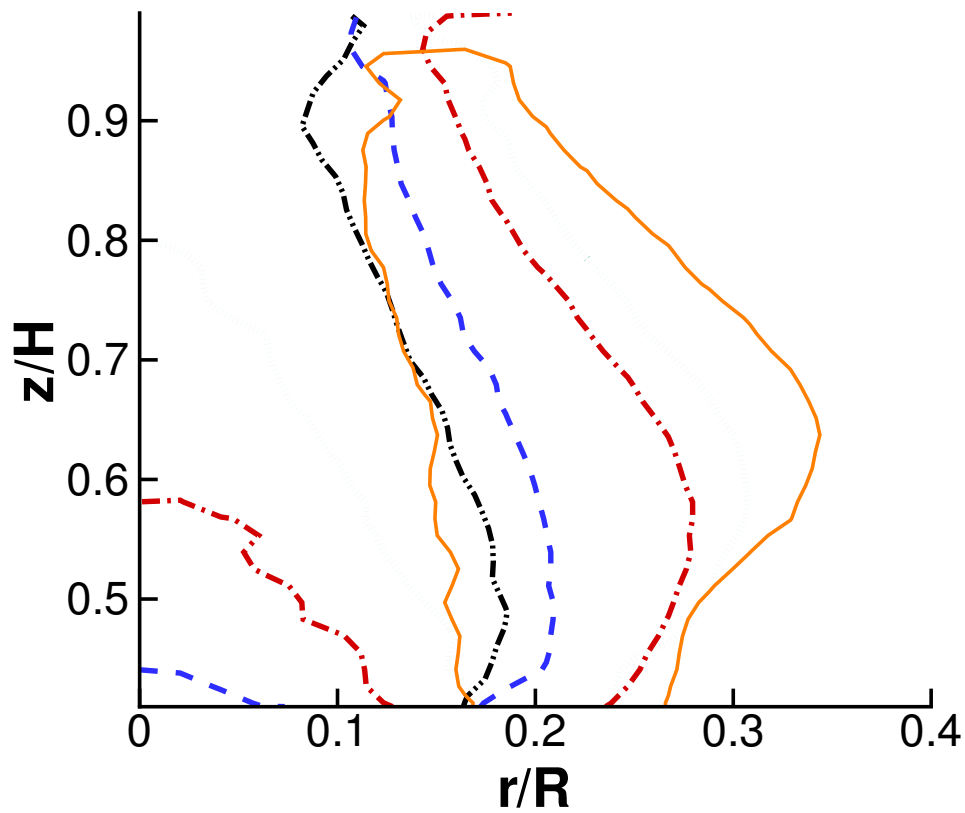


Figure 4.17: $v_z = 0$ contour lines at various Re in the *corner bubble* and *surface bubble* regimes. The z -axis intercept represents the downstream attachment point of the VB recirculation. $Re = 1000$: black dashed and double-dotted line; $Re = 1200$: blue dashed line; $Re = 1600$: red dashed and dotted line; $Re = 1800$: green dotted line; $Re = 2400$: orange solid line.

shape and colouring used in Subsection 4.4.1 is repeated here.

Several axial sections extracted from the $Re = 1200$ SPIV data are plotted in Figure 4.18. The magnitude of Γ varies substantially as a function of z , although barely changes in the region $0 \leq r/R \lesssim 0.4$. The circulation peak is largest in the profile closest to the disk. The peak is also very close to the sidewall at $z/H = 0.09$; indeed, the negative gradient on the outer side of the peak is outside the measurement field of view and its existence must be assumed because of the $v_\theta = 0$ condition at $r/R = 1.0$. At $z/H = 0.24$ the maximum value is already heavily diminished, and the peak is within the field of view. As z increases, the Γ maximum continues to decrease and move radially inward, until by $z/H = 0.92$ it is located at $r/R \approx 0.70$ and has a magnitude less than one fifth of the $z/H = 0.09$ peak. The translation and retraction of the peak is not compensated by an increase in Γ in another section of the radial axis, and thus a loss of azimuthal momentum ensues. In contrast, v_z tends to increase in magnitude at certain r values closer to the axis of symmetry as the maximum value decreases and shifts (see Fig. 4.10). Spohn *et al.* (1998) presented radial profiles of $\Gamma/(\omega R^2)$ corresponding to $(Re, H/R) = (1800, 1.75)$ at axial locations of $z/H = 0.21$, $z/H = 0.52$, and $z/H = 0.94$. The general shape of the curves and the reduction in the magnitude and radial position of the peak in their study are consistent with Figure 4.18.

The Γ profiles at $z/H = 0.09$ illustrate the azimuthal flow just above the Ekman layer. These curves have three distinct regions, each of which can be considered with reference to the four regions making up the three-dimensional vector plots of Figure 4.8. The first is the core vortex, which occupies the region $0 \leq r/R \lesssim 0.15$. Here, v_θ varies linearly with r , and the Γ curves align closely. This adjoins the ‘plateau’ region of Figure 4.8. In the plateau region, which occupies $0.15 \leq r/R \lesssim 0.7$, the flow is more dependent on Re , especially the azimuthal component. When $Re = 1200$, v_θ varies very little with r , so the Γ curve is linear in this region. As Re increases, Γ increases in magnitude and the Γ versus r relationship becomes progressively more parabolic. Approaching the sidewall, the profiles once again collapse into alignment. The side of the jet that is visible in Figure 4.19, e.g. within the region $0.8 \leq r/R \leq 0.96$, is similar in all four cases. This confirms the Re -independent nature of the flow immediately following its discharge from the Ekman region.

As illustrated by Figure 4.20, the three aforementioned regions remain in approximately the same radial positions at $z/H = 0.24$. The scale on the $\Gamma/(\omega R^2)$ axis is adjusted slightly from that of Figure 4.19, as the maximum value is substantially reduced. While Re once again has little effect on the flow in the core vortex and jet regions, the difference between the curves is

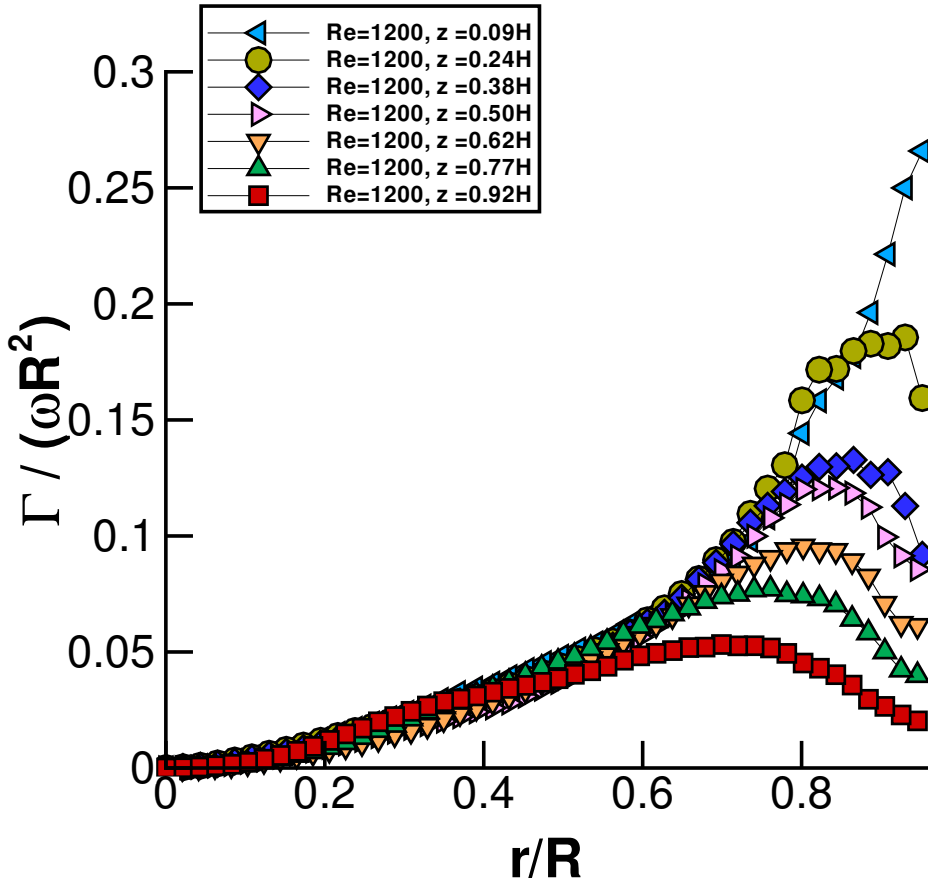


Figure 4.18: Radial profiles of $\Gamma/(\omega R^2)$ at $Re = 1200$. The different curves correspond to different axial sections.

accentuated in the middle region. For instance, when $Re = 1200$ the second derivative $\partial^2\Gamma/\partial r^2$ is positive in the region $0.3 \leq r/R \leq 0.6$, whereas it remains negative for the other three cases. It is worth remembering that the deviation between the curves is likely to be a product of the differences in breakdown geometry - the flow profile downstream of a wide bubble could be expected to differ from that downstream of a narrow bubble.

The spread between the Γ profiles in the middle region continues at $z/H = 0.50$ (see Figure 4.21). For the cases when $Re \leq 1400$, $\partial^2\Gamma/\partial r^2$ is positive in the region $0.15 \leq r/R \leq 0.45$. For the higher Re cases, $\partial^2\Gamma/\partial r^2$ is negative in the same region. The difference is most likely linked to the internal structure of the breakdown region; for instance, when $Re = 1400$ the VB recirculation is attached to the axis of symmetry at $z/H = 0.50$ whereas the downstream end of the recirculation is detached from the axis when $Re = 1800$. As at $z/H = 0.09$ and $z/H = 0.24$, Re has little effect on the azimuthal flow in the central column surrounding the axis of symmetry. However, unlike the profiles in Figures 4.19 and 4.20, the profiles diverge

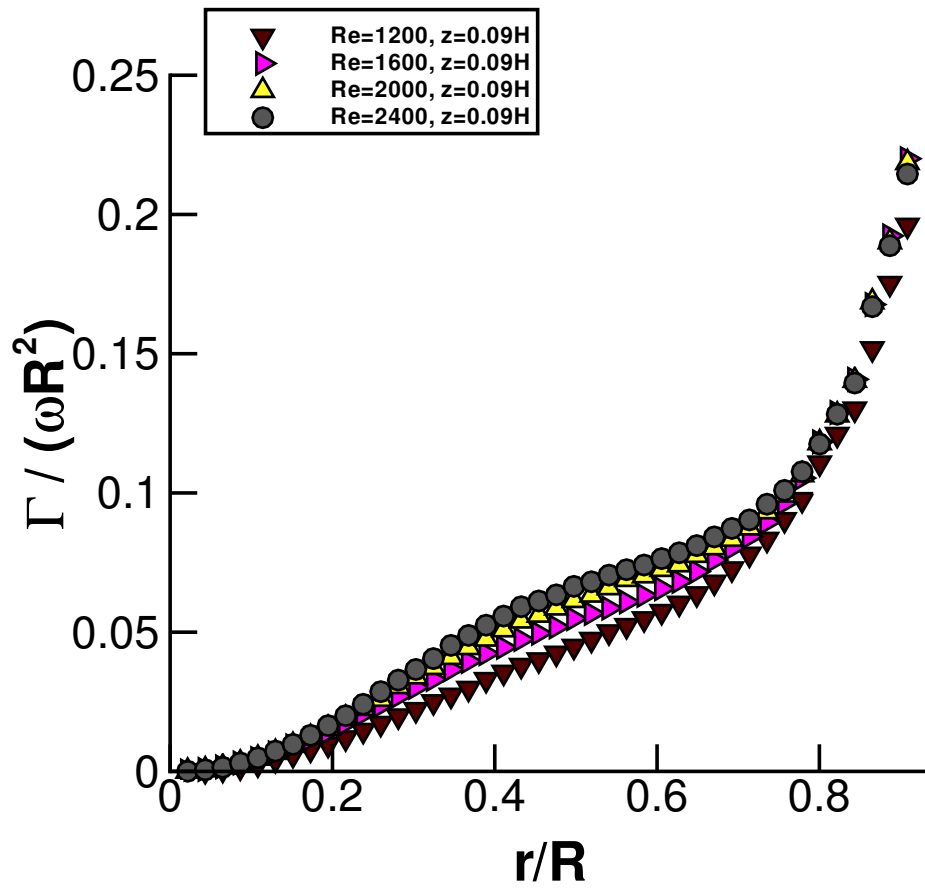


Figure 4.19: Radial profiles of $\Gamma/(\omega R^2)$ at $z/H = 0.09$. The different curves correspond to different Re values.

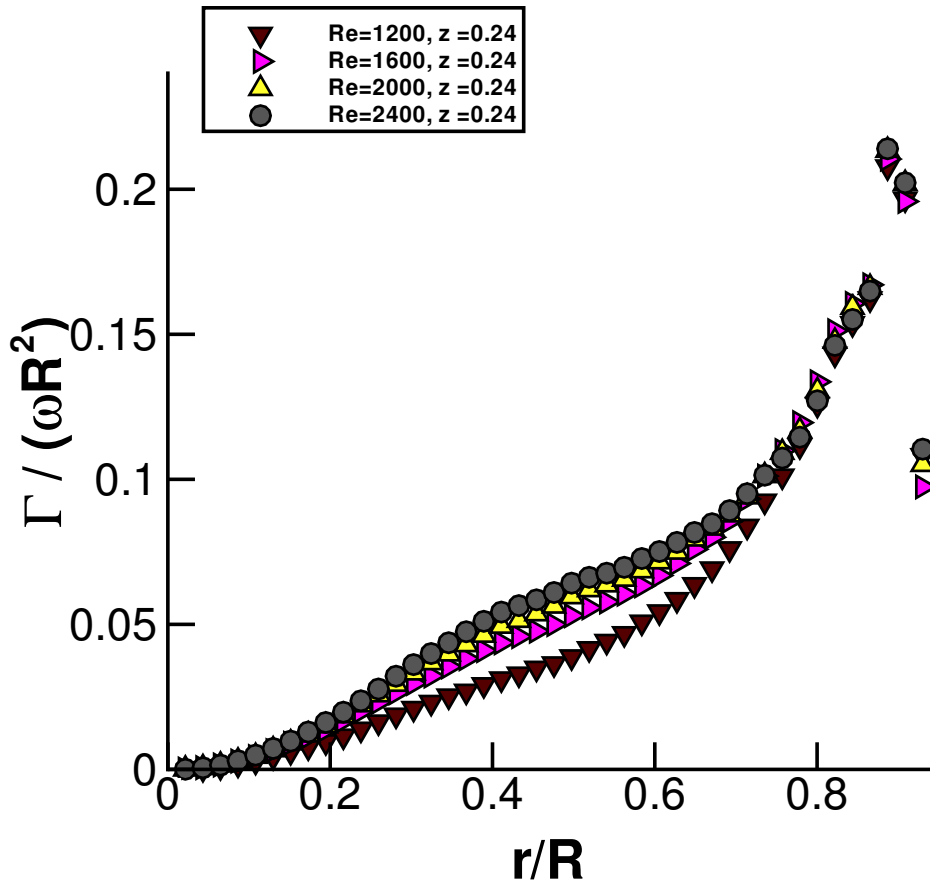


Figure 4.20: Radial profiles of $\Gamma/(\omega R^2)$ at $z/H = 0.24$. The different curves correspond to different Re values.

in the vicinity of the jet. The azimuthal flow at $z/H = 0.50$ is weakest when $Re = 600$, and becomes progressively stronger as Re is increased up to 1800. The curves remain fairly closely aligned for $Re \geq 1800$, the range in which the time-averaged breakdown geometry becomes more stabilised. The location of the maximum Γ value is controlled by Re in a similar manner. The peak is closest to the axis of symmetry at $Re = 600$, and moves radially outward as Re increases, before approaching a constant position around $r/R = 0.83$.

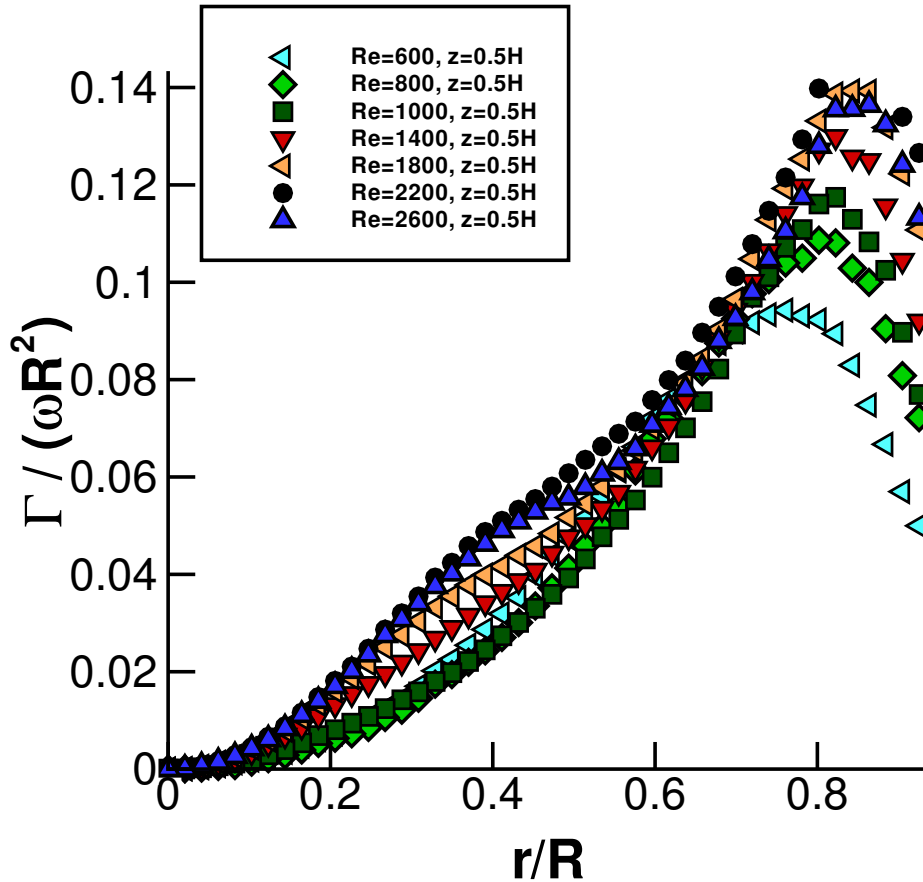


Figure 4.21: Radial profiles of $\Gamma/(\omega R^2)$ at $z/H = 0.50$. The different curves correspond to different Re values.

At $z/H = 0.77$ (Figure 4.22), the curve shapes are more consistent, particularly in the middle region. From this observation, it appears that the Γ profiles differ more downstream of the VB boundary than in the VB recirculation itself. While the curve geometries are similar at $z/H = 0.77$, the difference in magnitude between curves is much more pronounced than at $z/H = 0.50$. Once again, the profiles corresponding to $Re \geq 1800$ are more tightly aligned. Note that the azimuthal and radial velocity data near $r/R = 0.82$ were adversely affected by a small vertical reflection line. The resulting bias error necessitated the removal of these data

from Figures 4.22 and 4.23.

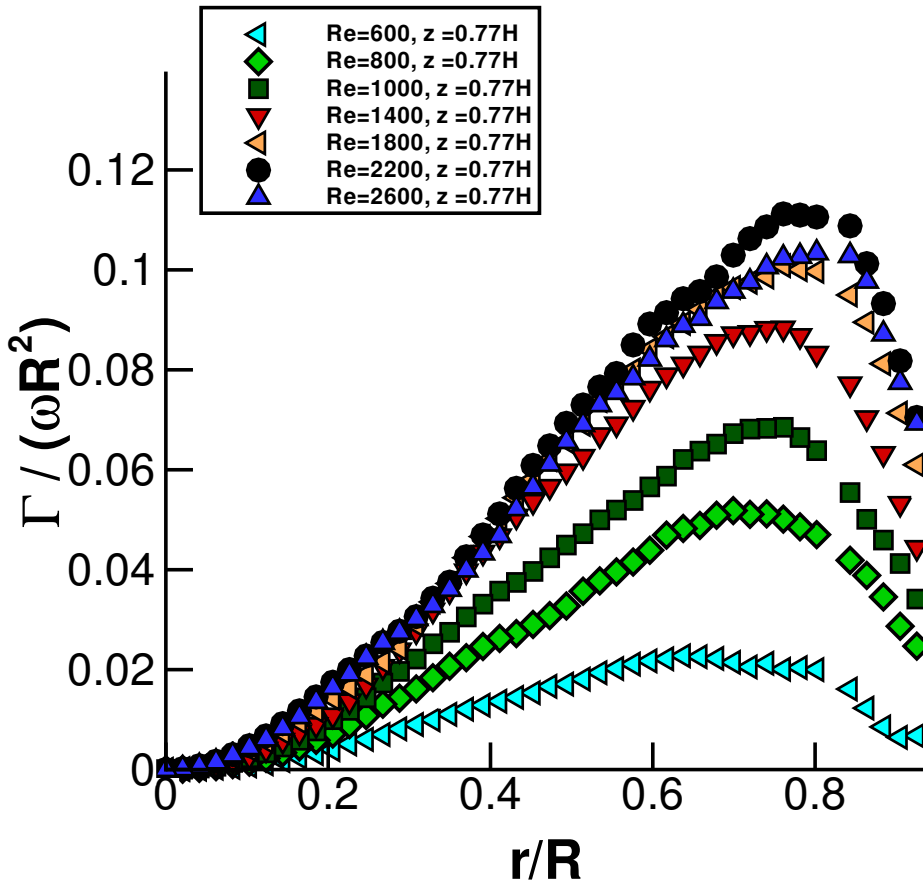


Figure 4.22: Radial profiles of $\Gamma/(\omega R^2)$ at $z/H = 0.77$. The different curves correspond to different Re values.

At $z/H = 0.92$ (Figure 4.23), the peak values are spread quite evenly between $\Gamma \approx 0.01$ and $\Gamma \approx 0.10$. The $Re = 1800$ profile lies well below the $Re = 2200$ and $Re = 2600$ profiles. It should be recalled that the noticeable difference between $Re = 1800$ and the higher Reynolds number cases at $z/H = 0.92$, is also reflected in the v_z profiles. These differences are more noticeable in the region near the free surface than in the remainder of the vessel. There is a slight difference in magnitude between the upper two curves, however the size of the difference lies within the spread of all the cases between $Re = 2200$ and $Re = 3000$, so is not regarded as significant. As a final point, it is worth noting that while there is no axial flow at $z/H = 0.77$ or $z/H = 0.92$ when $Re = 600$, a low-velocity azimuthal flow is apparent. The one-dimensionality of this flow is unlikely to be favourable for mixing, which is significant as the meridional plane motion is a key reason for the selection of this vessel configuration as a bioreactor model.

The linkage between the axial and azimuthal flow is presented pictorially in Figure 4.24.

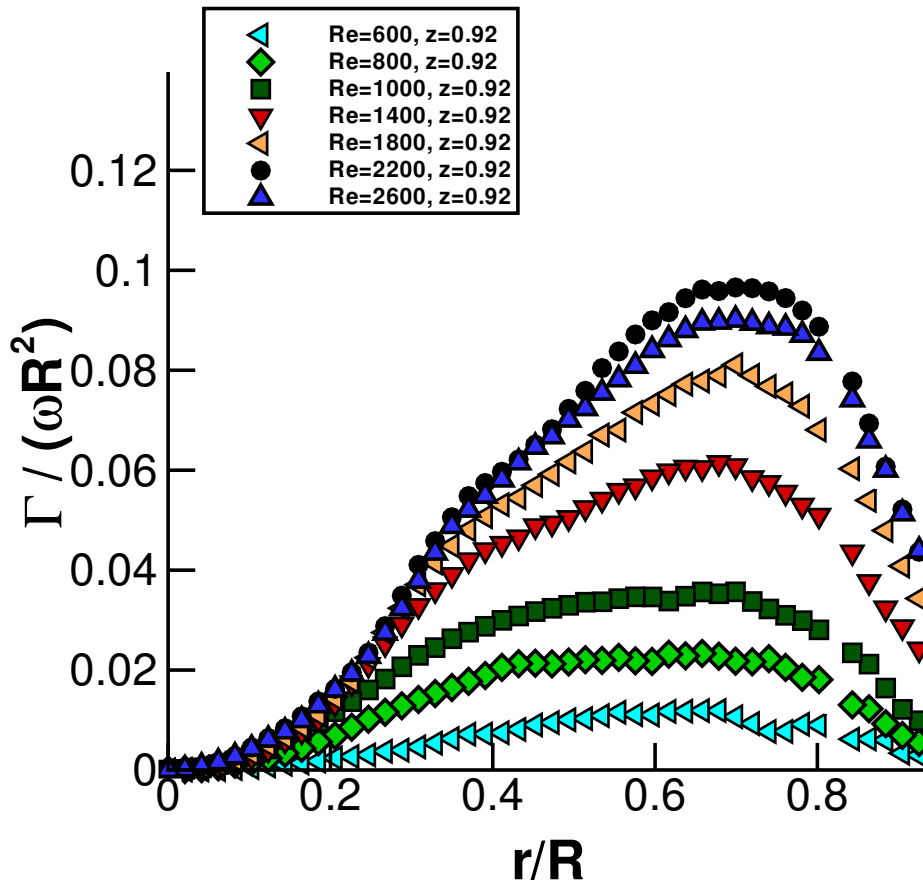


Figure 4.23: Radial profiles of $\Gamma/(\omega R^2)$ at $z/H = 0.92$. The different curves correspond to different Re values.

Contours of v_θ are superposed on a v_z surface map, so that any similarities in the distribution of these two components are apparent. To highlight the relative locations of the low-velocity breakdown region and the high-velocity outer region, both sides of the meridional plane are shown. The v_z surface is reflected evenly about $z = 0$, however the v_θ contours are coloured blue on the left hand side of the plane, even though the flow is in the same θ direction on both sides of the vessel. For this reason, it should be clarified that the red contours refer to fluid moving into the page, while the blue contours refer to fluid moving out of the page, rather than a change in azimuthal flow direction.

The breakdown region is clear in the v_z surface plot, as it is delineated by a flat, hump-like area surrounding the axis of symmetry. The hump widens slightly at z -positions corresponding to increased VB girth, and widens between $Re = 1200$ and $Re = 2400$ as the VB recirculation moves further from the axis of symmetry. The v_θ contours do not illustrate such a dramatic difference between the inner and outer zones as does the v_z surface plot. However, the contours

do spread slightly where the VB zone is wider. This justifies the consideration of the meridional plane flow and the azimuthal flow separately, although both transport the suspended cells simultaneously and so it is problematic to neglect either.

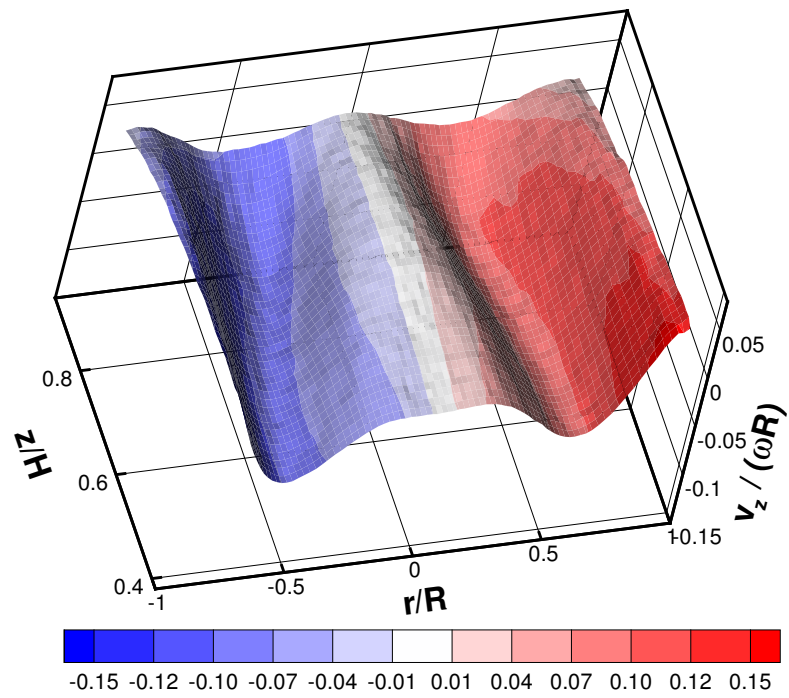
4.4.3 Azimuthal Vorticity

While the analyses of the v_z and Γ profiles contained in the preceding two subsections significantly add to an understanding of the flow, further information is provided by the vorticity distribution. The azimuthal component of vorticity, Ω_θ , is of particular interest as it illustrates the interaction between the outer and VB recirculation regions, and how their relative size, position, and strength are affected by a change in Re . The Ω_θ distribution is also relevant for a bioreactor application as it provides an indication of the rotational forces likely to be experienced by a suspended cell or microcarrier at a particular location in the vessel.

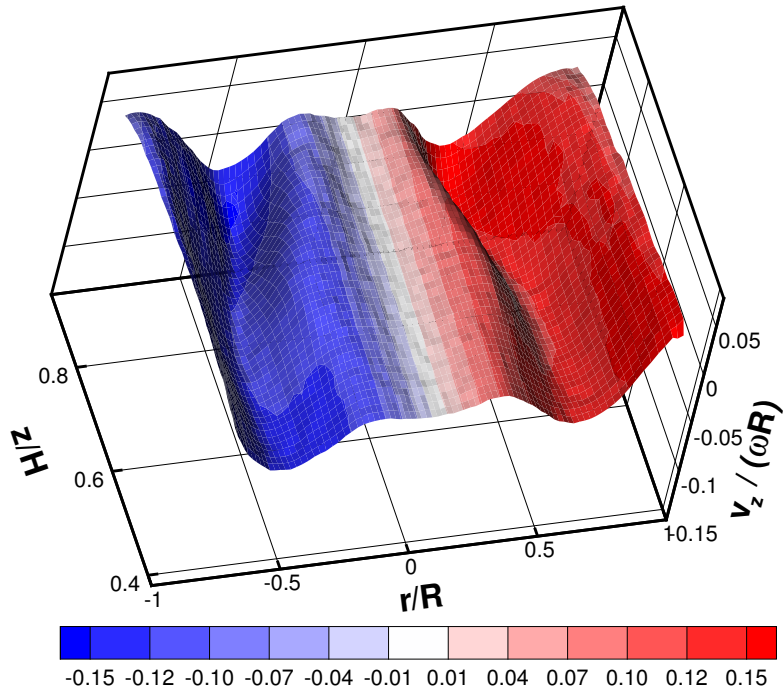
Figure 4.25 includes normalised azimuthal vorticity fields corresponding to the $Re = 1200$, $Re = 2000$ and $Re = 2800$ cases. Like the velocity component contour maps shown in Figure 4.9, the plots are collages of the upper and lower data sets. As indicated by the legend, red contours denote regions of positive Ω_θ and blue contours denote regions of negative Ω_θ . The blank zones represent regions where there is very little azimuthal vorticity. While the Ω_θ distribution delivers a broad indication of the location of the outer and VB recirculations, the $\Omega_\theta = 0$ contour that runs close to the middle of the measurement plane does not exactly correspond to the boundary of the VB region.

As Re increases, the $+\Omega_\theta$ region associated with the VB recirculation undergoes a transformation. The peak Ω_θ magnitude increases, particularly between $Re = 1200$ and $Re = 2000$. On the other hand, there is a decrease in the volume over which vorticity exceeds the lowest contour threshold, (i.e. $\Omega_\theta/\omega \geq 0.1$). The $+\Omega_\theta$ zone also moves radially outward and becomes more slanted, which is reminiscent of the manner in which the VB geometry evolves with an increase in Re . These observations portray an intensification of the azimuthal vorticity within and surrounding the VB recirculation as it pushes radially into the position occupied by the outer recirculation. Correspondingly, there is an increase in $-\Omega_\theta$ to the immediate right of the $+\Omega_\theta$ zone, even though the remainder of the large $-\Omega_\theta$ region remains relatively constant. The intensification of $+\Omega_\theta$ is also accompanied by the formation of a small pocket of $-\Omega_\theta$ near the axis of symmetry. The contraction of the region of high $+\Omega_\theta$ results in an expansion of the low Ω_θ region located near the centre of the bioreactor and downstream of the VB recirculation.

Regions of positive Ω_θ also occur along the bottom boundary layer, where there is a



(a)



(b)

Figure 4.24: Surface plots of $v_z / (\omega R)$, with colouring representing contours of $v_\theta / (\omega R)$. (a) $Re = 1200$; (b) $Re = 2400$.

strongly positive velocity gradient $\partial v_r / \partial z$, and in the upper part of the sidewall boundary layer, where there is strongly negative $\partial v_z / \partial r$. Although the data are slightly noisier near the boundaries, neither of these regions change substantially as Re is increased. The only observable transformation is a slight thinning of both shear layers.

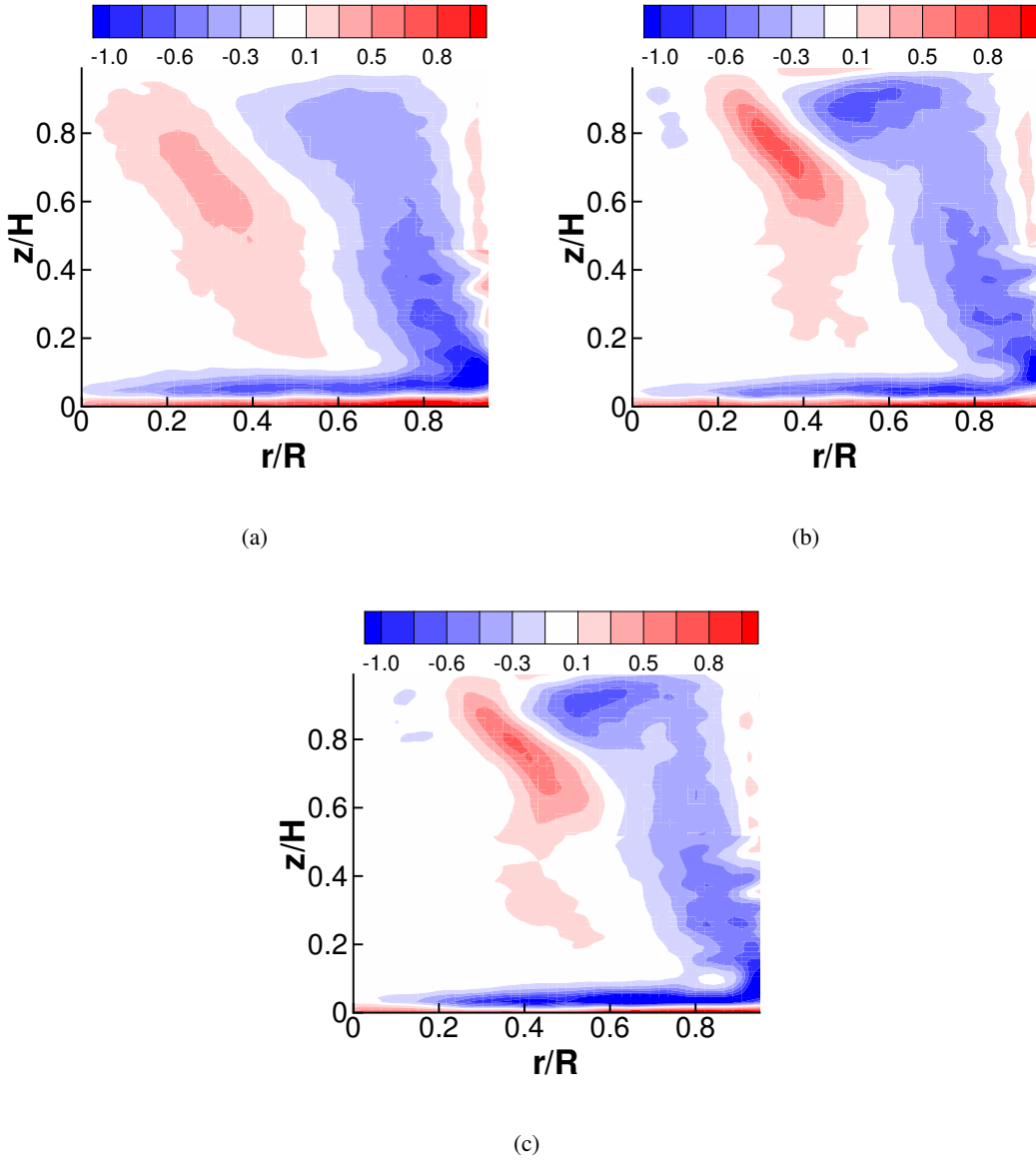


Figure 4.25: Distribution of Ω_θ/ω across the right hand side of the meridional plane when (a), $Re = 1200$; (b), $Re = 2000$; and (c), $Re = 2800$.

4.5 Swirl Ratio

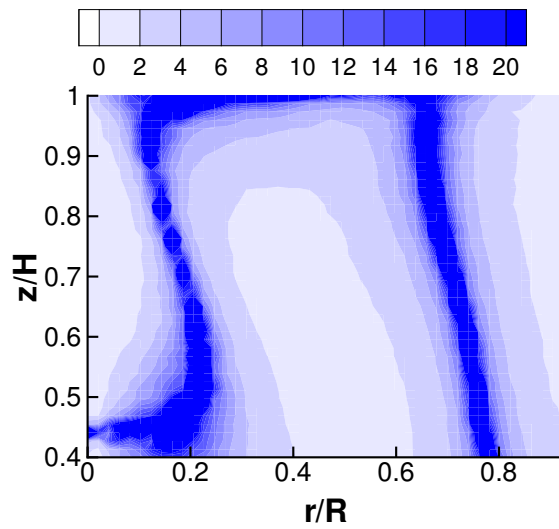
Along with downstream pressure gradient, the swirl level is crucial to the formation of Vortex Breakdown, as has been discussed in detail in the reviews by Lucca-Negro & O'Doherty (2001) and Leibovich (1978), for example. In open jets and swirling pipe flows, critical swirl numbers not only provide the threshold for vortex instability and vortex breakdown formation, but control the type of breakdown bubble which develops. For a free surface cylinder flow, a global swirl parameter is more difficult to define than in other mechanical devices because the upstream axial flow profile is spatially variable and the circulatory nature of the flow makes the upstream limit difficult to define. Consequently, H/R is used as the flow classification parameter, despite the fact that it is not a direct indicator of swirl. The distribution of swirl ratio $SR = |v_\theta|/|v_z|$ across the vessel volume is presented in the current section. A comparison across several cases is subsequently undertaken in order to determine the effect of Re on the swirl levels.

The measured SR distribution in the upper portion of the cylinder is presented in Figure 4.26 for $Re = 1200$ and $Re = 2400$. SR contour plots are useful for quantifying the flow geometry because, unlike the velocity components, the quantities within the inner flow region and the outer flow region are similar. When $v_z \rightarrow 0$, $SR \rightarrow \infty$, so the high-magnitude SR zones can be used to locate significant flow regions. For instance, slanted columns of high SR run through the centroid of the VB and outer recirculations, and therefore depict the orientation and position of both. Secondly, a high-magnitude SR zone illustrates the loss of axial momentum near the top surface. Thirdly, the high-magnitude SR denotes the stagnation zone immediately downstream of the breakdown region. Theoretically, $SR \rightarrow \infty$ at the free surface, however since no direct surface measurements were made, this may not be apparent in Figure 4.26.

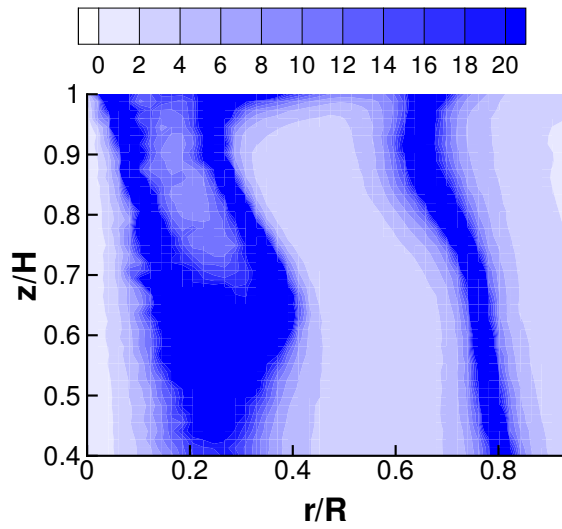
Because the recirculation motion, rather than a real loss of swirl, occasionally causes v_z to approach 0 and SR to approach infinity, the use of the ratio $|v_\theta|/|v_z|$ as a measure of swirl can be misleading. A superior approach is to define a modified swirl ratio:

$$SR_m = \frac{|v_\theta|}{\sqrt{v_r^2 + v_z^2}} \quad (4.1)$$

In Equation 4.1, the denominator represents the modulus of the velocity resolved in the meridional plane. Unlike SR , SR_m does not alter as axial momentum is transferred to radial momentum, and vice versa. It is clear from Figure 4.27 that the SR_m maps do not have a discontinuity corresponding to the $v_z = 0$ contour. Five cases are presented in the range $600 \leq$



(a)



(b)

Figure 4.26: Contours of swirl ratio, $SR = |v_\theta|/|v_z|$, at (a), $Re = 1200$; and (b), $Re = 2400$.

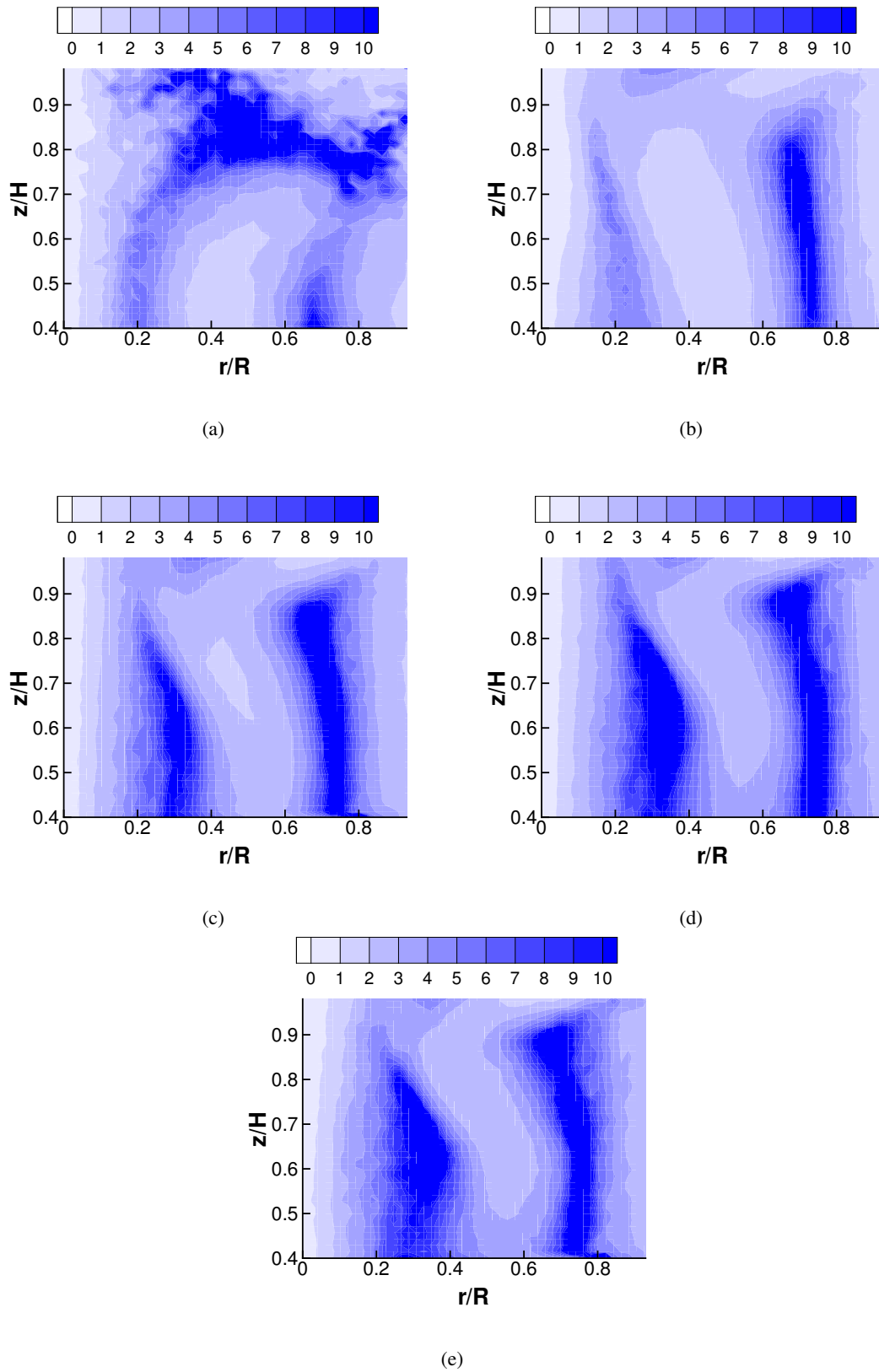


Figure 4.27: Contours of modified swirl ratio, SR_m , when (a), $Re = 600$; (b), $Re = 1200$; (c), $Re = 1800$; (d), $Re = 2400$; and (e), $Re = 3000$.

$Re \leq 3000$ at increments of 600. The only significant change in distribution occurs between $Re = 600$ and $Re = 1200$, i.e. before and after the onset of VB. At $Re = 600$, there is particularly high SR_m above the outer recirculation. The reason for this has been mentioned in Section 4.4; above the outer recirculation zone, the fluid appears quiescent in the meridional plane, however there is a slight azimuthal flow. The $Re = 600$ case has noisier regions than the other cases because the velocity vectors are of very low magnitude near the upper surface and the axis of symmetry.

Between $Re = 1200$ and $Re = 3000$ there is little alteration in the distribution of SR_m , despite the fact that the flow topology changes. The overall magnitude of SR_m , however, is strongly dependent on Re . A comparison between Figures 4.27(b) - (d) reveals that SR_m increases with Re in almost all regions of the flow. Between $Re = 2400$ and $Re = 3000$, (Fig. 4.27(e)), the levels of time-averaged SR_m do not increase significantly, if at all. It is worth remembering that the time-averaged flow topology also remains more constant in this Re range.

4.6 Temporal Variability

As discussed in Section 2.6.3, time-dependent behaviour has been reported at higher Re values for free surface cylinder flows. The unsteadiness, which has been detected as low as $Re = 1900$ for $H/R = 2.0$, may take the form of a low-energy rotating wave instability (Lopez *et al.*, 2004), or of a steady oscillation with twice the period of the disk (Young *et al.*, 1995). As the oscillations are of very low magnitude for the chosen experimental Re domain, the temporal variability of the flow structure appears too slight to be of consequence in cell and tissue culture applications, which generally have a timescale in the order of hours or days. However, the assumption of t -invariance is significant, and so a time series analysis has been undertaken.

The SPIV data was captured in a time series that lasted, depending on ω , between approximately 2 and 10 disk rotations. At relevant Re values ($Re \gtrsim 1900$), enough cycles were recorded to potentially capture any of the period doubling oscillations reported by Young *et al.* and the Nyquist frequency was sufficient to capture the strongest rotating waves reported by Lopez *et al.*, i.e. those of mode $k = 4$. Because the reported unsteadiness is stronger in certain regions of the vessel, a time series analysis was conducted at many different positions, however the results were similar at each. The four analysis points presented here represent positions in the four quadrants of the $r - z$ plane, and are listed in Table 4.1. UL represents the closest point to the VB recirculation.

Position	r/R	z/H
Upper Left (UL)	0.33	0.67
Upper Right (UR)	0.67	0.67
Lower Left (LL)	0.33	0.33
Lower Right (LR)	0.67	0.33

Table 4.1: Definition of the four positions used for the time series analyses.

The time series plots in Figure 4.28 include values of $|\mathbf{v}|$, the magnitude of the three-component velocity vector \mathbf{v} , normalised by impeller tip speed $u_{tip} = R\omega$. The time axis is normalised by T_d , the disk rotation period. The individual series represent time histories of velocity at a particular bioreactor location and Re . The data contain low-amplitude fluctuations, however there is no consistent periodicity or long-term gradient in the measurements. Spectral analysis confirms that the measured fluctuations do not include constant wavelength oscillations of significant strength. The spectral peaks barely exceed the background noise and do not

appear to match those of neighbouring points. The fluctuations in Figure 4.28 should therefore be attributed to experimental noise.

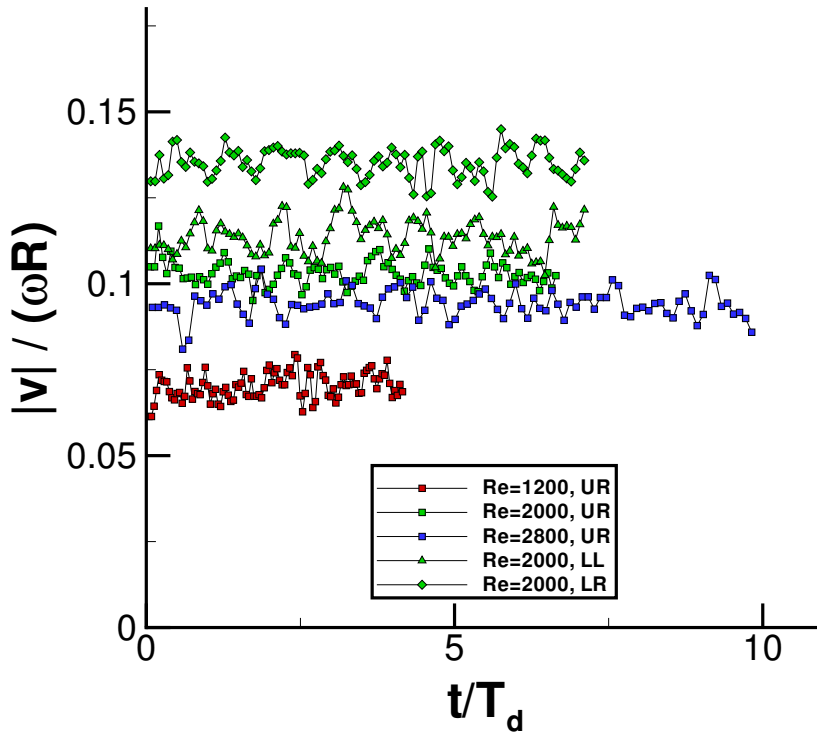


Figure 4.28: Measured time series profiles of $|v|/(\omega R)$. Symbol shape represents the spatial position of the measurement point, while symbol colour represents Re .

Despite the fact that the flow becomes progressively more unsteady as Re increases, the measured velocity fluctuation amplitude remains constant. As an illustration of this, the standard deviation of $|v|/(\omega R)$ is plotted against Re in Figure 4.29. Not only is the standard deviation (s.d.) relatively constant with respect to Re , but it is also independent of the analysis point location. If the fluctuations are due to physical flow unsteadiness rather than measurement uncertainty, then s.d. $|v|/(\omega R)$ would be expected to strongly increase with Re and to vary with respect to measurement location. While low amplitude, periodic fluctuations such as the rotating wave instabilities reported by Lopez *et al.* may exist, they could not be distinguished from the experimental noise.

As the flow has been verified as t -invariant to within the limitations of the measurement system, it is plausible to assume that it is t -invariant for the purposes of cell culture. This assumption is significant for two reasons. Firstly, it means that the measurements presented in Sections 4.3 - 4.5 approximately describe a steady flow, meaning that these time-averaged

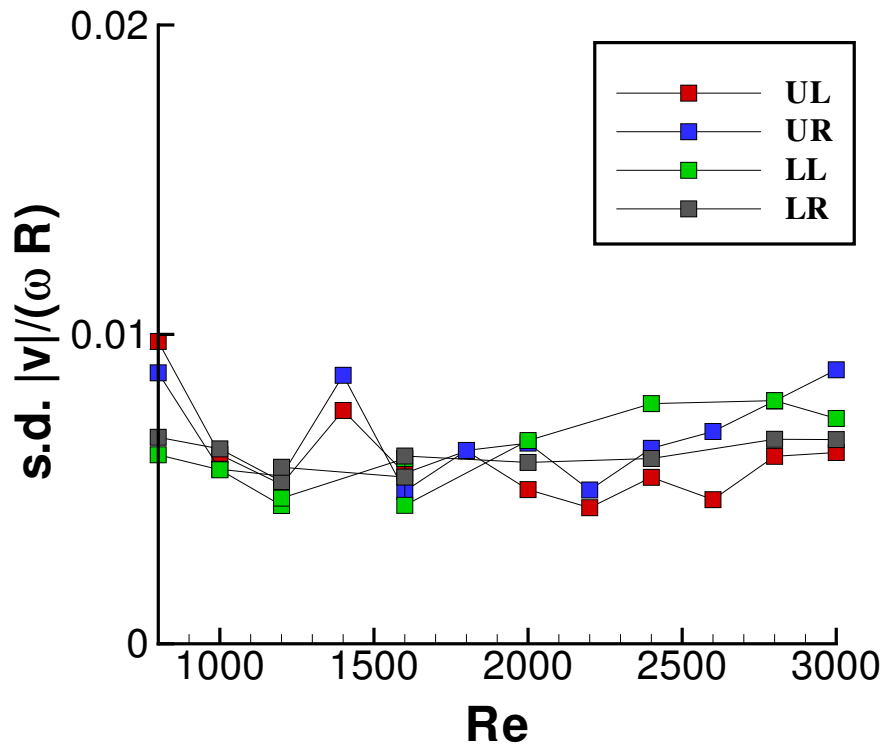


Figure 4.29: Standard deviation of $|v|/(\omega R)$ at different Re values. Symbol colour represents spatial position of the measurement point.

results can be assumed to describe the instantaneous flow field at any point in time. Secondly, it means that gradients in the azimuthal plane can be assumed to be negligible and that consequently all three three-component principal stress vectors can be derived (see Section 4.7). As an indication, the azimuthal stresses derived from the measured velocity fluctuations have an estimated upper limit of $\tau_{\theta\theta}/(\mu\omega) \approx 3 \times 10^{-2}$, although the typical values are much lower in magnitude. As the following section illustrates, the level of uncertainty this represents in the overall stress measurements is not excessive.

It should be remembered that the standard deviations recorded in Figure 4.29 are reasonable for a SPIV system, as care has been taken to minimise and quantify measurement uncertainty. We can therefore be confident that large temporal variance is not being hidden by excessive inaccuracies in the measurement technique. Conveniently, the measured fluctuations provide an upper limit of the Reynolds stresses in the vessel. As expected, these are several orders of magnitude below the mean viscous stresses.

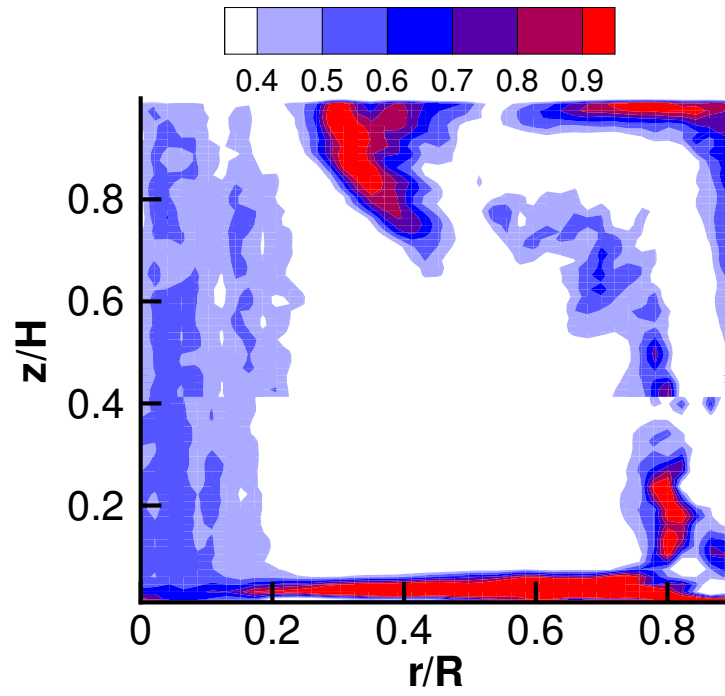
4.7 Principal Stress Fields

As the velocity fields are adequately resolved, it is possible to derive the stress tensor at a particular location in the measurement plane. A combination of the upper and lower measurement fields covers as much of the meridional plane as can reliably be measured using SPIV. As the stress vectors contain substantial information, Section 4.7 is broken into several subsections. In Subsections 4.7.1 and 4.7.2, the distribution of stress magnitude is presented in detail, including any Re dependency. In Subsection 4.7.3 the focus is on the direction in which the stresses act.

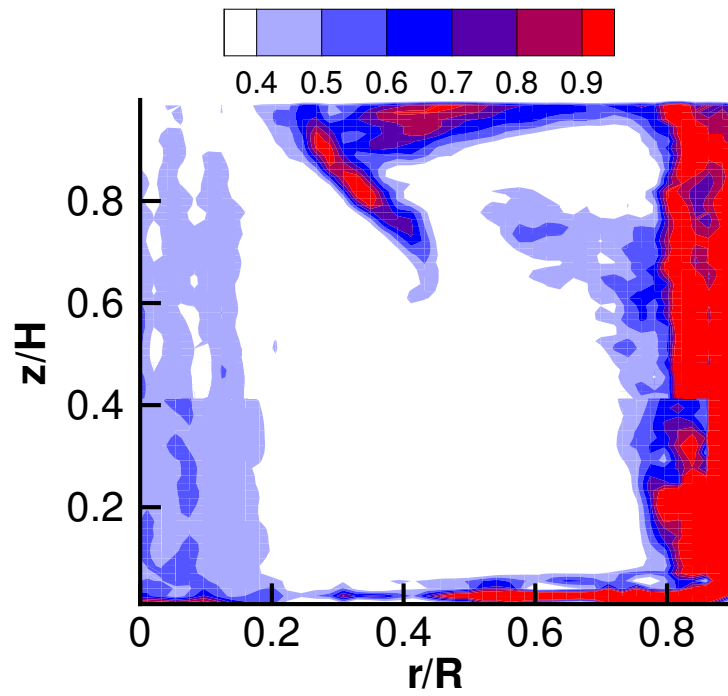
To progress with calculating the principal stresses from the three-dimensional stress tensor \mathcal{T} , all nine spatial velocity gradients need to be resolved. Standard SPIV only facilitates the measurement of six of these, i.e. those in the r and z directions. To complete \mathcal{T} , an assumption is made regarding the remaining three gradients, i.e. those along the azimuthal axis. An approximate flow symmetry has been demonstrated with flow visualisation images and a comparison of quantitative measurements on opposite halves of the vessel, e.g. Figure 4.24. In Section 4.6, the fluctuations in velocity with respect to time were shown to be negligible. It is therefore reasonable to assume that, for the purpose of the stress field estimate, the flow is steady and axisymmetric over the Re domain. In other words, that the three velocity gradients along the azimuthal axis are negligible in comparison with the six velocity gradients across the meridional plane. This validates the derivation of \mathcal{T} , from which it is possible to obtain all the information pertaining to the viscous stress acting on a fluid element or a cell being transported along a streamline.

4.7.1 Stress Magnitudes: Full Field

Figure 4.30 illustrates the distribution of the two most important principal stress magnitudes, non-dimensionalised by the product $\mu\omega$, at $Re = 2400$. The entire meridional plane is shown, as results from the upper and lower data sets are combined in each plot. σ_1 , presented in Figure 4.30(a), corresponds to the principal compressive stress acting on the fluid element, while σ_3 , in Figure 4.30(b), represents the principal tensile stress. σ_1 and σ_3 are distributed similarly, yet not identically. The remaining principal stress component, σ_2 , is typically much closer to 0 than σ_1 or σ_3 . σ_2 constitutes the difference $(\sigma_3 - \sigma_1)$, which allows satisfaction of the continuity criterion since σ_1 is compressive and σ_3 is tensile. The three principal stresses act along orthogonal axes, the directions of which vary with respect to spatial position in the bioreactor. These ‘principal axes’ are presented in Section 4.7.3. σ_2 is not presented in detail



(a)



(b)

Figure 4.30: Distribution of (a), $\sigma_1/(\mu\omega)$; and (b), $\sigma_3/(\mu\omega)$; across the right hand side of the meridional plane when $Re = 2400$.

here because its magnitude is insignificant compared to σ_1 and σ_3 , and its distribution does not illustrate important stress regions within the bioreactor. Despite σ_3 and σ_1 having slightly different distributions, the two plots in Figure 4.30 have some common features. In particular, in both cases the largest stresses seem to be located in three regions - along the surface of the disk, along the cylinder sidewall, and along the boundary of the VB bubble.

As with most other impeller-driven bioreactors (see Doran (1999)), high stresses are induced in the vicinity of the impeller. In the current vessel, the maximum stresses occur at the perimeter of the impeller, where the fluid being spun radially outward is turned abruptly upward by the cylinder wall, coinciding with the occurrence of an azimuthal jet. The high stresses along the side and bottom surfaces are the result of boundary layer shearing. This shearing is weaker along the upper portion of the sidewall, where much of the strong azimuthal and axial momentum has been dispersed, and near the free surface, which does not have a three-dimensional no-slip condition. The stress peak near the boundary of the VB region coincides with the interface of the counter-rotating recirculation regions, and is analysed in detail in Subsection 4.7.2.

Within the centre of the vortex breakdown region, the stresses are substantially lower than the peak stress regions. Particles or cells trapped within a VB bubble are, on average, subjected to a consistent, low-magnitude stress, whereas particles or cells trapped in the outer recirculation region are subjected to a greater variety of stress conditions. They may also experience a much higher peak stress, which occurs as they travel past the Ekman layer and through the bottom corner of the cylinder.

It is possible to convert the principal stresses to maximum shear stresses using Equations 2.5a - 2.5c. The largest of the maximum shear stresses is $\tau_{max,2}$, which is directed at an angle of 45° to both σ_1 and σ_3 . $\tau_{max,2}$ peaks in the zones where both σ_1 and σ_3 are of large magnitude. The maximum shear stresses are not plotted here as they have a similar distribution to the principal stress magnitudes and can be easily deduced from the results in this chapter.

4.7.1.1 Comparison with Numerically Derived Stress Fields

As the stress values are derived from six measured velocity derivatives, they contain a higher degree of uncertainty than the velocity measurements. To help validate their accuracy, the stress fields are compared to a set of principal stress distributions calculated from a numerical flow simulation conducted by Dr. B.T. Tan at Monash University. The flow was modelled by solving the incompressible time-dependent Navier-Stokes equation in cylindrical coordinates using a

spectral element code with a second-order accurate time splitting technique. This technique has been validated and has been applied extensively to other problems (Thompson *et al.* , 1996, 2001; Sheard *et al.* , 2003). As the flow is nearly axisymmetric, a two-dimensional 18×22 macro-element mesh was used, more concentrated toward the bottom and side walls where there are larger gradients. Each macro-element contained a further 10×10 computational nodes. To test that the solutions were adequately resolved, a single simulation was performed using higher order elements containing 13×13 computational nodes and a smaller time step. The difference between the two simulations of any velocity component at any node did not exceed 0.1% of the maximum azimuthal velocity component.

The experimental and numerical results are contrasted in Figures 4.31 and 4.32. All plots share the same contour levels, spatial domain, and axis scaling. The two comparisons presented here represent just a small sample of the cases for which numerical validation was undertaken. In addition, all three principal stresses, rather than just σ_3 , were compared in this manner. No major discrepancies between the numerical and experimental results are observed, although the additional measurement error near the axis of symmetry and the measurement boundaries results in marginally higher experimental uncertainty at these locations.

The three peak stress regions are reproduced in both the experimental and numerical results. Furthermore, the geometries of these peak stress regions are similar. In particular, the computationally derived stress distribution near the bottom corner of the vessel has a strong resemblance to that derived by experimental means. The σ_3 distributions in the vicinity of the VB zone are also similar; significantly, the slanted peak stress region is a common feature of both plots.

This third peak stress region is weaker at $Re = 1200$ than at $Re = 2400$, and so barely registers on either of the σ_3 plots shown in Figure 4.32. In general, the normalised σ_3 levels decrease in the upper half of the vessel and there is an increase in thickness of the bottom and sidewall stress layers. All of these differences between the higher and lower Re cases are observed in both the experimental and numerical results.

4.7.1.2 Stress Profile Comparison

The influence of Re on the principal stress distribution is illustrated to best effect by comparing radial profiles corresponding to each case. Problematically, the calculated σ values contain higher noise levels than the time-averaged velocity or circulation, making it more difficult to analyse the differences between each profile. To alleviate this problem, curves were gener-

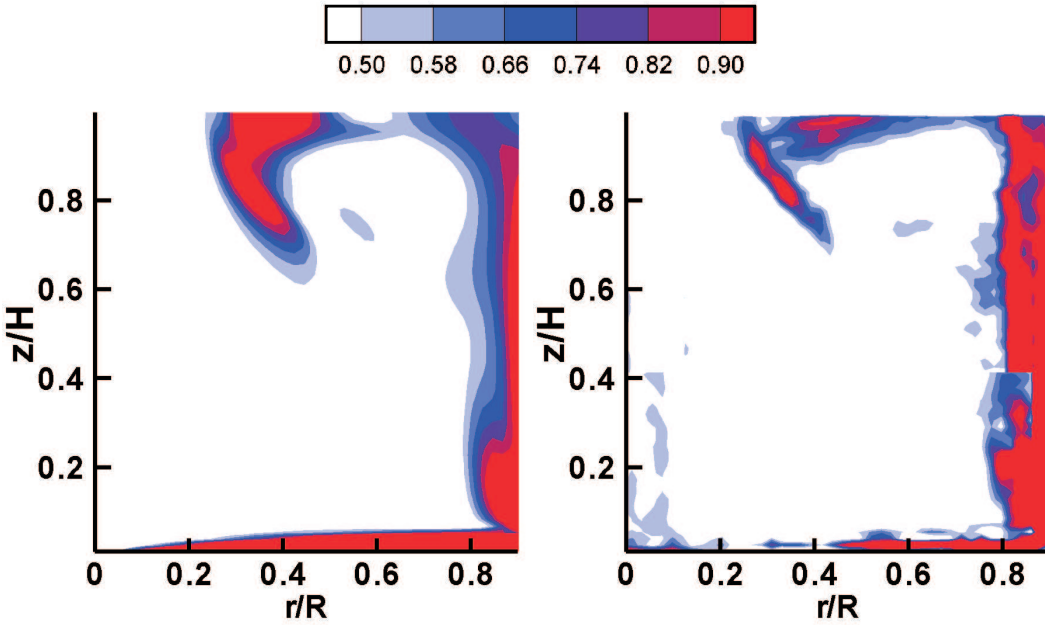


Figure 4.31: Distribution of $\sigma_3/(\mu\omega)$ across the right hand side of the meridional plane when $Re = 2400$. The left-situated contour plot was numerically derived. The right-situated plot shows experimental measurements.

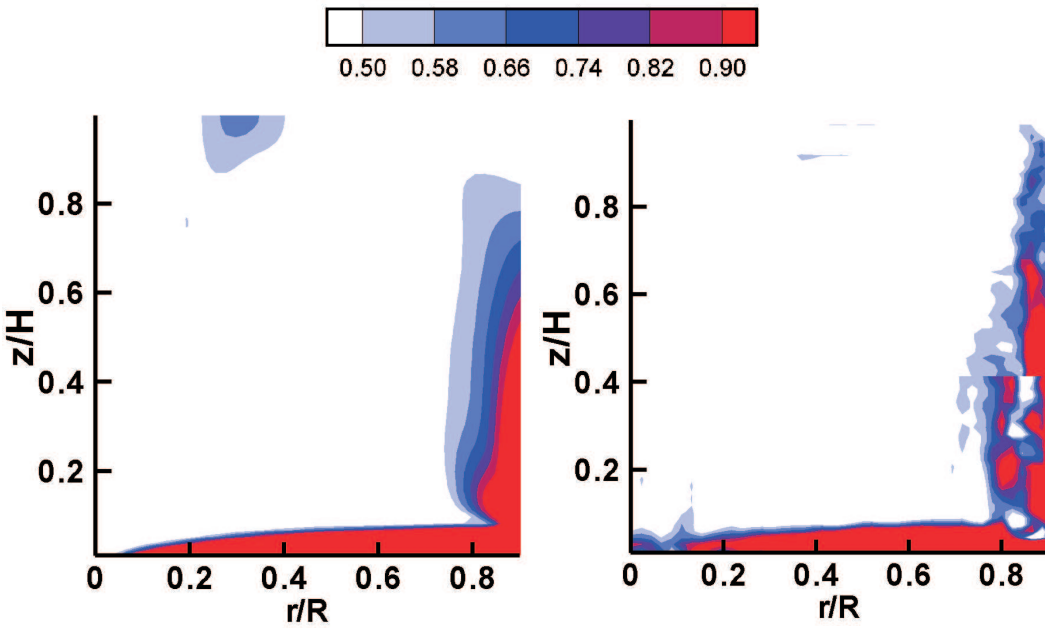


Figure 4.32: Distribution of $\sigma_3/(\mu\omega)$ across the right hand side of the meridional plane when $Re = 1200$. The left-situated contour plot was numerically derived. The right-situated plot shows experimental measurements.

ated by applying a high-order polynomial fit to the data in the domain $0.2 \leq r/R \leq 0.9$. The data in the region $r/R < 0.2$ were omitted from consideration because of the especially large

uncertainties associated with determining \mathcal{T} near the axis of symmetry. The success of the high-order polynomial functions as a fit for the σ data is demonstrated in Figure 4.33. The series of measurement points represents a radial profile of σ_3 at $z/H = 0.50$ for the $Re = 1400$ case, i.e. roughly in the middle of the parameter space. In this particular case, the curve is mostly flat for $r/R \lesssim 0.6$, although there is a minimum point at $r/R \approx 0.52$. As r increases, the curve rises steeply to a maximum at $r/R \approx 0.75$. It is clear from Figure 4.33 that the minimum and maximum points are not erroneous, but rather reflect the trend observed in the measured σ_3 values. Peaks similar to the maximum at $r/R \approx 0.75$ occur at all other Re in the VB regime. These coincide with the abrupt change of flow direction across the $v_z = 0$ contour of the outer recirculation region, as well as the strong increase in v_θ associated with its jet-like profile. The numerical simulations and theory suggest that the stresses are also strong as $r \rightarrow R$, however the stress tensors in the region $0.90 \leq r/R \leq 1.0$ could not be resolved experimentally as excessive image refraction prevented SPIV measurements near the sidewall.

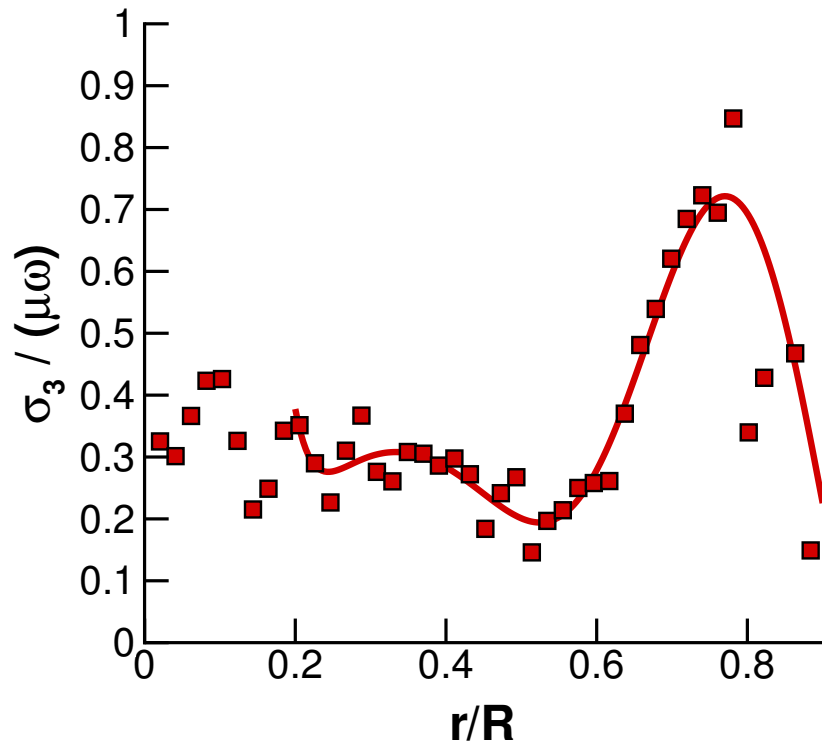


Figure 4.33: Radial profile of $\sigma_3/(\mu\omega)$ at $z/H = 0.50$, when $Re = 1400$.

As with the axial velocity and circulation profiles, shown respectively in Subsections 4.4.1 and 4.4.2, the degree to which Re affects the stress profiles is dependent on z/H . Figures 4.34 - 4.36 include profiles of σ_1 and σ_3 at axial positions of $z/H = 0.09$, $z/H = 0.50$, and

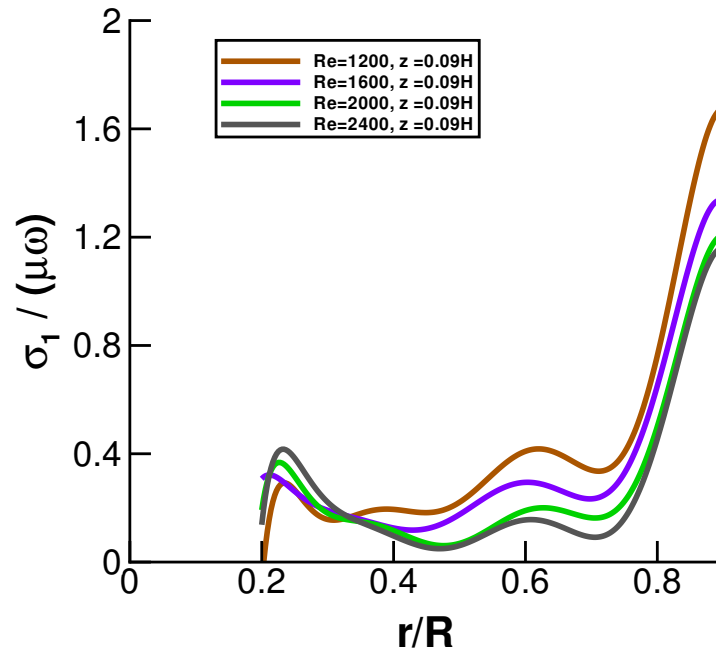
$z/H = 0.77$. The curve colouring is consistent across all the plots and is based on Re . At $z/H = 0.09$, (Fig. 4.34), the profiles are fairly similar. There are large σ_1 and σ_3 peaks near the outer radius, corresponding to the high stress region near the interface of the impeller and the sidewall. The magnitude of both $\sigma_1/(\mu\omega)$ and $\sigma_3/(\mu\omega)$ over the region $r/R \gtrsim 0.3$ decreases slightly with an increase in Re . This is associated with a gradual narrowing of the high stress region situated next to the impeller. This narrowing is consistent with theory, which states that for constant v , Ekman boundary thickness decreases as ω increases (see also Equation 2.30).

Figure 4.35 includes the σ_1 and σ_3 profiles at $z/H = 0.50$. The scale on the vertical axis is reduced from that of Figure 4.34 because the maximum value is much lower. The peak stresses shown here are nearer to the outer radius of the vessel than to the central region, however they do not reflect the sidewall boundary layer. The σ_1 peak is less obvious than the σ_3 peak, except at higher Re values, where the two peaks are of similar magnitude.

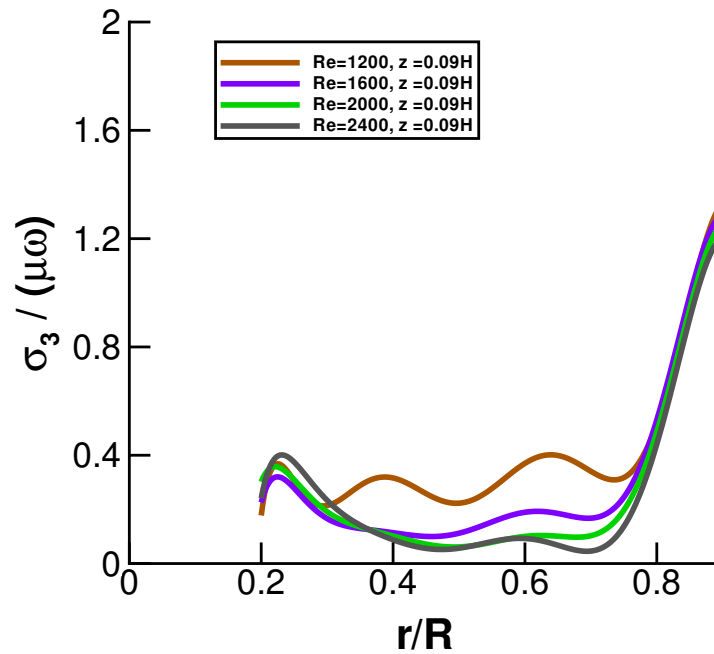
At $z/H = 0.77$, (Fig. 4.36), the σ_1 and σ_3 peaks near the outer region of the bioreactor are of even more diminished magnitude. For most cases, the largest peaks are those associated with the VB region. The exceptions include $Re = 600$, for which there is very little fluid deformation at this distance above the impeller, and $Re = 800$, for which the VB region is located within $r/R \leq 0.20$, meaning that the σ_1 and σ_3 peaks are outside the analysis zone. Compared with the other peak stress regions, the peak region near the VB boundary is highly dependent on Re . As this high stress zone may be of particular concern in the context of potential cell culture involving VB bubbles, it is analysed more comprehensively in Subsection 4.7.2.

4.7.2 Stress Magnitudes: Vortex Breakdown Region

Much of the normalised stress field illustrated in the $Re = 2400$ example (Fig. 4.30), is similar at other Re , however the distribution in the vicinity of the VB region exhibits some Re -dependency. A high stress region is consistently located along the upper edge of the bubble, and because the geometry and position of the VB region changes with Re , so too does the geometry and position of the stress region. In Figure 4.37, normalised σ_3 contours are presented at $Re = 1200$, $Re = 1800$, $Re = 2400$ and $Re = 3000$, on one side of the plot only. On the opposite side of each plot, the meridional plane vectors are shown. The left hand side of the plot represents the region $-0.58 \leq r/R \leq 0$, and the right hand side represents $0 \leq r/R \leq 0.58$, meaning that the $r - z$ space in the contour plot is a z -axis reflection of the $r - z$ space in the vector plot. Presenting the data in this manner facilitates a comparison between the stress distribution and the flow structure in the VB region. It is evident just from Figure 4.37 that the

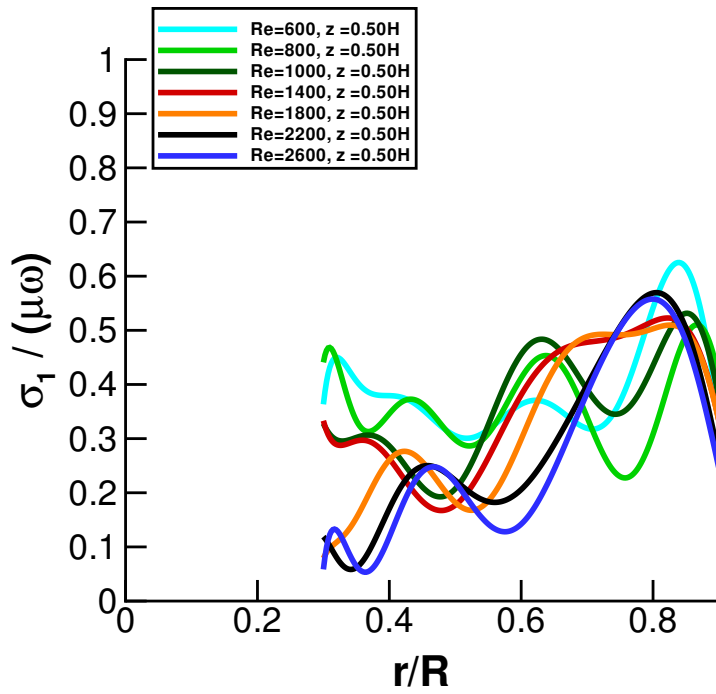


(a)

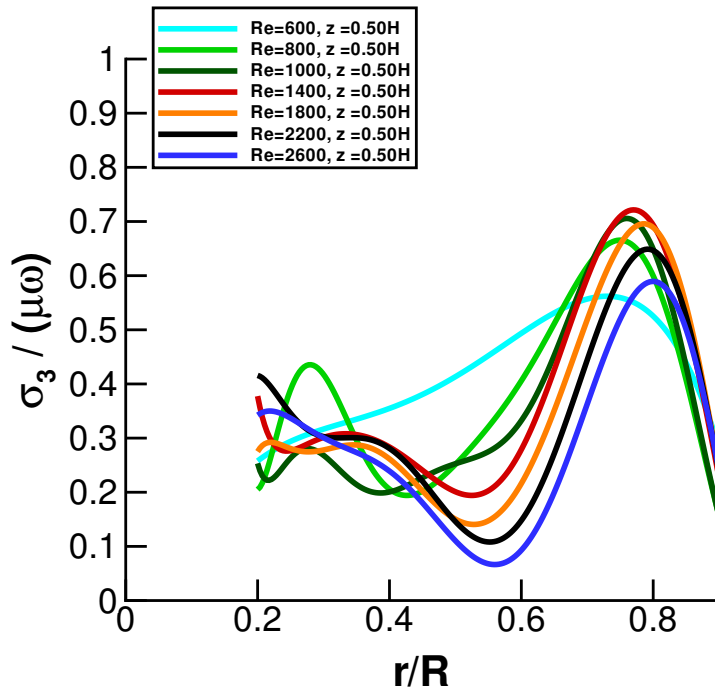


(b)

Figure 4.34: Radial profiles of (a), $\sigma_1/(\mu\omega)$; and (b), $\sigma_3/(\mu\omega)$; at $z/H = 0.09$. The different curves correspond to different Re values.

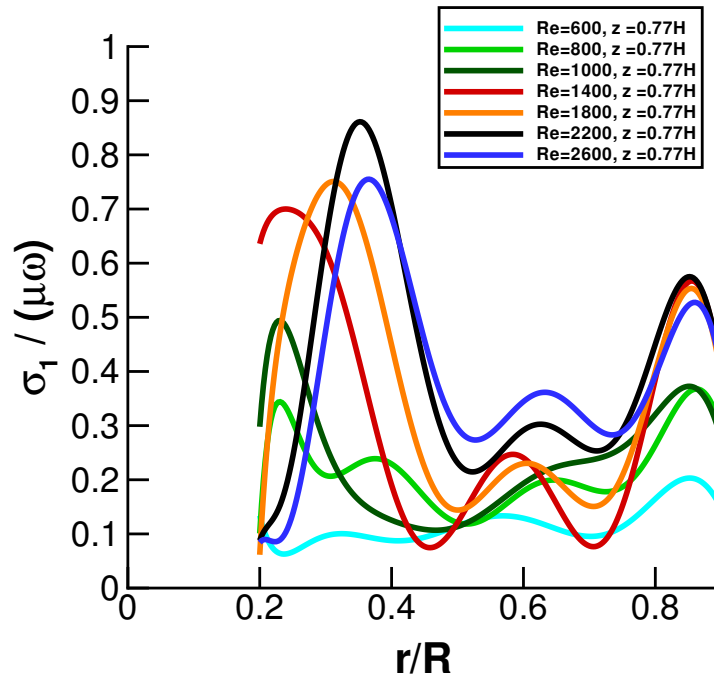


(a)

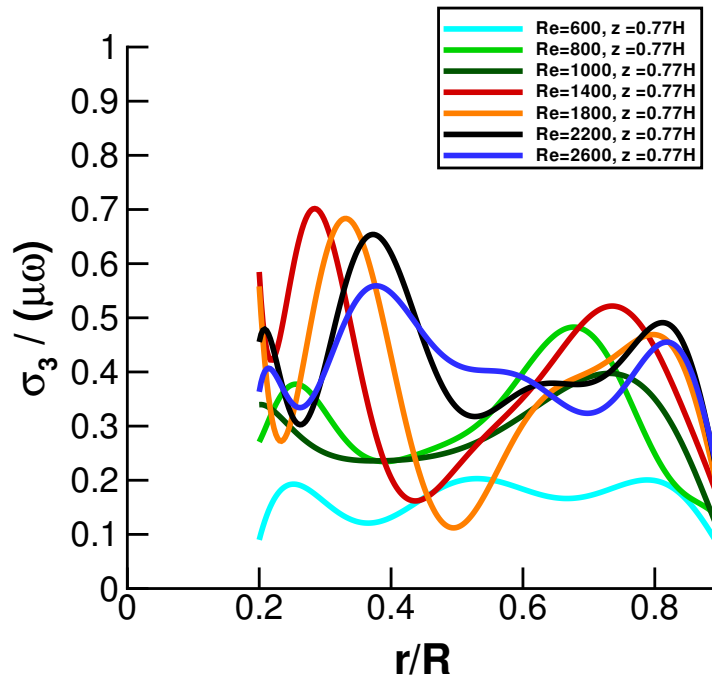


(b)

Figure 4.35: Radial profiles of (a), $\sigma_1 / (\mu\omega)$; and (b), $\sigma_3 / (\mu\omega)$; at $z/H = 0.50$. The different curves correspond to different Re values.



(a)



(b)

Figure 4.36: Radial profiles of (a), $\sigma_1/(\mu\omega)$; and (b), $\sigma_3/(\mu\omega)$; at $z/H = 0.77$. The different curves correspond to different Re values.

slanted high stress band is located where the VB recirculation and the outer recirculation are directly adjacent to one another.

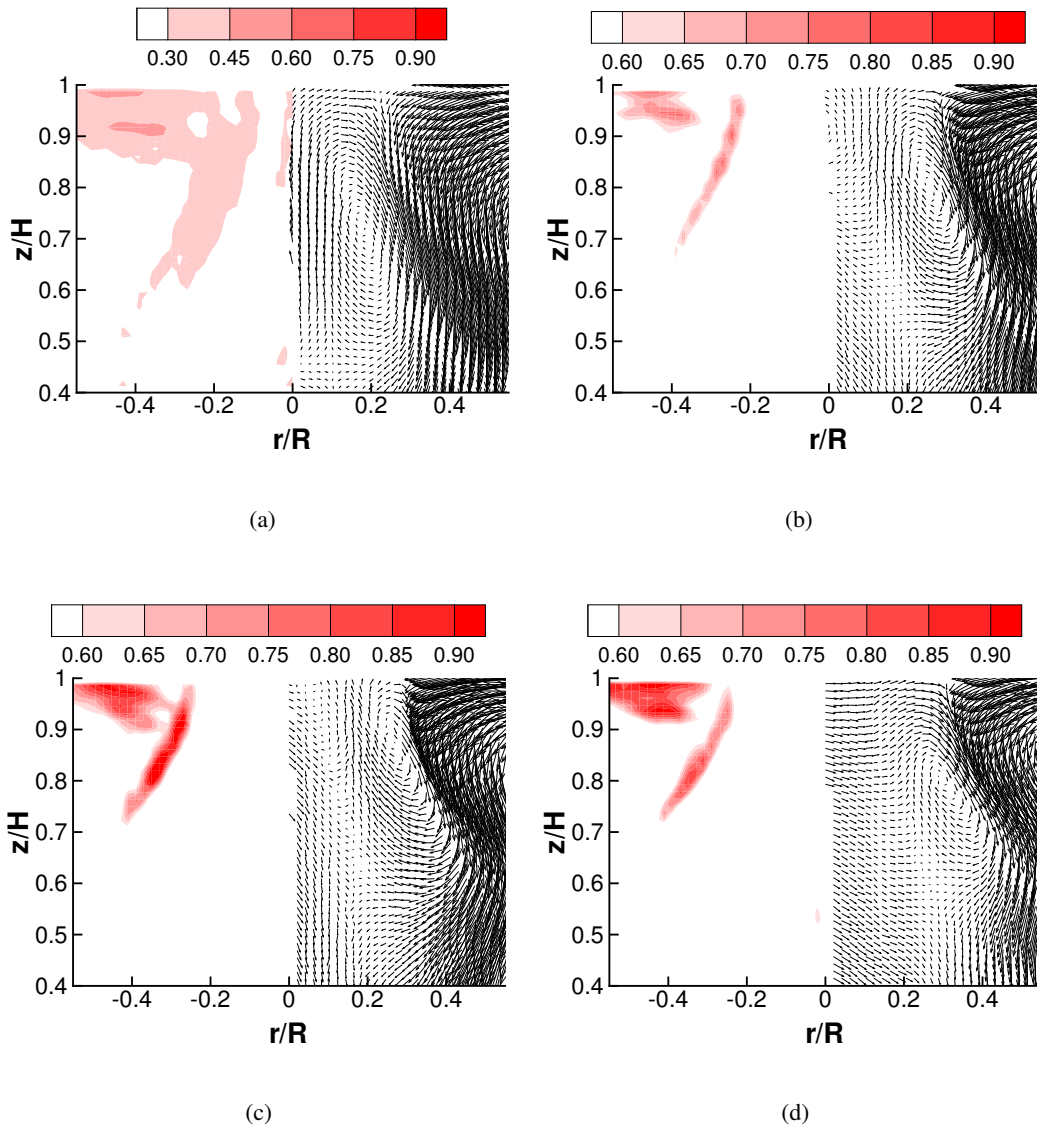


Figure 4.37: Contours of $\sigma_3/(\mu\omega)$ (left-hand side) with in-plane velocity vectors (right-hand side), for (a), $Re = 1200$; (b), $Re = 1800$; (c), $Re = 2400$; and (d), $Re = 3000$.

The plotted contours show a consistent and distinct pattern that evolves, as Re increases, in a manner related to changes in flow topology. At $Re = 1200$, where the VB region is limited to low r/R , the high stress band is closer to the central axis than the other cases, and is of such low magnitude as to require much reduced contour levels. As Re increases between $Re = 1200$ (Fig. 4.37(a)) and $Re = 2400$ (Fig. 4.37(c)), the VB boundary high stress region moves radially outward and becomes more slanted, reflecting a change in the VB recirculation geometry. There is also an increase in the magnitude of the peak stresses in this region, which is indicative of an

increase in the velocity gradients at the VB boundary. The difference between the $Re = 2400$ and $Re = 3000$ plots is not so marked. It has already been shown in this chapter that the time-averaged flow topology stabilises at these higher Re values. Correspondingly, the σ_3 distribution remains relatively unchanged between $Re = 2400$ and $Re = 3000$.

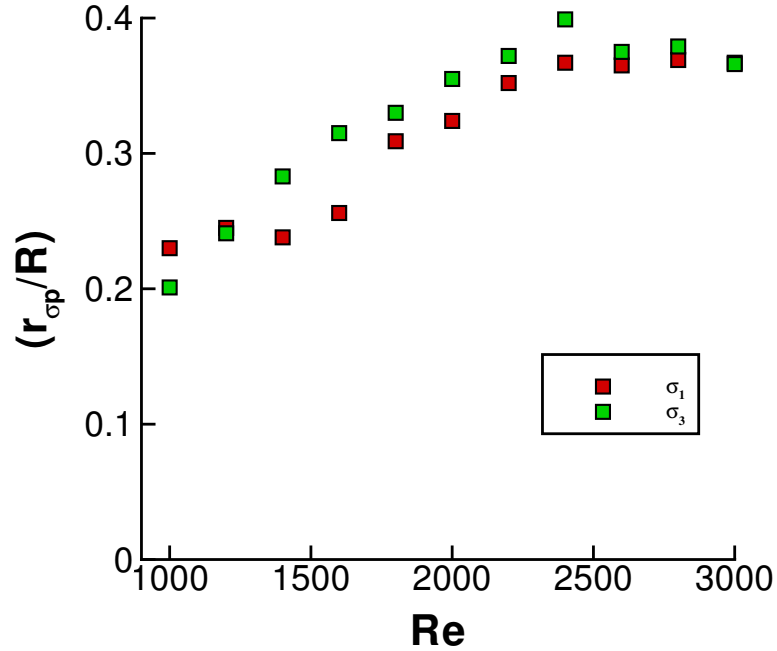


Figure 4.38: Location of the σ_1 and σ_3 maximum values in the VB boundary high stress region, on radial profiles at $z/H = 0.77$. $r_{\sigma p}/R$ values were identified using high order polynomial curve fitting.

The seemingly asymptotic nature of the stress distribution is emphasised by Figure 4.38, which presents $r_{\sigma p}$, the radial position of the peak stress at $z/H = 0.77$, as a function of Re . $r_{\sigma p}$ is plotted for both σ_1 and σ_3 , although the trends for these two principal stress components are similar. The measurement corresponding to $Re = 800$ is omitted because the peak stress is weak and lies within the noise-affected region surrounding the axis of symmetry. $r_{\sigma p}$ increases steadily in the region $1000 \leq r/R \leq 2200$ and then plateaus for $2200 \leq r/R \leq 3000$. A cross-section at $z/H = 0.77$ was chosen to measure $r_{\sigma p}$, as this roughly corresponds to the vertical centre of the VB recirculation. Similar trends of $r_{\sigma p}$ as a function of Re were observed at other axial positions.

Further tests were carried out to determine whether the average stress level in the VB region increases as a function of Re . SPIV measurements were undertaken on the region bounded by $0.6 \leq z/H \leq 0.9$ and $-0.45 \leq r/R \leq 0.45$, from which the spatially-averaged principal

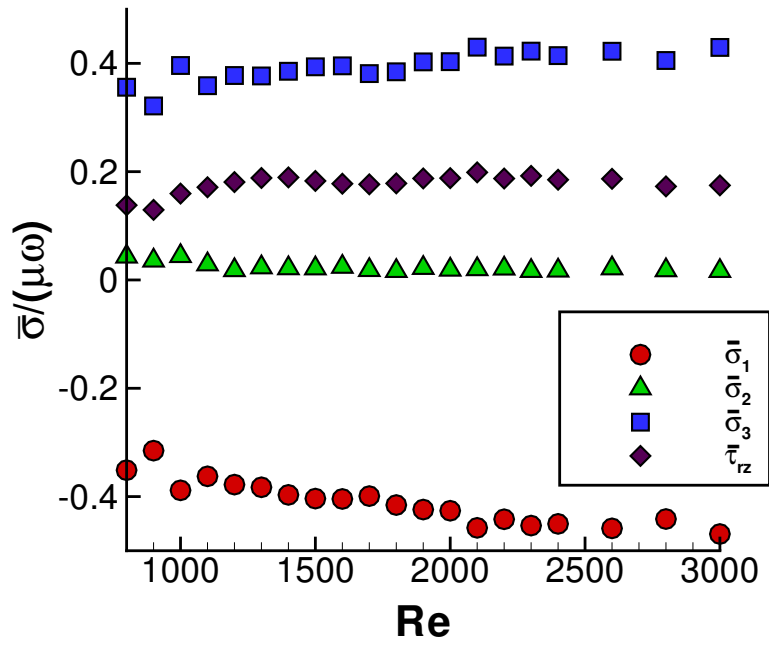


Figure 4.39: Stress magnitudes averaged over the region bounded by $0.6 \leq z/H \leq 0.9$ and $-0.45 \leq r/R \leq 0.45$, plotted as a function of Re . The different curves correspond to different stress components. For clarity, $\bar{\sigma}_1$ values are of opposite sign to $\bar{\sigma}_3$ values.

stresses, designated by $\bar{\sigma}_1$, $\bar{\sigma}_2$, and $\bar{\sigma}_3$, were derived and plotted against Re , as in Figure 4.39. The meridional plane shear stress component, $\bar{\tau}_{rz}$, is included in the plot in order to quantify its contribution to the overall stresses. $\bar{\sigma}_1$ is plotted below the horizontal axis for clarity and as a reminder that the stress mode is opposite to that of $\bar{\sigma}_3$. $\bar{\sigma}_1$ and $\bar{\sigma}_3$ appear to gradually increase with Re , although the strength of the trend is slight, especially compared with the Re -dependency shown in Figures 4.37 and 4.38. It is also impossible to detect any strong relationship between $\bar{\tau}_{rz}$ and Re in Figure 4.39. The magnitude of $\bar{\sigma}_2$ remains negligible over the entire Re domain. Despite the inability to locate any significant trends from Figure 4.39, the plot remains an important result as it indicates that the average stress experienced by cells randomly distributed through the upper breakdown region will remain constant despite an increase in the intensity of the VB boundary stresses with Re .

4.7.3 Principal Axes

As described in Section 2.3.1, the principal stresses are the normal stress components corresponding to when \mathcal{T} is oriented such that the shear components are equal to zero. σ_1 and σ_3 are, respectively, the maximum normal compressive and tensile stress acting on an element at a particular point in space, and are directed perpendicular to one another. The maximum shear stress acts at an angle of 45° to both σ_1 and σ_3 . The directions of σ_1 , σ_2 and σ_3 , (or, for that matter, $\tau_{max,1}$, $\tau_{max,2}$ and $\tau_{max,3}$), vary across the measurement plane. For a sophisticated culture application, it may be desirable to predict the directions in which stresses act on a suspended cell, rather than merely the magnitude of these stresses. In this respect, knowledge of the principal axes is particularly beneficial.

It is straightforward to derive the principal axes from \mathcal{T} , however their presentation in graphical form is complicated by the fact that each has an r , z , and θ component. For example, the principal axis corresponding to σ_1 is represented by $\hat{\sigma}_1 \cdot \mathbf{i}$, $\hat{\sigma}_1 \cdot \mathbf{j}$ and $\hat{\sigma}_1 \cdot \mathbf{k}$, the unit vector resolved in the r , z , and θ directions respectively. Subsection 4.7.3 includes the distribution of the principal axis unit vectors $\hat{\sigma}_1$ and $\hat{\sigma}_3$ when $Re = 1200$ and $Re = 2400$.

4.7.3.1 $Re=1200$, $\hat{\sigma}_1$

Figure 4.40 illustrates the $\hat{\sigma}_1$ distribution when $Re = 1200$. The vectors represent $\hat{\sigma}_1$ resolved in the meridional plane. Note that $\hat{\sigma}_1$ also acts in the direction opposite to the vectors shown. For example, if $\hat{\sigma}_1 = 0.5\mathbf{i} + 0.5\mathbf{j}$, then $\hat{\sigma}_1 = -0.5\mathbf{i} - 0.5\mathbf{j}$ also describes the principal axis projected onto the meridional plane. The length of the vectors indicates the relative strength of the in-plane component. Figure 4.40 includes three plots, which quantify the alignment of $\hat{\sigma}_1$ with

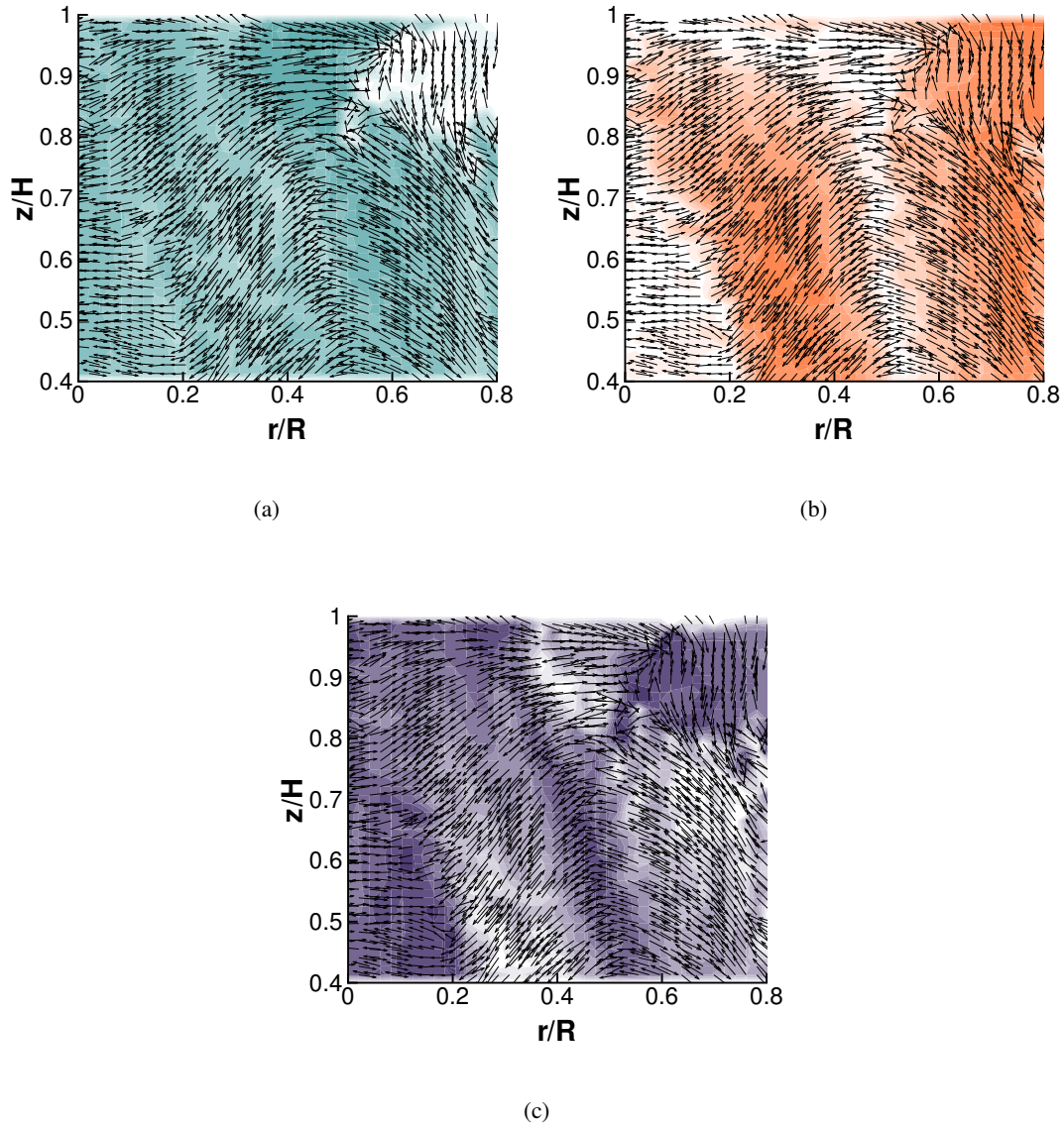


Figure 4.40: Spatial distribution of principal stress unit vector $\hat{\sigma}_1$ when $Re = 1200$. Vectors represent $\hat{\sigma}_1$ resolved on the meridional plane. Coloured contours represent levels of (a), $\hat{\sigma}_1 \cdot \mathbf{i}$; (b), $\hat{\sigma}_1 \cdot \mathbf{j}$; and (c), $\hat{\sigma}_1 \cdot \mathbf{k}$, on a scale from 0 (lightest shading) to 1 (darkest shading).

each of the cylinder axes. Where $\hat{\sigma}_1 \cdot \mathbf{k}$ is large relative to $\hat{\sigma}_1 \cdot \mathbf{i}$ and $\hat{\sigma}_1 \cdot \mathbf{j}$, σ_1 is more perpendicular to the $r-z$ plane than aligned with it. For ease of analysis, the contour levels are constant for all of these plots and all of the $\hat{\sigma}_1$ and $\hat{\sigma}_3$ plots shown hereafter. The contour colouring is such that a darker shading represents a value closer to 1 while a lighter shading denotes a value closer to 0.

The radial component of $\hat{\sigma}_1$ is the most consistent (Fig 4.40(a)). For most of the plane, $\hat{\sigma}_1 \cdot \mathbf{i}$ is of moderate strength, which means that the principal axes are rarely in alignment with the cylinder axes. It is only near the top corner, where the outer recirculating flow turns radially inward, that $\hat{\sigma}_1 \cdot \mathbf{i}$ is close to 0. However, as the fluid approaches the VB region, the compressive stresses become oriented toward the radial axis, which is illustrated by a region of high $\hat{\sigma}_1 \cdot \mathbf{i}$ immediately adjacent to the low $\hat{\sigma}_1 \cdot \mathbf{i}$ region. In the remainder of the measurement plane, $\hat{\sigma}_1$ alternates between having a relatively strong axial component and a weak azimuthal component, and having a strong azimuthal component and a weak axial component. The distribution of these components resembles the geometry of the flow structure. The regions where $\hat{\sigma}_1$ acts more in the axial direction, i.e. where $\hat{\sigma}_1 \cdot \mathbf{j}$ is large and $\hat{\sigma}_1 \cdot \mathbf{k}$ is small, include the right hand side of the VB recirculation and the right hand side of the outer recirculation. Interestingly, the fluid is transported in the negative axial direction in the right hand side of the VB recirculation and in the positive axial direction in the right hand side of the outer recirculation. The regions where $\hat{\sigma}_1$ acts more in the azimuthal direction, i.e. where $\hat{\sigma}_1 \cdot \mathbf{k}$ is large and $\hat{\sigma}_1 \cdot \mathbf{j}$ is small, include the near-axis side of the VB recirculation and the left hand side of the outer recirculation.

4.7.3.2 Re=1200, $\hat{\sigma}_3$

Because the unit vector $\hat{\sigma}_3$ is perpendicular to $\hat{\sigma}_1$, Figure 4.41 is not completely dissimilar to Figure 4.40. The extent to which $\hat{\sigma}_3 \cdot \mathbf{i}$, $\hat{\sigma}_3 \cdot \mathbf{j}$, and $\hat{\sigma}_3 \cdot \mathbf{k}$ differ from $\hat{\sigma}_1 \cdot \mathbf{i}$, $\hat{\sigma}_1 \cdot \mathbf{j}$, and $\hat{\sigma}_1 \cdot \mathbf{k}$ in each of these regions depends on how closely the principal axes align with the cylinder axes. For example, $\hat{\sigma}_3 \cdot \mathbf{i} \approx 0$ and $\hat{\sigma}_3 \cdot \mathbf{j} \approx 1$ at the top left hand side of the outer recirculation region, whereas $\hat{\sigma}_1 \cdot \mathbf{i} \approx 1$ and $\hat{\sigma}_1 \cdot \mathbf{j} \approx 0$ in the same region. In the remainder of the measurement plane, $\hat{\sigma}_1 \cdot \mathbf{i}$ is consistently of moderate strength, which means that $\hat{\sigma}_1$ is tilted toward r . $\hat{\sigma}_3 \cdot \mathbf{i}$ is similarly of moderate strength outside the top of the outer recirculation region, indicating that the principal axes are not in close alignment with the cylinder axes. Therefore, the differences between $\hat{\sigma}_3 \cdot \mathbf{j}$ (Fig. 4.41(b)) and $\hat{\sigma}_1 \cdot \mathbf{j}$ (Fig. 4.40(b)), and between $\hat{\sigma}_3 \cdot \mathbf{k}$ (Fig. 4.41(c)) and $\hat{\sigma}_1 \cdot \mathbf{k}$ (Fig. 4.40(c)), are moderate rather than extreme.

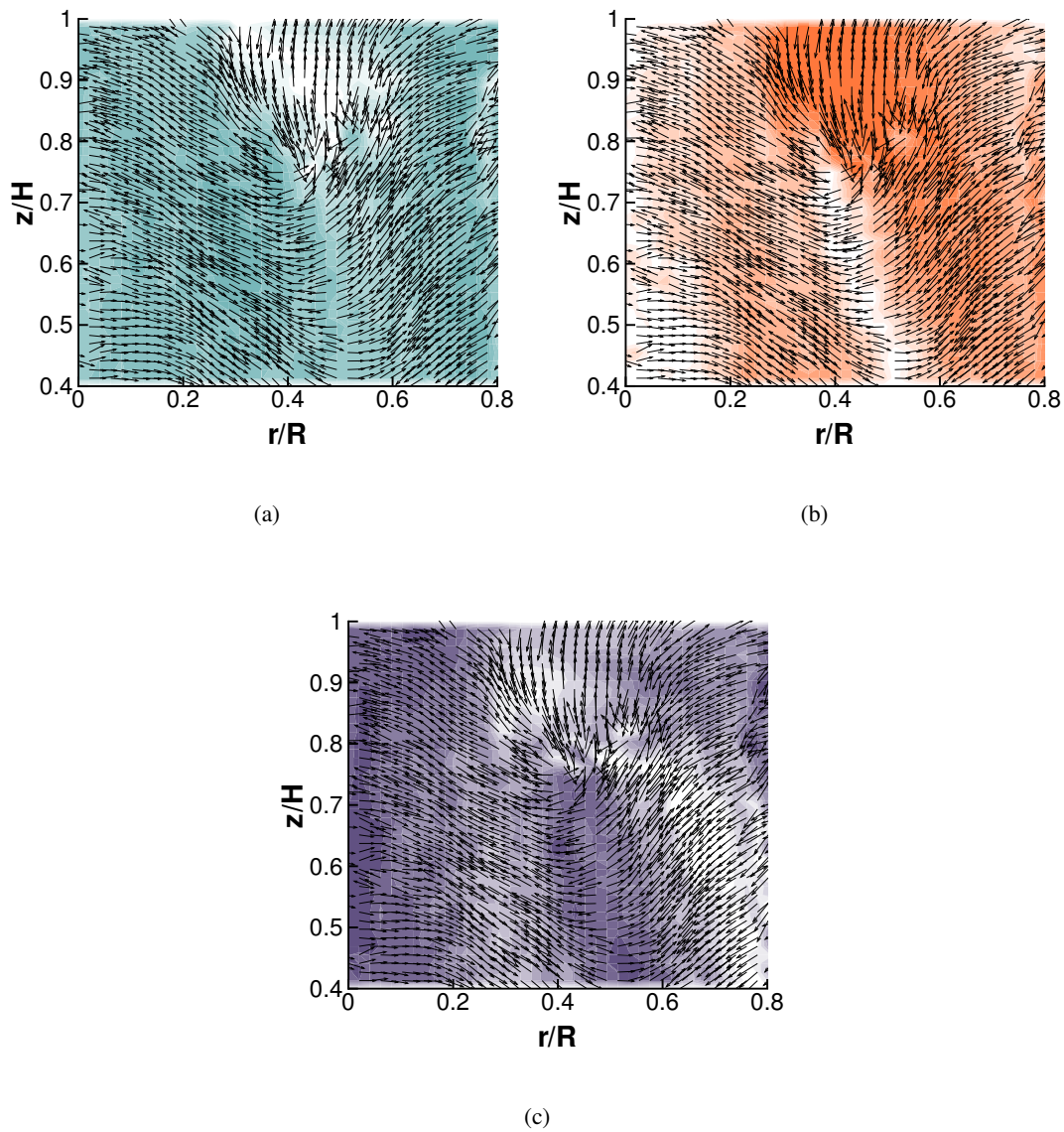


Figure 4.41: Spatial distribution of principal stress unit vector $\hat{\sigma}_3$ when $Re = 1200$. Vectors represent $\hat{\sigma}_3$ resolved on the meridional plane. Coloured contours represent levels of (a), $\hat{\sigma}_3 \cdot \mathbf{i}$; (b), $\hat{\sigma}_3 \cdot \mathbf{j}$; and (c), $\hat{\sigma}_3 \cdot \mathbf{k}$, on a scale from 0 (lightest shading) to 1 (darkest shading).

4.7.3.3 $Re=2400$

To extend the demonstration of the principal axes heterogeneity to another part of the parameter space, the $\hat{\sigma}_1$ and $\hat{\sigma}_3$ distributions corresponding to the $Re = 2400$ case are presented in Figures 4.42 and 4.43, respectively. At $Re = 2400$ the flow is complicated by the detachment of the VB recirculation from the axis of symmetry and the presence of a wider low-velocity, central vortex region. To accommodate a larger-radius VB region, the left hand side of the outer recirculation is more distorted, meaning that the negative axial flow diverges and then converges further

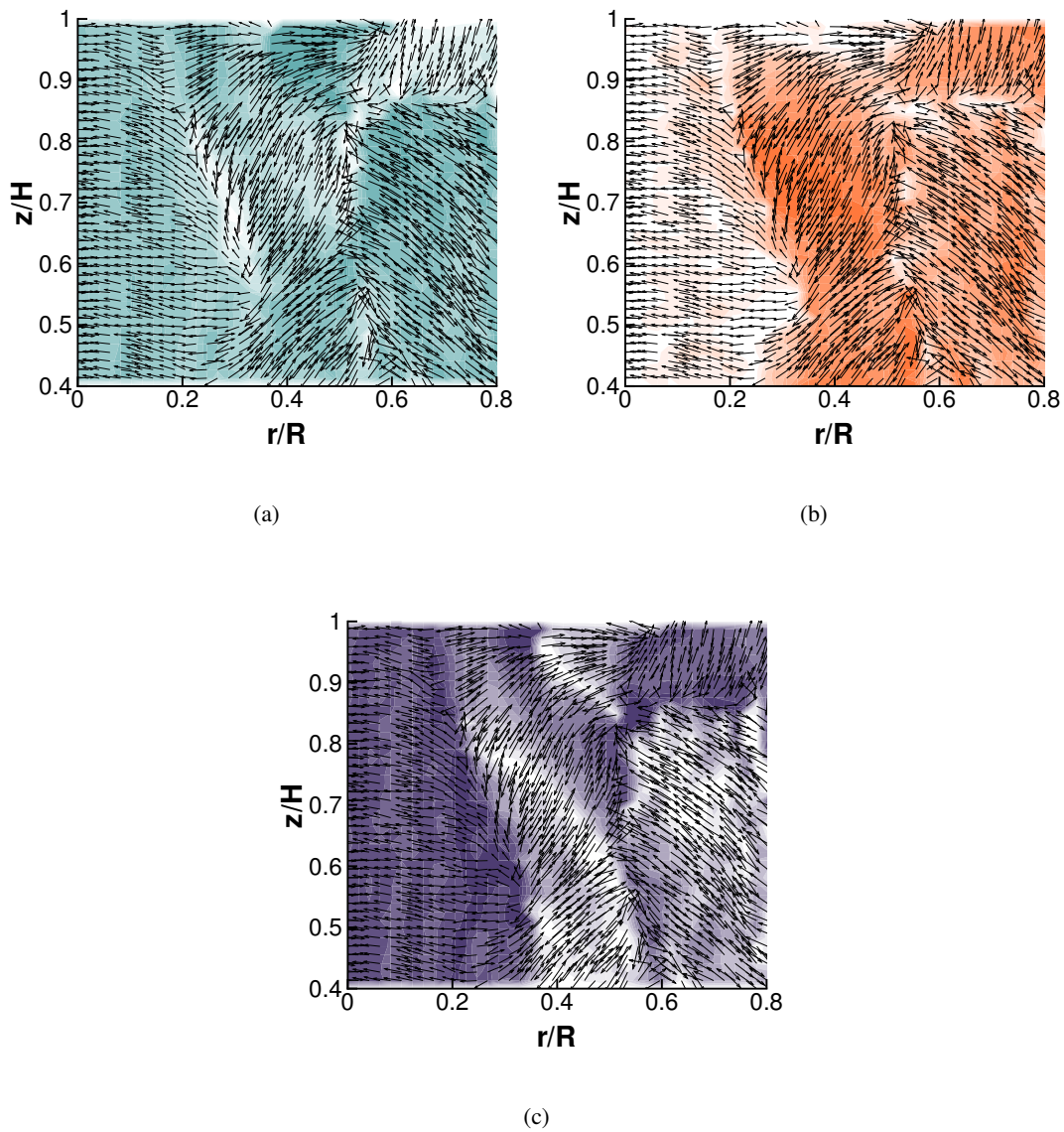


Figure 4.42: Spatial distribution of principal stress unit vector $\hat{\sigma}_1$ when $Re = 2400$. Vectors represent $\hat{\sigma}_1$ resolved on the meridional plane. Coloured contours represent levels of (a), $\hat{\sigma}_1 \cdot \hat{i}$; (b), $\hat{\sigma}_1 \cdot \hat{j}$; and (c), $\hat{\sigma}_1 \cdot \hat{k}$, on a scale from 0 (lightest shading) to 1 (darkest shading).

downstream. The orientation of the principal axes once again varies predominantly on the basis of flow region, but also within a particular flow region. The more distorted nature of the outer recirculation means that $\hat{\sigma}_1$ and $\hat{\sigma}_3$ vary to a greater extent across the measurement plane than at $Re = 1200$. For instance, cells in the outer recirculation region are transported through regions where $\hat{\sigma}_1$ is strongly oriented toward the azimuthal direction, regions where $\hat{\sigma}_1$ is more in line with the cylinder axis, and regions where $\hat{\sigma}_1$ is approximately at equal angle to the meridional and azimuthal planes. At $Re = 1200$, the $\hat{\sigma}_3$ distribution, shown in Figure 4.43,

has a similar pattern to the $\hat{\sigma}_1$ distribution, however the contour levels differ according to how closely the principal axes align with the cylinder axes.

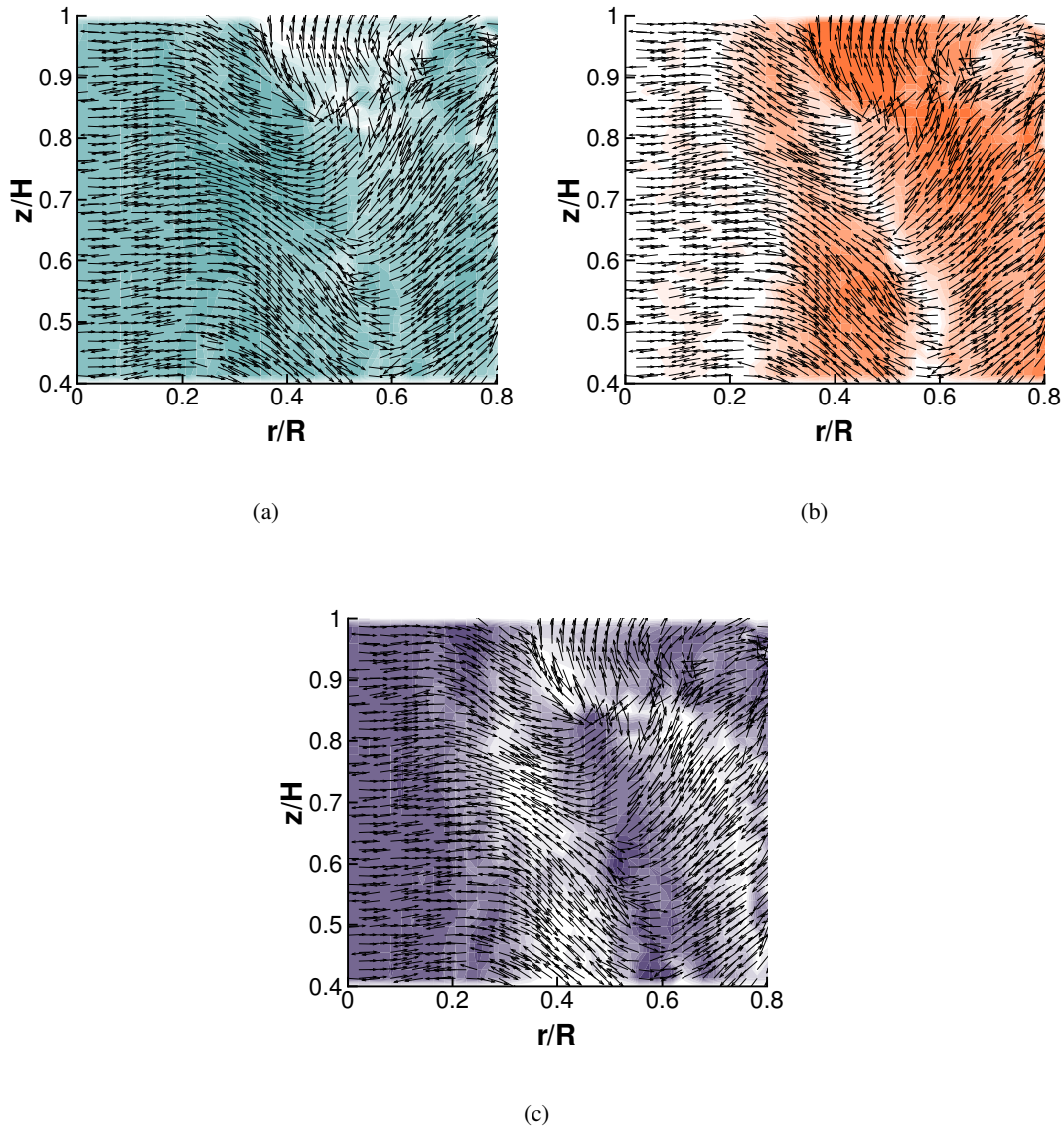


Figure 4.43: Spatial distribution of principal stress unit vector $\hat{\sigma}_3$ when $Re = 2400$. Vectors represent $\hat{\sigma}_3$ resolved on the meridional plane. Coloured contours represent levels of (a), $\hat{\sigma}_3 \cdot \mathbf{i}$; (b), $\hat{\sigma}_3 \cdot \mathbf{j}$; and (c), $\hat{\sigma}_3 \cdot \mathbf{k}$, on a scale from 0 (lightest shading) to 1 (darkest shading).

4.7.4 Shear Stress Components

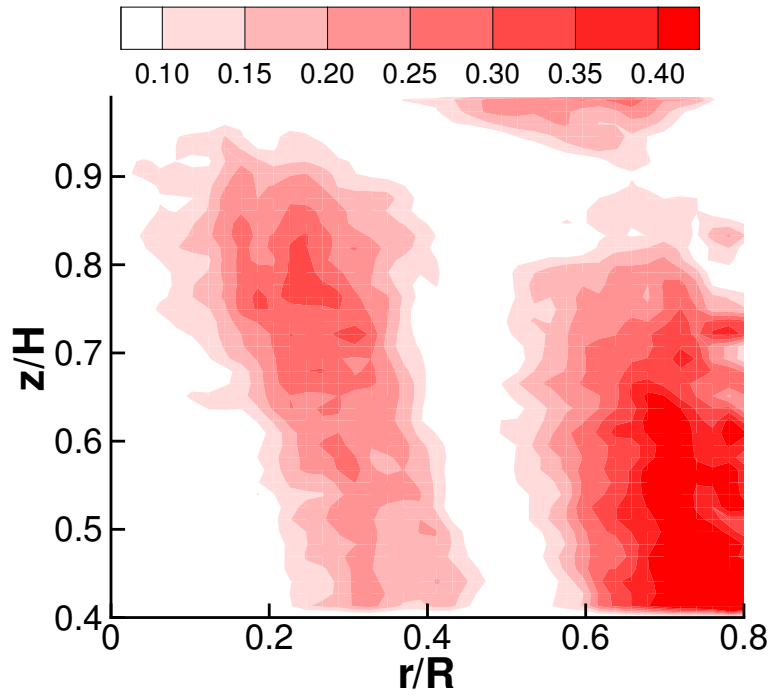
Given that the principal axes are typically oriented at an angle to the cylinder axes, the stresses measured in either the meridional or azimuthal plane are unlikely to be the maximum stresses experienced by cells at a particular point in time. For instance, the mean τ_{rz} magnitudes shown in Figure 4.39 are approximately 50% as large as the mean magnitudes of σ_1 or σ_3 . On the

other hand, the individual shear stress components do help illustrate the features of the flow that most contribute to the deformation stress tensor at a particular position in the bioreactor. This subsection briefly summarises the τ_{rz} , $\tau_{r\theta}$, and $\tau_{z\theta}$ shear stress fields in the upper cylinder region at $Re = 1200$ and $Re = 2400$.

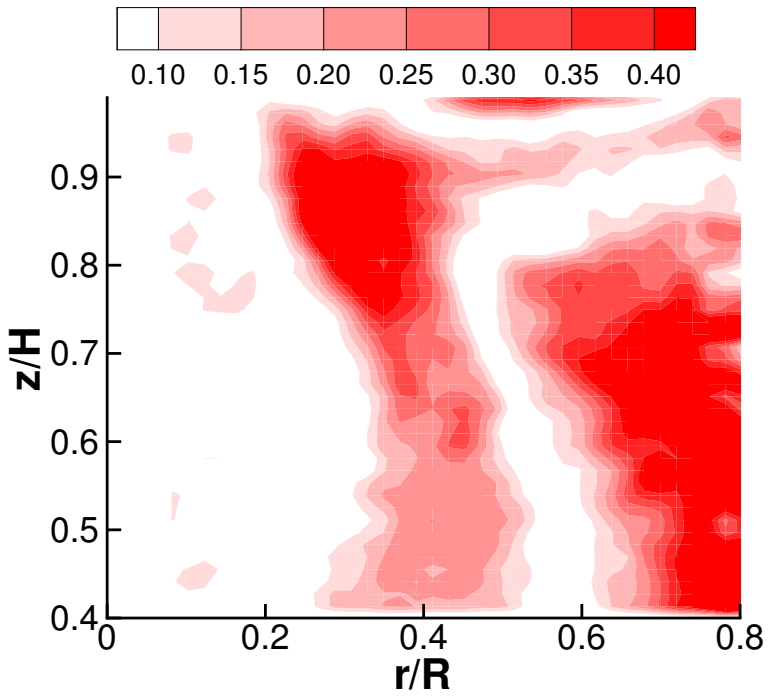
Figure 4.44 illustrates the spatial distribution of the meridional plane shear component τ_{rz} . At both $Re = 1200$ (Fig. 4.44(a)) and $Re = 2400$ (Fig. 4.44(b)), the peak τ_{rz} zones occur at the interface between the VB and outer recirculations, and toward the middle of the outer recirculation. τ_{rz} is moderate on the outer side of the VB recirculation, however is low in the remainder of the near-axis region. At $Re = 2400$ the VB recirculation contains higher shear levels than at $Re = 1200$ because its centroid is closer to the stronger, outer recirculation and therefore $|\partial v_z/\partial r|$ is larger. The peak τ_{rz} region covering the adjacent sides of the VB recirculation and the outer recirculation continues downstream of the VB recirculation, albeit with a reduced intensity.

Because of the assumption that $\partial v_r/\partial \theta \approx 0$, the shear stress component $\tau_{r\theta}$ is mostly determined by the gradient $|\partial v_\theta/\partial r|$. As illustrated by Figure 4.45, the $\tau_{r\theta}$ distribution differs substantially from the τ_{rz} distribution. At $Re = 1200$, $\tau_{r\theta}$ is of approximately the same magnitude in the inner region as it is in the outer recirculation region. However, at $Re = 2400$ there is a column of high $\tau_{r\theta}$, with a radius of $\sim 0.15R$, surrounding the axis of symmetry. This high-shear central column is caused by relatively strong $|\partial v_\theta/\partial r|$ gradients surrounding the axis of symmetry, as depicted by the closely spaced contours in Figure 4.24. For both cases, there is a narrow band of high $\tau_{r\theta}$ near the outer boundary of the VB recirculation, although unlike the equivalent band of τ_{rz} , it does not extend far into the recirculation itself. Interestingly, the magnitude of $\tau_{r\theta}$ is similar to, and often exceeds, the magnitude of τ_{rz} .

The $\tau_{z\theta}$ contours, which are derived predominantly from the $|\partial v_\theta/\partial z|$ distribution, are presented in Figure 4.46. Once again, a high shear stress band features in the vicinity of the VB outer boundary. A second region of relatively strong $\tau_{z\theta}$ is located near the top corner of the bioreactor, and is associated with the decay in azimuthal momentum as fluid discharged from the impeller region approaches the free surface (see Figure 4.18). Significantly, neither the high τ_{rz} zone in the outer recirculation region, nor the high $\tau_{r\theta}$ zone surrounding the axis of symmetry, are replicated in the $\tau_{z\theta}$ contours. This leaves the VB outer boundary as the only significant region in the upper half of the bioreactor that has relatively large τ_{rz} , $\tau_{r\theta}$ and $\tau_{z\theta}$ at both $Re = 1200$ and $Re = 2400$. The cumulative effect of these stresses explains why peak regions of σ_1 and σ_3 were derived in this part of the vessel. At this and other locations the

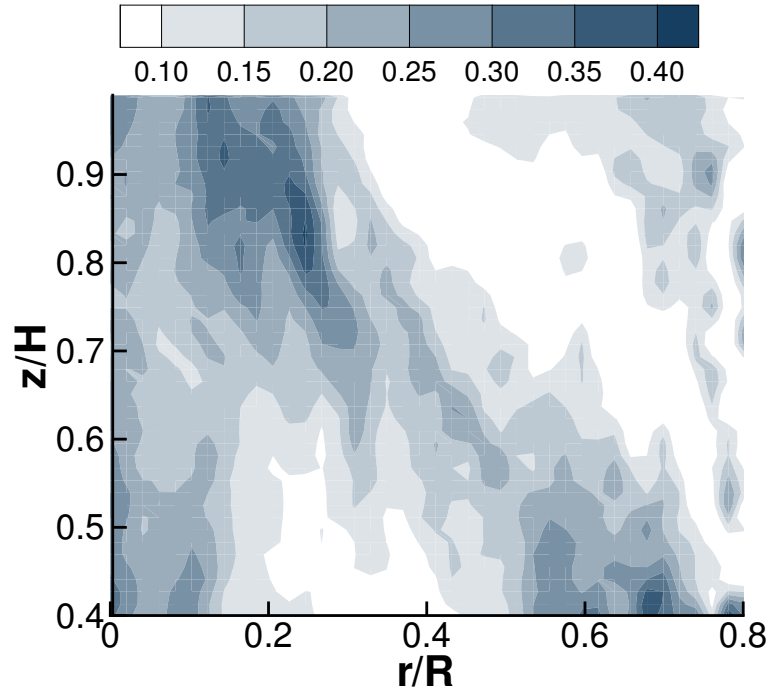


(a)

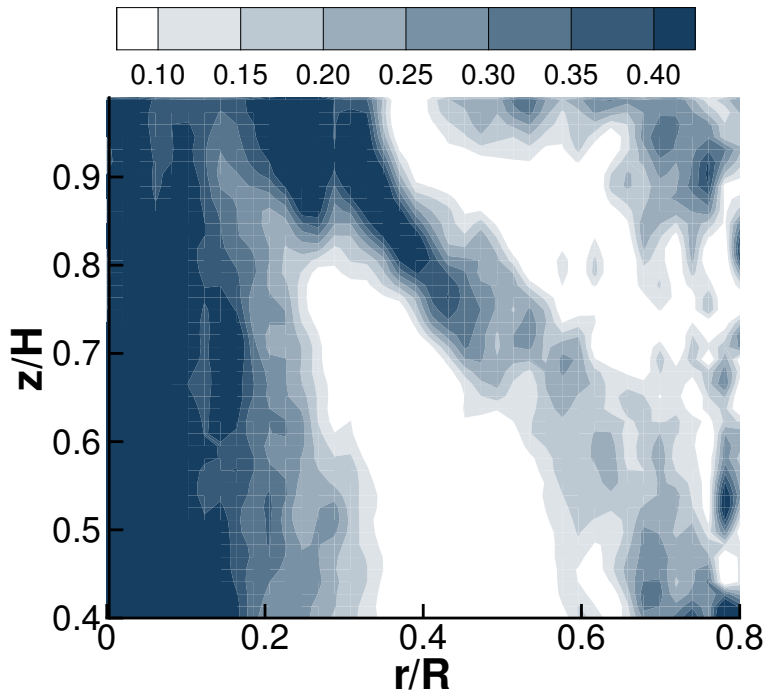


(b)

Figure 4.44: Distribution of $\tau_{rz}/(\mu\omega)$ when (a), $Re = 1200$; and (b), $Re = 2400$.



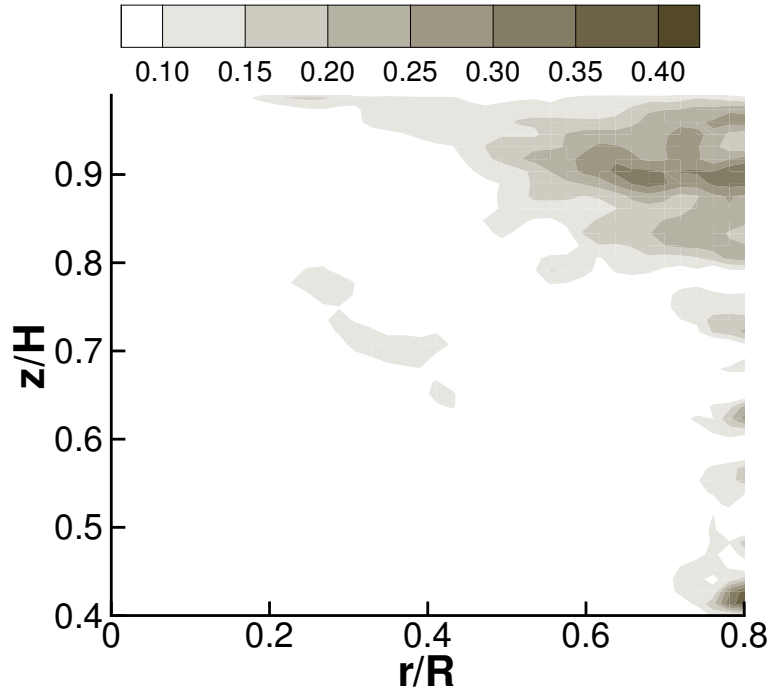
(a)



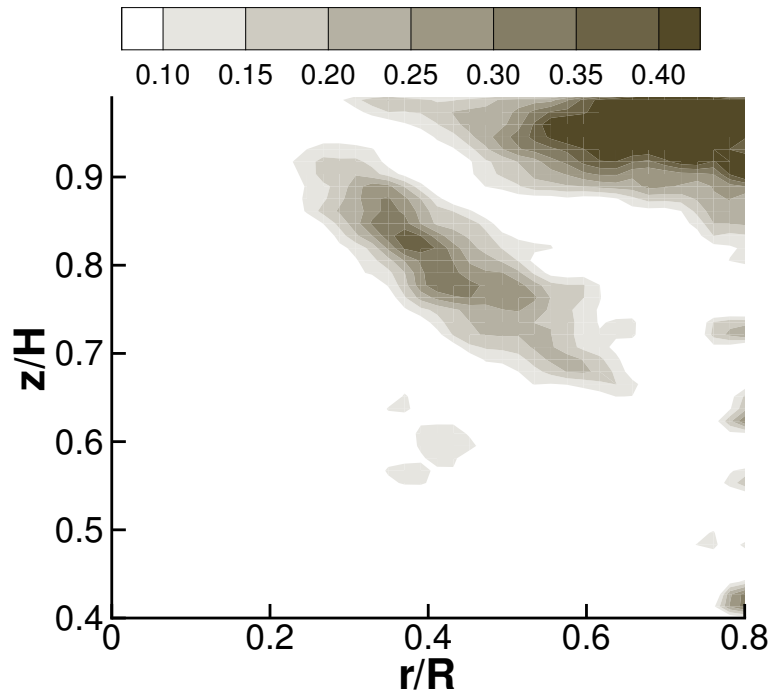
(b)

Figure 4.45: Distribution of $\tau_{r\theta}/(\mu\omega)$ when (a), $Re = 1200$; and (b), $Re = 2400$.

magnitudes of the individual shear stress components are relatively slight. However, the combination of three modes of shearing may result in much larger total stresses. This underlines the importance of considering all three shear stress components, rather than that just acting in one plane.



(a)



(b)

Figure 4.46: Distribution of $\tau_{z\theta}/(\mu\omega)$ when (a), $Re = 1200$; and (b), $Re = 2400$.

4.8 Conclusions and Further Discussion

An analysis of the flow topologies and stress fields suggests that controlled vortex breakdown flows within the bioreactor model are conducive to free-suspension cell or microcarrier culture under certain input conditions. Flows at Re below that for the onset of vortex breakdown may not have the momentum to provide adequate mixing or to suspend the cell aggregates for long periods of time. For instance, it is apparent that at $Re = 600$ the fluid above $z/H \approx 0.70$ rotates about the axis of symmetry but is fixed in the meridional plane. As Re increases, the disk rotation becomes sufficient to cause circulation through the entire meridional plane. Above a certain threshold ($Re \gtrsim 760$ for $H/R = 1.5$), a vortex breakdown bubble of the *axis bubble* variety appears on the central axis, albeit with a small radius at first. With an increase in Re , both the size and geometry of the vortex breakdown region changes. It is feasible, when considering the entrainment of particles in the VB region during flow visualisation, that this region will provide suitable conditions for cell culture within an environment isolated from the remainder of the fluid volume.

Flow visualisation images illustrate the location of the VB recirculation region, the central vortex, and the outer recirculation region. All of the observed flow structures are consistent with the classifications made by Spohn *et al.* (1993) and Brøns *et al.* (2001) at $H/R = 1.5$. The SPIV results go further by quantifying the velocities in these different regions. The approximate pathlines and convection speeds of small, neutrally buoyant cell clusters can be predicted from the velocity profiles. v_z profiles depict the relative strengths and locations of the recirculatory mixing regions. The peak positive axial flow occurs on the side of the outer recirculation nearest the cylinder wall, and the peak negative axial flow occurs on the side of the outer recirculation nearest the axis of symmetry. Similarly, the peak negative radial flow occurs at the top of the outer recirculation and the peak positive radial flow occurs at the bottom of the outer recirculation, in the Ekman region. The Γ profiles are more subtly linked to the vortex breakdown topology than the v_z profiles. There are regions of the flow where Γ is particularly strong, most notably alongside the impeller and near the end of the sidewall closest to the impeller. The flow loses azimuthal momentum as it travels up the sidewall from the impeller to the free surface. The v_z peak spreads out as the cells approach the free surface, however not with the rapidity of the Γ peak. Contour diagrams have previously been used to describe the azimuthal component of vortex breakdown flows (see, for example, Lopez (1990) and Mattner *et al.* (2003)), however not for the cases studied here, and not in the context of a cell bioreactor application.

The stress characterisation process undertaken in this chapter via the derivation of the \mathcal{T} field is superior to the more common approach of approximating the bioreactor stress output through an empirically derived constant. It is clear that an understanding of the internal fluid mechanics is necessary for an accurate prediction of the stress levels experienced by cells under certain input conditions. Also, many of the traditional parameters are not appropriate for vessels of the type described in this thesis or for other advanced low-shear bioreactors such as the rotating wall vessel. For example, the Integrated Shear Factor (Equation 2.19) cannot be applied to the case when the impeller radius, r_i , is equal to the bioreactor radius, R . This is because $ISF \rightarrow \infty$ as $r_i \rightarrow R$. Similarly, the average shear rate defined by Equation 2.20 goes to 0 when $r_i = R$. Of the other common parameters, the turbulent collision severity (Eqn. 2.21), and the energy dissipation rate (Eqn. 2.25), are not applicable to a laminar mixing flow absent of turbulent eddies. Even Nagata's power number, N_p , is flawed because it relies on an accurate prediction of the power transferred to the fluid by the impeller and does not take into full account the effects of vessel geometry or fluid viscosity. However, the key concern with global flow parameters is that they generally do not take into account spatial or temporal heterogeneity, or the mechanisms which lead to peak stress regions. The use of SPIV to undertake bioreactor flow characterisations is shown here to be far superior in this regard.

The principal stress fields measured here indicate that retaining suspended cell aggregates in the VB region would be desirable for cell or tissue cultures that require mixing for nutrient transport, but for which exposure to large stresses or stress gradients would be particularly damaging. Three-dimensional stresses peak at the interface between the rotating lid and the cylinder wall, and are relatively high near the bottom (Ekman) boundary layer and the side (Stewartson) boundary layer. Cells suspended within the large, outer recirculation region are likely to encounter both these high stress regions as they spiral around the central axis toward $z/H \rightarrow 0$, then get accelerated radially and azimuthally by the Ekman pumping mechanism, before being abruptly turned in the positive axial direction by the sidewall. Due to the relatively high velocities in the outer recirculation region, aggregates suspended in this zone are more likely to collide with the impeller or the cylinder sidewall. In contrast, the results indicate that suspensions within the VB region would be exposed to lower stress levels than those outside the VB region, but would nevertheless receive mixing through the internal bubble circulation and advection phenomena reported elsewhere in the literature (Sotiropoulos *et al.*, 2001). In addition, the distance of the centrally-located VB region from the impeller or wall prevents collision from being a major issue. For all Re considered in this study, a high stress zone

is located at the interface between the upper VB region and the outer recirculation region, however the size and intensity of this region is slightly less than the aforementioned peak regions. Moreover, as this stress band separates two distinct flow regions, it is unlikely to be crossed by cell or tissue suspensions.

The principal axes contain important information regarding the direction in which the principal and maximum stresses act on a fluid element or cell cytoskeleton. The principal axes are not often considered in stress analyses for bioreactor or other biofluids applications. However, their direction could be important as it may be unfavourable to expose cells to unbalanced forces. Promisingly, the orientation of the principal axes is heterogeneously distributed through the vessel, so cells travelling through the culture medium for long periods of time should be exposed to stresses from a variety of directions. The principal axes rarely align with the cylinder axes, so the measurement of only τ_{rz} , $\tau_{r\theta}$ or $\tau_{z\theta}$ does not adequately describe the stresses experienced by cells. Each of these shear stress components have their own distinct distribution across the meridional plane. In the upper half of the vessel, the only region for which all shear components are strong is at the boundary of the VB recirculation, i.e. the peak σ_1 and σ_3 region. This underlines the fact that the peak stresses can only thoroughly be defined using the stress tensor \mathcal{T} , and that the individual shear components will only provide a partial understanding of the stress field.

The results reveal that the success of culturing cells within an open surface bioreactor with vortex breakdown may depend on Reynolds number. Re determines whether the VB is of *axis bubble*, *corner bubble*, or *surface bubble* type. The most significant evolution of the VB flow structure with Re occurs within the *corner bubble* regime. In contrast, the *axis bubble* regime occurs over only a very small range of Re values, while the geometry of the VB region is nearly constant in the *surface bubble* regime. In the *corner bubble* regime, the degree to which the VB recirculation is attached to the axis is dependent on Re . The higher the Re value, the higher up the axis of symmetry the stagnation point is located, until eventually the VB recirculation becomes completely detached from the axis, leaving a central column within its internal radius. The fluid in this central vortex region is not as well mixed, as there is no meridional recirculation. Rather, there is a low-velocity flow in the negative z direction which eventually convects the cells in the core vortex region to the high stress impeller region. Therefore, care would need to be taken to ensure that cells intended for culture in the VB recirculation toroid are not accidentally seeded into the central vortex. In this respect, the *corner bubble* regime may be most favourable for seeding because the cells and/or nutrients can be

dispatched on the axis of symmetry into the VB recirculation, with less chance of them being sucked down into the Ekman region and then into the outer recirculation. For example, at $Re = 1200$ seeding can occur to within a radius of $\sim 0.2R$ at the free surface. The choice of flow regime also affects the volume of fluid within the VB recirculation region. The *corner bubble* regime, with its large recirculation region radius, is particularly favourable in this regard.

The peak stress band at the outer boundary of the VB recirculation alters with the VB topology. As the boundary moves radially outward, so too does the peak stress region. The size of the peak stress region decreases slightly, however the stresses are intensified. The slant angle of the stress band consistently resembles the slant of the VB boundary surface. At $Re \gtrsim 2200$, where the flow structure approaches a fixed geometry, σ_1 and σ_3 asymptote toward an Re -independent magnitude and distribution.

The flow immediately adjacent to the impeller is less dependent on Re than that in any other part of the vessel. At higher Re , the fluid being sucked into the impeller region travels slightly faster, and the bottom peak stress layer is marginally thinner than at lower Re , which is consistent with the theoretical decrease in Ekman boundary layer thickness. However, cells travelling through the impeller region are generally subjected to a stress peak that is similar for the measured range of Re cases. Similarly, the peak stress region near the sidewall and just above the impeller is not significantly affected by Re . On the other hand, Re has more of an effect on the near-wall flow at a higher z/H position. The axial velocity profile near the sidewall retains its magnitude to a greater degree at higher Re , and the v_z peak remains closer to $r/R = 1$. The azimuthal momentum is also maintained for a greater distance along the sidewall when Re is increased. Once again, the effect of Re on the sidewall flow is lessened for $Re \gtrsim 2200$.

During qualitative flow visualisation, the VB region was observed to become more oscillatory at high Re , however for $Re \leq 3000$ the temporal variability is not significant enough to affect a potential cell culture application. The measured velocity fluctuations did not reveal any flow periodicity and are likely to be due to noise. In any case, the maximum turbulent stresses are several orders of magnitude below the mean stresses.

An increase in Re leads to an overall increase in the modified swirl ratio, SR_m , until the flow topology becomes more constant with respect to Re . Since swirl is a critical parameter for vortex breakdown, it is possible that the most important contribution of Re to the flow structure is through the definition of the swirl conditions, rather than just controlling the convection of the swirl downstream. The dependency of swirl (a key physical parameter that defines VB) on Re is significant. An interesting extension to this study would be to measure the effect of H/R on

swirl, and thereafter try to decouple the effect of swirl from the $(Re, H/R)$ parameter space. In this way, it may be possible to classify the flow in terms of Re and a global swirl parameter, an approach which has helped researchers acquire an understanding of the mechanisms of vortex breakdown phenomena in swirling pipe and swirling jet flows.

While laminar mixing flows such as the current configuration appear suited to a controlled flow bioreactor application, there are some potential issues that need to be addressed. Firstly, the motion of cell aggregates or microcarrier beads may not be predictable by Eulerian fluid mechanics if their density exceeds a certain threshold. Indeed, as with all suspension bioreactors, the specific gravity should match that of the fluid medium as closely as possible in order to prevent the suspensions from floating to the surface or sinking to the vessel floor. Body forces are particularly important if cells are to be retained within the VB region. In addition, the issue of oxygen diffusion has not been addressed as part of this study. Whether the flow provides adequate oxygen transport is a question that may require further investigation on the basis of individual applications, however it should be noted that the vessel configuration provides scope for injection of materials at the free surface.

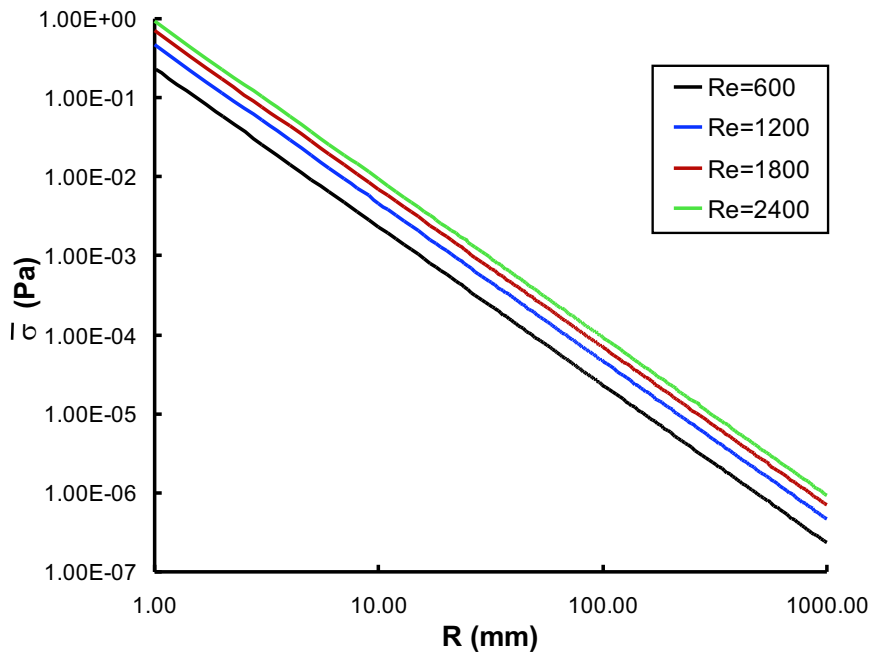


Figure 4.47: Relationship between vessel radius, (R), and approximate mean stress levels. The different curves correspond to different Re values.

The stress and velocity fields have been presented in dimensionless form in this chapter, in order to emphasise that bioreactors can and should be categorised in such a way that the

results have a general relevance, rather than being particular to a certain set of parameter values. Such an approach makes it easier to predict the performance of bioreactor designs under scaled conditions, and eventually to optimise the design of bioreactors on the basis of, say, the mean stress or the oxygen transfer coefficient. For example, it is possible to increase the absolute stress levels while keeping a constant flow topology by increasing ω but keeping Re constant. As a basic example, Figure 4.47 represents a logarithmic plot of $\bar{\sigma}$, in Pascals, against R , in millimeters, calculated by scaling. The curves pass through the $\bar{\sigma}$ values measured at the four different Re values shown in the current study (i.e. at $R = 32.5\text{mm}$). Because of the large domain, the difference in $\bar{\sigma}$ caused by Re appears slight compared to the difference caused by R , however this may be misleading. The engineer must take care, when scaling bioreactors based on Re , to not overlook other factors that may become important. For example, increasing the vessel size will require a slow rotational speed, (as ω scales with R^{-2}), which may in turn lead to practical issues or overly small deformation stresses. In addition, the applicability of the flow models may become limited by excessive Froude numbers, hydrostatic pressures or thermal gradients in very large tanks. A possible solution to this problem could be to scale out to multiple smaller bioreactors rather than use a single, scaled-up bioreactor.

Chapter 5

Flows within a Bioreactor with Vortex Breakdown and Stationary Submerged Scaffolds

5.1 Introduction

The results presented in this chapter measure the changes to Vortex Breakdown flows within open cylindrical bioreactors caused by submerging disks at different radial and axial locations. The disk size and position are varied in order to monitor their effect, if any, on the flow states corresponding to $(H/R, Re) = (1.5, 1200)$ and $(H/R, Re) = (1.5, 2400)$. The object geometry resembles that of a tissue engineering scaffold used within bioreactors (Vunjak-Novakovic *et al.*, 2002; Freed *et al.*, 1998; Sucusky *et al.*, 2004), i.e. a cylindrical disk supported by a thin support column. In this way, the bioreactor system modelled in Chapter 4 is extended in the current chapter to a scaffold/bioreactor system, as discussed in Subsection 2.4.4. The low-velocity Vortex Breakdown region is an important feature of the bioreactor flows previously described, and is once again of interest in the submerged scaffold case. This is because the VB region has the potential to provide the mixing and stress environment conducive to successful *in vitro* tissue construction, provided that it retains a similar geometry and internal flow profile when a scaffold is placed within it. The problem is addressed by undertaking a non-dimensionalised experimental characterisation of the velocity fields and stress levels resulting from various scaffold configurations and flow settings. This lays the foundation for optimising the bioreactor inputs for a particular cell or tissue culture application.

Once again, two different experimental techniques were used to undertake the investigation. Still photography was used to visualise the resulting flow states, while Stereoscopic Particle Image Velocimetry (SPIV) was applied to measure the three-component velocity field in the meridional plane, from which the various flow topologies are analysed and the stress fields

derived. In this chapter, the wall shear stress profiles along the surfaces of the disk are included with the principal stress fields. This is because the culture material in a scaffold/bioreactor system is seeded throughout the scaffold, rather than the liquid cell culture medium, and so the greatest stresses to which adherent cell or tissue material are exposed, are located at the surface.

While the key motivation of the research presented in this chapter is to investigate the potential for VB to be used in a scaffold/bioreactor application, a second aim is to more generally test the sensitivity of the VB states reported in Chapter 4 to the addition of intrusive objects. There is a precedence for investigating the effect of submerged solid bodies on VB flows. For instance, Mattner *et al.* (2003) suspended a sphere within a swirling pipe flow under swirl and Reynolds number conditions conducive to VB, and observed breakdown bubble and spiral formations similar to the no-sphere case. Upon increasing the swirl ratio, they observed changes in the length of the low-velocity bubble region, and the movement of the bubble from downstream to upstream of the sphere. In another experiment, Husain *et al.* (2003) added a rotating cylindrical rod to the axis of a rigid lid-driven cylinder. They found that VB can co-exist with the column, and that the rod can be used to enhance or suppress VB bubble formation. Mununga *et al.* (2004) added a small rotating disk to the top end of a bottom-driven cylinder, and managed to control the Re corresponding to the onset of VB by varying the speed and direction of this second impeller. The current study represents the first time that the effect of disks submerged within the breakdown bubble region has been observed and measured.

The chapter commences with a recap of the base flow vector fields at the two Re values investigated (Section 5.2). Lamp-illuminated particle images then provide a visual illustration of the flow structure resulting from the submersion of three different sized disks. Section 5.3 includes a detailed description of the measured velocity fields for three of the combinations of scaffold size and Re that were studied. It also contains an investigation into the effect of varying the scaffold vertical position, for each of the three case studies. In addition, the effect of varying the scaffold to bioreactor diameter ratio is examined. σ_3 fields similar to those plotted in Section 4.7 are compared in Section 5.4, and surface shear stresses are presented in Section 5.5. Finally, Section 5.6 includes an investigation into the effect of displacing the scaffolds in the radial direction.

5.2 Review of Flow Topology at $Re=1200$ and $Re=2400$ Without Scaffolds Added

A full description of the flow measurements captured when the cylinder is devoid of disks has already been provided in Chapter 4, however it is useful to briefly review the base flow at $Re = 1200$ and $Re = 2400$. The alterations in flow structure caused by the addition of scaffolds can be monitored by comparing them with these flow fields. The in-plane vector field and the azimuthal velocity field at $Re = 1200$ and $Re = 2400$ are shown in Figure 5.1. The field of view includes the upper portion of the vessel, or $0.4 \leq z/H \leq 1.0$. Because the flow is nearly axisymmetric, only the right hand side of the measurement plane is shown.

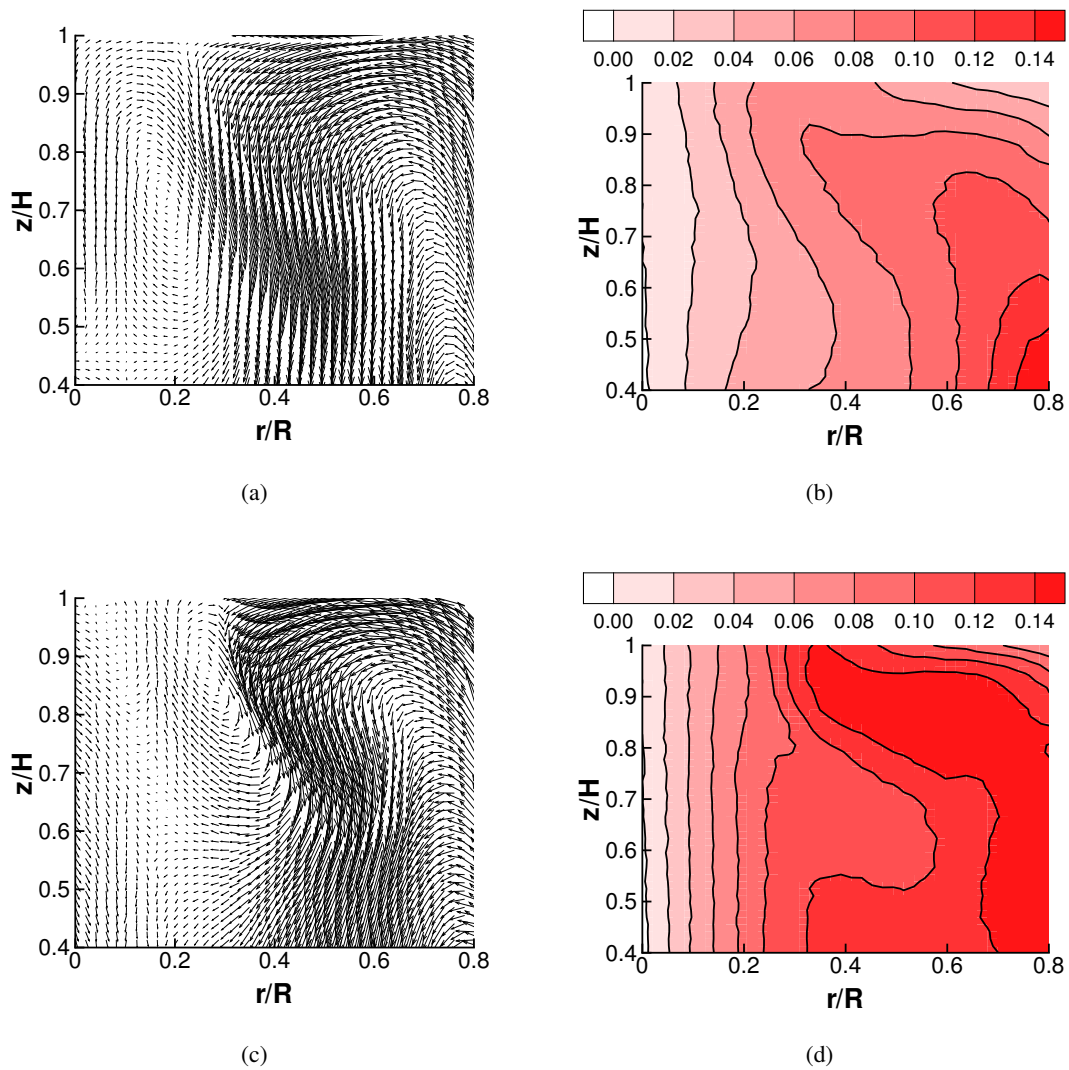


Figure 5.1: Time-averaged velocity fields for the case with no submerged objects. (a) In-plane velocity vectors, $Re = 1200$; (b) $v_\theta/(R\omega)$ contours, $Re = 1200$; (c) In-plane velocity vectors, $Re = 2400$; (d) $v_\theta/(R\omega)$ contours, $Re = 2400$.

For both the $Re = 1200$ case and the $Re = 2400$ case, the separate flow regions are distinguishable, particularly in the meridional plane vector plots (Figures 5.1(a) and (c)), which highlight the counter-rotating recirculation pattern. The larger recirculation is partially visible on the right hand side of the in-plane vector plots. The VB recirculation zone is fully visible, centred at approximately $(r/R, z/H) = (0.19, 0.70)$ for $Re = 1200$ and $(r/R, z/H) = (0.28, 0.86)$ for $Re = 2400$. In both cases the bubble is attached to the free surface, however at $Re = 2400$ the radial position of the outer-boundary attachment is further from the axis of symmetry. Indeed, at $Re = 1200$ the recirculation bubble is adjacent to the axis of symmetry, whereas at $Re = 2400$ the negative v_z core vortex region extends axially into the fluid volume between the recirculation bubble and the axis of symmetry. The $Re = 1200$ flow is an example of a *corner bubble* VB flow, while $Re = 2400$ lies within the *surface bubble* regime.

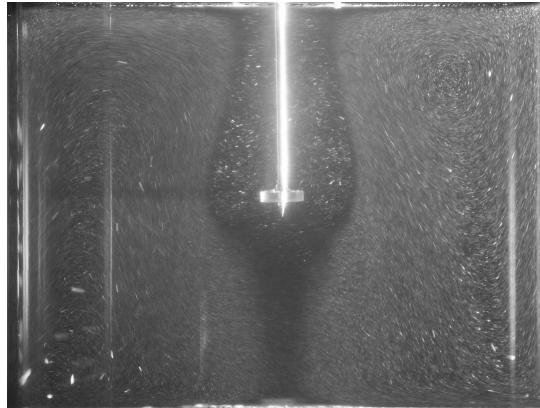
The presence of the breakdown region is also reflected in the v_θ contours (Figs. 5.1(b) and (d)), albeit to a much less obvious extent than in the meridional plane vector fields. While the azimuthal flow is relatively stronger at $Re = 2400$, in both cases the contour lines near the boundary between the two recirculation zones tend to be slightly affected by the geometry of the boundary surface. At $Re = 2400$, this is most clearly illustrated by the shape of the $v_\theta/(R\omega) = 0.12$ contour, which is drawn closer to the axis of symmetry downstream of the VB recirculation. In the central vortex column, the $\partial v_\theta/\partial r$ gradient is quite constant up to the left hand side of the VB recirculation, i.e. in the region $0 \leq r/R \lesssim 0.19$.

5.3 Flow Topology With Scaffolds Added

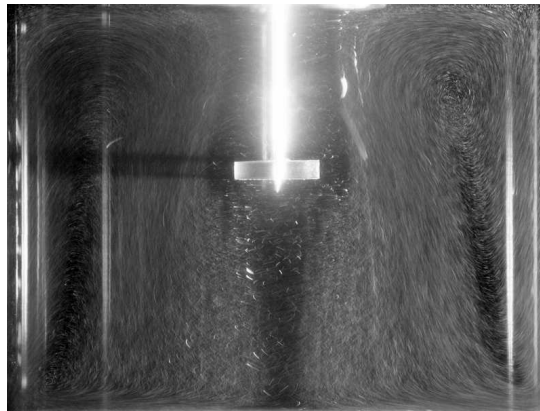
VB bubble formation occurs with any one of the three disks submerged in the bioreactor at a location on the upper half of the central axis. Furthermore, changing Re from 1200 to 2400 produces an alteration in the shape of the VB bubble similar in nature to the alteration which occurs without disks present. Nevertheless, the addition of scaffolds does result in a slightly different steady flow topology to the disk-free case, particularly in the low-velocity breakdown region. In general, it appears that the VB region has an expanded outer diameter in the vicinity of the axial position at which a disk is located. The precise change in VB geometry caused by submerging stationary circular disks in the cylinder depends on the size (indicated by radius r_s/R), and axial location (z_s/H), of the disks. This section commences with flow visualisation photographs, followed by an analysis of the velocity fields corresponding to three different case studies: $(Re, r_s/R) = (1200, 1/13)$, $(Re, r_s/R) = (1200, 3/13)$, and $(Re, r_s/R) = (2400, 3/13)$. The section concludes with a detailed quantitative study on the effect of disk size on the biore-

actor flow topology.

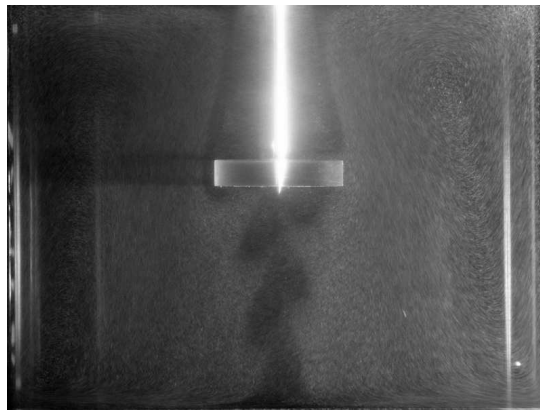
5.3.1 Flow Visualisation



(a)



(b)



(c)

Figure 5.2: Lamp-illuminated particle visualisation of the meridional plane flow for (a) $r_s/R = 1/13$, (b) $r_s/R = 2/13$, and (c) $r_s/R = 3/13$. In all cases $Re = 1200$, and the centre of the scaffold is at $(r/R, z/H) \approx (0, 0.5)$.

The effect of the different disk sizes is noticeable in the visualisation images presented in Figure 5.2. These images each capture the flow at a point in time where it is fully developed and the majority of the tracer particles have separated out to the outer recirculation region, leaving a darker inner region. The $r_s/R = 1/13$ disk is fully enclosed in the VB region and does not appear to greatly affect the VB recirculation toroid. For case (b), $r_s/R = 2/13$, the disk is still fully enclosed in the VB region, however the shape of the bubble is slightly distorted from case (a). For (c), $r_s/R = 3/13$, the diameter of the disk extends to the boundary of the breakdown region. Upstream of the disk the breakdown region is similarly distorted to case (b), however downstream of the disk the bubble geometry is profoundly different. Here, the bubble spirals around one side of the disk and joins a spiral column leading down around the central axis to the rotating bottom. Once the flow is fully developed, this spiral structure is steady in three-dimensional space. The particle distribution between the two regions appears to remain constant, which implies that the fluid transfer between the two regions occurs only very slowly, if at all. Repeated experiments produce different angular orientations of the spiral, indicating that the bubble/column asymmetry may be initiated by asymmetries in the disk alignment rather than the vessel. The spiral column occurs despite the considerable care taken to set up the scaffold suspension system (see Subsection 3.2.4).

5.3.2 Case A: Small Disk, $Re=1200$

The measured velocity fields more thoroughly describe the robustness of the flow structure to the addition of the submerged disk. They also shed light on any changes that occur within the low-velocity region as a result of blockage effects caused by these bluff bodies. Meridional plane vector fields and v_θ contours corresponding to different axial locations of the small disk at $Re = 1200$ are included in Figure 5.3. For ease of comparison with the no-disk case, the field of view and contour levels correspond to those used for the velocity plots shown in Figure 5.1. The approximate location of the disk and support column, including the region obscured by the front of the disk during imaging, is blanked out on all plots. The VB recirculation topology is retained particularly well when the small disk is used. In each of the cases shown in Figure 5.3, the VB bubble is centred at approximately the same location, and has roughly the same size and orientation. Because of the presence of the support column, the inner boundary of the recirculation is slightly off-axis. With $Re = 1200$ and the disk centred at $z_s/H = 0.50$ (see Fig. 5.3(a)-(b)), the recirculation bubble sits above and slightly to the right of the disk. Immediately below the disk, the fluid appears almost quiescent in the r - z plane, although it should be noted

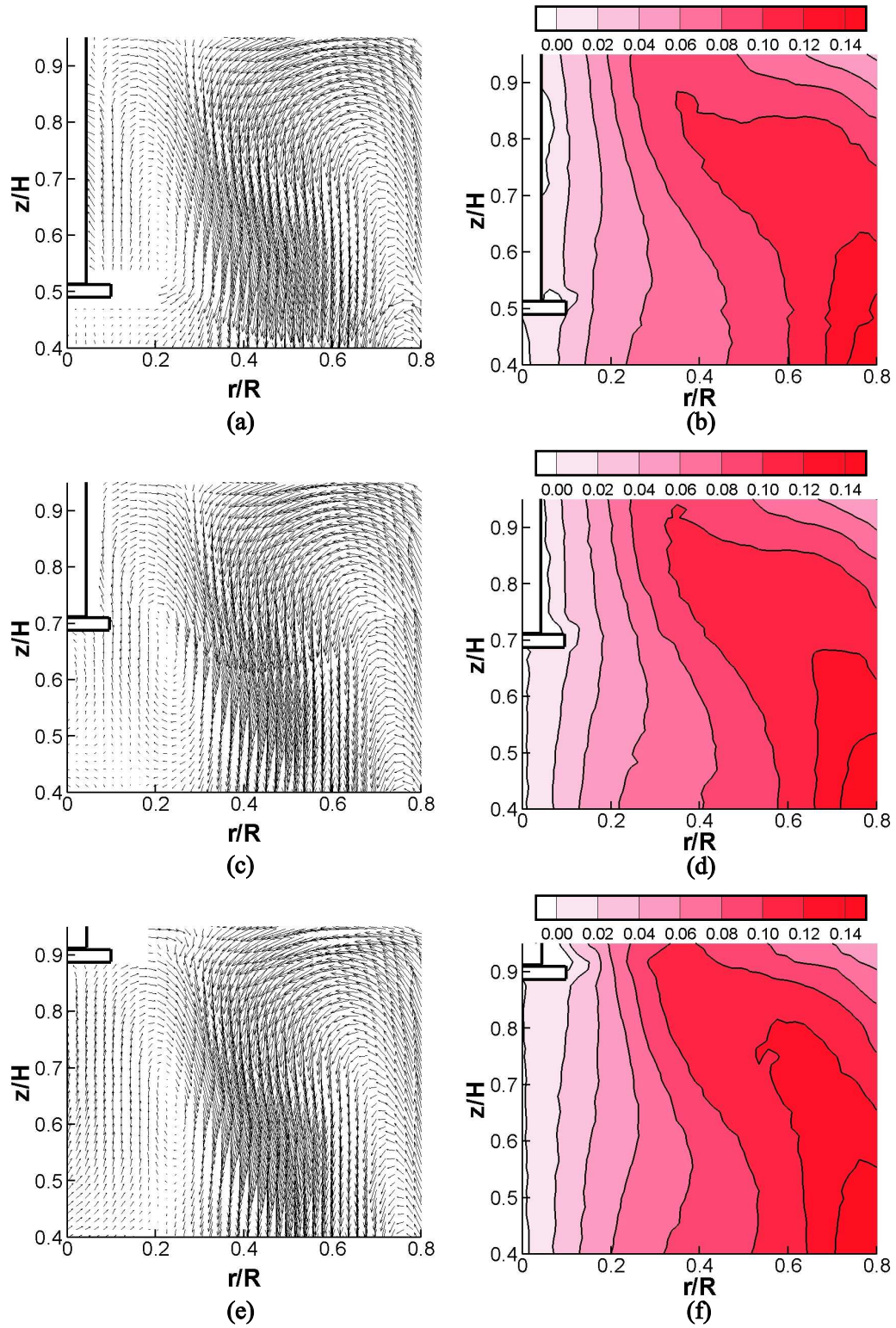


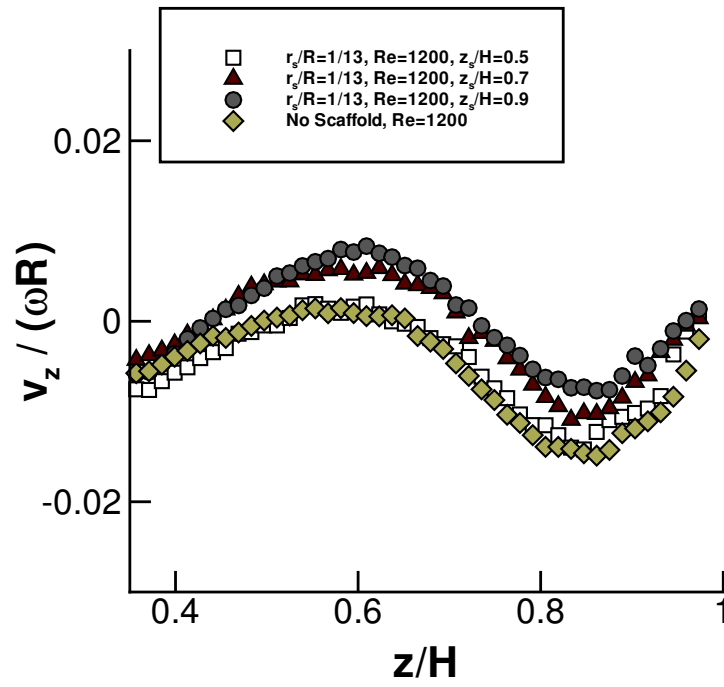
Figure 5.3: Time-averaged velocity fields when $Re = 1200$ and $r_s/R = 1/13$, for various disk locations. The scaffold position is marked. (a) In-plane velocity vectors, $z_s/H = 0.50$; (b) $v_\theta/(R\omega)$ contours, $z_s/H = 0.50$; (c) In-plane velocity vectors, $z_s/H = 0.70$; (d) $v_\theta/(R\omega)$ contours, $z_s/H = 0.70$; (e) In-plane velocity vectors, $z_s/H = 0.90$; (f) $v_\theta/(R\omega)$ contours, $z_s/H = 0.90$.

that this low-velocity, core vortex region occurs at much the same location for the no-disk case. When the disk is moved up to $z_s/H = 0.70$ (Fig. 5.3(c)-(d)), it is much closer to the centre of the VB recirculation toroid. The flow surrounding the disk is slightly affected, however the VB recirculation bubble essentially retains its geometry. The low-velocity region below the disk is extended to an axial position slightly above that of the $z_s/H = 0.50$ case and the no-disk case. When the small disk is centred at $z_s/H = 0.90$ (Fig. 5.3(e)-(f)), the recirculation bubble forms well below the disk. With the column absent, the axial flow near the axis of symmetry is more uniform. The v_θ distribution is barely affected by the presence of the small disk. At most, the $v_\theta/(R\omega) = 0.02$ contour line is displaced slightly in the positive radial direction in the vicinity of the disk.

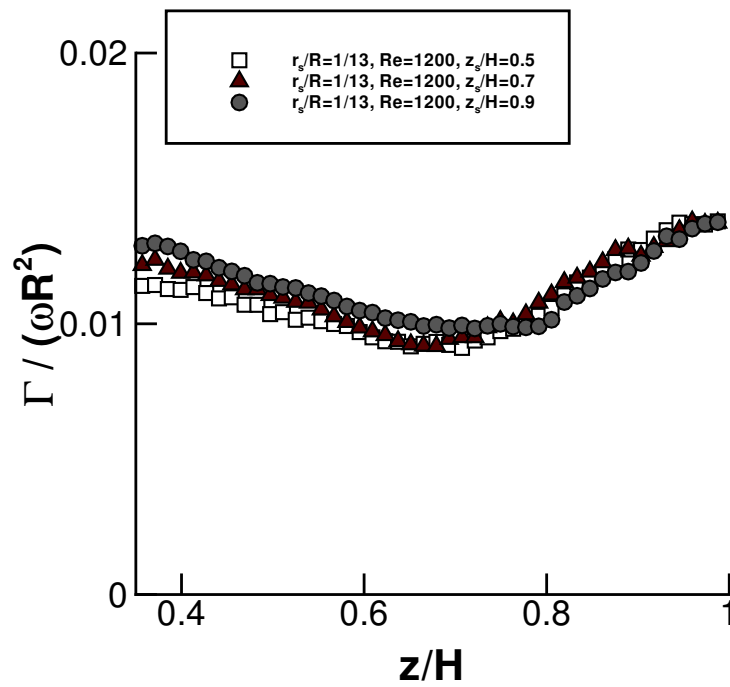
Figure 5.4 contains axial profiles of v_z and Γ taken at a radial position of $r/R = 0.20$, which is within the circumference of the low-velocity region. Disk position does not greatly affect the profiles. The curve corresponding to $z_s/H = 0.50$ sits slightly below the other two cases. This is on account of the fact that the recirculation zone is centred at a slightly wider radial position when $z_s/H = 0.70$ and $z_s/H = 0.90$ than when $z_s/H = 0.50$. At the downstream end, i.e. as $z/H \rightarrow 0$, the v_z curves converge. Significantly, none of the curves contain any special features at z/H values in the vicinity of z_s/H . As the profile location is less than $0.13R$ from the outer radius of the disk, this observation indicates that the small disk does not greatly affect the in-plane flow around its outer radius, despite the fact that flow streamlines must diverge slightly from the axis to pass around it. The Γ curves are even more similar than the v_z curves, and once again do not alter as the fluid passes the axial location of the disk.

5.3.3 Case B: Large Disk, $Re=1200$

In Case B, the small scaffold model used in Case A is replaced by a larger scaffold model. Figure 5.5 includes axial and azimuthal velocity distributions in the same format as Figure 5.3. A comparison between the two figures illustrates that the disk has more impact on the VB recirculation pattern when $(Re, r_s/R) = (1200, 3/13)$ than when $(Re, r_s/R) = (1200, 1/13)$. At a disk position of $z_s/H = 0.55$ (Fig. 5.5(a)-(b)), the top surface of the disk extends into the central region of the recirculation zone. While the vectors just above the disk were lost due to intense surface reflection, it can be seen that the recirculation bubble is compressed into the region above the disk. The low-velocity flow around the outside of the disk continues into a low-velocity region downstream, however there appears to be a significant loss of axial and azimuthal momentum immediately below the disk, implying the existence of a wake-like



(a)



(b)

Figure 5.4: Axial profiles of (a), $v_z/(\omega R)$; and (b), $\Gamma/(\omega R^2)$; at $r/R = 0.20$ when $Re = 1200$ and $r_s/R = 1/13$. The different curves correspond to different axial locations of the disk.

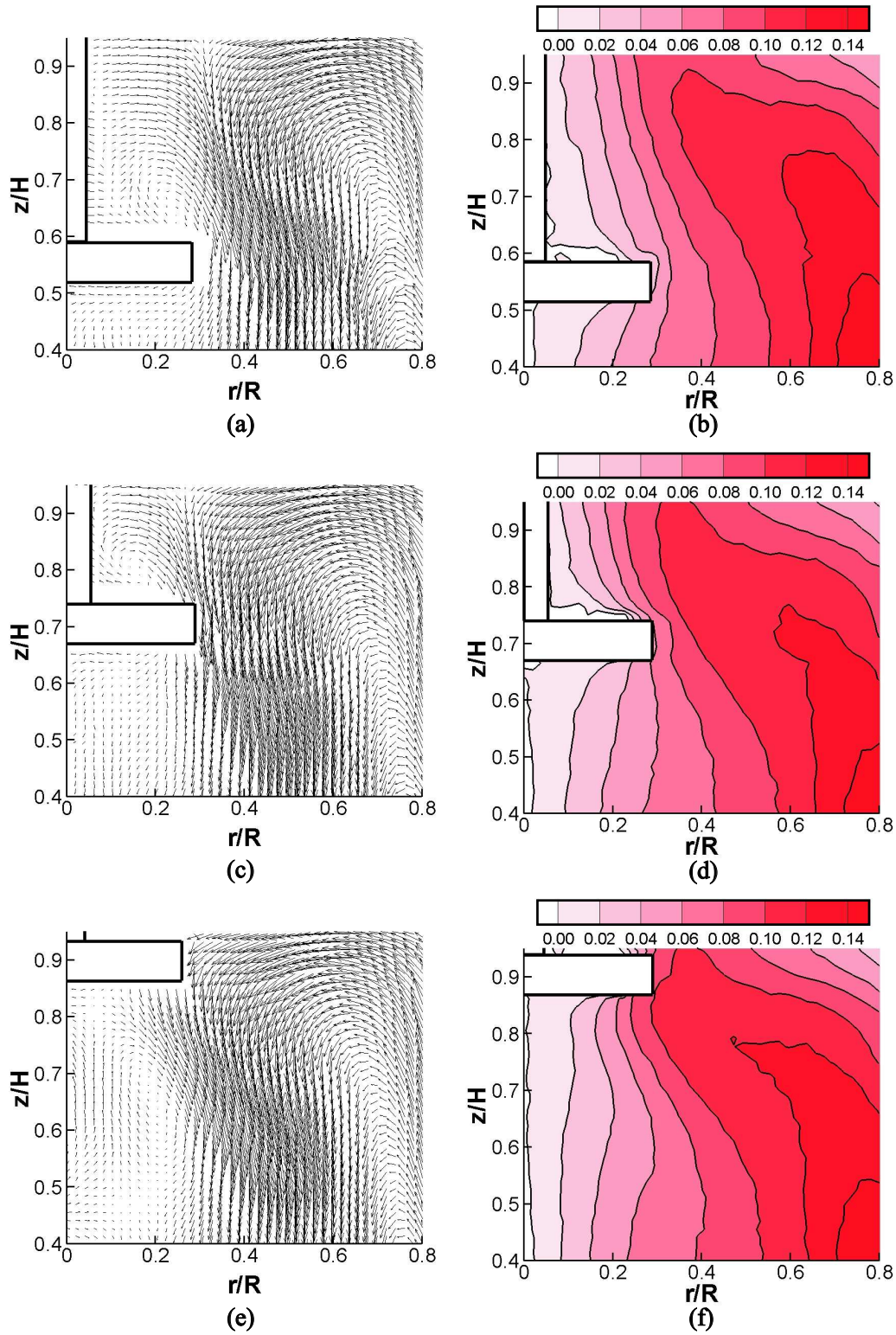


Figure 5.5: Time-averaged velocity fields when $Re = 1200$ and $r_s/R = 3/13$, for various disk locations. The scaffold position is marked. (a) In-plane velocity vectors, $z_s/H = 0.55$; (b) $v_\theta/(R\omega)$ contours, $z_s/H = 0.55$; (c) In-plane velocity vectors, $z_s/H = 0.70$; (d) $v_\theta/(R\omega)$ contours, $z_s/H = 0.70$; (e) In-plane velocity vectors, $z_s/H = 0.90$; (f) $v_\theta/(R\omega)$ contours, $z_s/H = 0.90$.

region. This region of low v_z and v_θ extends radially to the width of the disk. A negative radial flow on the underside of the disk appears to convect fluid toward the centre of the vessel. Further downstream, suction of fluid towards the Ekman layer causes an axial and azimuthal acceleration, so that eventually the in-plane flow in the central vortex region is mostly in the $-v_z$ direction and the azimuthal velocity contours are more evenly distributed across $0 \leq r/R \leq 0.4$. It is worth noting that the velocity field fails to show the spiralling pattern present in Figure 5.2 for similar Re and z_s/H conditions. This invites speculation that the spiral region does not have a flow distinctly different from the remainder of the central vortex region, but rather it is a thin tube of fluid with which the outer-recirculation region fluid does not mix as both descend axially toward the impeller.

For the case where the disk is at $z_s/H = 0.70$ (Fig. 5.5(c)-(d)), the affected region below the disk, which appears similar to that of the $z_s/H = 0.55$ case, is more fully illustrated within the measurement plane. With the disk at $z_s/H = 0.70$, it occupies the position at which the centroid of the VB recirculation zone is usually located; $(0.19, 0.70)$. This occupation causes a relocation, rather than a destruction, of the VB bubble. In this case, the recirculation moves to a position above the disk. The disk causes a radial blockage which almost extends to the boundary of the VB region. This results in an apparent bisection of the upper portion of the low-velocity region, including the recirculation bubble, from the lower portion of the low-velocity region. The fact that the disk lower surface, with its $v_\theta = 0$ condition, comprises the upper boundary of the lower region, accounts for the low azimuthal momentum measured immediately below the disk.

When the disk is at $z_s/H = 0.90$ (Fig. 5.5(e)-(f)), the recirculation centroid is located significantly closer to the original location of $(r/R, z/H) = (0.19, 0.70)$ than the previous two cases, i.e. at a location below, rather than above, the disk. Under further investigation, the transition from a VB recirculation location above the disk to below the disk is found to occur in the range $0.75 < z_s/H < 0.83$.

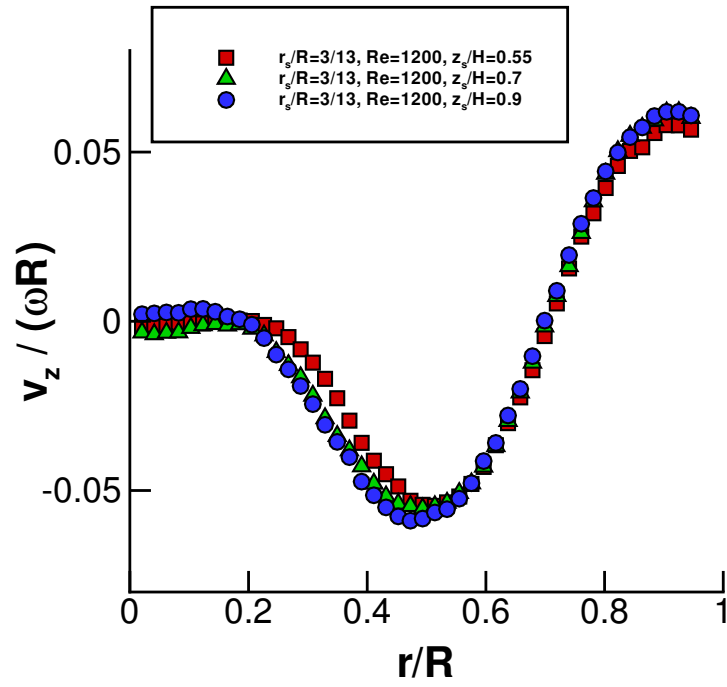
Figure 5.6 includes the normalised profiles of axial velocity, v_z , and circumferential circulation, Γ , across r at $z/H = 0.5$, and provides a comparison between the three cases included in Figure 5.5. Each curve represents the flow profile when $Re = 1200$ and a disk of size $r_s/R = 3/13$ is submerged in the flow, however the location of the disk is different for each curve. All v_z and Γ curves are flatter and have a lower magnitude in the inner radial region, reflecting the relatively slow motion of the fluid there. The profiles corresponding to when the disk is significantly upstream, i.e. at $z_s = 0.7H$ and $z_s = 0.9H$, are similar. When the disk

is much closer to the interrogation line, the r/R range for which velocities are close to zero is slightly larger than for the other two cases. This results from the region of low azimuthal and axial velocity on the underside of the large disk, with a girth of similar magnitude to the diameter of the disk. The locations of the velocity and circulation peaks, which occur in the helical flow region near the cylinder wall, are not affected by the disk.

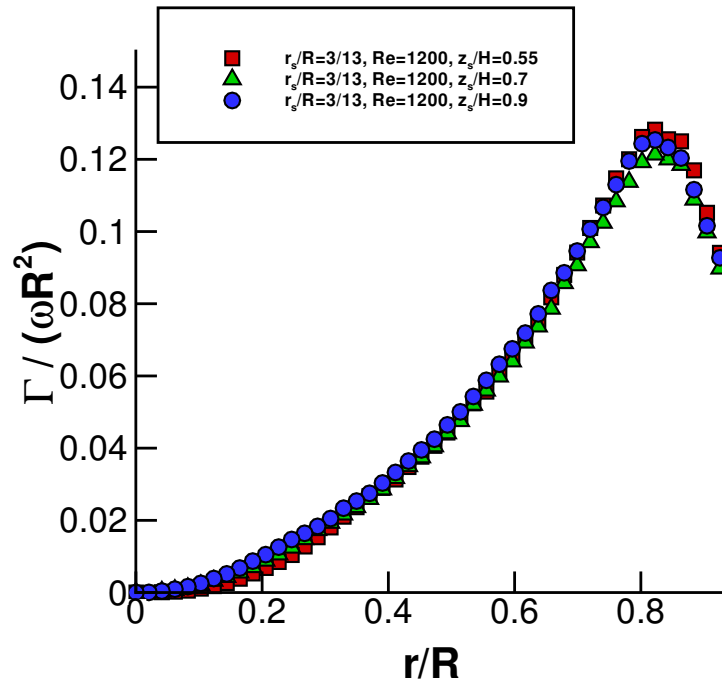
In contrast to Case A, the axial profiles taken at $r/R = 0.20$ differ significantly as z_s is changed (see Figure 5.7). Unlike Case A, the profiles include the disk itself, and so the effect of the blockage on the fluid immediately upstream or downstream is visible. From a distance of $0.1H$ above the top surface of the disk to the surface itself, the axial and azimuthal components decelerate toward $v_z = 0$ and $v_\theta = 0$ respectively. As a result of the recirculation zone being located below the disk, the curve corresponding to $z_s/H = 0.90$ is the most unique. Firstly, the acceleration below the bottom surface of the disk is strongest when $z_s/H = 0.9$, as is evident from the jump in both v_z and Γ to the first data point measured below the disk. Secondly, the $z_s/H = 0.9$ case has both a local minimum point of v_z and a local minimum of Γ beneath the disk. In contrast, the other two cases, corresponding to $z_s/H = 0.55$ and $z_s/H = 0.7$, have a local minimum of v_z above the disk, and no local minimum of Γ . Both of these differences reflect the fact that the recirculation zone is located above the disk when $z_s/H = 0.55$ and $z_s/H = 0.7$, and below the disk when $z_s/H = 0.9$. At locations closer to the disk, there is an increase in both the axial velocity and the circulation. This illustrates the considerable suction effect of the Ekman layer, which clearly has a strong influence on the flow in the downstream end of the breakdown region.

5.3.4 Case C: Large Disk, $Re=2400$

At $Re = 2400$ the submerged disks do not significantly interfere with the VB recirculation. As illustrated by Figure 5.8, this is the case even when $r_s/R = 3/13$. As with the no-disk case, the recirculation bubble is located further from the axis of symmetry at $Re = 2400$ than at $Re = 1200$. Rather than being adjacent to the axis of symmetry, the recirculation zone is toroidal in its three-dimensional geometry, with the region between the column and the inner diameter of the recirculation zone occupied by a low-velocity core vortex region. At $z_s/H = 0.5H$ (Fig. 5.8(a)-(b)), the disk is positioned well below the recirculation zone. At $z_s/H = 0.7$ (Fig. 5.8(c)-(d)), the z -location of the disk is near that of the recirculation centroid. However, the fact that the recirculation is located outside the radius of the disk means that the interference caused by the body is more limited than the corresponding case when $(Re, r_s/R) = (1200, 3/13)$. While

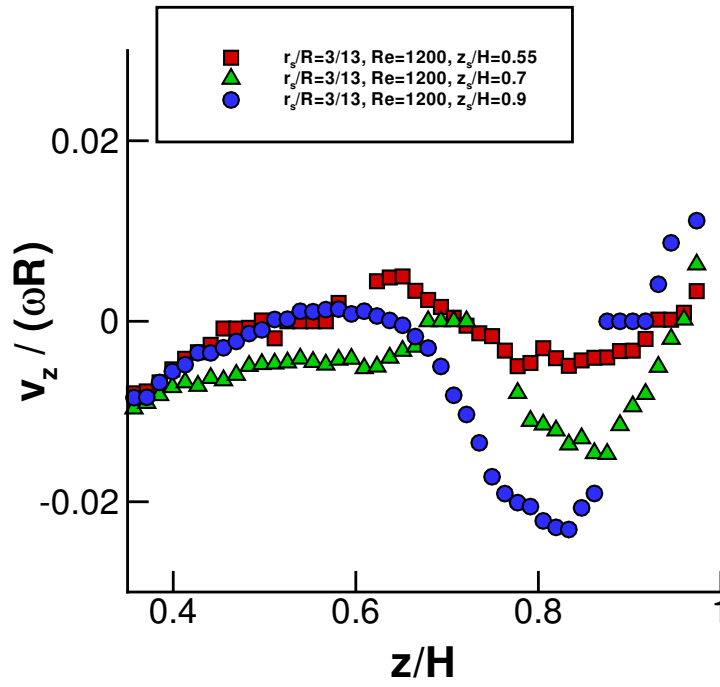


(a)

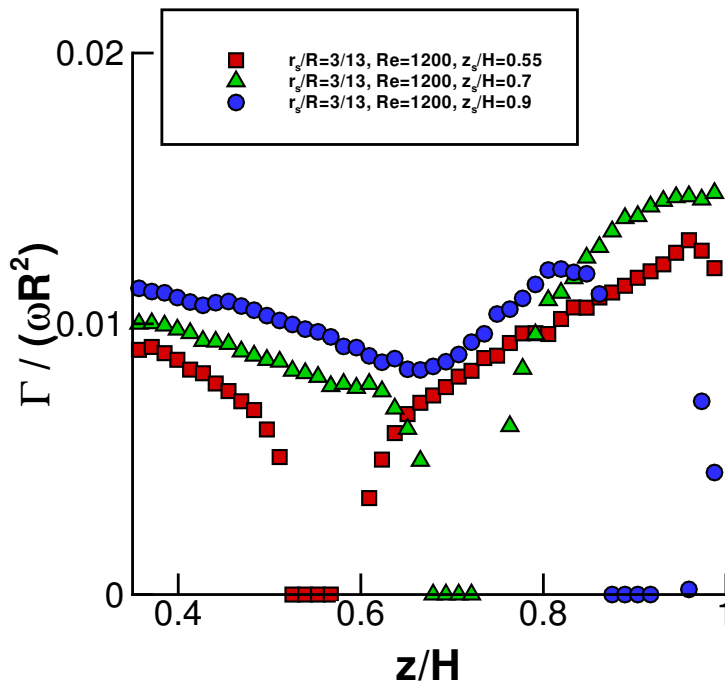


(b)

Figure 5.6: Radial profiles of (a), $v_z / (\omega R)$; and (b), $\Gamma / (\omega R^2)$; at $z/H = 0.50$ when $r_s/R = 3/13$ and $Re = 1200$. The different curves correspond to different axial locations of the disk.



(a)



(b)

Figure 5.7: Axial profiles of (a), $v_z / (\omega R)$; and (b), $\Gamma / (\omega R^2)$; at $r/R = 0.20$ when $Re = 1200$ and $r_s/R = 3/13$. The different curves correspond to different axial locations of the disk.

not all of the vectors on the left-hand side of the VB recirculation could be included in Figure 5.8(c) due to problems caused by reflection, it is clear that the recirculation occurs on the right-hand side of the disk. When the disk is moved to $z_s = 0.9H$, it sits upstream of the recirculation bubble in a similar fashion to when $Re = 1200$.

Significantly, the axial flow in the core vortex region is only in the $-z$ direction below the disk. Above the disk, the axial flow in the core vortex region is consistently in the $+z$ direction. In the absence of the disk, the axial flow in the core vortex region is entirely in the $-z$ direction. The low azimuthal velocity region below the disk does not appear to extend as far in the vertical direction as for Case B. For $z_s/H = 0.7$ and $Re = 2400$, the azimuthal velocity contours within the radius of the disk become parallel at $z/H \approx 0.65$ (or 0.07 disk diameters below the bottom surface of the disk), whereas for $z_s/H = 0.7$ and $Re = 1200$ this occurs closer to $z/H \approx 0.57$ (or 0.26 disk diameters). This indicates that the additional swirl imparted by the impeller on the fluid at higher Re more quickly restores the azimuthal momentum deficit caused by the disk.

The wider position of the VB recirculation zone at $Re = 2400$ means that the axial profiles at $r/R = 0.20$ do not quite pass through it (see Figure 5.9(a)). Thus, the profiles illustrate the effect of disk position near the outer radius of the core vortex region. Generally, $v_z < 0$ below the disk, and $v_z > 0$ above the disk, which, as has already been stated, is a characteristic of the central vortex flow when $Re = 2400$ and $r_s/R = 3/13$. When $z_s/H = 0.90$, the v_z curve crosses 0 at $z/H \approx 0.72$, which is well below the disk. This indicates that the $-v_z$ central vortex region is narrower near the top of the vessel. A gradual widening of the central vortex region occurs as $z/H \rightarrow 0$, which is reflected in an increase in $-v_z$ along the profile. This increase in $-v_z$ occurs in all three profiles, so is more likely dependent on the location of the recirculation zone than the location of the disk.

In contrast, the Γ profiles at $r/R = 0.20$, as shown in Figure 5.9(b), indicate a key role for z_s . As with Figure 5.7, Γ tends toward 0 as z/H approaches the disk from either the upstream or downstream surface, although this deceleration/acceleration process is more abrupt here than for Case B. Upstream of the deceleration region, the measured data points have lower magnitudes than those downstream of the acceleration region. It is evident that the disk separates the slower azimuthal flow near the top of the vessel from the more quickly rotating fluid in the remainder of the vessel. When there is no disk, v_θ increases more evenly in the domain $0.4 \leq z/H \leq 1$, with most of the acceleration occurring in the upper portion of the vessel. In this respect, a disk location of $z_s/H = 0.50$ has the greatest effect on the azimuthal flow in the breakdown region, as the low Γ zone is extended the greatest distance down the axis.

Downstream of the disk, the Γ curves are fairly flat, although there is a slight increase as z/H approaches the Ekman region.

5.3.5 Effect of disk size on flow topology

Analysis of the relative effect on the flow caused by different sized disks is best undertaken by plotting, on the one set of axes, a set of flow profiles corresponding to the same ($Re, z_s/H$) values but different r_s/R values. Figure 5.10 illustrates the effect of disks of varying size on the flow profile upstream. All of the profiles included in this plot were recorded at $z = 0.77H$ and $Re = 2400$. The profile for the no-disk case is included along with those for the three different sized disks, all of which are located at $z_s/H = 0.5$. The large disk causes the greatest deviation in flow profile from the no-disk case. This is most clearly illustrated by the v_z profiles (Fig. 5.10(a)), particularly in the domain $0 < r/R < 0.2$. While the $r_s/R = 3/13$ case retains a fairly flat profile, the smaller and medium-sized disks have profiles which more closely resemble the curved profile of the no-disk case. This is because the larger disk slows a wider region of the near-axis flow than the other two disks. The circulation profiles appear to be not so affected by disk size, although it is worth noting that the Γ value at $r/R \approx 0.2$, i.e. at the boundary of the breakdown region for the no-disk case, reduces slightly as disk diameter increases. This latter observation seems to indicate an additional azimuthal momentum loss caused by the larger disk. The flow profiles in the outer recirculation region do not appear to be affected by the disk.

Figure 5.11 includes flow profiles at the same axial location ($z/H = 0.77$), and at the same Re (2400), as Figure 5.10, however in this case the disk is located above the analysis line, at $z_s/H = 0.90$. Once again, the deviation of the flow from that of the no-disk case is proportional to the size of the disk, and once again there is little difference between the flow profiles in the high-velocity, outer recirculation region, or between the various Γ curves. In contrast to when the disk is located below the analysis line, the axial velocities near $r/R = 0$ are stronger for the submerged-disk cases than for the no-disk case. The strongest downward flow in the core vortex region occurs when the largest disk is used.

Figures 5.12 and 5.13 compare profiles at the same Re as those presented in Figures 5.10 and 5.11, although this time the profiles are vertical and correspond to radial locations of $r/R = 0.20$ and $r/R = 0.80$, respectively. At $r/R = 0.20$, which lies within the near-axis, low-velocity region, there is a positive correlation between the size of the submerged disk and the discrepancy between the respective v_z and Γ curves and the no-disk curve. At the axial location of the disk ($z/H = z_s/H = 0.90$), the difference between the curves is at its greatest.

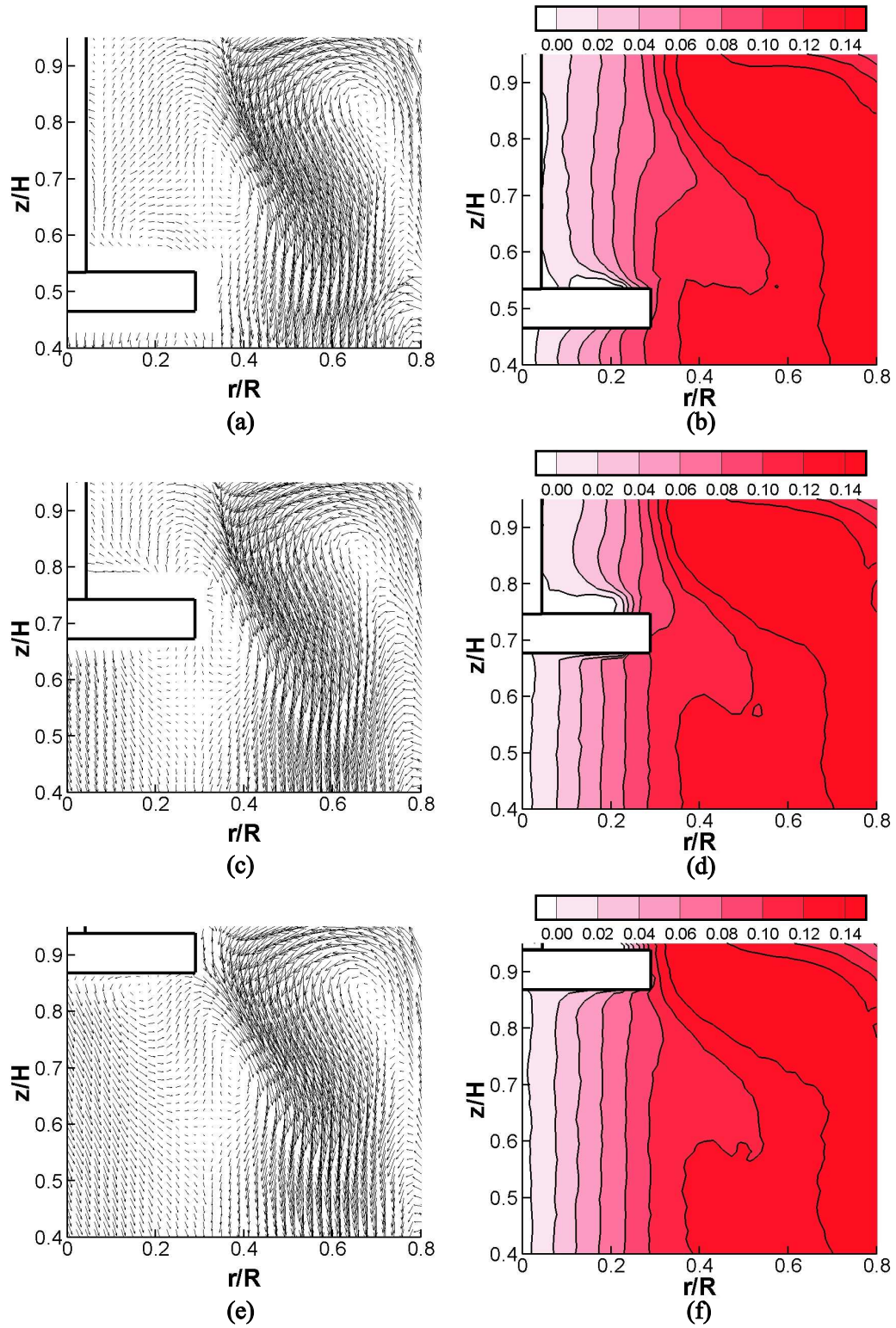
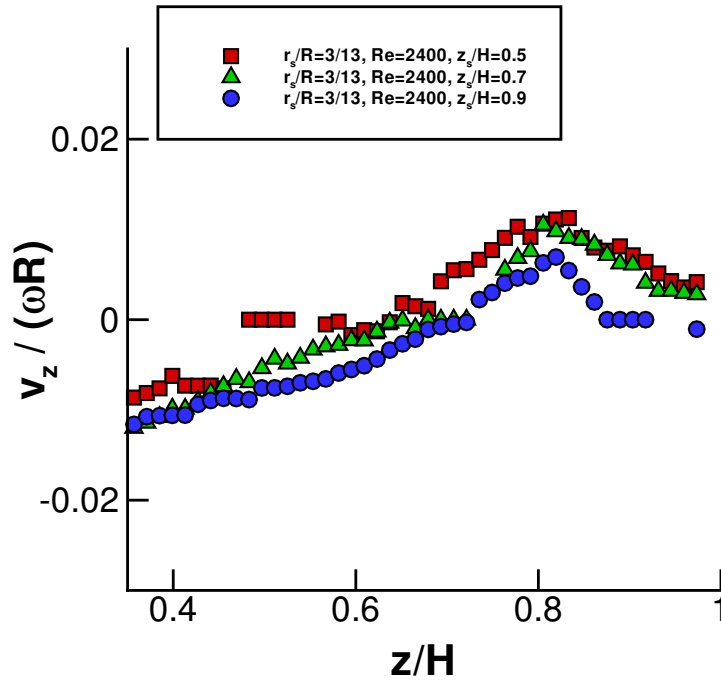
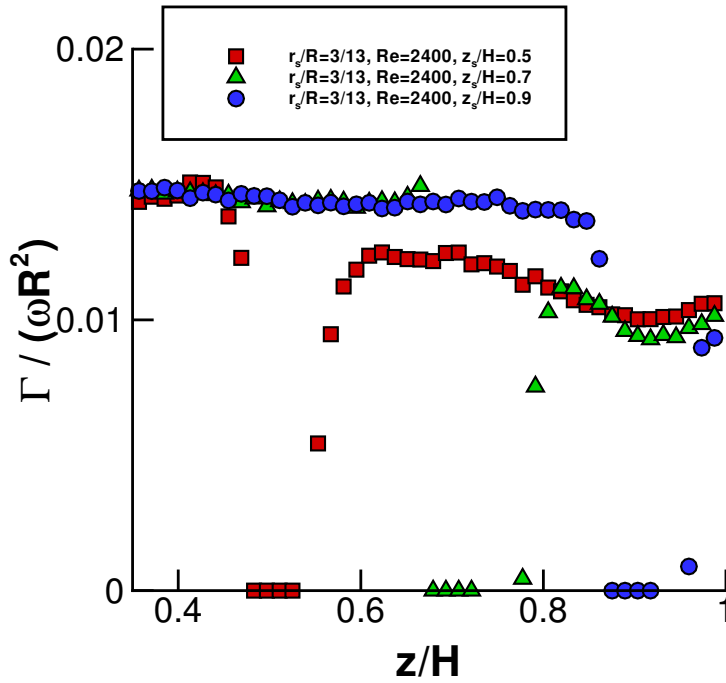


Figure 5.8: Time-averaged velocity fields when $Re = 2400$ and $r_s/R = 3/13$, for various disk locations. The scaffold position is marked. (a) In-plane velocity vectors, $z_s/H = 0.50$; (b) $v_\theta/(R\omega)$ contours, $z_s/H = 0.50$; (c) In-plane velocity vectors, $z_s/H = 0.70$; (d) $v_\theta/(R\omega)$ contours, $z_s/H = 0.70$; (e) In-plane velocity vectors, $z_s/H = 0.90$; (f) $v_\theta/(R\omega)$ contours, $z_s/H = 0.90$.

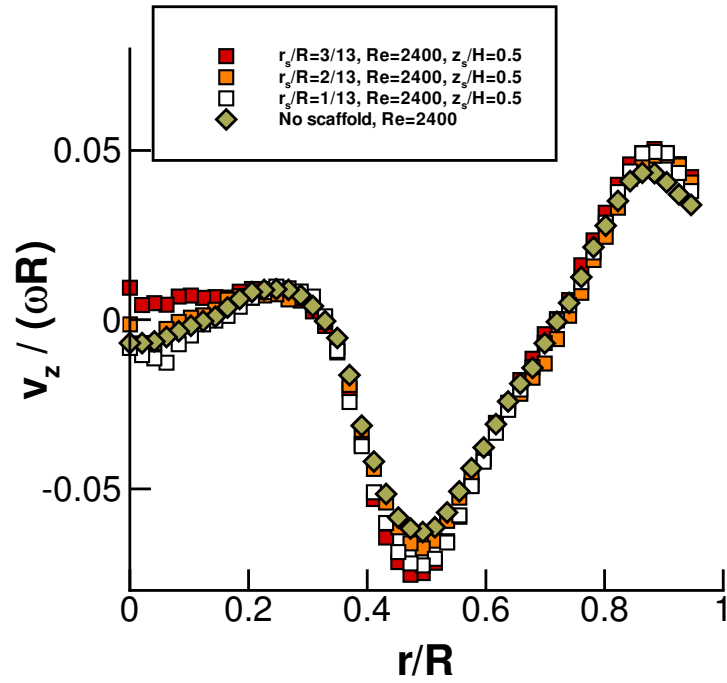


(a)

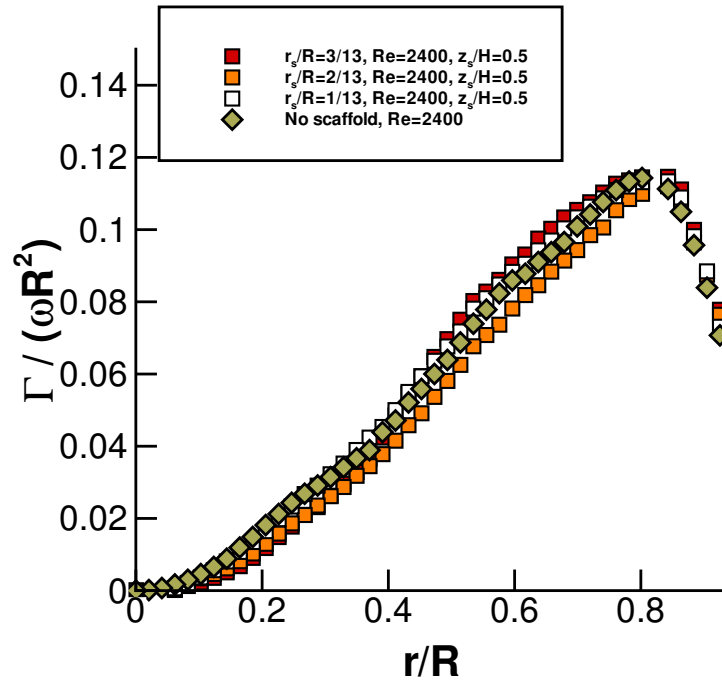


(b)

Figure 5.9: Axial profiles of (a), $v_z / (\omega R)$; and (b), $\Gamma / (\omega R^2)$; at $r/R = 0.20$ when $Re = 2400$ and $r_s/R = 3/13$. The different curves correspond to different axial locations of the disk.

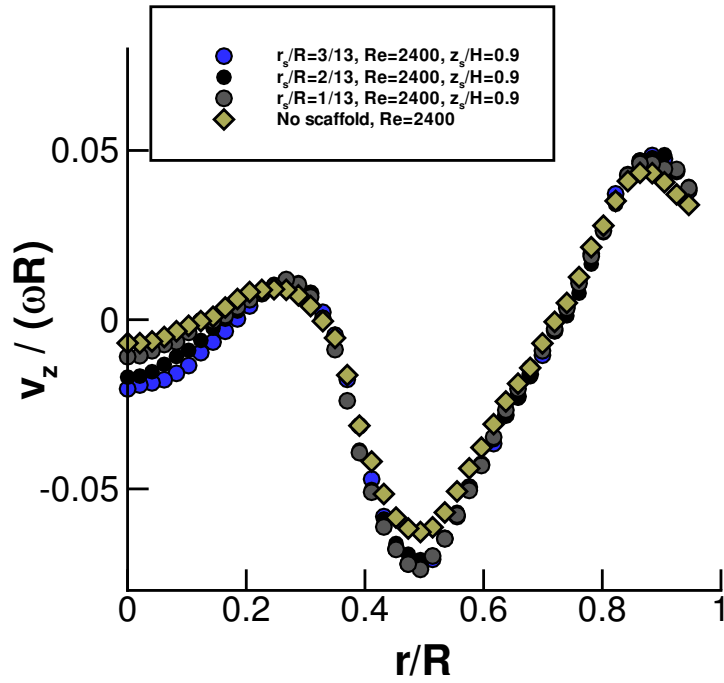


(a)

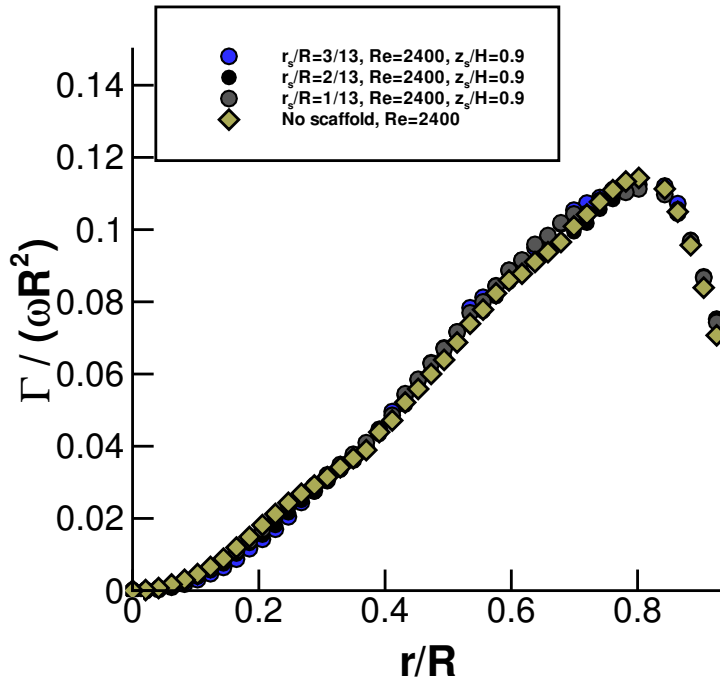


(b)

Figure 5.10: Radial profiles of (a), $v_z / (\omega R)$; and (b), $\Gamma / (\omega R^2)$; at $z/H = 0.77$ when $Re = 2400$, and a disk is located at $z_s/H = 0.50$. The different curves correspond to different disk sizes.



(a)

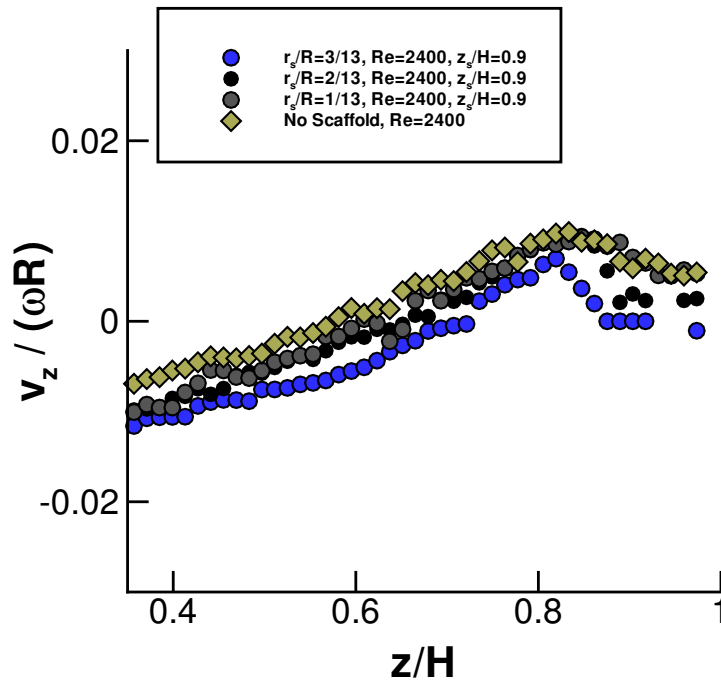


(b)

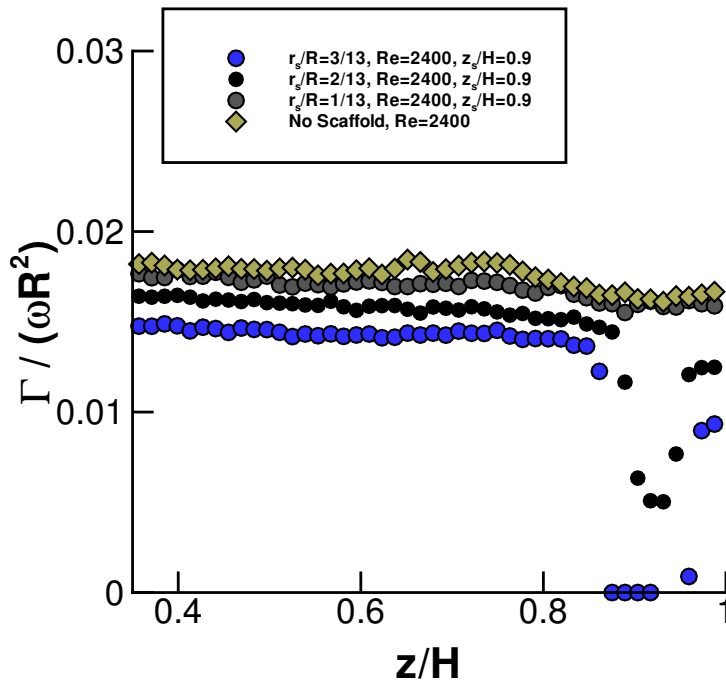
Figure 5.11: Radial profiles of (a), $v_z / (\omega R)$; and (b), $\Gamma / (\omega R^2)$; at $z/H = 0.77$ when $Re = 2400$, and a disk is located at $z_s/H = 0.90$. The different curves correspond to different disk sizes.

This is because the interrogation line ($r/R = 0.20$) lies a significant radial distance from the outer edge of the small disk, just outside the outer radius of the medium-sized disk, and within the outer radius of the large disk. Consequently, v_z and Γ curves in the vicinity of $z/H = 0.9$ do not diverge from the no-disk curve when $r_s/R = 1/13$, are slightly retarded when $r_s/R = 2/13$, and are equal to 0 when $r_s/R = 3/13$.

As illustrated by Figure 5.13, the differences caused by disk size are less noticeable at a radial section of $r/R = 0.80$, which is located well within the outer recirculation region. The spread of the four curves taken at $r/R = 0.80$ is much less than of those taken at $r/R = 0.20$, and the shape of the curves corresponding to the submerged-disk cases show a stronger resemblance to the no-disk case. Indeed, when $z_s = 0.5$ and $Re = 2400$, as shown in Fig. 5.13, the difference in profiles is negligible. This represents further evidence that submerged disks of the sizes investigated here have very little influence on the flow in the outer recirculation region.

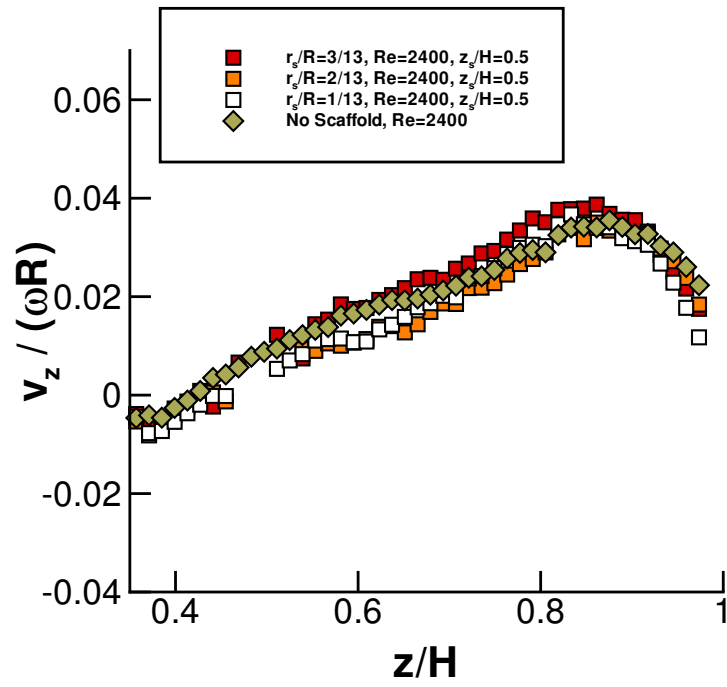


(a)

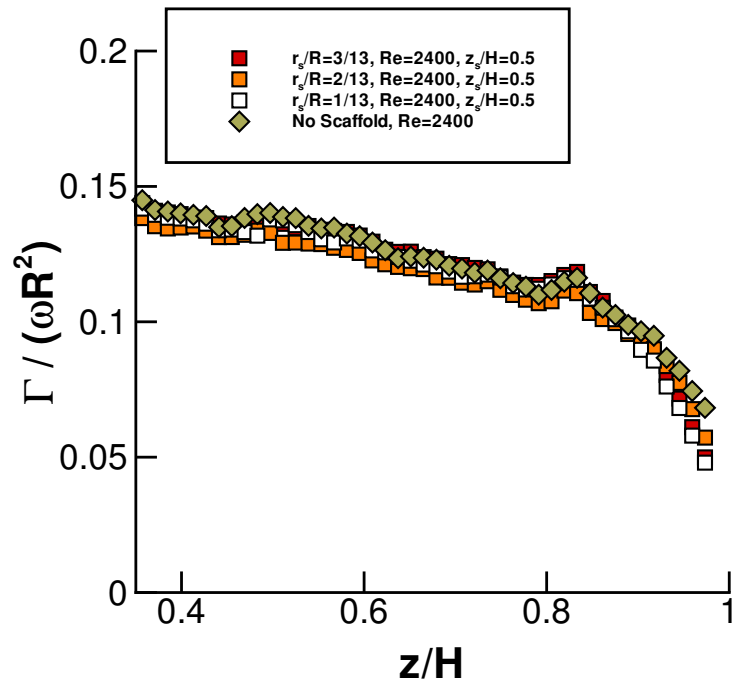


(b)

Figure 5.12: Axial profiles of (a), $v_z/(\omega R)$; and (b), $\Gamma/(\omega R^2)$; at $r/R = 0.20$ when $Re = 2400$ and a disk is located at $z_s/H = 0.90$. The different curves correspond to different disk sizes.



(a)



(b)

Figure 5.13: Axial profiles of (a), $v_z / (\omega R)$; and (b), $\Gamma / (\omega R^2)$; at $r/R = 0.80$ when $Re = 2400$ and a disk is located at $z_s/H = 0.50$. The different curves correspond to different disk sizes.

5.4 Principal Stress Fields

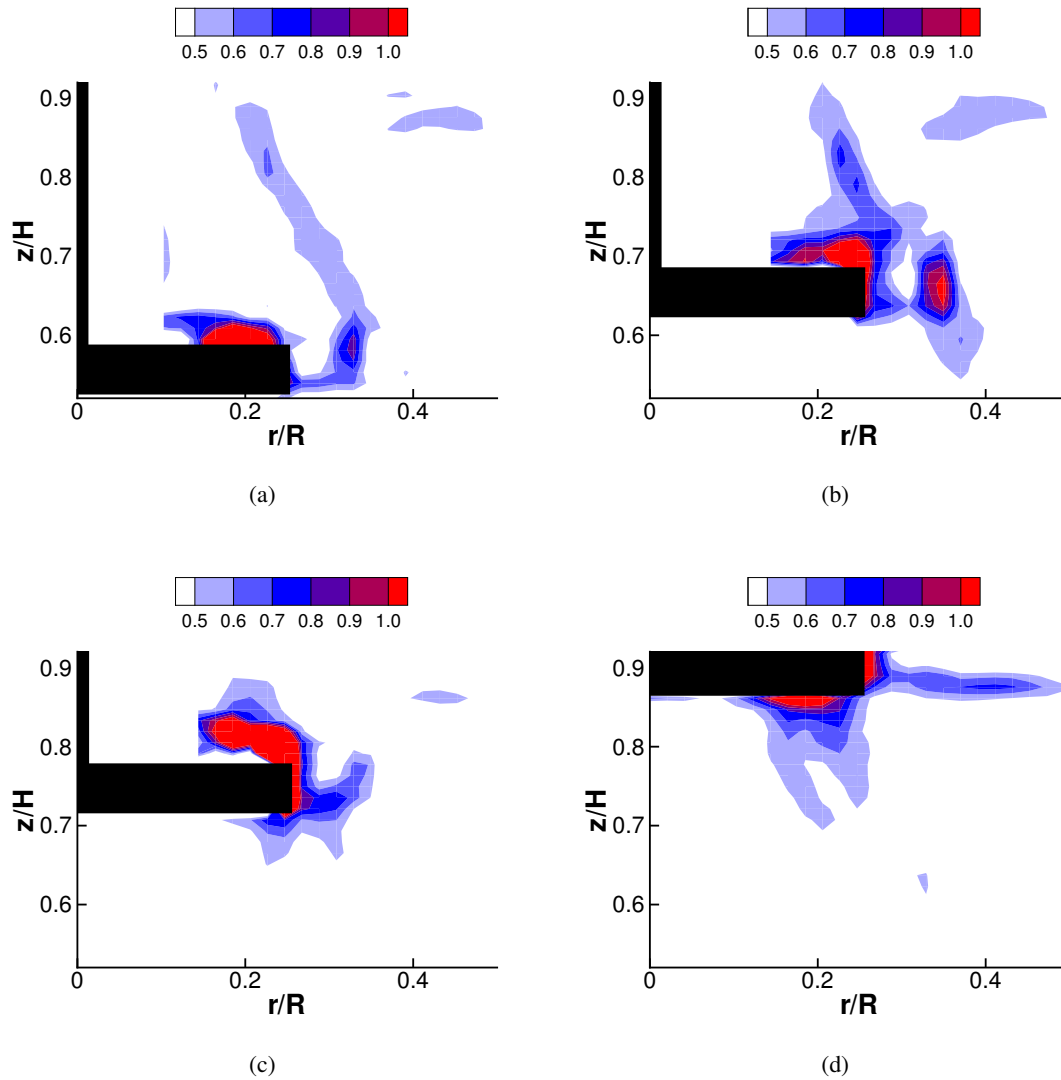


Figure 5.14: Contours of $\sigma_3/(\omega\mu)$ when $r_s/R = 3/13$ and $Re = 1200$. The bluff body position is blanked out. The scaffold axial position is (a) $z_s/H = 0.55$; (b) $z_s/H = 0.65$; (c) $z_s/H = 0.75$; and (d) $z_s/H = 0.90$.

As demonstrated in Chapter 4, the magnitude and direction of viscous stresses in the bioreactor can be estimated from the three-component velocity measurements. Figure 5.14 represents various spatial distributions of σ_3 , the largest principal stress component, non-dimensionalised by the product $\omega\mu$. The plotted area is enclosed by $0 \leq r/R \leq 0.5$ and $0.5 \leq z/H \leq 0.9$, which includes the VB recirculation region and a scaffold located on the axis of symmetry. Four plots are shown, corresponding to different axial positions of the large disk. Due to the significant processing noise, only peak stress regions, corresponding to $\sigma_3/(\omega\mu) > 0.5$, are presented in the plots. One peak stress region, consistent in all the plots, corresponds to

the interface between the outer radius of the vortex breakdown region and the outer recirculation region. It has been shown in the previous chapter that this peak stress region also occurs when the disk is not present. The other peak stress region, not found in the plots in Section 4.7, is concentrated around the upper and side surfaces of the disk, and is caused by the imposition of the body on the fluid. As seen in Figure 5.14, moving the large disk toward the surface causes an interference with the peak stress region at the interface of the VB region. At $z_s/H = 0.90$ the outer radius of the disk occupies part of the outer recirculation region, rather than the breakdown region, and so the location of the interfacial peak stress zone becomes more ambiguous.

The stress measurements nearest to the disk are noisy, as the processing magnifies any PIV error caused by surface reflections, and the σ_3 values nearest to the column have been omitted for this reason. However, it is apparent that the peak stress levels surrounding the disk are of higher magnitude than the vortex breakdown boundary stresses. It can be inferred from this that adherent cells or tissue constructs on the outer surface of the disk will experience higher mean principal stresses than non-adherent cells suspended within the vortex breakdown region. It is worth remembering that the peak stresses experienced by cells suspended in the outer recirculation region are higher than those experienced by cells suspended within the VB region. The three-dimensionally resolved wall shear stress profiles are of particular interest to a cell or tissue culture application, and so are discussed at length in the following section.

5.5 Wall Shear Stresses

Wall shear stress, τ_w , is given by Equation 2.9. In the current investigation, the velocity v_t is the magnitude of the velocity vector resolved in the plane parallel to the surface. As this resolved vector takes into account all relevant velocity components, it is possible to obtain the full value of τ_w rather than a meridional plane approximation. Since the velocity data just outside the radius of the disk were unreliable due to blockage of the measurement plane caused by the front of the disk, only the upper and lower surfaces of the scaffold are considered. For this reason, the horizontal tangential velocity component v_t is given by $v_t = \sqrt{v_r^2 + v_\theta^2}$. During the calculation of $\partial v_t / \partial z$, velocity vectors up to a distance of $0.02H$ away from the surface were used, and $v_t = 0$ was assumed at the scaffold surface.

Primarily because of the manner in which v_θ increases with r , τ_w typically increases steadily from the centre to the radius of the disk. Changing the motion of the fluid in the immediate vicinity of the scaffold, e.g. by changing Re , z_s , or R_s , can affect the wall shear distribution, but a positive relationship between τ_w and r is consistently observed. Figures 5.15 and 5.16 include profiles of τ_w for Case B, $(Re, r_s/R) = (1200, 3/13)$, and Case C, $(Re, r_s/R) = (2400, 3/13)$, when the disks are located at various axial positions. The r/R axis is adjusted to $0 \leq r/R \leq 0.23$, which encompasses, but does not extend beyond, the full radius of the largest disk. Due to the resolution constraints inherent in the measurement system, only a small number of data points were recorded across the surface of the small scaffold, and so Case A, $(Re, r_s/R) = (1200, 1/13)$, is not plotted. Fewer grid points are included in the plots corresponding to the upper surface τ_w profiles because intense surface reflections in the vicinity of the support column usually prevented correct PIV correlation in the region $0 \leq r/R \lesssim 0.06$.

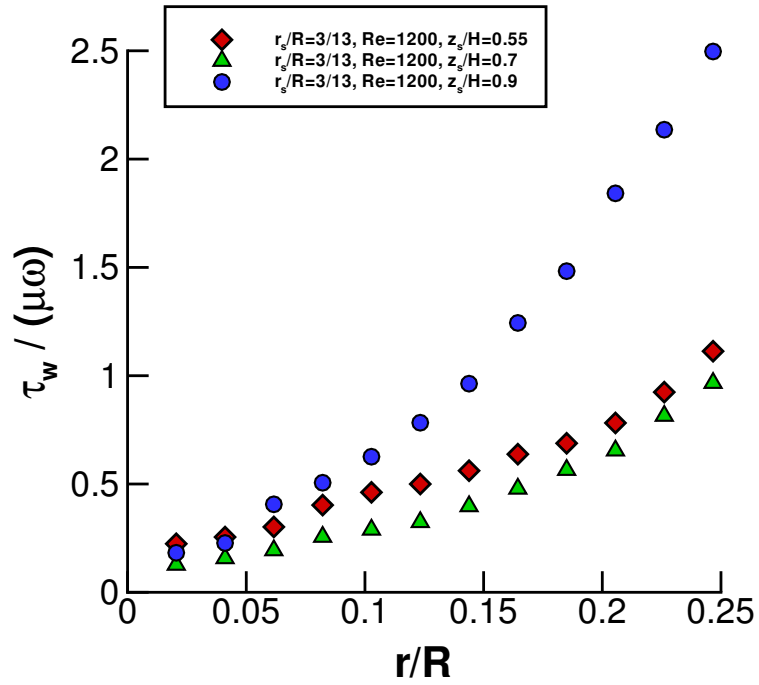
For Case B, τ_w approaches 0 as $r/R \rightarrow 0$ and peaks as $r/R \rightarrow r_s/R$. As illustrated by Figure 5.15(a), similar shear profiles occur along the bottom surface of the disk when $z_s/H = 0.55$ and $z_s/H = 0.70$. It is worth remembering that for these cases, the VB recirculation bubble is located above the disk, and a region of low v_θ and low v_z is located below the disk. At $z_s/H = 0.90$ the recirculation occurs below the disk. The τ_w values are higher for this case, as there are relatively strong radial and azimuthal flows just below the shear layer on the bottom surface of the disk. This is because the upper end of the recirculation zone appears to be located on or very near the surface. For $r/R > 0.10$ the difference between the τ_w profile for $z_s/H = 0.90$ and the other two τ_w profiles becomes, in percentage terms, increasingly large. Because the breakdown bubble narrows upstream of the VB recirculation, the fluid slightly below the outer part of the disk bottom surface, i.e. in the region $0.13 \lesssim r/R \lesssim r_s/R$, constitutes

part of the outer recirculation zone. The higher velocities in the outer recirculation region lead to a stronger wall shear layer.

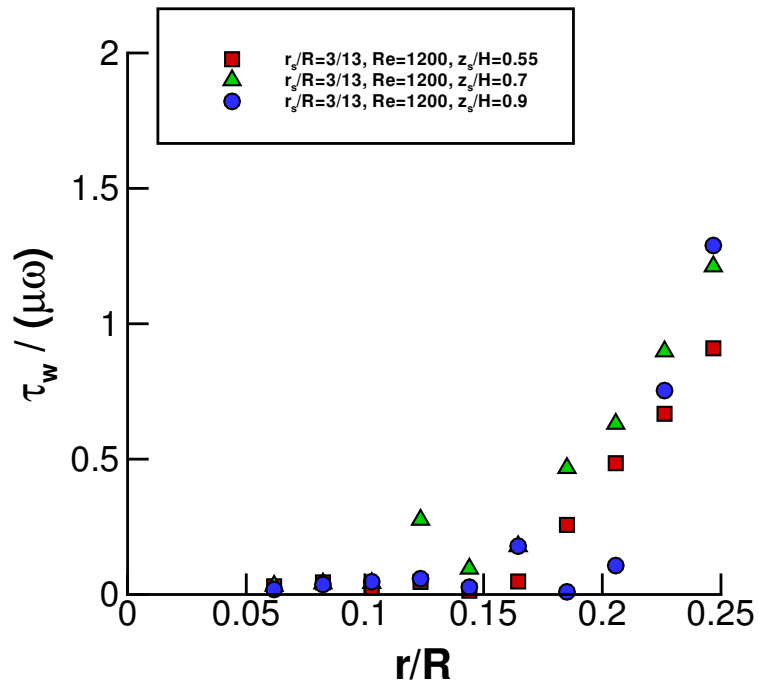
On the upper surface of the disk, the curves corresponding to the three disk positions have a greater similarity (Fig. 5.15(b)). τ_w is of very low magnitude up to $r/R \sim 0.13$, as the flow is almost stagnant in the region where the support column and the disk are joined. From $r/R \approx 0.13$ to $r/R \approx 0.21$ the data becomes noisier, but it appears that τ_w increases more steeply for the $z_s/H = 0.55$ and $z_s/H = 0.70$ cases than for $z_s/H = 0.90$. This is possibly because this region of the r -axis corresponds to the VB recirculation bubble, where larger radial velocities occur above the disk. For $r/R \gtrsim 0.21$, τ_w increases rapidly with respect to r . The steep curve is a result of there being much higher azimuthal velocities near the outer radius of the disk than near the axis. The difference in v_θ between $r/R = 0.20$ and $r/R = r_s/R$, measured at a distance of $0.02H$ above the top surface, is greater than the equivalent difference measured at a distance of $0.02H$ below the bottom surface. This appears to be because the distribution of the v_θ contours approaching the disk surface differs on the upstream side to the downstream side (as illustrated in Figs. 5.5(b), (d), and (f)). It should be noted that at an axial location closer to the scaffold than $z/H = 0.02$, the estimated $\partial v_t / \partial r$ values may change on both sides of the disk. Optical issues prevented the capture of velocities closer to the wall, however the velocity fields obtained still facilitate useful approximations of τ_w .

Top and bottom surface wall shear profiles corresponding to $(Re, r_s/R) = (2400, 3/13)$ are presented in Figure 5.16. The τ_w values along the bottom surface once again increase with r , although in this case the relationship is considerably more linear than for Case B. Theoretically the curves should pass through the origin, however in the results presented in Figure 5.16 some radial cross-flow on the measurement plane near the axis of symmetry prevented this from occurring. As the centroid of the VB recirculation bubble is located just outside the radius of the disk when $Re = 2400$, the position of the recirculation in relation to the disk seems to less affect the τ_w distribution than when $Re = 1200$. In contrast to the linear τ_{rz} profiles on the underside of the disk, the profiles on the upper side differ in the inner and outer radial regions. In this regard, the profiles in Figure 5.16(b) are similar to those corresponding to when $Re = 1200$ (Fig.5.15(b)). At the inner radii, τ_w is quite low as a result of the near-stagnant region. At the outer radii ($r/R \gtrsim 0.21$), the azimuthal velocity just above the disk increases rapidly with r , causing an increase in τ_w , as discussed previously.

For the sake of comparison, Figure 5.17 includes τ_w profiles along the bottom surface of disks of all three different sizes at both $Re = 1200$ and $Re = 2400$. For most of the profiles

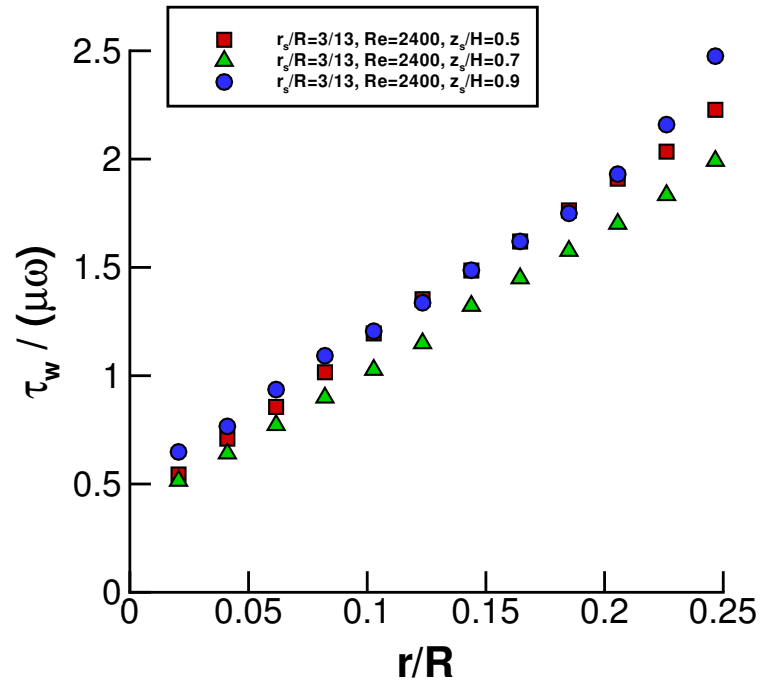


(a)

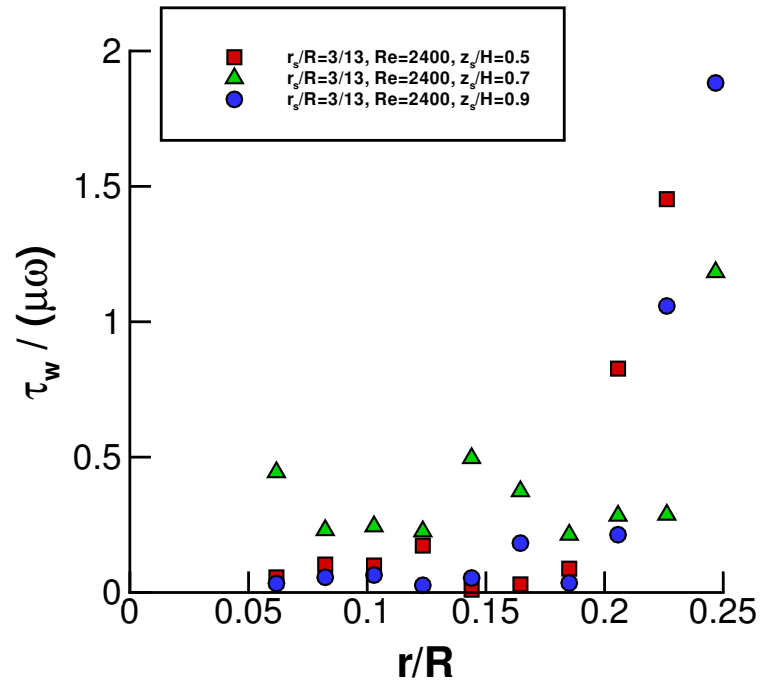


(b)

Figure 5.15: $\tau_w / (\mu\omega)$ distribution along (a), the bottom surface of the disk; and (b), the top surface of the disk; when $r_s/R = 3/13$ and $Re = 1200$. The different curves correspond to different axial locations of the disk.



(a)



(b)

Figure 5.16: $\tau_w/(\mu\omega)$ distribution along (a), the bottom surface of the disk; and (b), the top surface of the disk; when $r_s/R = 3/13$ and $Re = 2400$. The different curves correspond to different axial locations of the disk.

plotted in this graph, the scaffold location is $z_s/H = 0.5$. The exception is the $(Re, r_s/R) = (1200, 3/13)$ case, which was successfully recorded closer to $z_s/H = 0.55$ than $z_s/H = 0.5$. The first points of interest include the noticeable differences between $Re = 1200$ and $Re = 2400$. The τ_w values are consistently of higher magnitude at $Re = 2400$ than at $Re = 1200$. This results from the considerably stronger v_θ component in the central vortex region when $Re = 2400$. Furthermore, the $Re = 2400$ curves are more linearly distributed with respect to r than those of $Re = 1200$. Once again, this reflects the nature of the respective v_θ distributions outside the shear layer.

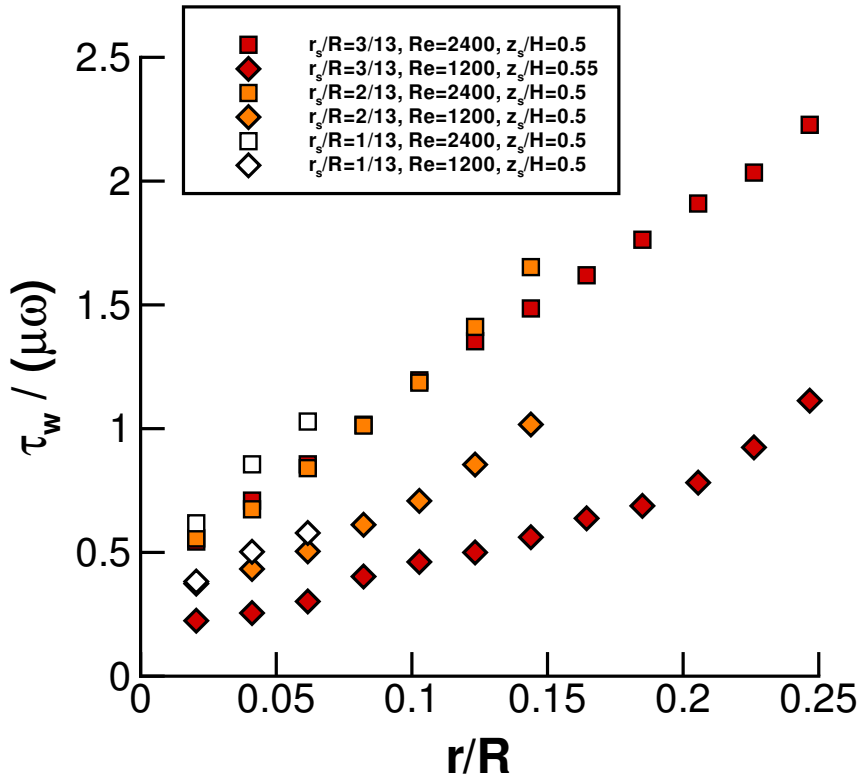


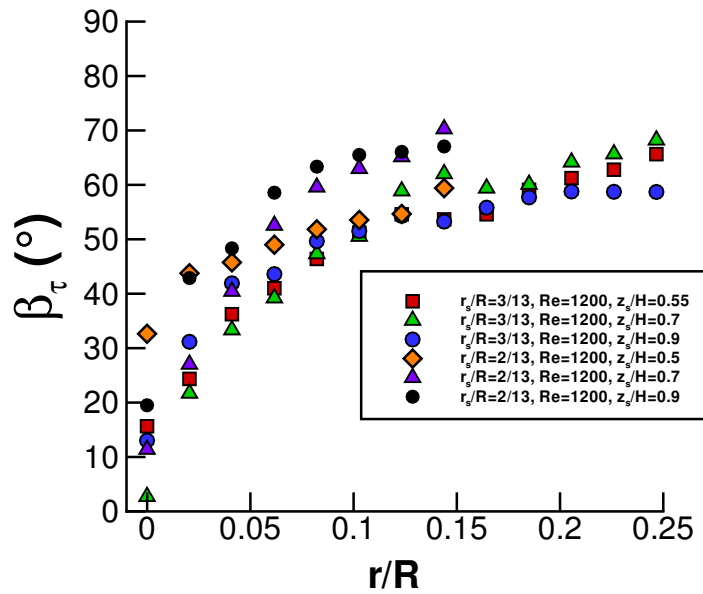
Figure 5.17: Comparison of $\tau_w/(\mu\omega)$ profiles along the bottom surface of a disk located at or near $z_s/H = 0.5$. Symbol colours represent different values of r_s/R , while \diamond symbols represent $Re = 1200$ and \square symbols represent $Re = 2400$.

A comparison between disk sizes is also of interest. Except for the single case corresponding to an axial disk location of $z_s/H = 0.55$, there is close alignment between the curves corresponding to the same Re value but different r_s/R values. Due to the small amount of data obtainable near the surface of the small disks, the white symbols provide little information about the distribution of the stresses along these disks. However, it is clear that the τ_w values along the small disks are of a similar magnitude to those along the medium-sized and larger disks.

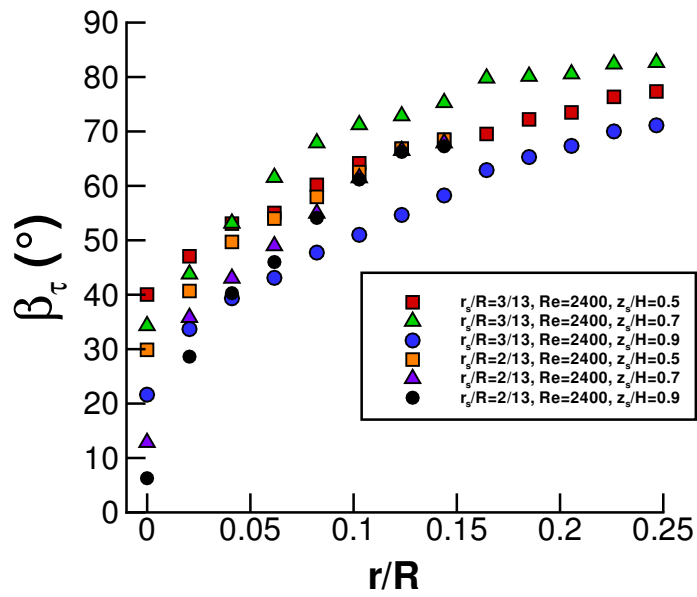
The τ_w curves corresponding to $(Re, r_s/R) = (2400, 2/13)$ and $(Re, r_s/R) = (2400, 3/13)$ are aligned until $r/R \approx 0.12$, from which point the $(Re, r_s/R) = (2400, 2/13)$ curve gradually deviates to a higher magnitude. Similarly, the curves corresponding to $(Re, r_s/R) = (2400, 3/13)$, $(Re, r_s/R) = (1200, 2/13)$ and $(Re, r_s/R) = (1200, 3/13)$ turn upward near the outer radius of the disk, although the increase is relatively greater for the $Re = 1200$ cases. The consistency of this observation leads to the conclusion that cell or tissue material near the radius of the scaffold will be exposed to a higher level of wall shear stress than that closer to the axis of symmetry.

The direction in which the resolved wall shear stress acts relative to the meridional plane, β_τ , varies across the radius of the scaffold. As illustrated by the line plots in Figure 5.18, the β_τ distribution is similar for all the $r_s/R = 2/13$ and $r_s/R = 3/13$ cases investigated. Due to a lack of data, the $r_s/R = 1/13$ cases are not included in Figure 5.18. As $r \rightarrow 0$, β_τ asymptotes toward zero, meaning that τ_w becomes more aligned with the meridional plane. As r increases, β_τ increases logarithmically then plateaus in the outer half of the disk radius. The positive β_τ trend with respect to r reflects an increasing dominance of the azimuthal flow over the meridional plane flow at positions further from the axis of symmetry. The point at which β_τ crosses 45° represents the radial position at which v_θ begins to exceed v_r .

The spread between the curves can be attributed to the measured differences in the internal region flow topology, which result in different v_θ/v_r ratios local to the scaffold surface. For example, when the VB recirculation is located below the scaffold surface, such as when $r_s/R = 3/13$, $Re = 1200$ and $z_s/H = 0.9$, the ratio of azimuthal to in-plane flow near the scaffold perimeter is slightly lower than in other cases, and therefore the β_τ curve remains relatively low (see Fig. 5.18(a)). Similarly, at $Re = 1200$ the β_τ profiles asymptote toward a slightly lower value than at $Re = 2400$. This is probably because the region of reduced azimuthal momentum downstream of the bluff body is spatially larger at $Re = 1200$ than at $Re = 2400$, (see Subsection 5.3.4), and therefore the ratio v_θ/v_r is of lower magnitude at the measurement location.



(a)



(b)

Figure 5.18: The distribution of wall shear stress angle β_τ along the bottom surface of the disk when (a), $Re = 1200$; and (b), $Re = 2400$. The different curves correspond to different sizes and axial locations of the disk.

5.6 Radial Displacement of Scaffold Models

As scaffolds submerged within bioreactors are often located away from the cylinder axis of symmetry, it is important to consider the effect of displacing the scaffolds in the radial direction by an amount x_s . The structural distortion of the breakdown region and the changes to the τ_w distribution are particularly relevant to a scaffold/bioreactor application. The radial displacement experiments described in this section were carried out with parameter values of $Re = 1200$, $r_s/R = 3/13$, and $z_s/R = 0.75$. These values correspond to a case where the scaffold has a relatively strong effect on the surrounding breakdown region flow. Beneficially, this means that the robustness of the flow structure to changes in x_s was tested under circumstances where the flow is likely to be most sensitive to a shift in scaffold position.

5.6.1 Axial Velocity Field

Figure 5.19 represents the normalised axial velocity field when the scaffold is located at radial positions in the range $0 \leq x_s/R \leq 0.35$. Due to the asymmetry enforced by the off-centre disk, the flow fields presented include data on both the left and right hand side of the cylinder's axis of symmetry. The measurement plane field of view is enclosed by $-0.5 \leq r/R \leq 0.5$ and $0.6 \leq z/H \leq 0.9$, meaning that the aspect ratio of the vertical axis to the horizontal axis is substantially greater on the plotted figure than in real space. While blockages of the laser light-sheet by the scaffold model reduced the signal to noise levels on the left hand side of the model, sufficient light passed through the semi-transparent disk material to resolve the flow on this side. Axial velocity contours provide the simplest illustration of the effect of x_s on the velocity field in the vicinity of the breakdown region, particularly since the other velocity component measurements contain more experimental noise.

When the disk is located on the cylinder's axis of symmetry (i.e. $x_s/R = 0.00$), the v_z field is approximately axisymmetric. The VB recirculation bubble can be distinguished by the light red contours (representing positive v_z), adjacent to the light blue contours (representing negative v_z), immediately above the disk. The fluid below the disk has a very low axial velocity. Interestingly, at $z_s = 0.75$, a scaffold vertical position near the upper limit of the cases for which the recirculation bubble is located above the disk, the $-v_z$ flow in the near-disk central vortex region is very weak. Indeed, a slight positive axial velocity was recorded at some locations in the VB region between $z/H = 0.6$ and $z/H = 0.72$. Of course, it is worth recalling that when there is no disk the axial flow near the axis of symmetry is in the positive direction for $0.6 \leq z/H \leq 0.9$. The strong negative v_z region, designated by the dark blue contours,

represents the downward flow near the inner radius of the outer recirculation region.

It has already been shown how stable the $Re = 1200$ outer recirculation region flow profile is to the introduction of scaffolds. Figure 5.19 shows that the space occupied by the low-velocity region can increase as the distance x_s increases, thereby forcing the outer recirculation region to distort. At $x_s/R = 0.05$ (Fig. 5.19(b)), the contours still appear nearly axisymmetric about $r/R = 0$, despite the slight displacement of the scaffold. As the flow is generated by a turntable aligned with the cylinder, the azimuthal recirculation tends to be centred on the cylinder's axis of symmetry. It is then perhaps not surprising that such a slight displacement of the disk is not matched by an equal displacement of the VB region.

Around $x_s/R = 0.15$ (Fig. 5.19(c)), the low-velocity zone immediately above and below the disk makes a noticeable impression on the boundary of the breakdown region. The higher magnitude v_z contours (e.g. $v_z/(R\omega) = -0.02$ and $v_z/(R\omega) = -0.03$) on the side of the plane with no disk are mostly unchanged except for a slight shift toward the $-r$ direction between $x_s/R = 0.00$ and $x_s/R = 0.15$. This minor shift results from a slight narrowing of the breakdown region on the right-hand side of the measurement plane caused by the gradual removal of the disk from that side.

By $x_s/R = 0.25$ (Fig. 5.19(d)), the v_z contours on the left-hand side of the measurement plane are substantially affected. The low-velocity region extends to a much wider radius at z_s , and v_z is reduced above the disk in the region $-0.5 < r/R \leq -0.25$. This reduction represents a distortion of the outer recirculation region to accommodate the local widening of the left-hand side of the breakdown region. This trend continues at $x_s/R = 0.35$, (Fig. 5.19(e)), where the low-velocity region is extended even further than at $x_s/R = 0.25$. Consequently, the outer recirculation pattern is heavily distorted on the side of the bioreactor where the scaffold is located, as the flow approaching this region must diverge radially to bypass the near-stagnant zone surrounding the disk. On the opposite side of the cylinder, the v_z contours are virtually unchanged from the previous cases. No measurements were taken to test the $r - z$ plane flow fields at different azimuthal positions, however this was not necessary as the two halves of the cylinder shown here are of most interest. It was observed that the side of the vessel toward which the scaffold is displaced, (i.e. the left hand side of the images), represents the θ cross-section with the greatest breakdown region distortion, while the opposite side (the right-hand side) represents the θ cross-section with the least breakdown region distortion. Interestingly, the axial flow field in the $r/R \approx 0.2$ region, i.e. near the edge of the VB recirculation bubble, is similar to the no-disk case. Furthermore, the flow near the axis of symmetry is almost entirely

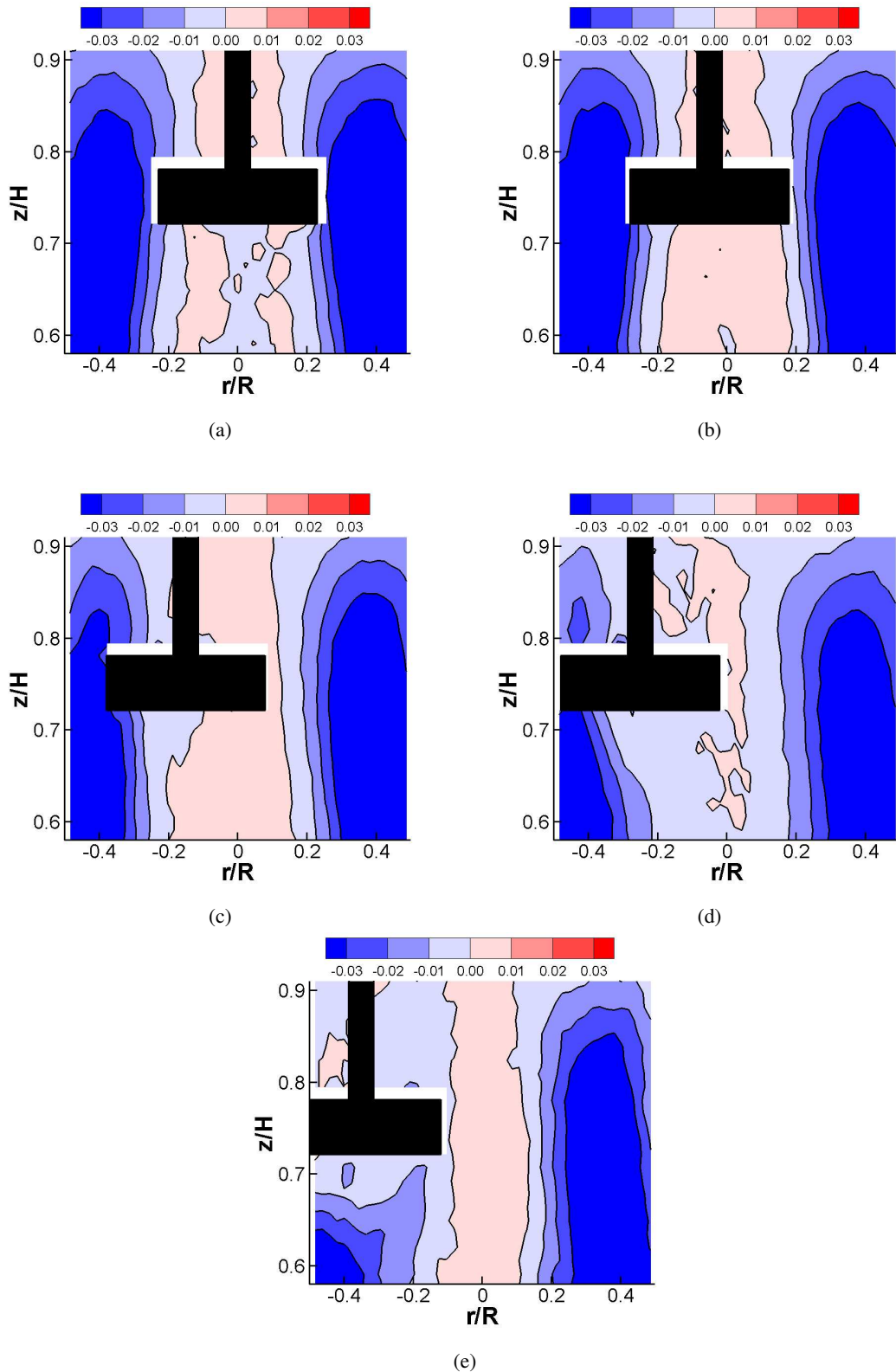


Figure 5.19: Time-averaged $v_z/(\omega R)$ fields when $Re = 1200$, $r_s/R = 3/13$, $z_s/H = 0.75$ and the disk is placed at various radial locations: (a) $x_s/R = 0.00$; (b) $x_s/R = 0.05$; (c) $x_s/R = 0.15$; (d) $x_s/R = 0.25$; and (e) $x_s/R = 0.35$.

in the positive axial direction, meaning that the VB recirculation extends over $0.6 \leq z/H \leq 0.9$, just as it does when there is no disk. This once again demonstrates the very minor influence the disk blockage has on the development of VB, even when the body is located significantly off the axis of symmetry.

5.6.2 Wall Shear Stresses

The profiles shown in Figure 5.20 indicate that as the scaffold is moved away from the cylinder's axis of symmetry, the wall shear stress distribution along the bottom surface becomes progressively asymmetric. Unlike in Figure 5.19, the plotted frame of reference is fixed relative to the scaffold rather than the bioreactor, i.e. the radial position data are normalised by the scaffold radius and the origin is at the centre of the disk. The new normalisation is used to illustrate the changing τ_w levels at certain positions along the disk. The edge corresponding to the side of the bioreactor to which the scaffold is displaced experiences roughly a 50% increase in τ_w , while the opposite edge experiences an 86% decrease between $x_s/R = 0.00$ and $x_s/R = 0.25$. This causes an increasing disparity in the τ_w values seen by the two edges of the disk. The $x_s/R = 0.35$ case is not included in Figure 5.20 because the measurement field of view did not encompass the disk's full diameter. However, it should be noted that the τ_w curve loses much of its parabolic nature when $x_s/R = 0.35$.

As described in Section 5.5, τ_w increases sharply toward the edge of the disk. Around the minimum τ_w value the profiles are flatter. An increase in x_s/R does not appear to drastically alter the shape of the τ_w profile, but rather shifts it in the positive r/r_s direction. While the magnitude of the minimum shear level remains constant at around 0.1, its location relative to the scaffold surface varies with x_s/R . The location of minimum τ_w also varies relative to the cylinder's axis of symmetry, and, as shown in Table 5.1, the distance that the minimum point moves from the bioreactor axis, ξ_b , is generally greater than the displacement of the minimum point from the scaffold's axis of symmetry, ξ_s . Aside from the $x_s/R = 0.00$ case, the τ_w minimum is shifted away from the axis of symmetry in the direction of the scaffold displacement, but ξ_b is restricted by the fact that the VB recirculation toroid, and therefore much of the central low-velocity region, remains centred on the cylinder's axis of symmetry. As x_s increases, the difference between ξ_s and ξ_b decreases, until by $x_s/R = 0.25$ the shear stress minimum point is located slightly closer to the bioreactor axis of symmetry than the centre of the scaffold.

The fourth column in Table 5.1 includes normalised values of mean wall shear, $\overline{\tau_w}$. It is

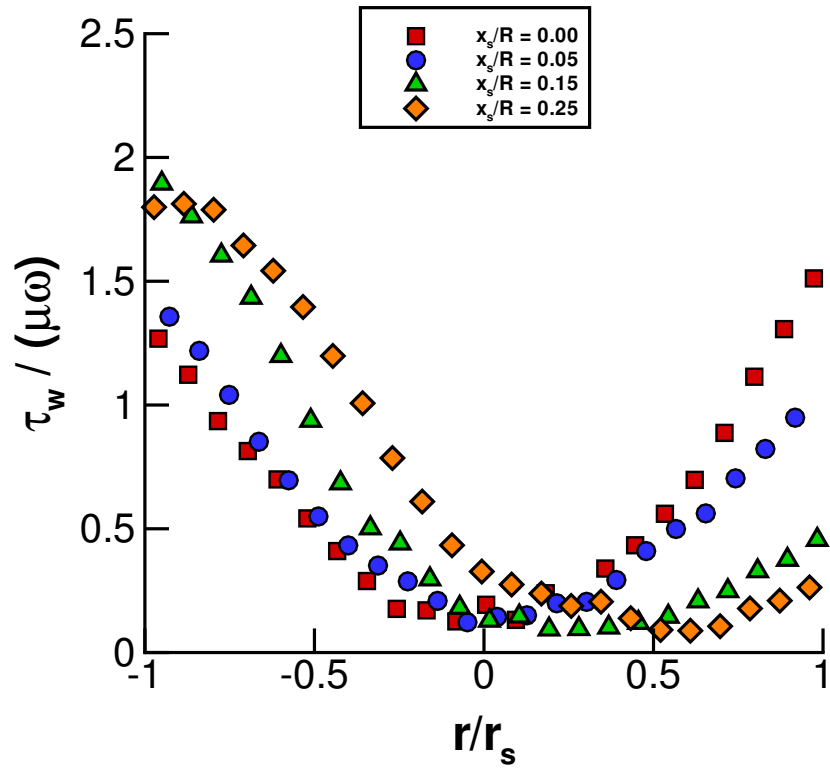


Figure 5.20: Comparison of $\tau_w/(\mu\omega)$ profiles along the bottom surface of a disk of size $r_s/R = 3/13$ at a vertical location $z_s/H = 0.75$, when $Re = 1200$. The various symbols represent different values of normalised radial displacement x_s/R .

x_s/R	$\xi_b/R(\%)$	$\xi_s/R(\%)$	$\overline{\tau_w}/(\mu\omega)$	s.d. $\tau_w/(\mu\omega)$
0.00	0.0	0.0	0.67	0.45
0.05	3.7	1.3	0.55	0.36
0.15	9.5	5.5	0.58	0.59
0.25	12.3	12.7	0.66	0.62

Table 5.1: Distance of the minimum measured τ_w value from the axis of symmetry of the bioreactor (ξ_b/R), and from the axis of symmetry of the scaffold (ξ_s/R), when the scaffold is displaced various radial distances (x_s/R). The fourth and fifth columns include, respectively, the mean and standard deviation shear stress levels, ($\overline{\tau_w}/(\mu\omega)$ and s.d. $\tau_w/(\mu\omega)$), along the bottom surface of the scaffold for the different cases.

apparent that $\overline{\tau_w}$ does not vary significantly with x_s . For all cases presented, the scaffold is surrounded by a similar low-velocity region. This most likely explains why the magnitude of wall stress barely changes, despite intuition suggesting that a disk located closer to the higher-velocity, outer region would experience higher wall stresses. The standard deviations, also shown in Table 5.1, are relatively large compared to $\overline{\tau_w}$ because τ_w varies significantly across the surface.

5.7 Conclusions and Further Discussion

The structure of the flows within free surface cylinders with an aspect ratio $H/R = 1.5$ and a Reynolds number of 1200 or 2400, is mostly unaffected by the presence of submerged disks on the axis of symmetry. In particular, the recirculation zone external to the vortex breakdown region appears to not be affected when the disks used in the present study are centred at $r/R = 0$. The flow profiles within this outer recirculation region, which constitutes the larger fluid volume, are constant to within experimental random error. On the other hand, the flow within the boundary of the vortex breakdown bubble is affected to some degree dependent on the parameters Re , r_s , and z_s .

The breakdown region is affected to a greater extent than the outer recirculation region, with the obvious reason being that the disks occupy a much larger percentage volume of the former than of the latter. Nevertheless, under most of the conditions tested, the location and topology of the VB recirculation is still fairly similar to when there is no disk. The most significant alteration to the bubble structure occurs when the disk is located in part of the region occupied by the VB recirculation in the no-disk case. This occurs more frequently when the disk has a larger diameter, is positioned away from $r = 0$, or is positioned axially toward the centre of the VB region. Alternatively, this can occur when the breakdown recirculation forms closer to $r = 0$, such as in the VB *axis bubble* or *corner bubble* regimes.

When the disk directly interferes with the ‘natural’ location of the recirculation zone, the recirculation reforms at a displaced location. From the three case studies, there is evidence of this displacement occurring in the radial direction (e.g. Case A, with the disk located at $z_s/H = 0.70$), the positive axial direction (e.g. Case B, with the disk located at $z_s/H = 0.70$), and the negative axial direction (e.g. Case B again, but this time with the disk located at $z_s/H = 0.90$). The magnitude of the displacement depends on the extent of the disk interference. A larger displacement of the recirculation region has more effect on the internal Vortex Breakdown topology. Under some circumstances, a large displacement of the VB recirculation can cause a slight radial displacement of the VB region outer boundary. For example, Figure 5.6 reveals that the low-velocity breakdown region extends a slightly larger radial distance at an axial position of $z/H = 0.5$ when the disk is located at $z_s/H = 0.55$ (i.e. near the interrogation line), than at $z_s/H = 0.70$ or $z_s/H = 0.90$ (i.e. a significant distance upstream of the interrogation line). In contrast, the presence of a small disk in the ‘natural’ location of the VB recirculation causes only a small displacement of the recirculation.

The degree to which fluid passing the disks is disturbed depends on the size of the body.

For the larger disks, the fluid region on the underside of the disk has a low axial and azimuthal momentum; this is particularly evident for the $r_s/R = 3/13$ case. This separate region is the closest manifestation of a wake region downstream of the body. Further below the disk, the three-dimensional velocity field is restored by the Ekman suction mechanism to a condition similar to the no-disk case. As the fluid in the vortex breakdown bubble surrounding the disk has relatively low momentum, the wake region does not extend far below the disk: approximately 0.26 disk diameters when $Re = 1200$ and $z_s/H = 0.7$ and approximately 0.07 disk diameters when $Re = 2400$ and $z_s = 0.7H$. The flow upstream of the disk has a non-uniform profile and a three-dimensional orientation, so the nature of the fluid/structure interaction is not trivial.

Disturbances caused by the presence of the disk appear to be sensitive to slight displacement of the model from the central axis. This is not surprising, given the sensitivity of bubble topology to misalignments in experimental rig construction (Thompson & Hourigan, 2003). Asymmetry was minimised by accurately positioning the models, however all recorded fields had some degree of asymmetry. Measurements of the radial velocity component, v_r , were affected the most by flow asymmetry as a shifting in the central axis of the bubble region away from the measurement plane resulted in an erroneous cross-flow. For this reason, the comparative flow analyses presented in this chapter mostly consist of v_z and v_θ profiles. The measurements of these two components had a higher degree of symmetry about the vertical axis at $r = 0$ than v_r .

Husain *et al.* (2003) studied closed cylinder vortex breakdown flows for the case where a smaller-radius cylinder is located on the axis of symmetry, and is rotated in (a), the same direction as the impeller, and (b), the opposite direction to the impeller. They used their results to illustrate that vortex breakdown remains strong when there is a high adverse pressure gradient in the downward axial flow near the axis of symmetry, and weakens or disappears completely with the reduction of the near-axis axial pressure gradient. For Husain *et al.* the co-rotating inner cylinder caused a reduction of the adverse pressure gradient that suppressed the vortex breakdown recirculation. The results presented in the current study appear to support the work of Husain *et al.* In this case, the adverse pressure gradient is maintained, or even enhanced, by the presence of the downstream disk. A strong adverse pressure gradient occurs in the meridional plane flow between the high velocities in the upper part of the outer recirculation region and the low velocities in the disk stagnation region. In other words, the disk reinforces the adverse pressure gradient, without contributing to a significant loss of upstream azimuthal

momentum, and so vortex breakdown occurs.

The retention of vortex breakdown despite the intrusion of a wide variety of disk sizes and axial positions, is not overly surprising given the previous observations of submerged bodies within vortex breakdown bubbles. When the rod used by Husain *et al.* (2003) was kept stationary, no significant changes were observed, although no velocity measurements were completed to analyse the internal bubble topology in detail. Greater changes to the breakdown structure were induced by rotating the rod to induce swirl. Husain *et al.* used a body radius of $0.04R$, so the physical presence of the rod was not imposing on radial positions near the centroid of the VB recirculations. In contrast, the diameter ratios used here are significantly larger, so the results provide a stronger demonstration of the robustness of VB structure when bluff bodies are added. Mattner *et al.* (2003), who also left their solid body stationary, did not directly compare flow fields corresponding to different sized spheres, or to the case where there was no sphere.

The results in this chapter clarify the potential role of Vortex Breakdown in a bioreactor system that includes submerged scaffolds. With the cells or tissue held stationary in the bioreactor, it is necessary to characterise the relevant stresses in a different manner to the case where there is no scaffold and the cells are freely suspended. For the scaffold/bioreactor system, the three-dimensional wall shear stresses are of more interest than the complete principal stress field. This is because the cell aggregates or tissue constructs must be considered as part of the solid scaffold structure rather than as elements of the fluid, which is how they are modelled in suspension bioreactor systems. It should be recognised that unlike suspended cells, cells attached to scaffolds experience nearly constant stresses if the scaffold remains stationary and if the flow remains in the steady regime. This could be problematic for culturing adherent cells that prefer time-variant stress magnitudes and directions. A solution could be to gradually vary the position and orientation of the scaffolds, although this movement would need to be over a long timescale compared to the disk rotation period if it is to not affect the formation of the flows described here. A second major difference between suspension and scaffold culture is the magnitude of stresses experienced by cells. Stresses experienced by cells attached to the outer surface of scaffolds in the VB region can be substantially higher than stresses experienced by cells freely suspended in the VB region. On the other hand, cells located near the scaffold's axis of symmetry may experience maximum stresses that are far below the mean stress levels experienced by cells suspended in the breakdown region at the same Re . Cells initially seeded within scaffolds would not be exposed to the bulk flow, but would instead be exposed

to microflows internal to the scaffold. The stresses associated with the internal scaffold fluid dynamics are beyond the scope of the current investigation.

It is important in the context of culturing sensitive adherent cells that vortex breakdown can co-exist with scaffold systems held within the central region of the bioreactor. The fact that the internal VB recirculation, which provides the main low-shear mixing mechanism, remains intact despite the presence of relatively large scaffolds located at various axial and radial positions, bodes well for its use in applications involving shear-sensitive adherent cells. Characterising the effect of scaffold size and position is also helpful in this regard. The scaffold to bioreactor diameter ratios described in the literature tend to be at the small end of the range of r_s/R tested in the current study. For instance, the early studies of Vunjak-Novakovic *et al.* (1996) used multiple scaffolds of size $r_s/R = 1/13$. Under these conditions, the VB recirculation is virtually unimpeded by the scaffold or the scaffold support, and the vertical placement of the scaffold seems to make little difference to this. However, the successful development of a breakdown region with enclosed recirculation structure at $r_s/R = 3/13$ implies the possibility, from a bioreactor fluid dynamics perspective, to scale-up to a much larger scaffold volume. As scaling up of tissue constructs to large sizes can lead to problems, such as necrosis, an alternative is to scale-out to a larger number of smaller scaffolds. This solution is already possible for a scaffold size of $r_s/R = 1/13$ using the experimental rig studied here, however it may be preferable to scale the bioreactor up so that r_s/R is reduced while the absolute size of the scaffold remains constant, say at an optimal level for necrosis prevention. In this way, multiple scaffolds may be able to fit within the low-shear region, thus increasing the yield without reducing the VB mixing capabilities.

When choosing a scaffold/bioreactor configuration it is beneficial to consider in advance the τ_w profile that will result, as well as the angle the resolved flow vector makes relative to the scaffold (β_τ). When the scaffold is located on the axis of symmetry, the stresses are axisymmetrically distributed across its upper and lower surfaces. Along both of these surfaces, τ_w is of lower magnitude near the centre than near the circumference. Regardless of scaffold size, the lower surface τ_w profile rises steeply as $r \rightarrow r_s$ when $Re = 1200$, and more linearly with respect to r when $Re = 2400$. In general, the maximum τ_w is marginally higher for $r_s/R = 3/13$ than for $r_s/R = 2/13$, and is higher for $r_s/R = 2/13$ than for $r_s/R = 1/13$. Re and scaffold position can also affect the stress distribution, especially for the larger scaffold ($r_s/R = 3/13$). When Re is increased to 2400, τ_w is greater because of the stronger azimuthal flow in the central vortex region, where the on-axis scaffold is located. The axial position of the scaffold,

z_s , does not cause a noticeable change in the τ_w profile when $Re = 2400$ because the disk is located within the inner radius of the VB recirculation toroid, regardless of z_s or r_s . In contrast, z_s strongly controls the bottom surface τ_w profile when $Re = 1200$. This is because the τ_w magnitudes along this surface are greater when the VB recirculation is located below the scaffold, rather than above the scaffold. The angle β_τ consistently increases with r , and asymptotes toward 0 as $r/R \rightarrow 0$. This is because the ratio of v_θ to v_r increases at locations further from the axis of symmetry.

A VB bubble forms despite a slight radial displacement of the scaffold, however an increase in the magnitude of the displacement, x_s , causes the low-velocity region to become progressively more distorted, and the overall flow to become more asymmetric. The retention of a low stress region about the scaffold is positive, particularly if an array of scaffolds similar to that studied by Sucusky *et al.* (2004) were to be considered for use in a scaffold/bioreactor system with VB. A radially displaced scaffold has a similar τ_w profile along its bottom surface to a scaffold located on the bioreactor's axis of symmetry, however the minimum stress point is located increasingly further from the centre of the scaffold as x_s increases. The fact that the mean wall stress, $\overline{\tau_w}$, is fairly constant for all measured x_s cases, has positive implications for cell culture applications if the scaffold is to be displaced from the cylinder's axis of symmetry. However, the variation in τ_w across the surface renders it impossible to obtain a local hydrodynamic environment that is axisymmetrically distributed across the scaffold, let alone uniform. This is not such a problem if a flow measurement technique such as SPIV is used to predict the stress profiles, meaning that action can be taken to redesign a bioreactor system to compensate for irregular τ_w distributions. The fact that the τ_w curves shift relative to the scaffold while $\overline{\tau_w}$ remains constant implies that gradual rotation and radial translation of the scaffold over the entire culturing period may allow all parts of the scaffold surface to experience a range of stress levels suitable for cell and tissue production. It is worth also considering that the nearly stagnant flow region surrounding a radially displaced scaffold may not necessarily undergo convective mixing to the extent found in a VB bubble at $Re = 1200$. For instance, if the recirculation pattern is located closer to the cylinder's axis of symmetry than the scaffold then there may be issues associated with insufficient nutrient delivery.

Chapter 6

Conclusions and Recommendations for Further Research

6.1 Final Conclusions

Experimental fluid dynamics provides an opportunity to study novel but practically realistic bioreactor flows. Stereoscopic particle image velocimetry facilitates the characterisation of internal flow features in terms of properties relevant to cell and tissue culture in a manner that is far superior to that possible using less advanced techniques. For example, SPIV can be used to derive spatially and temporally resolved stress fields that take into account all three directional components of velocity. With this capability, it is possible to attempt to locate flows which are suitable for a particular cell culture application. This increased control should provide improved repeatability of culture outcomes, which is significant considering the general drive to design better *in vitro* scale-up processes for biomedical, pharmaceutical, industrial, and research purposes.

In this study, vortex breakdown flows within free surface cylindrical vessels have been measured using SPIV and analysed in the context of a potential bioreactor application. As reported by others, at an aspect ratio of $H/R = 1.5$ and at Reynolds numbers above that for the onset of VB, there are two distinct and counter-rotating recirculations in the $r - z$ plane. In the outer region, the fluid generally has a higher velocity, including a larger component in the dominant azimuthal direction. The strongest flow is in the Ekman region, which accelerates fluid in the near-axis region toward the impeller and discharges it near the cylinder wall. Along the sidewall, the fluid experiences a loss of azimuthal momentum as it moves away from the impeller, and then a loss of axial momentum as it turns radially inward near the free surface. The highest stresses are induced near the radial extremity of the impeller, where the fluid is turned in the positive axial direction by the sidewall. Significant fluid stresses also occur along

the impeller and side boundaries and at the outer surface of the VB recirculation bubble. The stresses are not caused solely by the meridional plane recirculation, or the increases in v_θ with r , but a combination of the two. Often the contribution of these two mechanisms is roughly of equal magnitude. Therefore, the principal axes are usually not aligned with the cylindrical axes of the bioreactor, and so it is misleading to approximate the hydrodynamic stresses experienced by suspended cells by a single component such as τ_{rz} .

Within the VB region the velocities and stresses are, on average, of reduced magnitude. While the flow has not been tested with live cells, it appears possible to entrain cell-sized particles within the VB recirculation so that they are transported about the upper-inner volume of the vessel and kept isolated from the higher stresses near the impeller. It also possible to submerge a stationary tissue engineering scaffold within the VB region and maintain the presence of a recirculation capable of transporting cell culture media.

The conditions within and surrounding the VB region are controlled by the Reynolds number. At low Re , the VB recirculation is small and located on the axis. As Re increases, the VB recirculation toroid increases in volume and attaches to the free surface. It is in this *corner bubble* regime that VB appears most favourable to cell seeding, and it is also in this regime that the VB recirculation is most affected by a scaffold located on the axis. At higher Re , the VB recirculation detaches from the axis of symmetry so that the central vortex region - in which it is often possible to locate the full girth of a scaffold model while barely affecting the VB geometry - extends to the free surface. With a further increase in Re , the VB recirculation moves radially outward. Furthermore, the positive azimuthal vorticity associated with the VB recirculation increases in intensity. At $Re \gtrsim 2200$ the flow topology becomes less affected by changes in Re . Similarly, the swirl ratio SR_m , which has a fairly Re -independent distribution, increases in magnitude until $Re \simeq 2200$, at which point it becomes more constant. The high stress zone along the outside boundary of the VB recirculation undergoes a change in intensity, location and orientation that reflects the transitions in the VB topology. At the high end of the experimental Re range, both the distribution and magnitude of σ_1 and σ_3 become more constant. Aside from a slight narrowing of the Ekman layer, the velocity and stress distribution close to the impeller become less dependent on Re .

For adherent cell or tissue culture, the size and placement of the scaffolds is of consequence to the flow structure. Disks located near the z/H position at which the VB recirculation centroid is located when there is no scaffold cause the greatest distortion and/or displacement of the recirculation, although the azimuthal component is less affected than the meridional com-

ponent. Increasing the normalised radius of the scaffold or the displacement of the scaffold from the axis of symmetry also causes a greater disruption of the flow. Due to the effect of the bluff body, the shear stresses experienced by cell and tissue material attached to the exterior of the scaffolds are higher than those experienced by cells freely suspended within the VB region. The wall shear on the upper and lower surfaces of the scaffold is strongly dependent on radial position, even when the centre of the scaffold is displaced from $r = 0$. The direction in which the maximum wall shear acts is also non-uniformly distributed along the surface of the scaffold, although both τ_w and β_τ profiles are predictable with the aid of SPIV.

In summary, the findings represent a contribution to the overall field of knowledge in both the areas of bioreactor development and vortex breakdown. The approach to modelling bioreactor flows demonstrated in this thesis has been shown to be of value in the following ways:

- Velocity measurements facilitate the identification of different flow regions and the dynamic conditions therein. These in turn can be used to determine the suitability of the mass transport performance for a culture application.
- Spatially resolved stress measurements reveal a significantly heterogeneous distribution, meaning that vessel-averaged parameters are misleading. Stress fields are useful for predicting stress conditions experienced by freely suspended and stationary aggregates. Individual shear stress components resolved in seemingly arbitrary directions are often inadequate representations of the stress conditions. Principal stress fields more thoroughly predict the location and magnitude of the peak stresses experienced by suspended cells or microcarriers.
- Bioreactor flow conditions are characterised non-dimensionally as functions of relevant input conditions, thus assisting the design of more generalist bioreactors.
- Flows within cylindrical vessels with a rotating bottom and a free surface seemingly provide a viable alternative to turbulent flow bioreactors such as spinner flasks, and complicated vessels such as rotating wall bioreactors. Vortex breakdown bubbles, particularly in the *corner bubble* regime, provide low-shear mixing conditions and the ability to isolate particles from the impeller region, which may potentially be useful for some *in vitro* culture applications. Vortex breakdown flows also may be viable for use in bioreactor applications involving stationary scaffolds, as the addition of disks on or near the axis of symmetry does not significantly disturb the VB recirculation formation.

The research described in this thesis also represents one of the more advanced experimental analyses undertaken to date on vortex breakdown flows within lid-driven cylinders. In particular, the following novel accomplishments that add to the body of knowledge have been made:

- Simultaneous measurement of all three velocity components has been undertaken. This facilitates quantification of the relative strength of each component, e.g. via swirl ratio SR_m , and an analysis of the transfer between radial, axial and azimuthal momentum. In particular, the azimuthal jet-like structure near the interface of the rotating disk and the sidewall is quantified experimentally, as is the decay of azimuthal momentum as z/H increases.
- The principal stress vector distribution across the meridional plane has been quantified. Peak stress regions occur near the impeller, sidewall and the vortex breakdown boundary and are caused by a combination of v_θ gradients and in-plane velocity gradients. The change with Re is described, and compared to numerically derived principal stress fields that show similar trends.
- The effect of adding disks to the vortex breakdown region has been visualised and quantified experimentally. Three-component velocity fields have been characterised in terms of disk size and position.

6.2 Recommendations for Further Research

The direction of the research described in this thesis is quite novel, and so there is significant scope for further investigation along similar lines. The following are suggested studies relating to utilising vortex breakdown for the purposes of cell and tissue culture:

- 1.) The potential use of these flows in a specific culture application should eventually be tested by constructing prototype bioreactors with matching geometries. The effect of necessary practical processes, e.g. the disturbances caused by cell passaging and media replenishment processes, should be quantified. The optimal seeding level of a particular cell or tissue also needs to be determined as a function of Re .
- 2.) The ability to isolate real cells and microcarriers within certain regions of the flow needs to be fully tested.
- 3.) In order to broaden the parameter base, it may be worth measuring the effect of height ratio on stress fields using the techniques described in this thesis.

- 4.) The potential of scaffold/bioreactor systems involving vortex breakdown could be further investigated by measuring the effect of submerging multiple disks simultaneously. This study could also be used to further analyse the limits at which vortex breakdown is retained when bluff bodies are added.
- 5.) The submerged disk case should also be modelled numerically, particularly to test whether any asymmetries are caused by disk or rig misalignment.

From a broader perspective, progress in large scale bioreactor design depends on researchers undertaking the following investigations:

- 1.) Similar characterisations should be made of different vortex breakdown and laminar mixing flows in order to find other conditions potentially suited to cell culture.
- 2.) In order to fully predict the performance of bioreactor systems, significantly more information is required regarding the impact of fluid stresses at the cellular and subcellular levels. In the near future it would be desirable to quantify the proliferation rate of cells as a function of the principal stresses to which the cells are exposed. This would have major ramifications for the bioreactor design process, particularly if these models could be coupled to bioreactor flow characterisations, such as that described here.

Bibliography

- Adrian, R.J. 1986. Multi-point optical measurements of simultaneous vectors in unsteady flow - a review. *International Journal of Heat and Fluid Flow*, **7**, 127–145.
- Adrian, R.J. 1991. Particle-imaging techniques for experimental fluid mechanics. *Annual Review of Fluid Mechanics*, **23**, 261–304.
- Ainslie, K.M., Garanich, J.S., Dull, R.O., & Tarbell, J.M. 2005. Vascular smooth muscle cell glycocalyx influences shear stress-mediated contractile response. *Journal of Applied Physiology*, **98**, 242–249.
- Alam, I., Warden, S.J., Robling, A.G., & Turner, C.H. 2005. Mechanotransduction in bone does not require a functional cyclooxygenase-2 (COX-2) gene. *Journal of Bone and Mineral Research*, **20**(3), 438–446.
- Ameer, G.A., Grovender, E.A., Obradovic, B., Cooney, C.L., & Langer, R. 1999. RTD analysis of a novel taylor-couette flow device for blood detoxification. *American Institute of Chemical Engineering Journal*, **45**(3), 633–638.
- Ameer, G.A., Grovender, E.A., Ploegh, H., Ting, D., Owen, W.F., Rupnick, M., & Langer, R. 2001. A novel immunoabsorption device for removing β 2-microglobulin from whole blood. *Kidney International*, **59**, 1544–1550.
- Anayiotos, A.S., Jones, S.A., Giddens, D.P., Glagov, S., & Zarins, C.K. 1994. Shear stress at a compliant model of the human carotid bifurcation. *Journal of Biomechanical Engineering*, **116**, 98–106.
- Aris, R. 1962. *Vectors, tensors and the basic equations of fluid mechanics*. Eaglewood Cliffs, USA: Prentice-Hall.
- Aunins, J.G., Woodson, B.A., Hale, T.K., & Wang, D.I.C. 1989. Effects of paddle impeller geometry on power input and mass transfer in small-scale animal cell culture vessels. *Biotechnology and Bioengineering*, **34**, 1127–1132.

- Bacabac, R.G., Smit, T.H., Mullender, M.G., Loon, J.J. Van, & Klein-Nulend, J. 2005. Initial stress-kick is required for fluid shear stress-induced rate dependent activation of bone cells. *Annals of Biomedical Engineering*, **33**(1), 104–110.
- Bachrach, N.M., Valhmu, W.B., Stazzone, E., Ratcliffe, A., Lai, W.M., & Mow, V.C. 1995. Changes in proteoglycan synthesis of chondrocytes in articular cartilage are associated with the time-dependent changes in their mechanical environment. *Journal of Biomechanics*, **28**(12), 1561–1569.
- Barbee, K.A. 2002. Role of subcellular shear-stress distributions in endothelial cell mechanotransduction. *Annals of Biomedical Engineering*, **30**(4), 472–482.
- Barbee, K.A., Davies, P.F., & Lal, R. 1994. Shear stress-induced reorganization of the surface topography of living endothelial cells imaged by atomic force microscopy. *Circulation Research*, **74**(1), 163–171.
- Bauer, M., & Eigenberger, G.A. 1999. A concept for multi-scale modeling of bubble columns and loop reactors. *Chemical Engineering Science*, **54**(21), 5109–5117.
- Bauer, M., & Eigenberger, G.A. 2001. Multiscale modeling of hydro-dynamics, mass transfer and reaction in bubble column reactors. *Chemical Engineering Science*, **56**(3), 1067–1074.
- Bee, J.A., Liu, H.X., N.Clarke, & Abbott, J. 1994. Modulation of cartilage extracellular matrix turnover by pulsed electromagnetic fields (PEMF). *Pages 244–269 of: Lyall, F., & El Haj, A.J. (eds), Biomechanics and cells*. Cambridge, UK: Cambridge University Press.
- Begley, C.M., & Kleis, S.J. 2000. The fluid dynamic and shear environment in the NASA/JSC rotating-wall perfused-vessel bioreactor. *Biotechnology and Bioengineering*, **70**, 32–40.
- Begley, C.M., & Kleis, S.J. 2002. RWPV bioreactor mass transport: earth-based and in microgravity. *Biotechnology and Bioengineering*, **80**, 465–476.
- Bezzo, F., Macchietto, S., & Pantelides, C.C. 2003. General hybrid multizonal/CFD approach for bioreactor modeling. *AIChE Journal*, **49**(8), 2133–2148.
- Birch, J.R., Thompson, P.W., Lambert, K., & Boraston, R. 1985. The large scale cultivation of hybridoma cells producing monoclonal antibodies. *Pages 1–18 of: Feder, J., & Tolbert, W.R. (eds), Large-scale mammalian cell culture*. London: Academic Press, Inc.

- Bird, R.B., Stewart, W.E., & Lightfoot, E.N. 1960. *Transport Phenomena*. New York: John Wiley and Sons.
- Blackburn, H.M., & Lopez, J. M. 2000. Symmetry breaking of the flow in a cylinder driven by a rotating end wall. *Physics of Fluids*, **12**(11), 2698–2701.
- Bödewardt, U.T. 1940. Die drehströmung ber festem grunde. *Zeitschrift für Angewandte Mathematik und Mechanik*, **20**, 241–253.
- Born, C., Zhang, Z., Al-Rubeai, M., & Thomas, C.R. 1992. Estimation of disruption of animal cells by laminar shear stress. *Biotechnology and Bioengineering*, **40**, 1004–1010.
- Botchwey, E.A., Pollack, S.R., Levine, E.M., Johnston, E.D., & Laurencin, C.T. 2004. Quantitative analysis of three-dimensional fluid flow in rotating bioreactors for tissue engineering. *Journal of Biomedical Materials Research*, **69**(2), 205–215.
- Boysan, F., Cliff, K.R., Leckie, F., & Scragg, A.H. 1988. The growth of *Catharanthus roseus* in stirred tank bioreactors. *Pages 245–258 of: 2nd International Conference on Bioreactor Fluid Dynamics*. Cambridge, UK: Elsevier Applied Science Publishers.
- Brittberg, M., Lindahl, A., Nilsson, A., Ohlsson, C., Isaksson, O., & Peterson, L. 1994. Treatment of deep cartilage defects in the knee with autologous chondrocyte transplantation. *New England Journal of Medicine*, **331**(14), 879–895.
- Brøns, M., Voigt, L. K., & Sørensen, J.N. 2001. Topology of vortex breakdown bubbles in a cylinder with a rotating bottom and a free surface. *Journal of Fluid Mechanics*, **428**, 133–148.
- Brown, G.L., & Lopez, J.M. 1990. Axisymmetric vortex breakdown. Part 2: physical mechanism. *Journal of Fluid Mechanics*, **221**, 553–576.
- Brown, T.D. 2000. Techniques for mechanical stimulation of cells in vitro: a review. *Journal of Biomechanics*, **33**, 3–14.
- Bueno, E.M., Bilgen, B., Carrier, R.L., & Barabino, G.A. 2004. Increased rate of chondrocyte aggregation in a wavy-walled bioreactor. *Biotechnology and Bioengineering*, **88**(6), 767–776.
- Caro, L.G., Fitz-Gerald, J.M., & Schroter, R.C. 1971. Atheroma and arterial wall shear: observation, correlation and proposal of a shear dependent mass transfer mechanism, for athero-

- genesis. *Philosophical Transactions of the Royal Society of London, Series B: Biological Sciences*, **177**, 109–159.
- Carrier, R.L., Papadaki, M., Schoen, F.J., Bursac, N., Langer, R., Freed, L.E., & Vunjak-Novakovic, G. 1999. Cardiac tissue engineering: cell seeding, cultivation parameters, and tissue construct characterization. *Biotechnology and Bioengineering*, **64**, 580–589.
- Cascalho, M., & Platt, J.L. 2005. New technologies for organ replacement and augmentation. *Mayo Clinic Proceedings*, **80**(3), 370–378.
- Chen, C.S., Tan, J., & Tien, J. 2004. Mechanotransduction at cell-matrix and cell-cell contacts. *Annual Review of Biomedical Engineering*, **6**, 275–302.
- Cherry, R.S., & Papoutsakis, E.T. 1986. Hydrodynamic effects on cells in agitated tissue culture reactors. *Bioprocess Engineering*, **1**, 29–41.
- Cherry, R.S., & Papoutsakis, E.T. 1988. Physical mechanisms of cell damage in microcarrier cell culture bioreactors. *Biotechnology and Bioengineering*, **32**, 1001–1014.
- Ciofalo, M., Brucato, A., Grisafi, F., & Torraca, N. 1996. Turbulent flow in closed and free-surface unbaffled tanks stirred by radial impellers. *Chemical Engineering Science*, **51**(14), 3557–3573.
- Civelek, M., Ainslie, K., Garanich, J.S., & Tarbell, J.M. 2002. Smooth muscle cells contract in response to fluid flow via a Ca²⁺ - independent signaling mechanism. *Journal of Applied Physiology*, **93**(6), 1907–1917.
- Collins, P.C., Miller, W.M., & Papoutsakis, E.T. 1998. Stirred culture of peripheral and cord blood hematopoietic cells offers advantages over traditional static systems for clinically relevant applications. *Biotechnology and Bioengineering*, **59**, 534–543.
- Croughan, M.S., Hamel, J.-F., & Wang, D.I.C. 1987. Hydrodynamic effects on animal cells grown in microcarrier cultures. *Biotechnology and Bioengineering*, **24**, 130–141.
- Curran, S.J., & Black, R.A. 2004. Quantitative experimental study of shear stresses and mixing in progressive flow regimes within annular-flow bioreactors. *Chemical Engineering Science*, **59**, 5859–5868.
- Darling, E.M., & Athanasiou, K.A. 2003. Articular cartilage bioreactors and bioprocesses. *Tissue Engineering*, **9**, 9–26.

- Davies, P.F. 1995. Flow-Mediated Endothelial Mechanotransduction. *Physiological Reviews*, **75**, 519–560.
- Davies, P.F., Remuzzi, A., Gordon, E.J., Dewey, C.F., & Gimbrone, M.A. 1986. Turbulent fluid shear stress induces vascular endothelial cell turnover *in vitro*. *Proceedings of the National Academy of Sciences of the United States of America*, **83**, 2114–2117.
- Davies, P.F., Mundel, T., & Barbee, K.A. 1995. A Mechanism for Heterogeneous Endothelial Responses to Flow *In Vivo* and *In Vitro*. *Journal of Biomechanics*, **28**(12), 1553–1560.
- De Witt, M.T. 1982. *Studies on the effects of mechanical stress on chondrocytes*. Ph.D. thesis, Monash University, Melbourne.
- Demartean, O., Jakob, M., Schafer, D., & Martin, I. 2003. Development and validation of a bioreactor for physical stimulation of engineered cartilage. *Biorheology*, **40**, 331–336.
- Dewey, C.F., Bussolari, S.R., Gimbrone, M.A., & Davies, P.F. 1981. The dynamic response of vascular endothelial cells to fluid shear stress. *Journal of Biomechanical Engineering*, **103**, 177–185.
- Dillaman, R.M., Roer, R.D., & Gay, D.M. 1991. Fluid Movement in Bone: Theoretical and Empirical. *Journal of Biomechanics*, **24**(suppl.1), 163–177.
- Donnelly, R.J. 1991. Taylor-couette flow: the early days. *Physics Today*, **44**, 32–39.
- Doran, P.M. 1999. Design of mixing systems for plant cell suspensions in stirred reactors. *Biotechnology Progress*, **15**, 319–335.
- Doran, P.M. 2000. Stirred tank bioreactors. *Pages 249–278 of: Spier, R.E. (ed), Encyclopedia of Cell Technology*. New York, USA: John Wiley & Sons.
- Dunlop, E.H., & Namdev, P.K. 1993. Effect of fluid forces on plant cell suspensions. *Pages 447–455 of: 3rd International Conference on Bioreactor and Bioprocess Fluid Dynamics*. Cambridge, UK: BHR Group.
- Dussault, C., Young, D.I., & Duncan, N.A. 2002. A new system for cyclical tensile loading of cultured connective tissue cells in a three-dimensional gel matrix. *In: ASME International Mechanical Engineering Congress & Exposition*. New Orleans: American Society of Mechanical Engineers.

- Edgington, S.M. 1992. New horizons for stem-cell bioreactors. *Bio/Technology*, **10**(10), 1099–1106.
- Engelmayr, G.C., Hildebrand, D.K., Sutherland, F.W., Mayer, J.E., & Sacks, M.S. 2003. A novel bioreactor for the dynamic flexural stimulation of tissue engineered heart valve biomaterials. *Biomaterials*, **24**, 2523–2532.
- Eringen, A.C. 1967. *Mechanics of Continua*. New York, USA: John Wiley and Sons, Inc.
- Escudier, M.P. 1984. Observations of the flow produced in a cylindrical container by a rotating endwall. *Experiments in Fluids*, **2**, 189–196.
- Escudier, M.P. 1988. Vortex breakdown: observations and explanations. *Progress in Aerospace Sciences*, **25**, 189–229.
- Fouras, A., & Soria, J. 1998. Accurate out-of-plane vorticity calculation from in-plane velocity vector field data. *Experiments in Fluids*, **25**, 409–430.
- Fouras, A., Hourigan, K., Kawahashi, M., & Hirahawa, H. 2006. An improved free surface topographic technique. *Journal of Visualization (in press)*, **29**.
- Fournier, R.L. 1999. *Basic transport phenomena in biomedical engineering*. First edn. Philadelphia, USA: Taylor and Francis.
- Frangos, J.A., Eskin, S. G., McIntire, L.V., & Ives, C.L. 1985. Flow effects on prostacyclin production by cultured human endothelial cells. *Science*, **227**, 1477–1479.
- Frederick, D., & Tien, S.C. 1965. *Continuum Mechanics*. Boston, USA: Allyn and Bacon.
- Freed, L.E., & Vunjak-Novakovic, G. 1995. Cultivation of cell-polymer tissue constructs in simulated microgravity. *Biotechnology and Bioengineering*, **46**, 306–313.
- Freed, L.E., & Vunjak-Novakovic, G. 1998. Culture of organized cell communities. *Advanced Drug Delivery Reviews*, **33**, 15–30.
- Freed, L.E., & Vunjak-Novakovic, G. 2000. Tissue Engineering Bioreactors. *Pages 143–156 of: Lanza, R.P., Langer, R., & Vacanti, J. (eds), Principles of Tissue Engineering*. San Diego, USA: Academic Press.
- Freed, L.E., Vunjak-Novakovic, G., Biron, R.J., Eagles, D., D.Lesnoy, Barlow, S.K., & R.Langer. 1994. Biodegradable polymer scaffolds for tissue engineering. *Bio/Technology*, **12**, 689–693.

- Freed, L.E., R.Langer, I.Martin, N.R.Pellis, & Vunjak-Novakovic, G. 1997. Tissue engineering of cartilage in space. *Proceedings of the National Academy of Sciences USA*, **94**, 13885–13890.
- Freed, L.E., Hollander, A.P., I.Martin, Barry, J.R., R.Langer, & Vunjak-Novakovic, G. 1998. Chondrogenesis in a cell-polymer-bioreactor system. *Experimental Cell Research*, **240**, 57–65.
- Freed, L.E., Martin, I., & Vunjak-Novakovic, G. 1999. Frontiers in tissue engineering - In vitro modulation of chondrogenesis. *Clinical Orthopaedics & Related Research*, **367**(Suppl S), S46–S58.
- Freshney, R. I. 2000. *Culture of animal cells: a manual of basic technique*. Fourth edn. New York: Wiley-Liss.
- Fry, D.L. 1968. Acute vascular endothelial changes associated with increased. *Circulation Research*, **22**, 165–197.
- Fukushima, S., Nagatsu, A., Kaibara, M., Oka, K., & Tanishita, K. 2001. Measurement of surface topography of endothelial cell and wall shear stress distribution on the cell. *JSME International Journal Series C- Mechanical Systems Machine Elements and Manufacturing*, **44**(4), 972 – 981.
- Gai, S. L., Roberts, N., Barker, A., Kleczaj, C., & Riley, A.J. 2004. Vortex interaction and breakdown over double-delta wings. *The Aeronautical Journal*, **108**(1079), 27–34.
- Gelfgat, A.Y., Bar-Yoseph, P.Z., & Solan, A. 1996a. Stability of confined swirling flow with and without vortex breakdown. *Journal of Fluid Mechanics*, **311**, 1–36.
- Gelfgat, A.Y., Bar-Yoseph, P.Z., & Solan, A. 1996b. Steady states and oscillatory instability of swirling flow with rotating top and bottom. *Physics of Fluids*, **8**(10), 2614–2625.
- Gelfgat, A.Y., Bar-Yoseph, P.Z., & Solan, A. 2001. Three-dimensional instability of axisymmetric flow in a rotating lid-cylinder enclosure. *Journal of Fluid Mechanics*, **438**, 363–377.
- Genetos, D.C., Geist, D.J., Liu, D.W., Donahue, H.J., & Duncan, R.L. 2005. Fluid shear-induced ATP secretion mediates prostaglandin release in MC3T3-E1 osteoblasts. *Journal of Bone and Mineral Research*, **20**(1), 41–49.

- Goller, H., & Ranov, T. 1968. Unsteady rotating flow in a cylinder with a free surface. *Transactions of ASME: Journal of Basic Engineering*, **90**, 445–454.
- Goodwin, T.J., Prewett, T.L., Wolf, D.A., & Spaulding, G.F. 2003. Reduced shear stress: A major component in the ability of mammalian tissues to form three-dimensional assemblies in simulated microgravity. *Journal of Cellular Biochemistry*, **51**, 301–311.
- Gottleib, D.I. 2002. Large-scale sources of neural stem cells. *Annual Review of Neuroscience*, **25**, 381–407.
- Guilak, F., Erickson, G.R., & Ting-Beall, H.P. 2002. The effects of osmotic stress on the viscoelastic and physical properties of articular chondrocytes. *Biophysical Journal*, **82**, 720–727.
- Hall, M. G. 1972. Vortex breakdown. *Annual Review of Fluid Mechanics*, **4**, 195–217.
- Hammond, T.G., & Hammond, J.M. 2001. Optimized suspension culture: the rotating wall vessel. *American Journal of Physiology: Renal Physiology*, **281**, F12–F25.
- Han, Y., Cowin, S.C., Schaffler, M.B., & S.Weinbaum. 2004. Mechanotransduction and strain amplification in osteocyte cell processes. *Proceedings of the Nation Academy of Sciences of the United States of America*, **101**(47), 16689–16694.
- Harnby, N., Edwards, M.F., & Nienow, A.W. 1992. *Mixing in the Process Industries*. Second edn. Oxford, UK: Butterworth-Heinemann Ltd.
- Hart, D.P. 2000. PIV error correction. *Experiments in Fluids*, **29**, 13–22.
- Harvey, J.K. 1962. Some observations of the vortex breakdown phenomenon. *Journal of Fluid Mechanics*, **14**, 585–592.
- He, X., & Ku, D.N. 1996. Pulsatile flow in the human left coronary artery bifurcation: average conditions. *Journal of Biomechanical Engineering*, **118**, 74–82.
- Helmke, B.P. 2004. Molecular control of cytoskeletal mechanics by hemodynamic forces. *Physiology*, **20**, 43–53.
- Helmlinger, G., Geiger, R.V., Schreck, S., & Nerem, R.M. 1991. Effects of pulsatile flow on cultured vascular endothelial cell morphology. *Journal of Biomechanical Engineering*, **113**, 123–131.

- Hillsley, M.V., & Frangos, J.A. 1994. Review: bone tissue engineering: the role of interstitial fluid flow. *Biotechnology and Bioengineering*, **43**, 573–581.
- Hillsley, M.V., & Tarbell, J.M. 2002. Oscillatory shear alters endothelial hydraulic conductivity and nitric oxide levels. *Biochemical and Biophysical Research Communications*, **293**(5), 1466–1471.
- Hinze, J.O. 1971. Turbulent fluid and particle interaction. *Pages 433–452 of: Hetsroni, S, et al. (eds), Progress in Heat and Mass Transfer*, vol. 6. Pergamon Press.
- Hirsa, A.H., Lopez, J.M., & Miraghaie, R. 2001. Measurement and computation of hydrodynamic coupling at an air/water interface with an insoluble monolayer. *Journal of Fluid Mechanics*, **443**, 271–292.
- Hirsa, A.H., Lopez, J.M., & Miraghaie, R. 2002. Symmetry breaking to a rotating wave in a lid-driven cylinder with a free surface: experimental observation. *Physics of Fluids*, **14**, L29–L32.
- Hodgson, L., & Tarbell, J.M. 2002. Solute transport to the endothelial intercellular cleft: the effect of wall shear stress. *Annals of Biomedical Engineering*, **30**(7), 936–945.
- Hoi, P.L., Savarese, T.M., & Schwartz, W.J. 2001. Neural Precursor Cells form Rudimentary Tissue-like Structures in a Rotating-Wall Vessel Bioreactor. *In Vitro Cellular and Developmental Biology*, **37**, 141–147.
- Hooker, B.S., Lee, J.M., & An, G. 1989. Response of plant tissue culture to a high shear environment. *Enzyme and Microbial Technology*, **11**, 484–490.
- Hourigan, K., Graham, L.J.W., & Thompson, M.C. 1995. Spiral streaklines in pre-vortex breakdown regions of axisymmetric swirling flows. *Physics of Fluids*, **7**(12), 3126–3128.
- Huang, H., Kamm, R.D., & Lee, R.T. 2004. Cell mechanics and mechanotransduction: pathways, probes, and physiology. *Physics of Fluids*, **287**, C1–C11.
- Humphrey, J. D. 2001. Stress, strain and mechanotransduction in cells. *Journal of Biomechanical Engineering*, **123**, 638–641.
- Humphrey, J. D. 2002. On mechanical modeling of dynamic changes in the structure and properties of adherent cells. *Mathematics and Mechanics of Solids*, **7**(5), 521–539.

- Husain, H.S., Shtern, V., & Hussain, F. 2003. Control of vortex breakdown by addition of near-axis swirl. *Physics of Fluids*, **15**(2), 271–279.
- Iosilevskii, G., Brenner, H., & Moore, C.M.V. 1993. Mass transport and chemical reaction in Taylor-vortex flows with entrained catalytic particles: applications to a novel class of immobilized enzyme biochemical reactors. *Philosophical Transactions of the Royal Society of London, Series A: Physical Sciences and Engineering*, **345**(1675), 259–294.
- Iqbal, J., & Zaidi, M. 2005. Molecular regulation of mechanotransduction. *Biochemical and Biophysical Research Communications*, **328**, 751–755.
- Ishizuka, S. 2002. Flame propagation along a vortex axis. *Progress in Energy and Combustion Science*, **28**, 477–542.
- Iwatsu, R. 2004. Analysis of flows in a cylindrical container with rotating bottom and top undeformable free surface. *JSME International Journal*, **47**(3), 549–556.
- Iwatsu, R. 2005. Numerical study of flows in a cylindrical container with rotating bottom and top flat free surface. *Journal of the Physical Society of Japan*, **74**(1), 333–344.
- J.-J. Zhong, K. Fujiyama, T. Seki, & Yoshida, T. 1994. A quantitative analysis of shear effects on cell suspension and cell culture of perilla frutescus in bioreactors. *Biotechnology and Bioengineering*, **44**, 649–654.
- Jacobs, C.R., Yellowley, C.E., Davis, B.R., Zhou, Z., & Donahue, H.J. 1998. Differential effect of steady versus oscillating flow on bone cells. *Journal of Biomechanics*, **31**, 969–976.
- Jenne, M., & Reuss, M. 1999. A critical assessment on the use of $k - \epsilon$ models for simulation of the turbulent liquid flow induced by a Rushton-turbine in baffled stirred-tank reactors. *Chemical Engineering Science*, **54**, 3921–3941.
- Jessup, J.M., Brown, D., Fitzgerald, W., Ford, R.D., Nachman, A., Goodwin, T.J., & Spaulding, G. 1994. Growth of human colorectal-carcinoma cells in NASA rotating wall vessel (RWV) produces high cell yields with differentiation and reduced glucose consumption. *Journal of Cellular Biochemistry*, **S18C**, 275.
- Jo, H., Dull, R.O., Hollis, T.M., & Tarbell, J.M. 1991. Endothelial permeability is shear-dependent, time-dependent and reversible. *American Journal of Physiology: Heart and Circulatory Physiology*, **260**, H1992–H1996.

- Kallos, M.S., Reynolds, B.A., Vescovi, A.L., & Behie, L.A. 1998. High cell density growth of mammalian neural stem cells as aggregates in bioreactors. *Pages 653–660 of: Fan, L.S., & Knowlton, T.M. (eds), Fluidization*. New York: Engineering Foundation.
- Kamm, R.D. 2002. Cellular Fluid Mechanics. *Annual Review of Fluid Mechanics*, **34**, 211–232.
- Kannan, R.Y., Salanski, H.J., Sales, K., Butler, P., & Seitalian, A.M. 2005. The roles of tissue engineering and vascularisation in the development of micro-vascular networks: a review. *Biomaterials*, **26**(14), 1857–1875.
- Kawase, Y., & Moo-Young, M. 1990. Mathematical models for design of bioreactors: applications of Kolmogoroff's theory of isotropic turbulence. *Chemical Engineering Journal*, **43**, B19–B41.
- Keane, R.D., & Adrian, R.J. 1992. Theory of cross-correlation analysis of PIV images. *Applied Scientific Research*, **49**, 191–215.
- Kim, Y., Bonassar, L.J., & Grodzinsky, A.J. 1995. The role of cartilage streaming potential: fluid flow and pressure in the stimulation of chondrocyte biosynthesis during dynamic compression. *Journal of Biomechanics*, **28**(9), 1055–1066.
- Kizito, J., Barlow, K., Adamson, J.R., & Griffin, D. 2004. Effects of flow rate on the environment in a micro-bioreactor for bone cells. *Pages IMECE2004–59897 of: 2004 ASME International Mechanical Engineering Congress and R&D Expo (CDROM)*.
- Kleis, S.J., Schreck, S., & Nerem, R.M. 1990. A viscous pump bioreactor. *Biotechnology and Bioengineering*, **36**, 771–777.
- Ku, D.N., & Giddens, D.P. 1987. Laser doppler anemometer measurements of pulsatile flow in a model carotid bifurcation. *Journal of Biomechanical Engineering*, **20**, 407–421.
- Kwon, J., Kim, B.-S., Kim, M.-J., & Park, H.-W. 2003. Suspension culture of hematopoietic stem cells in stirred bioreactors. *Biotechnology Letters*, **25**, 179–182.
- Lapin, A., Muller, D., & Reuss, M. 2004. Dynamic behavior of microbial populations in stirred bioreactors simulated with euler-lagrange methods: traveling along the lifelines of single cells. *Industrial and Engineering Chemistry Research*, **43**, 4647–4656.

- Latimer, D.C., Roth, B.J., & Parker, K.K. 2003. Analytical model for predicting mechanotransduction effects in engineered cardiac tissue. *Tissue Engineering*, **9**(2), 283–289.
- Laurencin, C.T., Ambrosio, A.M.A., Borden, M.D., & Jr, J.A. Cooper. 1999. Tissue engineering: orthopaedic applications. *Annual Review of Biomedical Engineering*, **1**, 19–46.
- Lavik, E., & Langer, R. 2004. Tissue engineering: current state and perspectives. *Applied Microbiology and Biotechnology*, **65**(1), 1455–1464.
- Leckie, F., Scragg, A.S., & Cliffe, K.C. 1991. Effect of bioreactor design and agitator speed on the growth and alkaloid accumulation by cultures of *catharanthus roseus*. *Enzyme and Microbial Technology*, **13**, 296–305.
- Lee, H.S., Millward-Sadler, S.J., & Wright, M.O. 2002. Activation of integrin - RACK1/PKC alpha signalling in human articular chondrocyte mechanotransduction. *Osteoarthritis Cartilage*, **10**(11), 890 – 897.
- Leibovich, S. 1978. Vortex Breakdown. *Annual Review of Fluid Mechanics*, **4**, 185 – 217.
- Levenberg, S., & Langer, R. 2004. Advances in Tissue Engineering. *Current Topics in Developmental Biology*, **61**, 113 – 134.
- Lever, M.J., Tarbell, J.M., & Caro, C.G. 1992. The effect of luminal flow in rabbit carotid artery on transmural fluid transport. *Experimental Physiology*, **77**, 553–563.
- Levesque, M.J., Nerem, R.M., & Sprague, E.A. 1989. The influence of shear stress on cultured vascular endothelial cells: the stress response of an anchorage-dependent mammalian cell. *Biotechnology Progress*, **5**, 1–8.
- Levins, R.M., & Glastonbury, J.R.G. 1972. Application of Kolmogoroff's theory to particle-liquid mass transfer in agitated vessels. *Chemical Engineering Science*, **27**, 537–543.
- Liu, C.-M., & Hong, L.-N. 2001. Development of a shaking bioreactor system for animal cell cultures. *Biochemical Engineering Journal*, **7**, 121–125.
- Lopez, J. M. 1994. On the bifurcation structure of axisymmetric vortex breakdown in a constricted pipe. *Phys. Fluids*, **6**, 3683 – 3693.
- Lopez, J.M. 1990. Axisymmetric vortex breakdown. Part 1. Confined swirling flow. *Journal of Fluid Mechanics*, **221**, 533–552.

- Lopez, J.M., & Hirska, A. 1998. Direct determination of the dependence of the surface shear and dilational viscosities on the thermodynamic state of the interface: theoretical foundations. *Journal of Colloid and Interface Science*, **206**, 231–239.
- Lopez, J.M., & Hirska, A. 2000. Surfactant-induced gas-liquid interfaces: nonlinear equation of state and finite surface viscosities. *Journal of Colloid and Interface Science*, **229**, 575–583.
- Lopez, J.M., & Marques, F. 2004. Mode competition between rotating waves in a swirling flow with reflection symmetry. *Journal of Fluid Mechanics*, **507**, 265–288.
- Lopez, J.M., & Perry, A.D. 1992. Axisymmetric vortex breakdown. Part 3. Onset of periodic flow and chaotic advection. *Journal of Fluid Mechanics*, **234**, 449–471.
- Lopez, J.M., Marques, F., Hirska, A.H., & Miraghaie, R. 2004. Symmetry breaking in free-surface cylinder flows. *Journal of Fluid Mechanics*, **502**, 99–126.
- Lucca-Negro, O., & O’Doherty, T. 2001. Vortex breakdown: a review. *Progress in Energy and Combustion Science*, **27**, 431–481.
- Lugt, H.J., & Abboud, M. 1997. Axisymmetric vortex breakdown with and without temperature effects in a container with a rotating lid. *Journal of Fluid Mechanics*, **179**, 179–200.
- Ma, P.X., Zhang, R., Xiao, G., & Franceschi, R. 2000. Engineering new bone tissue in vitro on highly porous poly(alpha-hydroxyl acids)/hydroxyapatite composite scaffolds. *Journal of Biomedical Materials Research*, **54**, 284–293.
- Mandelbaum, B.R., Browne, J.E., Fu, F., Micheli, L.J., Mosely, B.J., Erggelet, C., Minas, T., & Peterson, L. 1998. Articular cartilage lesions of the knee. *American Journal of Sports Medicine*, **26**(6), 853–861.
- Marques, F., & Lopez, J.M. 2001. Precessing vortex breakdown mode in an enclosed cylinder flow. *Physics of Fluids*, **13**(6), 1679–1682.
- Martin, I., Wendt, D., & Heberer, M. 2004. The role of bioreactors in tissue engineering. *Trends in Biotechnology*, **22**, 80–86.
- Martins-Green, M. 2000. Dynamics of Cell-ECM Interactions. *Pages 33–54 of: R.P. Lanza, Langer, R., & Vacanti, J. (eds), Principles of Tissue Engineering*. San Diego, USA: Academic Press.

- Mattner, T.W., Joubert, P.N., & Chong, M.S. 2003. Vortical flow. Part 2. Flow past a sphere in a constant-diameter pipe. *Journal of Fluid Mechanics*, **481**, 1–36.
- McDonald, F., Somasundaram, B., McCann, T.J., & Mason, W.T. 1996. Calcium waves in fluid flow stimulated osteoblasts are G protein mediated. *Archives of Biochemistry and Biophysics*, **326**(1), 31–38.
- McKnight, N.L., & Frangos, J.A. 2003. Strain rate mechanotransduction in aligned human vascular smooth muscle cells. *Annals of Biomedical Engineering*, **31**(3), 239–249.
- Meinhart, C.D., Wereley, S.T., & Santiago, J.G. 1999. PIV measurements of a microchannel flow. *Experiments in Fluids*, **27**, 414–419.
- Millward-Sadler, S.J., & Salter, D.M. 2004. Integrin-dependent signal cascades in chondrocyte mechanotransduction. *Annals of Biomedical Engineering*, **32**(3), 435 – 446.
- Miraghaie, R., Lopez, J.M., & Hirs, A.H. 2003. Flow induced patterning at the air-water interface. *Physics of Fluids*, **15**, L45 – L48.
- Moore, J.E., Xu, C., Glagov, S., Zarins, C.K., & Ku, D.N. 1994. Fluid wall shear stress measurements in a model of the human abdominal aorta: oscillatory behaviour and relationship to atherosclerosis. *Atherosclerosis*, **110**(2), 225–240.
- Muite, B.K. 2004. The flow in a cylindrical container with a rotating end wall at small but finite Reynolds number. *Physics of Fluids*, **16**(10), 3614–3626.
- Mununga, L., Hourigan, K., Thompson, M. C., & Lewke, T. 2004. Confined flow vortex breakdown control using a small rotating disk. *Physics of Fluids*, **16**(12), 4750–4753.
- Nagata, S. 1975. *Mixing: Principles and Applications*. New York, USA: Halsted Press.
- Nielsen, L.K. 1999. Bioreactors for Hematopoietic Cell Culture. *Annual Review of Biomedical Engineering*, **1**, 129–152.
- Nienow, A.W. 1975. Agitated vessel particle-liquid mass transfer: a comparison between theories and data. *Chemical Engineering Journal*, **9**, 153–160.
- Niklason, L.E., J.Gao, Abbott, W.M., Hirschi, K.K., Houser, S., Marini, R., & Langer, R. 1999. Functional arteries grown *in vitro*. *Science*, **284**, 489–493.

- Okulov, V.L., Sørensen, J.N., & Voigt, L.K. 2005. Vortex scenario and bubble generation in a cylindrical cavity with rotating top and bottom. *European Journal of Mechanics B*, **24**, 137–148.
- Pathi, P., Ma, T., & Locke, B.R. 2005. Role of nutrient supply on cell growth in bioreactor design for tissue engineering of hematopoietic cells. *Biotechnology and Bioengineering*, **89**(7), 743–758.
- Pavalko, F.M., Norvell, S.M., Burr, D.B., Turner, C.H., Duncan, R.L., & Bidwell, J.P. 2003. A model for mechanotransduction in bone cells: the load-bearing mechanosomes. *Journal of Cellular Biochemistry*, **88**(1), 104–112.
- Pei, M., Solchaga, L.A., Seidel, J., Zeng, L., Vunjak-Novakovic, G., Caplan, A.I., & Freed, L.E. 2002. Bioreactors mediate the effectiveness of tissue engineering scaffolds. *The FASEB Journal*, **16**(10), U392–U412.
- Perrard, M., Sauze, N. Le, Xuereb, C., & Bertrand, J. 2000. Characterisation of the turbulence in a stirred tank using particle image velocimetry. *Pages 345–352 of: Akker, H. E. A. Van Den, & Derksen, J. J. (eds), 10th European Conference on Mixing*. Delft, The Netherlands: Elsevier Science B.V.
- Pettersson, M., & Rasmuson, A.C. 1998. Hydrodynamics of suspensions agitated by pitched-blade turbine. *AIChE Journal*, **44**, 513–527.
- Planchamp, C., Vu, T.L., Mayer, J.M., Reist, M., & Testa, B. 2003. Hepatocyte hollow-fibre bioreactors: design, set-up, validation and applications. *Journal of Pharmacy and Pharmacology*, **55**, 1181–1198.
- Prasad, A.K. 2000. Stereoscopic particle image velocimetry. *Experiments in Fluids*, **29**, 103–116.
- Prasad, A.K., & Adrian, R.J. 1993. Stereoscopic particle image velocimetry applied to liquid flows. *Experiments in Fluids*, **15**, 49–60.
- Raffel, M., Willert, C. E., & Kompenhans, J. 1998. *Particle Image Velocimetry: A Practical Guide*. Berlin, Germany: Springer.
- Ramirez, L. E. S., & Lim, E.A. 2003. On the dynamics of a spherical scaffold in rotating bioreactors. *Biotechnology and Bioengineering*, **84**, 382–389.

- Reubinoff, B. E., Itsykson, P., Turetsky, T., Pera, M., Reinhartz, E., Itzik, A., & Ben-Hur, T. 2001. Neural progenitors from human embryonic stem cells. *Nature Biotechnology*, **19**, 1134–1140.
- Rusak, Z., Wang, S., & Whiting, C. H. 1998. The evolution of a perturbed vortex in a pipe to axisymmetric vortex breakdown. *J. Fluid Mech.*, **366**, 211–237.
- Saarenrinne, P., & Piirto, M. 2002. Turbulence control in a mixing tank with PIV. *In: 11th International Symposium of Applications of Laser Techniques to Fluid Mechanics*.
- Saini, S., & Wick, T. M. 2001. Modulation of biochemical properties of engineered cartilage constructs. *Pages 185–186 of: 2001 Bioengineering Conference ASME 2001*.
- Sanford, G. L., Ellerson, D., Melhado-Gardiner, C., Sroufe, A.E., & Harris-Hooker, S. 2002. Three-dimensional growth of endothelial cells in the microgravity-based rotating wall vessel bioreactor. *In vitro animal cellular and developmental biology*, **38**, 493–504.
- Saris, D. B. F., & O’Driscoll, S. W. 1999. Periosteum responds to dynamic fluid pressure by proliferating *in vitro*. *Journal of Orthopaedic Research*, **17**, 668–677.
- Schlichting, H. 1968. *Boundary-layer theory*. 6 edn. New York, USA: McGraw-Hill.
- Schmalzriedt, S., Jenne, M., Mauch, K., & Reuss, M. 2003. Intergration of physiology and fluid dynamics. *Advances in Biochemical Engineering / Biotechnology*, **49**(8), 19–68.
- Schreiber, R. E., Dunkelman, N.S., Naughton, G., & Ratcliffe, A. 1999. A method for tissue engineering of cartilage by cell seeding on bioresorbable scaffolds. *Annals of the New York Academy of Sciences*, **875**, 398–404.
- Scragg, A.H., Allan, E.J., & Leckie, F. 1988. Effect of shear on the viability of plant cell suspensions. *Enzyme and Microbial Technology*, **10**, 361–367.
- Sen, A., & Behie, L. A. 1999. The development of a medium for the *in vitro* expansion of mammalian neural stem cells. *Canadian Journal of Chemical Engineering*, **77**, 963–972.
- Sen, A., Kallos, M. S., & Behie, L. A. 2001. Effects of hydrodynamics on cultures of mammalian neural stem cell aggregates in suspension bioreactors. *Industrial and Engineering Chemistry Research*, **40**, 5350–5357.

- Sen, A., Kallos, M. S., & Behie, L. A. 2002a. Expansion of mammalian neural stem cells in bioreactors: effect of power input and medium viscosity. *Developmental Brain Research*, **134**, 103–113.
- Sen, A., Kallos, M. S., & Behie, L. A. 2002b. Passaging protocols for mammalian neural stem cells in suspension bioreactors. *Biotechnology Progress*, **18**, 337–345.
- Sen, A., Kallos, M. S., & Behie, L. A. 2004. New tissue dissociation protocol for scaled-up production of neural stem cells in suspension bioreactors. *Tissue Engineering*, **10**, 904–913.
- Serre, E., & Bontoux, P. 2002. Vortex breakdown in a three-dimensional swirling flow. *Journal of Fluid Mechanics*, **459**, 347–370.
- Shachar, M., & Cohen, S. 2003. Cardiac tissue engineering, ex-vivo: design principles in biomaterials and bioreactors. *Heart Failure Reviews*, **8**, 271–276.
- Sharma, R., Yellowley, C.E., M.Civelek, *et al.* . 2002. Intracellular calcium changes in rat aortic smooth muscle cells in response to fluid flow. *Annals of Biomedical Engineering*, **30**(3), 371–378.
- Sharp, K. V., & Adrian, R. J. 2001. PIV study of small-scale flow structure around a rushton turbine. *American Institute of Chemical Engineering Journal*, **47**, 766–778.
- Sheard, G.S., Thompson, M.C., & Hourigan, K. 2003. From spheres to circular cylinders: classification of bluff ring transitions and structure of bluff ring wakes. *Journal of Fluid Mechanics*, **492**, 147–180.
- Shraiman, B.I. 2005. Mechanical feedback as a possible regulator of tissue growth. *Proceedings of the National Academy of Sciences of the United States of America*, **102**(9), 3318–3323.
- Shtern, V., Borissov, A., & Hussain, F. 1997. Vortex sink with axial flow: solution and application. *Physics of Fluids*, **9**, 2941–2959.
- Sinsky, A.J., Fleischaker, R.J., Tyo, M.A., Giard, D.J., & Wong, D.J.C. 1981. Production of cell-derived products: virus and interferon. *Annals of the New York Academy of Sciences*, **369**, 47–59.
- Smith, R.L., Donlon, B.S., Gupta, M.K., M.Mohtai, P.Das, Carter, D.R., Cooke, J., Gibbons, G., N.Hutchinson, & Schurman, D.J. 1995. Effects of Fluid-Induced Shear on Articular

- Chondrocyte Morphology and Metabolism *In Vitro*. *Journal of Orthopaedic Research*, **13**, 824–831.
- Sodian, R., Lemke, T., Fritsche, C., Hoerstrup, S.P., Fu, P., Potapov, E.V., Hausmann, H., & Hetzer, R. 2002. Tissue engineering bioreactors: a new combined cell-seeding and perfusion system for vascular tissue engineering. *Tissue Engineering*, **8**(5), 863–870.
- Soloff, S. M., Adrian, R. J., & Liu, Z.-C. 1997. Distortion compensation for generalized stereoscopic particle image velocimetry. *Measurement Science and Technology*, **8**, 1441–1454.
- Sørensen, J.N., & Christensen, E.A. 1995. Direct numerical simulation of rotating fluid flow in a closed cylinder. *Physics of Fluids*, **7**(4), 764–778.
- Sotiropoulos, F., & Ventikos, Y. 1998. Transition from bubble-type vortex breakdown to columnar vortex in a confined swirling flow. *International Journal of Heat and Fluid Flow*, **19**, 446–458.
- Sotiropoulos, F., & Ventikos, Y. 2001. The three-dimensional structure of confined swirling flows with vortex breakdown. *Journal of Fluid Mechanics*, **426**, 155–175.
- Sotiropoulos, F., Ventikos, Y., & Lackey, T.C. 2001. Chaotic advection in three-dimensional stationary vortex-breakdown bubbles: Sil'nikov's chaos and the devil's staircase. *Journal of Fluid Mechanics*, **444**, 257–297.
- Sotiropoulos, F., Webster, D.R., & Lackey, T.C. 2002. Experiments on Lagrangian transport in steady vortex-breakdown bubbles in a confined swirling flow. *Journal of Fluid Mechanics*, **466**, 215–248.
- Spohn, A., Mory, M., & Hopfinger, E. J. 1993. Observations of vortex breakdown in an open cylindrical container with a rotating bottom. *Experiments in Fluids*, **14**, 70–77.
- Spohn, A., Mory, M., & Hopfinger, E. J. 1998. Experiments on vortex breakdown in a confined flow generated by a rotating disk. *Journal of Fluid Mechanics*, **370**, 73–99.
- Stathopoulos, N. A., & Hellums, J. D. 1984. Shear Stress Effects on Human Embryonic Kidney Cells *In Vitro*. *Biotechnology and Bioengineering*, **27**, 1021–1026.
- Steck, R., Niederer, P., & Tate, M.L.K. 2003. A finite element analysis for the prediction of load-induced fluid flow and mechanochemical transduction in bone. *Journal of Theoretical Biology*, **220**(2), 249–259.

- Stevens, J.L., Lopez, J. M., & Cantwell, B.J. 1999. Oscillatory flow states in an enclosed cylinder with a rotating endwall. *Journal of Fluid Mechanics*, **389**, 101–118.
- Stoker, M. G. P. 1973. Role of diffusion boundary layer in contact inhibition of growth. *Nature*, **246**, 200–203.
- Sucosky, P., Osorio, D. F., Brown, J. B., & Neitzel, G. P. 2004. Fluid mechanics of a spinner-flask bioreactor. *Biotechnology and Bioengineering*, **85**, 34–46.
- Szafranski, J.D., Grodzinsky, A.J., E.Burger, V.Gaschen, Hung, H.H., & Hunziker, E.B. 2004. Chondrocyte mechanotransduction: effects of compression on deformation of intracellular organelles and relevance to cellular biosynthesis. *Osteoarthritis Cartilage*, **12**(12), 937–946.
- Takeda, T., Seki, M., & Furusaki, S. 1997. Hydrodynamic damage of culture cells of carthamus tinctorius in a stirred tank reactor. *Journal of Chemical Engineering of Japan*, **27**, 466–471.
- Tarbell, J.M. 2003. Mass transport in arteries and the localization of atherosclerosis. *Annual Review of Biomedical Engineering*, **5**, 79–118.
- Tate, M.L.K. 2003. "Whither flows the fluid in bone?" An osteocyte's perspective. *Journal of Biomechanics*, **36**, 1409 – 1424.
- Taylor, C.A., & Draney, M.T. 2004. Experimental and computational methods in cardiovascular fluid mechanics. *Annual Review of Fluid Mechanics*, **36**, 197–231.
- Taylor, G. I. 1923. Stability of a viscous liquid contained between two rotating cylinders. *Philosophical Transactions of the Royal Society of London, Series A: Mathematical and Physical Sciences*, **223**, 289–343.
- Thompson, M. C., & Hourigan, K. 2003. The sensitivity of steady vortex breakdown bubbles in confined cylinder flows to rotating lid misalignment. *Journal of Fluid Mechanics*, **496**, 129–138.
- Thompson, M. C., Hourigan, K., & Sheridan, J. 1996. Three-dimensional instabilities in the wake of a circular cylinder. *Experimental Thermal and Fluid Science*, **12**(2), 190–196.
- Thompson, M. C., Leweke, T., & Provansal, M. 2001. Kinematics and dynamics of sphere wake transition. *Journal of Fluids and Structures*, **15**, 575–586.
- Townsend, A.A. 1976. *The structure of turbulent shear flow*. Second edn. Cambridge: Cambridge University Press.

- Tramper, J., Joustra, D., & Vlak, J.M. 1987. Bioreactor design for growth of shear-sensitive insect cells. In: Webb, C., & Mavituna, F. (eds), *Plant and animal cells: process possibilities*. Chichester, England: Ellis Horwood Ltd.
- Truesdell, C. 1968. *Essays in the history of mechanics*. New York, USA: Springer-Verlag.
- Truesdell, C. 1977. *A first course in rational continuum mechanics*. Vol. 1. New York, USA: Academic Press.
- Tsao, Y.-M.D., Boyd, E., Wolf, D.A., & Spaulding, G. 1994. Fluid dynamics within a rotating bioreactor in space and earth environments. *Journal of spacecraft and rockets*, **31**(6), 937–943.
- Tsao, Y.-S., Gould, S.L., & Robinson, D.K. 2000. Animal cell culture media. Pages 35–41 of: Spier, R. E. (ed), *Encyclopedia of Cell Technology*. New York, USA: John Wiley & Sons.
- Valentine, D.T., & Jahnke, C.C. 1994. Flows induced in a cylinder with both end walls rotating. *Physics of Fluids*, **6**(8), 2702–2710.
- van't Riet, K. 1979. Review of measuring methods and results in nonviscous gas-liquid mass transfer in stirred vessels. *Ind. Eng. Chem. Process Des. Dev.*, **18**, 357–363.
- Venkat, R. V., Stock, R., & Chalmers, J. J. 1996. Study of hydrodynamics in microcarrier culture spinner vessels: a particle tracking velocimetry approach. *Biotechnology and Bioengineering*, **29**, 456–466.
- Vogel, H.U. 1968. *Experimentelle ergebnisse ber die laminare strmung in einem zylindrischen gehise mit darin rotierender scheinbe*. Tech. rept. 6. Max-Planck-Institute für Strmungs-forschung, Göttingen.
- Vunjak-Novakovic, G., Freed, L.E., Biron, R. J., & Langer, R. 1996. Effects of mixing on the composition and morphology of tissue-engineered cartilage. *American Institute of Chemical Engineers Journal*, **42**, 850–860.
- Vunjak-Novakovic, G., Obradovic, B., Bursac, P., Martin, I., Langer, R., & Freed, L.E. 1998. Dynamic cell seeding of polymer scaffolds for cartilage tissue engineering. *Biotechnology Progress*, **14**, 193–202.
- Vunjak-Novakovic, G., Martin, I., Obradovic, B., Treppo, S., Grodzinsky, A.J., R.Langer, & Freed, L.E. 1999. Bioreactor cultivation conditions modulate the composition and mechanical properties of tissue-engineered cartilage. *Journal of Orthopaedic Research*, **17**, 130–138.

- Vunjak-Novakovic, G., Obradovic, B., Martin, I., & Freed, L.E. 2002. Bioreactor studies of native and tissue engineered cartilage. *Biorheology*, **39**, 259–268.
- Wang, S., & Rusak, Z. 1996. On the stability of an axisymmetric rotating flow in a pipe. *Physics of Fluids*, **8**, 1007–1015.
- Wang, S., & Rusak, Z. 1997. The dynamics of a swirling flow in a pipe and transition to axisymmetric vortex breakdown. *Journal of Fluid Mechanics*, **340**, 177–223.
- White, C.R., Haidekker, M., Bao, X., & Frangos, J.A. 2001. Temporal gradients in shear, but not spatial gradients, stimulate endothelial cell proliferation. *Circulation*, **103**, 2508–2513.
- Wiggins, P., & Phillips, R. 2005. Membrane-protein interactions in mechanosensitive channels. *Biophysical Journal*, **88**, 880–902.
- Willert, C. 1996. The fully digital evaluation of photographic PIV recordings. *Applied Scientific Research*, **56**, 79–102.
- Williams, K.A., Saini, S., & Wick, T.M. 2002. Computational fluid dynamics modeling of steady-state momentum and mass transport in a bioreactor for cartilage tissue engineering. *Biotechnology Progress*, **18**, 951–963.
- Wilson, J. R., & Duncan, N. A. 2002. Modelling the ion channel behaviour of articular chondrocytes. In: *ASME International Mechanical Engineering Congress & Exposition*. New Orleans: ASME.
- Wongsamuth, R., & Doran, P. M. 1997. The filtration properties of atropa belladonna plant cell suspensions; effects of hydrodynamic shear and elevated carbon dioxide levels on culture and filtration parameters. *Journal of Chemical Technology and Biotechnology*, **69**, 15–26.
- Wood, F. 2003. Clinical potential of autologous epithelial suspension. *Wounds*, **15**(1), 16–22.
- Woodroffe, P.J., King, J.R., Varley, C.L., & Southgate, J. 2005. Modelling cell signalling and differentiation in the urothelium. *Bulletin of Mathematical Biophysics*, **67**(2), 369–389.
- Wootton, D.M., & Ku, D.N. 1999. Fluid mechanics of vascular systems, diseases, and thrombosis. *Annual Review of Biomedical Engineering*, **1**, 299–329.
- Wu, F., Dunkelman, N., Peterson, A., Davisson, T., la Torre, R. De, & Jain, D. 1999. Bioreactor development for tissue-engineered cartilage. *Annals of the New York Academy of Sciences*, **875**, 405–411.

Young, D.F. 1979. Fluid mechanics of arterial stenoses. *Journal of Biomechanical Engineering*, **101**, 157–175.

Young, D.L., Sheen, H.J., & Hwu, T.Y. 1995. Period doubling route to chaos for a swirling flow in an open cylindrical container with a rotating disk. *Experiments in Fluids*, **18**, 389–396.